

EXPERIMENTAL AND NUMERICAL ANALYSIS OF  
PERFORMANCE ENHANCEMENTS TO A MULTI-STAGE  
TWO-EVAPORATOR TRANSCRITICAL CARBON DIOXIDE  
REFRIGERATION CYCLE

A Dissertation

Submitted to the Faculty

of

Purdue University

by

Riley B. Barta

In Partial Fulfillment of the

Requirements for the Degree

of

Doctor of Philosophy

December 2020

Purdue University

West Lafayette, Indiana

**THE PURDUE UNIVERSITY GRADUATE SCHOOL  
STATEMENT OF DISSERTATION APPROVAL**

Dr. Eckhard A. Groll, Chair

School of Mechanical Engineering

Dr. James E. Braun

School of Mechanical Engineering

Dr. W. Travis Horton

School of Civil Engineering and School of Mechanical Engineering

Dr. Nicole L. Key

School of Mechanical Engineering

Dr. Davide Ziviani

School of Mechanical Engineering

**Approved by:**

Dr. Eckhard A. Groll

Head of the School of Mechanical Engineering

For my mother.

## ACKNOWLEDGMENTS

First, I would like to thank my family. Their endless support, motivation, and desire to celebrate milestones helped make this thesis possible.

To my adviser, Professor Groll, thank you for your patience, guidance, and overwhelming support. Your passion and love for Thermodynamics is contagious, and once I stopped getting nervous when you stood up and went to the screen out of excitement during presentations, I came to the conclusion that I would be lucky to retain half of the passion for our subject that you convey every day. I would be remiss if I did not mention the lessons I learned from you outside of the laboratory about global engineering, education, and how to have both a successful career and family life, which broadened the education I received at Herrick in the most significant sense of the word.

Professor Braun, your guidance on research and education over the years has been invaluable, and the semester I spent teaching Thermo with you will always be one of my most challenging and rewarding experiences at Purdue. I admire your ability to balance excellence with being easy-going, and will recall your demeanor and humility if I ever feel in danger of taking myself too seriously. To Professor Horton, your kindness and thorough research guidance over the years exemplify the notion that people are humans first and researchers second. Furthermore, our discussions about dirt biking in between psychrometric chamber tests offered more reprieve to my stress than I can explain. Professor Key, I enjoyed every one of our interactions thoroughly, and also learned about administrative growth from watching you step into the position as Graduate Chair.

Davide, or at this point, Professor Ziviani, watching your path from visiting scholar in 2015 to Assistant Professor in 2020 has been more helpful than I could ever explain. Your openness about the positive, and not so positive, aspects of this journey



have given me understanding of the academic process that would have been nearly impossible to gain otherwise. Your hands-on guidance, patience, and friendship are in no small part why I am able to write this thesis, and I am beyond grateful for the time and effort you've spent on helping me develop as a researcher and educator.

To my colleagues at the Herrick Labs, you are the key to making the Herrick environment such an amazing place to conduct research. Never being too busy to help one another, always showing kindness, and balancing a drive for excellence without taking anyone too seriously are all pillars of our lab, and I have been incredibly fortunate to benefit greatly from them. In particular, I would like to thank Alejandro Lavernia, Leon Brendel, Jon Ore, Vatsal Shah, Parveen Dhillon, Haotian Liu, Andreas Hoess, Orkan Kurtulus, Tyler Shelly, Junyan Ren, Cai Rohleder, Nick Salts, Xinye Zhang, Bin Yang, Ammar Bahman, Harshad Inamdar, Nick Czapla, Lennart Stania, and Florian Simon for their friendship and support over the course of my time at Herrick. The list of people that have helped me through this process is endless, and I am grateful for all who have helped make my time at the Herrick Labs so fantastic.

I would also like to acknowledge the shop and Jeff at Research Machining Services for all of their patience, guidance, and hard work over the years. This was yet another dimension of education I gained at Herrick, and I will be forever thankful for it. Special thanks go to Frank for his patience, guidance, and humor, Bob for his commitment to student success at very early hours, and Charlie for his diverse knowledge and endless willingness to help. Ingo Frohboese at TLK Thermo was also instrumental in all dynamic modeling efforts. Additionally, the Fall 2018 ME Senior design teams were very helpful in initial construction of the test stand. I would also like to acknowledge the sponsors Bechtel, Regal Beloit, and Inventherm for their support. Norm, Steve, Jason, and David offered lessons from industry that undoubtedly helped round out my education.

# TABLE OF CONTENTS

	Page
LIST OF TABLES . . . . .	x
LIST OF FIGURES . . . . .	xv
SYMBOLS . . . . .	xxi
NOMENCLATURE . . . . .	xxiii
ABBREVIATIONS . . . . .	xxv
ABSTRACT . . . . .	xxvii
1 INTRODUCTION . . . . .	1
1.1 Motivation . . . . .	1
1.2 Transcritical Carbon Dioxide Cycles . . . . .	4
1.2.1 Conventional and Advanced Cycles . . . . .	4
1.2.2 Stationary Refrigeration Applications . . . . .	19
1.2.3 Transportation Refrigeration Applications . . . . .	31
1.2.4 Discussion, Challenges, and Future Prospects . . . . .	33
1.3 Research Focus and Open Questions . . . . .	37
1.3.1 Multi-Stage Two-Evaporator Carbon Dioxide Cycles . . . . .	37
1.3.2 System Design . . . . .	38
1.3.3 Ejector Design . . . . .	38
1.3.4 Dynamic Behavior . . . . .	39
1.4 Research Objectives and Approach . . . . .	40
1.5 Overview . . . . .	42
2 SYSTEM DESIGN . . . . .	43
2.1 System Design Introduction . . . . .	44
2.2 Cycle Design and Thermodynamic Modeling . . . . .	46
2.2.1 Cycle Design Overview . . . . .	46

	Page
2.2.2 Thermodynamic Model Overview . . . . .	55
2.2.3 Design Constraints and Results from Modeling . . . . .	60
2.3 Component Selection and Test Stand Construction . . . . .	62
2.3.1 Primary Component Selection . . . . .	62
2.3.2 Selection of Measurement Devices . . . . .	64
2.4 Experimental Operation and Validation . . . . .	68
2.5 System Design Conclusions . . . . .	77
3 EJECTOR DESIGN . . . . .	79
3.1 Ejector Design Introduction . . . . .	79
3.2 Approach and Sub-Models . . . . .	82
3.2.1 Sub-Component Modeling Strategy . . . . .	83
3.2.2 Cycle Description . . . . .	88
3.3 Numerical Description and Solution Schemes . . . . .	90
3.3.1 Numerical Strategy for Validation . . . . .	93
3.3.2 Solution Scheme for Design . . . . .	93
3.3.3 Cycle Analysis and Optimization . . . . .	94
3.4 Results and Discussion . . . . .	97
3.4.1 Experimental Validation . . . . .	97
3.4.2 Trends of Component Efficiency and Geometry . . . . .	99
3.4.3 Effects of Operating Condition on Geometry . . . . .	104
3.4.4 Effects of Cycle Efficiency Optimization on Geometry . . . . .	107
3.5 Practical Considerations . . . . .	111
3.6 Ejector Design Conclusions . . . . .	114
4 DYNAMIC MODELING . . . . .	117
4.1 Dynamic Modeling Introduction . . . . .	117
4.2 Model Overview . . . . .	119
4.3 Boundary Conditions and Solution Schemes . . . . .	123
4.4 Component Models . . . . .	129

	Page
4.4.1 Heat Exchangers . . . . .	130
4.4.2 Compressors . . . . .	133
4.4.3 Expansion Valves, Flash Tanks, and Tubing . . . . .	142
4.5 Model Application for Controls Development . . . . .	146
4.6 Dynamic Modeling Conclusions . . . . .	149
5 EXPERIMENTAL TESTING . . . . .	150
5.1 Experimental Testing Introduction . . . . .	150
5.2 System Overview . . . . .	153
5.2.1 Overall Design . . . . .	153
5.2.2 Analyzed Cycles . . . . .	154
5.3 Parametric Comparison Between Architectures . . . . .	157
5.4 Ejector Control and Performance Assessment . . . . .	168
5.5 System Behavior . . . . .	177
5.5.1 Cycle Control and Liquid Level Management . . . . .	177
5.5.2 Pump Operation . . . . .	181
5.5.3 Relative Timescales of System Dynamics . . . . .	182
5.6 Experimental Testing Conclusions . . . . .	184
6 DYNAMIC MODEL VALIDATION AND EVALUATION . . . . .	186
6.1 Steady State Validation . . . . .	186
6.1.1 Compressor Sub-Model . . . . .	186
6.1.2 Cycle Performance . . . . .	190
6.2 Transient Validation . . . . .	194
6.2.1 Validation Strategy . . . . .	194
6.2.2 Charge Migration . . . . .	196
6.2.3 Model Validation Results . . . . .	200
6.3 Control Scheme Exploration and Case Study Validation . . . . .	210
6.4 Dynamic Model Validation and Evaluation Conclusions . . . . .	215
7 CONCLUSIONS, CHALLENGES, AND FUTURE WORK . . . . .	217

	Page
7.1 Conclusions . . . . .	217
7.2 Challenges and Lessons Learned . . . . .	219
7.3 Future Work . . . . .	224
A Appendix A: Tabulated Experimental Steady State Data . . . . .	227
B Appendix B: Tabulated Experimental Transient Data . . . . .	275
C Appendix C: Post-Processing Code . . . . .	305
C.1 Baseline Cycle Analysis . . . . .	305
C.2 MT Economization Cycle Analysis . . . . .	313
C.3 Ejector Cycle Analysis . . . . .	324
C.4 Ejector and Pump Cycle Analysis . . . . .	336
REFERENCES . . . . .	349

## LIST OF TABLES

Table	Page
1.1 Summary of common cycle modifications, excluding expansion work recovery (Experimental, Optimization, Theoretical). . . . .	9
1.2 Summary of select research on expansion work recovery methods. . . . .	17
1.3 Summary of reported control schemes. . . . .	30
2.1 Summary of select cycle modification studies. . . . .	45
2.2 Possible cycle architectures for the CO <sub>2</sub> test stand. . . . .	52
2.3 Recommended design velocities throughout a refrigeration system [113]. . .	59
2.4 Summary of chosen design points for the CO <sub>2</sub> test stand. . . . .	59
2.5 Summary of evaporator design points for the CO <sub>2</sub> test stand. . . . .	61
2.6 EXV operating conditions and valve selections for the CO <sub>2</sub> test stand. . . .	62
2.7 Summary of sensors and corresponding uncertainties for the CO <sub>2</sub> test stand.	65
2.8 Experimental results from preliminary CO <sub>2</sub> test stand operation. . . . .	75
3.1 Ratios and angles applied in the ejector design model. . . . .	89
3.2 Compressor map coefficients applied in the ejector system model. . . . .	97
3.3 MAE obtained during validation of component diameters throughout the ejector. . . . .	99
4.1 Map for the three cell types utilized in the TIL Suite [127]. . . . .	124
4.2 Pressure node initial values used in the dynamic test stand simulation. .	125
4.3 PHX geometric parameters input to the dynamic test stand model. . . .	131
4.4 MCHX geometric parameters input to the dynamic test stand model. . .	132
4.5 Summary of applied Pi groups for the mapping of the compressors in the CO <sub>2</sub> test stand [139]. . . . .	135
4.6 Summary of scaling coefficients $a_1$ applied to expressions for efficiencies of the compressors in the CO <sub>2</sub> test stand, shown in Equations 4.7, 4.8, and 4.9.	137
5.1 Overview of the tests conducted with the CO <sub>2</sub> test stand. . . . .	156

Table	Page
5.2 Statistical parameters regarding the consistency of test conditions for the reported experimental results. . . . .	159
5.3 Summary of the obtained data at maximum COP gas cooler outlet pressures over a range of ambient temperatures for all reported steady state tests. . . . .	165
6.1 Results from simulated variation of the test stand charge in LT economization mode. . . . .	200
6.2 EXV PI controller parameters applied in control scheme simulations. . .	211
A.1 Baseline cycle, temperatures 1 of 2, steady state raw data, tests 1 of 2. .	228
A.2 Baseline cycle, temperatures 1 of 2, steady state raw data, tests 2 of 2. .	229
A.3 Baseline cycle, temperatures 2 of 2, steady state raw data, tests 1 of 2. .	230
A.4 Baseline cycle, temperatures 2 of 2, steady state raw data, tests 2 of 2. .	231
A.5 Baseline cycle, pressures 1 of 2, steady state raw data, tests 1 of 2. . . .	232
A.6 Baseline cycle, pressures 1 of 2, steady state raw data, tests 2 of 2. . . .	233
A.7 Baseline cycle, pressures 2 of 2, steady state raw data, tests 1 of 2. . . .	234
A.8 Baseline cycle, pressures 2 of 2, steady state raw data, tests 2 of 2. . . .	235
A.9 Baseline cycle, additional measurements, steady state raw data, tests 1 of 2.	236
A.10 Baseline cycle, additional measurements, steady state raw data, tests 2 of 2.	237
A.11 Baseline cycle, specific enthalpies, steady state data, tests 1 of 2. . . . .	238
A.12 Baseline cycle, specific enthalpies, steady state data, tests 2 of 2. . . . .	239
A.13 Baseline cycle, pressures, steady state data, tests 1 of 2. . . . .	240
A.14 Baseline cycle, pressures, steady state data, tests 2 of 2. . . . .	241
A.15 Baseline cycle, primary cycle parameters, steady state data, tests 1 of 2.	242
A.16 Baseline cycle, primary cycle parameters, steady state data, tests 2 of 2.	243
A.17 Baseline cycle, additional parameters, steady state data, tests 1 of 2. . .	244
A.18 Baseline cycle, additional parameters, steady state data, tests 2 of 2. . .	245
A.19 MT economization cycle, temperatures 1 of 2, steady state raw data. . .	246
A.20 MT economization cycle, temperatures 2 of 2, steady state raw data. . .	247
A.21 MT economization cycle, pressures 1 of 2, steady state raw data. . . . .	248

Table	Page
A.22 MT economization cycle, pressures 2 of 2, steady state raw data. . . . .	249
A.23 MT economization cycle, additional measurements, steady state raw data. . . . .	250
A.24 MT economization cycle, specific enthalpies, steady state data. . . . .	251
A.25 MT economization cycle, specific enthalpies and pressures, steady state data. . . . .	252
A.26 MT economization cycle, primary cycle parameters, steady state data. . . . .	253
A.27 MT economization cycle, additional parameters, steady state data. . . . .	254
A.28 Ejector cycle, temperatures 1 of 2, steady state raw data. . . . .	255
A.29 Ejector cycle, temperatures 2 of 2, steady state raw data. . . . .	256
A.30 Ejector cycle, pressures 1 of 2, steady state raw data. . . . .	257
A.31 Ejector cycle, pressures 2 of 2 and mass flow rate, steady state raw data. . . . .	258
A.32 Ejector cycle, additional measurements, steady state raw data. . . . .	259
A.33 Ejector cycle, specific enthalpies, steady state data. . . . .	260
A.34 Ejector cycle, specific enthalpies and pressures, steady state data. . . . .	261
A.35 Ejector cycle, primary cycle parameters, steady state data. . . . .	262
A.36 Ejector cycle, additional parameters, steady state data. . . . .	263
A.37 Ejector and pump cycle, temperatures 1 of 2, steady state raw data. . . . .	264
A.38 Ejector and pump cycle, temperatures 2 of 2, steady state raw data. . . . .	265
A.39 Ejector and pump cycle, pressures 1 of 2, steady state raw data. . . . .	266
A.40 Ejector and pump cycle, pressures 2 of 2 and mass flow rate, steady state raw data. . . . .	267
A.41 Ejector and pump cycle, additional measurements, steady state raw data. . . . .	268
A.42 Ejector and pump cycle, pump measurements, steady state raw data. . . . .	269
A.43 Ejector and pump cycle, specific enthalpies, steady state data. . . . .	270
A.44 Ejector and pump cycle, specific enthalpies and pressures, steady state data. . . . .	271
A.45 Ejector and pump cycle, parameters 1 of 3, steady state data. . . . .	272
A.46 Ejector and pump cycle, parameters 2 of 3, steady state data. . . . .	273
A.47 Ejector and pump cycle, parameters 3 of 3, steady state data. . . . .	274



Table	Page
B.1 Specific enthalpies from experimental data from transient validation case study 1, time segment 1 of 2. . . . .	276
B.2 Specific enthalpies from experimental data from transient validation case study 1, time segment 2 of 2. . . . .	277
B.3 Specific enthalpies and pressures from experimental data from transient validation case study 1, time segment 1 of 2. . . . .	278
B.4 Specific enthalpies and pressures from experimental data from transient validation case study 1, time segment 2 of 2. . . . .	279
B.5 Parameters from experimental data from transient validation case study 1, time segment 1 of 2. . . . .	280
B.6 Parameters from experimental data from transient validation case study 1, time segment 2 of 2. . . . .	281
B.7 Specific enthalpies from experimental data from transient validation case study 2, time segment 1 of 2. . . . .	282
B.8 Specific enthalpies from experimental data from transient validation case study 2, time segment 2 of 2. . . . .	283
B.9 Specific enthalpies and pressures from experimental data from transient validation case study 2, time segment 1 of 2. . . . .	284
B.10 Specific enthalpies and pressures from experimental data from transient validation case study 2, time segment 2 of 2. . . . .	285
B.11 Parameters from experimental data from transient validation case study 2, time segment 1 of 2. . . . .	286
B.12 Parameters from experimental data from transient validation case study 2, time segment 2 of 2. . . . .	287
B.13 Specific enthalpies from experimental data from transient validation case study 3, time segment 1 of 2. . . . .	288
B.14 Specific enthalpies from experimental data from transient validation case study 3, time segment 2 of 2. . . . .	289
B.15 Specific enthalpies and pressures from experimental data from transient validation case study 3, time segment 1 of 2. . . . .	290
B.16 Specific enthalpies and pressures from experimental data from transient validation case study 3, time segment 2 of 2. . . . .	291
B.17 Parameters from experimental data from transient validation case study 3, time segment 1 of 2. . . . .	292

Table	Page
B.18 Parameters from experimental data from transient validation case study 3, time segment 2 of 2. . . . .	293
B.19 Specific enthalpies from experimental data from transient validation case study 4, time segment 1 of 2. . . . .	294
B.20 Specific enthalpies from experimental data from transient validation case study 4, time segment 2 of 2. . . . .	295
B.21 Specific enthalpies and pressures from experimental data from transient validation case study 4, time segment 1 of 2. . . . .	296
B.22 Specific enthalpies and pressures from experimental data from transient validation case study 4, time segment 2 of 2. . . . .	297
B.23 Parameters from experimental data from transient validation case study 4, time segment 1 of 2. . . . .	298
B.24 Parameters from experimental data from transient validation case study 4, time segment 2 of 2. . . . .	299
B.25 Single-stage compressor validation raw data, 1 of 2 . . . . .	300
B.26 Single-stage compressor validation raw data, 2 of 2 . . . . .	301
B.27 Two-stage compressor validation raw data, 1 of 3 . . . . .	302
B.28 Two-stage compressor validation raw data, 2 of 3 . . . . .	303
B.29 Two-stage compressor validation raw data, 3 of 3 . . . . .	304

## LIST OF FIGURES

Figure	Page
1.1 P-T and T-s diagrams of CO <sub>2</sub> generated using CoolProp [13,14]. . . . .	6
1.2 Map of common transcritical CO <sub>2</sub> cycle modifications to increase cycle performance. . . . .	8
1.3 Summary of potential COP improvements of modifications to transcritical CO <sub>2</sub> cycles relative to 4-component cycles. . . . .	19
1.4 (a) Schematic of a transcritical CO <sub>2</sub> booster cycle for supermarket application [66]; (b) State points of a transcritical CO <sub>2</sub> booster cycle operation for supermarket application on a P-h diagram [66]. . . . .	22
1.5 Schematic of parallel compression, ejector, and flooded evaporator cycle in a transcritical CO <sub>2</sub> supermarket application [79]. . . . .	26
1.6 Overview of a hierarchical control scheme applied in a multi-stage transcritical CO <sub>2</sub> refrigeration cycle [82]. . . . .	28
1.7 Visual representation of Q-learning algorithm differences resulting from the analysis of a hierarchical control scheme applied in a multi-stage transcritical CO <sub>2</sub> refrigeration cycle [82]. . . . .	28
2.1 Photo of the completed transcritical CO <sub>2</sub> test stand inside of a psychrometric chamber. . . . .	43
2.2 (a) Schematic of the experimental CO <sub>2</sub> test stand in EXV mode; (b) Theoretical state points of the experimental CO <sub>2</sub> test stand in EXV mode on a P-h diagram. . . . .	47
2.3 (a) Schematic of the experimental CO <sub>2</sub> test stand in ejector mode; (b) Theoretical state points of the experimental CO <sub>2</sub> test stand in ejector mode operation on a P-h diagram. . . . .	49
2.4 (a) Photo of the adjustable ejector applied in the CO <sub>2</sub> test stand; (b) Technical drawing of the adjustable ejector applied in the CO <sub>2</sub> test stand. . . . .	50
2.5 Photo of the CO <sub>2</sub> pump installed in the test stand. . . . .	51
2.6 Detailed P&ID schematic of the CO <sub>2</sub> test stand. . . . .	52
2.7 Photo of liquid level measurements in the CO <sub>2</sub> test stand. . . . .	54

Figure	Page
2.8 Summary of the EXV to Ejector transition in the CO <sub>2</sub> test stand. . . . .	55
2.9 Flowchart of the ejector solver integrated into the CO <sub>2</sub> test stand model shown in Figure 2.3(b) . . . . .	57
2.10 Rear view of the CO <sub>2</sub> test stand placed inside of a psychrometric chamber.	66
2.11 Power measurement wiring diagram for the CO <sub>2</sub> test stand. . . . .	67
2.12 CO <sub>2</sub> test stand power supply schematic. . . . .	68
2.13 CO <sub>2</sub> test stand energy balance in schematic form. . . . .	70
2.14 MT evaporator energy balance: Comparison of heat transfer rates between refrigerant- and EG-sides. . . . .	72
2.15 P-h diagram of the experimental cycle achieved with the CO <sub>2</sub> test stand using MT evaporator economization, cycle 2. . . . .	73
2.16 P-h diagram of the experimental cycle achieved with the CO <sub>2</sub> test stand using LT evaporator economization, cycle 3. . . . .	74
2.17 P-h diagram of the experimental cycle achieved with the CO <sub>2</sub> test stand using an ejector, cycle 5. . . . .	74
2.18 System pressure variation over time during the transition from EXV to ejector mode in the CO <sub>2</sub> test stand. . . . .	76
3.1 (a) Ejector components and internal states; (b) Ejector process applied in transcritical CO <sub>2</sub> operation shown on a P-h diagram. . . . .	83
3.2 Schematic of the CO <sub>2</sub> ejector cycle used in the optimization studies. . . . .	90
3.3 Flowchart for the ejector solver utilized for ejector design and validation. . .	92
3.4 Flowchart for analysis of the ejector cycle used in the optimization studies.	95
3.5 Ejector model validation with: (a) Nozzle data input simulation; and, (b) Fully numerical simulation. . . . .	98
3.6 Through variation of the efficiency of one component at a time, with the other two component efficiencies held constant at 0.75, the assessment of: (a) Ejector efficiency variation with component efficiency; and, (b) Ejector mixing section diameter variation with component efficiency. . . . .	101
3.7 (a) Ejector efficiency variation with gas cooler pressure and evaporating temperature; and, (b) Variation of ejector system COP difference relative to a four component system with gas cooler pressure and evaporating temperature. . . . .	106

Figure	Page
3.8 Resulting diameters of the: (a) Ejector motive nozzle throat with varying gas cooler pressure and evaporating temperature; and, (b) Ejector mixing section with varying gas cooler pressure and evaporating temperature. . .	107
3.9 Ejector efficiency and COP variation with ratios of: (a) Ejector motive to suction nozzle diameters; and, (b) Ejector mixing section to diffuser outlet diameters. . . . .	108
3.10 Motive to suction nozzle throat diameter ratio variation with gas cooler pressure and evaporating temperature for the case of: (a) Ejector efficiency optimization; and, (b) System COP optimization. . . . .	109
3.11 Variation with gas cooler pressure and evaporating temperature of: (a) Ejector pressure rise for the case of system COP optimization; and, (b) Ejector efficiency for the case of system COP optimization. . . . .	111
3.12 CO <sub>2</sub> ejector with broken solder joint and galled threads. . . . .	112
3.13 CO <sub>2</sub> ejector with: (a) Tapped threads; and, (b) Tapped threads and clean welds. . . . .	112
3.14 CO <sub>2</sub> ejector with clean welds and tapped threads. . . . .	113
3.15 Proposed double o-ring design for additional leak protection on variable nozzle outer diameters. . . . .	114
3.16 (a) CAD rendering of ejector design for traditional manufacturing; (b) CAD rendering of ejector design for additive manufacturing. . . . .	115
4.1 TIL library structure [127]. . . . .	121
4.2 List of possible fluid types and connectors available within the TIL library [127]. . . . .	122
4.3 Cycle assessed in the Dymola environment [127]. . . . .	123
4.4 (a) Example of using the $(dp/dt)$ module provided within the TIL library [127]; (b) Pressure node in Dymola environment [127]. . . . .	126
4.5 Dymola finite-volume heat exchanger analysis method overview [127]. . .	128
4.6 (a) PHX schematic with examples of modifiable parameters in TIL Library [127]; (b) MCHX schematic with examples of modifiable parameters in TIL Library [127]. . . . .	131
4.7 First stage compressor operating envelope with experimental operating data of the experimental campaign in the CO <sub>2</sub> test stand. . . . .	134
4.8 P-h diagram of a two-stage compression process using a transcritical CO <sub>2</sub> compressor with intercooling. . . . .	137

Figure	Page
4.9 Schematic of heat and mass flow within a two-stage compressor. . . . .	138
4.10 Refrigerant superheat before and after cooling the motor of a semi-hermetic CO <sub>2</sub> compressor. . . . .	139
4.11 (a) First stage CO <sub>2</sub> compressor overall efficiency with motor superheating and varying heat loss distribution between stages; (b) Second stage CO <sub>2</sub> compressor overall efficiency with varying heat loss distribution between stages. . . . .	141
4.12 (a) Experimental discharge temperatures from both compression stages of the two-stage compressor in the CO <sub>2</sub> test stand;(b) Heat transfer path between compressor stages. . . . .	142
4.13 Curves of CCMT EXV capacities over the range of opening percentages. . . . .	143
4.14 (a) Comparison of effective flow areas calculated for EXV 1; (b) Resulting EXV discharge coefficient calculation, $C_d$ , from EXV 1 data. . . . .	145
4.15 Visualization of the: (a) Ramp structure in the Dymola environment [127]; and, (b) Ramp connected to an EXV in the Dymola environment [127]. . . . .	148
5.1 P-h diagram of experimental test stand data from the baseline cycle at four ambient temperatures. . . . .	159
5.2 P-h diagram of experimental test stand data from the MT economization cycle at four ambient temperatures. . . . .	160
5.3 P-h diagram of experimental test stand data from the ejector cycle at four ambient temperatures. . . . .	160
5.4 P-h diagram of experimental test stand data from the ejector and pump cycle at four ambient temperatures. . . . .	161
5.5 Baseline cycle COP with gas cooling pressure variation at four ambient temperatures. . . . .	162
5.6 MT economization cycle COP with gas cooling pressure variation at four ambient temperatures. . . . .	163
5.7 Ejector cycle COP with gas cooling pressure variation at four ambient temperatures. . . . .	163
5.8 Summary of maximum COP values at the corresponding gas cooler outlet pressures over a range of ambient temperatures for all cycles tested. . . . .	164
5.9 Summary of cooling capacities over a range of ambient temperatures for all reported steady state tests for each architecture.. . . .	167

Figure	Page
5.10 Ejector efficiency variation with motive nozzle modulation at four ambient temperatures. . . . .	169
5.11 Ejector entrainment ratio variation with motive nozzle modulation at four ambient temperatures. . . . .	171
5.12 Ejector pressure lift variation with motive nozzle modulation at four ambient temperatures. . . . .	171
5.13 Ejector efficiency variation with pump outlet pressure modulation at two ambient temperatures. . . . .	173
5.14 Ejector entrainment ratio variation with pump outlet pressure modulation at two ambient temperatures. . . . .	174
5.15 Ejector pressure lift variation with pump outlet pressure modulation at two ambient temperatures. . . . .	175
5.16 CO <sub>2</sub> test stand schematic with valve labels. . . . .	179
6.1 Compressor map mass flow rate validation for: (a) Single-stage compressor; and, (b) Two-stage compressor. . . . .	188
6.2 Compressor map discharge temperature validation for: (a) Single-stage compressor; and, (b) Two-stage compressor. . . . .	188
6.3 Compressor map power consumption validation for: (a) Single-stage compressor; and, (b) Two-stage compressor. . . . .	189
6.4 Test stand system model steady state validation of: (a) LT evaporation temperature; and, (b) MT evaporation temperature. . . . .	191
6.5 Test stand system model steady state validation of: (a) LT evaporator cooling capacity; and, (b) MT evaporator cooling capacity. . . . .	192
6.6 Test stand system model steady state validation of: (a) First stage power consumption; and, (b) Second and third stage compressor power consumption. . . . .	193
6.7 Test stand system model steady state validation of: (a) Gas cooling pressure; and, (b) Gas cooler outlet temperature. . . . .	194
6.8 Comparison of simulated and experimental flash tank liquid level variation.	197
6.9 Comparison of simulated charge variation effects on the test stand operating in LT economization mode. . . . .	199
6.10 Transient case study 1, MV actuation, comparison of experimental and simulated values. . . . .	202

Figure	Page
6.11 Transient case study 2, MT EXV actuation, comparison of experimental and simulated values. . . . .	204
6.12 Transient case study 3, LT EXV actuation, comparison of experimental and simulated values. . . . .	207
6.13 Transient case study 4, GC outlet EXV actuation, comparison of experimental and simulated values. . . . .	208
6.14 Pull down controls development scenario simulated values. . . . .	213
6.15 Excitation controls development scenario simulated values. . . . .	215



## SYMBOLS

$A$	Area	$[\text{m}^2]$
$a$	Area per total ejector flow rate	$[(\text{m}^2 \cdot \text{s}) \cdot \text{kg}^{-1}]$
$a_i$	Compressor map coefficient	$[-]$
$c_p$	Specific heat at constant pressure	$[\text{kJ} \cdot (\text{kg-K})^{-1}]$
$C_t$	Diffuser lift coefficient	$[-]$
$d$	Diameter	$[\text{mm}]$
$\Delta$	Difference	$[\text{Units Vary}]$
$E$	Energy	$[\text{kWh}]$
$\dot{E}$	Energy transfer rate	$[\text{kW}]$
$\eta$	Efficiency	$[-]$
$F$	Correction factor	$[-]$
$f$	Frequency	$[\text{Hz}]$
$h$	Specific enthalpy	$[\text{kJ} \cdot \text{kg}^{-1}]$
$k_v$	Flow coefficient	$[\text{m}^3 \cdot \text{hr}^{-1}]$
$L$	Length	$[\text{m}]$
$m$	Mass	$[\text{kg}]$
$\dot{m}$	Mass flow rate	$[\text{kg} \cdot \text{s}^{-1}]$
$n$	Rotational speed	$[1 \cdot \text{min}^{-1}]$
$P$	Pressure	$[\text{kPa}]$
$\dot{Q}$	Heat transfer rate	$[\text{kW}]$
$RH$	Relative humidity	$[\%]$
$\rho$	Density	$[\text{kg} \cdot \text{m}^{-3}]$
$s$	Specific entropy	$[\text{kJ} \cdot (\text{kg-K})^{-1}]$
$T$	Temperature	$[\text{°C}]$

$tol$	Tolerance	[Units Vary]
$\Theta$	Angle	[°]
$U$	Uncertainty	[Units Vary]
$u$	Velocity	[m · s <sup>-1</sup> ]
$\nu$	Specific volume	[m <sup>3</sup> · kg <sup>-1</sup> ]
$V$	Volume	[m <sup>3</sup> ]
$\dot{V}$	Volumetric flow rate	[m <sup>3</sup> · sec <sup>-1</sup> ]
$w$	Entrainment ratio	[—]
$\dot{W}$	Power	[kW]
$wt\%$	Mass Percentage	[%]
$x$	Quality	[—]

## NOMENCLATURE

AC	Air Conditioning
BV	Ball Valve
CFC	Chlorofluorocarbon
CFD	Computational Fluid Dynamics
COP	Coefficient of Performance
CO <sub>2</sub>	Carbon Dioxide
DX	Direct Expansion
DHW	Domestic Heating of Water
EG	Ethylene Glycol
EXV	Electronic Expansion Valve
FS	Full Scale
GC	Gas Cooler
GWP	Global Warming Potential
HC	Hydrocarbon
HCFC	Hydro Chlorofluorocarbon
HCFO	Hydro Chlorofluoroolefin
HEM	Homogeneous Equilibrium Model
HFC	Hydrofluorocarbon
HFO	Hydrofluoroolefin
HP	High Pressure
HRM	Homogeneous Relaxation Model
HVAC&R	Heating, Ventilation, Air Conditioning and Refrigeration
HX	Heat Exchanger
IC	Intercooler

IHX	Internal Heat Exchanger
LP	Low Pressure
LRA	Locked Rotor Amperage
LT	Low Temperature
LTE	Low Temperature Evaporator
MAE	Mean Absolute Error
MC	Microchannel
MCHX	Microchannel Heat Exchanger
MIMO	Multi-Input Multi-Output
MOPD	Maximum Operating Pressure Differential
MT	Medium Temperature
MTE	Medium Temperature Evaporator
MV	Metering Valve
PHX	Plate Heat Exchanger
PI	Proportional Integral
PRV	Pressure Relief Valve
P&ID	Piping and Instrumentation Diagram
RDG	Reading
RE	Relative Error
RLA	Rated Load Amperage
SISO	Single-Input Single-Output
SLHX	Suction-to-Liquid Line Heat Exchanger
TC	Thermocouple
TEWI	Total Equivalent Warming Impact
TXV	Thermostatic Expansion Valve
VFD	Variable Frequency Drive

## ABBREVIATIONS

Amb	Ambient
bal	Balance
C	Speed of Sound
calc	Calculated
comp	Compressor
cool	Cooling
disp	Displacement
d	Ejector Diffuser, Discharge
e	Energy
EG	Ethylene-Glycol
eject	Ejector
evap	Evap
f	Liquid
g	Vapor
GC	Gas Cooler
HP	High Pressure
i	Iteration
in	Inlet
is	Isentropic
LP	Low Pressure
LT	Low Temperature
m	Mass, Motive
mb	Ejector Motive Receiving
mi	Ejector Motive Inlet

mix	Ejector Mixing Section
motive	Ejector Motive Inlet
MT	Medium Temperature
out	Outlet
p	Momentum
ref	Refrigerant
s	Isentropic, Suction
sat	Saturated
sb	Ejector Suction Receiving
si	Ejector Suction Inlet
suc	Suction
suction	Ejector Suction
X	Measured Quantity
Y	Calculated Quantity
1,2,3...	State Points

## ABSTRACT

Barta, Riley B. PhD, Purdue University, December 2020. Experimental and Numerical Analysis of Performance Enhancements to a Multi-Stage Two-Evaporator Transcritical Carbon Dioxide Refrigeration Cycle. Major Professor: Eckhard A. Groll.

Due to increasing environmental concerns and stringent regulations, the Heating, Ventilation, Air Conditioning, and Refrigeration (HVAC&R) industry is working to develop technologies that utilize low-global warming potential (GWP) refrigerants and remain within competitive coefficient of performance (COP) values and capacities of current hydrofluorocarbon (HFC) systems. Carbon Dioxide ( $\text{CO}_2$ ) has been investigated extensively over the past 25 years as a potential substitute for HFCs in refrigeration applications in mild ambient climates. Through efforts to increase the efficiency of  $\text{CO}_2$  systems, researchers and industry have identified cycle modifications that are particularly beneficial in transcritical  $\text{CO}_2$  cycle applications, such as expansion work recovery and economization. Yet, systematic experimental comparisons between these cycle enhancements are still lacking in the open literature. This thesis presents the design, assembly, and operation of a multi-stage, two-evaporator transcritical  $\text{CO}_2$  cycle with a combined capacity between the two independently-controlled evaporators of approximately 8 kW. The cycle utilizes three stages of compression, intercooling between the second and third stages, and flash tank economization at the medium-temperature (MT) evaporator. Furthermore, the test stand was designed to enable on-line transition between three methods of expansion without the need to stop the compressors. In particular, expansion through an electronic expansion valve (EXV), ejector, and through an ejector with a pump used to modulate the ejector inlet state is investigated. The purpose of this experimental work is to provide a comprehensive comparison between these cycle architectures and methods of expansion

work recovery as well as to assess both the pump and variable motive nozzle diameter as means of ejector control and system performance enhancement. Experimental testing assessed the performance of cycles utilizing economization, an ejector, and an ejector with a pump over four ambient conditions from 14 °C to 28 °C. The evaporator source temperatures were fixed to simulate refrigeration and freezing conditions. The pump controlled the ejector effectively and increased the ejector efficiency by up to 41%, despite decreasing the cycle COP. COP improvements of 6% and 5% were achieved with the open economization and ejector cycles, respectively.

In addition to the experimental aspects, a numerical ejector design tool that can be applied to a vapor compression cycle was developed. The model solves each sub-component of the ejector intensively, and receives inputs of mass flow rates, geometric angles, and ratios to output physical dimensions of an ejector. The design tool agreed with experimental dimensions with a mean absolute error (MAE) of 3% to 4%.

A second numerical aspect of this thesis consists of a dynamic model of the transcritical CO<sub>2</sub> vapor compression cycle test stand used for experimental testing. The dynamic model can be used to predict both steady state performance and dynamic performance of the system, and employs component models for the heat exchangers (HX), compressors, and expansion valves utilized in the experimental setup. Steady state validation resulted in maximum MAE of 18.7% and 11.9% for cooling capacity and power consumption, respectively, and dynamic validation resulted in similar thermal time scales between experimental data and the simulation. An evaporator pull down and an evaporator excitation simulation were successfully implemented to validate the ability of the model to develop control schemes.

Experimental future work consists of both cycle modification recommendations and control method implementation. Ejector design future work is the implementation of higher-fidelity sub-component models, and future work for the dynamic model is the thorough characterization of mass transfer and development of models of additional cycle architectures.



# 1. INTRODUCTION

## 1.1 Motivation

Growing global energy consumption (2.2% in 2017 [1]) and environmental concerns, such as global warming and pollution, are primary drivers in the quest of designing more efficient and sustainable energy systems. Specifically, the U.S. Energy Information Administration reported that approximately 38% of U.S. primary energy consumption in 2017 was attributed to residential and commercial buildings [2]. Therefore, improving both the energy utilization and system efficiencies in this sector is vital. Heating, cooling, and refrigeration systems rely heavily on refrigerants. Despite being a small percentage (approximately 2.5% of the 37.1 Gtons of Carbon Dioxide (CO<sub>2</sub>) equivalence emitted worldwide in 2018 [3,4]) of the total Green House Gases responsible for increasing global warming, hydrofluorocarbons (HFC) have been found to have significant impact, and the Kyoto protocol regarded HFCs as the second major source of global warming after CO<sub>2</sub> emissions from burning fossil fuels [5]. Although systems that utilize HFCs are designed to be closed-loops, perpetual leaking from open-drive compressors and catastrophic failures lead to releasing significant amounts of HFCs into the atmosphere. For instance, an average automotive air conditioning (AC) system contains up to 2 kg of refrigerant that either slowly leaks out or sustains a total loss of charge in the case of a crash. By considering the number of vehicles on the road, the total potential loss of refrigerant is significant. Another example is a centralized supermarket refrigeration system with long pipelines that serve display cabinets. In such a system, the total charge of the system is on the order of several hundred kilograms, and refrigerant leaks are significant due to having been installed in the field. Tassou et al. [6] estimated that centralized direct expansion (DX) supermarkets leak approximately 10% - 30% of their charge annually.

In an effort to phase out high-global warming potential (GWP) refrigerants, the EU F-gas (fluorinated gas) regulation 517/2014 was enacted. Preliminary results of this action were summarized by the European Environment Agency [7], which noted that F-gas production was reduced by 5% in 2015 relative to 2014, and that F-gas imports to the EU decreased by 40% in 2015 compared to 2014 levels. Two years later, the Kigali Amendment to the Montreal Protocol was ratified by nearly 200 countries, laying the foundation for the continued phase-out of HFCs over the coming decades in an effort to keep the warming of the earth below 0.5 °C by the year 2100. One aspect of accomplishing this goal is to phase out approximately 80% of HFC consumption before 2050 [8]. In response to the growing need for solutions to high-GWP systems for heating, cooling, and refrigeration applications, technical solutions that employ low-GWP or natural refrigerants need to be developed to the point of comparable efficiency and capacity to HFC systems.

A comprehensive analysis of a multitude of refrigerant types and their relative advantages and disadvantages is presented in Abas et al. [9]. Environmental, physical, transport, performance, and economic properties of many of the environmentally-friendly fluids were quantified, and overall recommendations for future transitions to environmentally-friendly vapor compression cycle fluids were provided. Systems utilizing low-GWP refrigerants should also strive to achieve increased efficiency with comparable cost to current solutions in order to motivate widespread acceptance of alternative fluids. Some families of low-GWP refrigerants being investigated as potential alternatives to refrigerants are hydrocarbons (HC) such as isobutane (R-600a) and propane (R-290), natural refrigerants such as CO<sub>2</sub> (R-744) and ammonia (NH<sub>3</sub> or R-717), and hydro fluoroolefins/hydro chlorofluoroolefins (HFOs/HCFOs) and their mixtures with HFCs, such as R-1234yf, R-450A, R-513A, among others. Heredia-Aricapa et al. [10] specifically assessed alternatives from several refrigerant groups to three common HFCs: R-134a, R-404A, and R-410A. Applications and operating conditions of the low-GWP refrigerants were taken into account with investigation of

their proposed replacements, and extensive discussion on their properties and performance relative to HFCs was provided.

While a disadvantage of  $\text{CO}_2$  is the high pressures and transcritical operation necessary to achieve adequate heat rejection to a heat sink at a temperature above the critical point, cycle enhancements and modifications enable performance that is competitive to cycles that utilize HFC refrigerants. Because  $\text{CO}_2$  has a negligible GWP, high volumetric heat capacity, and is non-explosive, it is attractive for certain applications such as military transport, areas where space is at a premium, enclosed spaces, and applications where leaks could be exposed to consumables, among others. While it has been shown that the coefficient of performance (COP) values achieved with  $\text{CO}_2$  cycles can be competitive with COP values associated with conventional HFC cycles, increased cycle complexity and higher initial capital costs are often necessary to achieve this competitiveness. To mitigate these inherent disadvantages,  $\text{CO}_2$  system designers and researchers need to develop systems for particular applications that will take advantage of the thermodynamic properties of  $\text{CO}_2$ , balance complexity with robustness, and accompany the designs with validated control methods to increase system reliability.

Given the aforementioned low critical temperature of  $\text{CO}_2$  (30.98 °C) [11], many applications will require transcritical operation in order to adequately reject heat to the ambient. It is well known that the high pressures associated with transcritical operation are a disadvantage from a practical standpoint. However, the decoupling of the relationship between pressure and temperature opens up a number of possibilities for cycle design and operation that, if used effectively, can decrease the performance gap that  $\text{CO}_2$  cycles face relative to cycles utilizing HFCs and other refrigerants. Furthermore, the thermodynamic properties of  $\text{CO}_2$  allow transcritical cycles to respond more positively to modifications that may not provide as much of a benefit in other applications. Background on the thermodynamic properties of  $\text{CO}_2$ , how those properties relate to performance modifications, and both details and applications of a broad array of cycle architectures are discussed herein.

## 1.2 Transcritical Carbon Dioxide Cycles

This section will provide background on different types of transcritical CO<sub>2</sub> cycle and examples of their application in stationary and transport refrigeration cycles.

### 1.2.1 Conventional and Advanced Cycles

There are a number of common cycle modifications that have been thermodynamically proven to provide increased efficiency in transcritical CO<sub>2</sub> cycles. While the degree of the benefit of cycle modifications and additional considerations depend on the specific application, the fundamental thermodynamic reasons behind the performance improvements hold true. Therefore, a number of improvements are introduced here before specific applications are discussed, in which modifications will be referenced and elaborated upon.

### Unique Transcritical Carbon Dioxide Cycle Characteristics

Kim et al. [11] provided an overview of the fundamental characteristics of transcritical CO<sub>2</sub> cycles, from fluid properties to application challenges. This work identified that the volumetric heat capacity of CO<sub>2</sub> is 3 to 10 times larger than chlorofluorocarbon (CFC), hydro chlorofluorocarbon (HCFC), HFC, or HC refrigerants. Pertaining to the transcritical nature of many operating conditions in CO<sub>2</sub> cycles, charge control strategies and the thermodynamic reasons for the high second-law losses in the gas cooling and expansion portion of transcritical CO<sub>2</sub> cycles were provided. One particularly challenging aspect of modeling transcritical CO<sub>2</sub> systems is characterizing thermo-physical properties of the fluid near the critical point. In an effort to characterize heat transfer in characteristics near the critical point, Ma et al. [12] experimentally studied the effects of CO<sub>2</sub>-side pressure, temperature, and mass flux in addition to water-side mass flux on the heat transfer properties of CO<sub>2</sub>. While the resulting updated Nusselt correlation had an accuracy of  $\pm 30\%$ , heat transfer

coefficient tests for various parameters showed consistent trends with the common occurrence of the maximum heat transfer coefficient occurring slightly above the critical temperature. The authors also noted a strong correlation between CO<sub>2</sub> buoyancy and heat transfer coefficients near the critical point, offering insight into the source of the notable property variation in the region near the critical point. This property variation then creates a challenge with accurate modeling of heat exchangers (HX) during phase transitions near the critical point. To offer a computationally-efficient solution to the challenge of characterizing near-critical point properties, Bahman et al. [13] have developed and validated a moving-boundary gas cooler model that was able to predict heat rejection rates within  $\pm 4.7\%$  mean absolute error (MAE) and gas cooler outlet temperatures within 3 K over a broad range of conditions. This prediction was achieved through separating the properties near and above the critical point into supercritical liquid and supercritical vapor through the thermo-physical property library COOLPROP [14]. To help visualize the transition of states surrounding the critical point of CO<sub>2</sub>, a pressure-temperature (P-T) and temperature-specific entropy (T-s) diagram are provided in Figure 1.1. There are three sub-types of fluids that occur in supercritical operation. Supercritical fluid corresponds to a state when the pressure and temperature of the fluid are above their respective critical values, supercritical liquid is when the pressure of a fluid is above the critical pressure but the temperature is below the critical temperature, and supercritical vapor is when the pressure is below the critical pressure but the temperature is above the critical temperature.

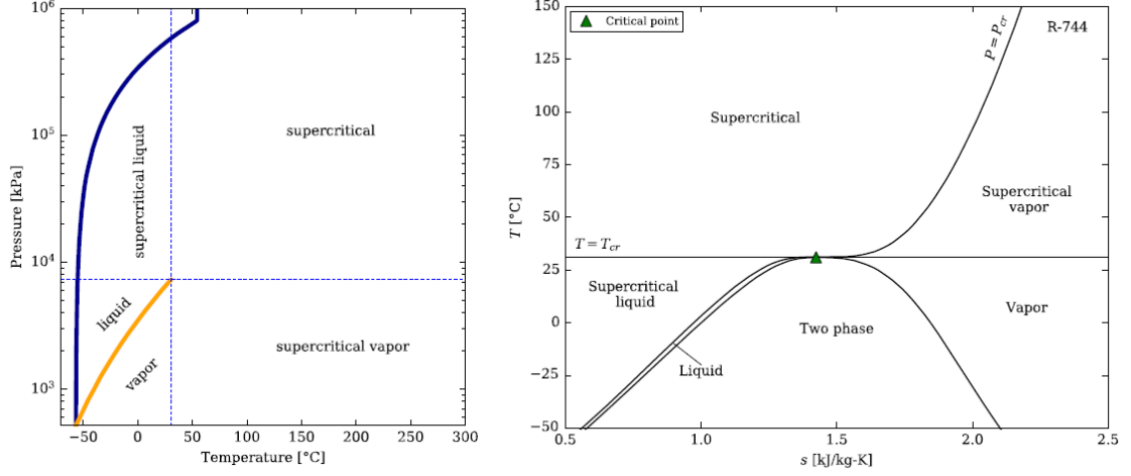


Fig. 1.1. P-T and T-s diagrams of CO<sub>2</sub> generated using CoolProp [13,14].

Brown et al. [15] performed a theoretical analysis comparing CO<sub>2</sub> and R-134a for automotive AC and found that, while the CO<sub>2</sub> cycle COP was lower than the R-134a cycle COP by up to 34%, the approach temperature between the air and CO<sub>2</sub> during heat rejection was over 50% smaller than the approach temperature in the R-134a cycle. Although the smaller approach temperature in the case of CO<sub>2</sub> did not offer enough performance benefit to overcome the cycle performance disparity, it was concluded that a counter-flow gas cooler may offer additional performance benefits for the CO<sub>2</sub> cycle over a cross-flow gas cooler if glide matching with the external heat transfer fluid was utilized. Sarkar [16] compared several aspects of transcritical CO<sub>2</sub> refrigeration cycles with conventional solutions using HFCs and HCs, among others. A broad array of conclusions was drawn, but key to this aspect of the literature is that the superior heat transfer coefficients of CO<sub>2</sub>, ranging from 20% higher to more than 100% higher than HCs and HFCs in saturated liquid form between -20 °C and -40 °C, could facilitate the use of smaller HXs for a given capacity.

## Common Cycle Architecture Enhancements

Given the fact that transcritical CO<sub>2</sub> cycles are inherently less efficient than subcritical HFC cycles, a number of studies have been carried out over the years to improve the system efficiency. Considered modifications to improve vapor compression cycle efficiency include single-stage compression with oil flooding and an internal heat exchanger (IHX), two-stage compression with either compressor intercooling or vapor injection, economization, sub-cooling, and expansion work recovery, among others. Yu et al. [17] provided a comprehensive overview of techniques to increase the efficiency of transcritical CO<sub>2</sub> cycles. A map summarizing the most common transcritical CO<sub>2</sub> cycle modifications is shown in Figure 1.2 and a condensed overview of the comparison studies discussed is provided in Table 1.1. As some of the literature reported gas cooler outlet temperatures and others reported ambient temperatures, the gas cooler outlet temperatures were assumed to be 5 K above the ambient temperature, evaporator outlet superheat was assumed to be 10 K, and evaporator pinch was assumed to be 5 K in the cases where the authors did not specify the pinch and superheat assumptions. Consistent assumptions for these values were made in order to provide common reference temperatures for a more meaningful comparison.

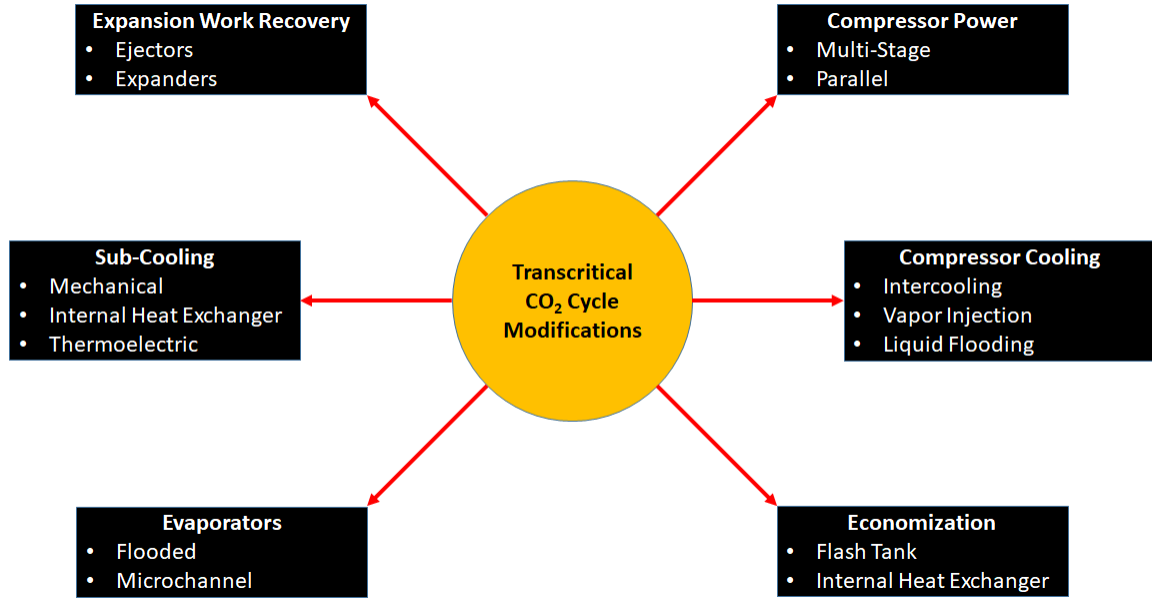


Fig. 1.2. Map of common transcritical CO<sub>2</sub> cycle modifications to increase cycle performance.

Baek et al. [18] assessed the optimum pressure ratio distribution across each compression stage in a two-stage transcritical CO<sub>2</sub> cycle with intercooling. They found that the maximum performance occurs with a larger pressure ratio across the first stage of compression than the second stage, and that the work needed for the second stage of compression was approximately equal to the amount of work extracted using an expander. Cecchinato et al. [19] found that intercooling is often more advantageous in multistage transcritical CO<sub>2</sub> compressors than traditional HFC applications due to higher first stage discharge temperatures. Furthermore, the researchers found that a two-stage transcritical CO<sub>2</sub> cycle with intercooling and an IHX was capable of COP increases of 29.3% and 28.7% at evaporating temperatures of -10 °C and -30 °C, respectively, compared to a single-stage CO<sub>2</sub> cycle. However, it was also noted that implementation of control for these cycles could be challenging, and that complexity needed to be weighed against desired performance benefits.



Table 1.1.  
Summary of common cycle modifications, excluding expansion work recovery (Experimental, Optimization, Theoretical).

System Design	Ref. System	Ref. COP	$T_{\text{source}}$ (°C)	$T_{\text{sink}}$ (°C)	COP Increase (%)	Analysis	Ref.
2-Stage, IC, IHX, Opt. Pr	4-component cycle	2.37	5	35	11.29	Opt., Th.	[18]
2-Stage, IC, IHX, Opt. Pr, Expander	4-component cycle	2.37	5	35	25.15	Opt., Th.	[18]
2-Stage, IC, IHX, Closed Econ.	4-component cycle	2	-7	30	30	Th.	[19]
2-Stage, IC, IHX, Open Econ.	4-component cycle	2	-7	30	29.4	Th.	[19]
2-Stage, IC	4-component cycle	3.25	-25	30	6.2	Th., Opt.	[20]
2-Stage, Flash Tank IC	4-component cycle	3.25	-25	30	15.4	Th., Opt.	[20]
2-Stage, Flash Tank Bypass	4-component cycle	3.25	-25	30	16.9	Th., Opt.	[20]
Flash Gas Bypass, Microchannel Evap	4-component cycle	1.18	32.1	43.3	7.0	Exp., Th., Opt.	[21]
Flash Gas Bypass, IHX	Single-stage, IHX	1.11	5.0	35.0	7.0	Exp., Opt.	[22]
Mechanical Subcooling	4-component cycle	0.95	0.0	35.0	30.3	Exp., Opt.	[23]
Thermoelectric Subcooling	4-component cycle	1.95	15.0	40.0	22.6	Th., Opt.	[24]
Oil Flooding with Regeneration	4-component cycle	-	-40.0	28.0	22.0	Th., Opt.	[25]
Single-Stage, IHX	4-component cycle	1.72	12.0	36.0	30.2	Exp., Opt.	[26]

Open economization is accomplished through the use of a component called a flash tank. In a flash tank, the two-phase refrigerant at the inlet is separated using gravity, and the saturated liquid is sent from the bottom of the flash tank to the evaporator while the saturated vapor is sent out the top of the flash tank directly to the compressor. The other form of economization is called closed economization, an example of which would be an IHX, which entails heat transfer between two separate fluid streams in the system, hence being referred to as closed. Heat is often rejected from an IHX at the outlet of the condenser or gas cooler, thus further decreasing the expansion inlet temperature, or increasing the sub-cool, in exchange for heating another fluid path within the system, such as a compressor vapor injection inlet flow. An in-depth review on thermodynamic and applications aspects of transcritical CO<sub>2</sub> cycle modifications can be found in Groll and Kim [27]. This paper covered the first decade of heavy research into transcritical CO<sub>2</sub> cycles after the resurgence of CO<sub>2</sub> as a refrigerant. Both theoretical and practical aspects were covered, as were future prospects. Agrawal et al. [20] conducted the optimization of a two-stage transcritical CO<sub>2</sub> heat pump cycle and found that the cycles with either flash or compressor intercooling did not perform as well as cycles utilizing a flash-gas bypass, thus providing a motivation for the prioritization of implementation of flash-gas bypass technology. The analysis conducted thoroughly analyzed the three proposed modifications, and provided a broad parametric study on optimal cycle intermediate and gas cooling pressures with varying ambient and evaporation temperatures. Another key takeaway was the reduced optimal gas cooling pressure with two-stage compression, and that compressor intercooling resulted in a higher gas cooling pressure than the flash gas bypass or flash tank intercooling cycles. Elbel and Hrnjak [21] experimentally investigated the impact of applying flash gas bypass and a microchannel (MC) evaporator in a transcritical CO<sub>2</sub> cycle. They concluded that the cooling capacity and COP could be increased by 9% and 7%, respectively, at the same time, but that a variable speed compressor could facilitate up to 19% increased cooling capacity under conditions producing COP values equivalent to that of the DX system. The effects

of evaporator outlet quality were also investigated, and well-defined optimum values for COP and capacity were found to occur with evaporator outlet qualities between 0.9 and 1, and 0.8 and 0.9, respectively. The findings regarding the application of flash-gas bypass helped open the possibility of using MC evaporators, which is yet to be widely accepted but is known to be feasible.

Mechanical sub-cooling is another technology that has been applied in transcritical CO<sub>2</sub> cycles. The use of an entirely separate vapor compression cycle to facilitate increased sub-cooling at the condenser outlet during subcritical operation or reduced gas cooler outlet temperatures in transcritical operation has the advantage of not increasing the CO<sub>2</sub> compressor suction superheat as would occur through the use of a suction-to-liquid line HX (SLHX). However, increased cost is incurred due to the need of an entirely separate vapor compression cycle and thus, this additional cost should be weighed against the evaporator cooling capacity benefit realized through a decreased evaporator inlet quality. Llopis et al. [23] concluded experimentally that maximum increases in cooling capacity and COP of 55.7% and 30.3%, respectively, could be achieved through application of mechanical sub-cooling under optimal conditions. Lower evaporating temperatures and higher ambient temperatures resulted in greater performance increases, and the positive impact of the mechanical sub-cooling system was found to be directly correlated with the capacity of the mechanical sub-cooling vapor compression cycle. Sub-cooling using thermoelectrics was investigated numerically by Yazawa et al. [24], resulting in a maximum COP benefit of 22.6%. The unique thermodynamic behavior of thermoelectrics was assessed and optimized in the context of the COP of the overall heat pump. While scaling challenges were not discussed in-depth in this study, the relative performance enhancements provide an intriguing proposition for the future development of thermoelectrics applied in vapor compression cycle enhancement. A review of sub-cooling efforts for CO<sub>2</sub> refrigeration cycles can be found in Llopis et al. [28]. This review provided significant insights, spanning from fundamental thermodynamic reasoning for the benefits of sub-cooling to in-depth design and architecture analyses.

Chesi et al. [26] developed a test stand to assess various configurations applied to transcritical CO<sub>2</sub> cycles, such as multi-stage compression, internal heat exchange, economization, and flash vapor bypass, among others, up to a 50 kW capacity. This work concluded that internal heat exchange can increase COP and cooling capacity up to 30% and 20%, respectively, but can result in excessive second stage discharge temperatures up to 180 °C. Furthermore, it was concluded that COP and capacity calculations resulted in high uncertainty when the gas cooler outlet was near the critical point due to the high specific heat of CO<sub>2</sub> near the critical point, which is defined as the partial derivative of specific enthalpy over the partial derivative of temperature at constant pressure. Discharge pressures that returned the highest COP were assessed over a range of conditions, and the optimum pressures were found to be very similar for both cycles with and without an IHX.

### **Expansion Work Recovery**

Researchers have shown interest in the development of expansion work recovery devices for potential capacity and COP improvement as energy efficiency becomes increasingly important. In fact, initial textbook contributions are being made on this topic, as can be seen in Bahman et al. [29]. The concept of expansion work recovery is particularly attractive in transcritical CO<sub>2</sub> cycles due to the significant pressure differential across the expansion portion of the cycle relative to an HFC cycle. Expansion work recovery has been investigated using several working fluids and operating principles, such as turbomachinery, positive-displacement machines, and ejectors, among others.

Robinson and Groll [30] developed thermodynamic models to compare transcritical CO<sub>2</sub> cycles with and without expansion work recovery, concluding that the cycle with an expansion work recovery device with an isentropic efficiency of 60% had a 25% higher COP than the cycle with 100%-effective internal heat exchange and no expansion work recovery. This work epitomized the need for thermodynamic analysis

to determine the best combination of performance-enhancing cycle modifications to be made to CO<sub>2</sub> cycles to maximize performance with as few modifications as possible. Baek et al. [31] designed and tested a prototype piston-cylinder expansion device in a transcritical CO<sub>2</sub> cycle and increased the system performance by up to 10%. Valve timing was found to be a significant challenge for the reciprocating expander application, but it was on the cutting edge of experimental work on expansion work recovery in CO<sub>2</sub> cycles when published. Turbomachine expanders have also begun to be investigated as a potential method for expansion work recovery. Czapla et al. [32] performed a theoretical analysis of a turbomachine expansion work recovery device applied in a two-stage transcritical CO<sub>2</sub> cycle. By assessing the placement of an expander between high and intermediate-pressures, intermediate and low-pressures, and in both locations over a range of five experimental baseline conditions, it was concluded that COP improvement potential was from 1% - 11%. Yang et al. [33] experimentally evaluated a rotary vane expander in a transcritical CO<sub>2</sub> cycle and, through analysis of internal losses, were able to improve the volumetric and isentropic efficiencies from 17% - 30% and 9% - 23%, respectively. Barta et al. [34] conducted a theoretical analysis on a two-evaporator multi-stage transcritical CO<sub>2</sub> transportation refrigeration cycle with a novel compressor-expander device known as the Energy Recovery Compressor. The cycle was able to achieve a COP of 1.28 at an ambient condition of 57.2 °C, and over and under-expansion losses were isolated through a fixed volume ratio expander analysis. The researchers concluded that up to 8.1% of recovered expansion power can be lost at a pressure ratio that is 70% of the expander design pressure ratio, highlighting the sensitivity of fixed volume ratio expansion work recovery technology to internal volume ratios.

Hays and Brasz [35] experimentally tested a transcritical CO<sub>2</sub> turbine compressor, where the turbine outlet shaft was connected directly to the compressor input shaft. An increase in COP of 39% over a simple throttle valve cycle was achieved for a 6-ton (21.1 kW) refrigeration or heat pump cycle. The authors stated that a higher capacity system would further increase the efficiency of the component due to partial admission

effects on the turbine, highlighting the practical challenges of scaling turbomachine expanders applied in two-phase flow. Finite element analysis and computational fluid dynamics (CFD) analyses were utilized to design a scroll CO<sub>2</sub> expander by Westphalen and Dieckmann [36], resulting in a predicted expander efficiency of 70%. If a 60% expander efficiency was conservatively estimated, the net power input to the cycle would be reduced by 20%. The authors also partitioned the losses within the expander, providing helpful, experimentally-validated insights into contributions to friction loss within expanders, in addition to the losses associated with four unique distribution strategies of the recovered work within the cycle. A review of additional expander technologies applied in vapor compression cycles can be found in Murthy et al. [37]. For completeness, it should be noted that the majority of transcritical CO<sub>2</sub> compression is performed by reciprocating compressors. However, scroll, rotary, and turbomachine compressors for transcritical CO<sub>2</sub> application have been commercially developed.

Another expansion technology suitable for transcritical CO<sub>2</sub> applications that has been under development by both researchers and manufacturers is an ejector, which can reduce the load on compressors by increasing the suction pressure without penalizing cycle functionality. To the best knowledge of the authors, a patent by Gay [38] is credited with the invention of the two-phase flow ejector used in a refrigeration system, and the design was further improved by Newton [39] and Kemper et al. [40]. Lucas and Koehler [41] experimentally tested an ejector in a CO<sub>2</sub> refrigeration cycle over a range of conditions and found a maximum ejector efficiency of 22%. The ejector efficiency used was defined by Elbel and Hrnjak [42] and was derived from Koehler et al. [43]. Additionally, a COP increase of 17% was achieved. Elbel and Hrnjak [42] experimentally tested a prototype ejector with a variable nozzle in a transcritical CO<sub>2</sub> cycle and achieved increases in cooling capacity and COP of up to 8% and 7%, respectively. The performance of the adjustable ejector showed significant promise for variable geometry ejectors, which could then provide control over a range of operating conditions. Liu et al. [44] experimentally assessed a variable geometry

ejector that allowed modulation of both the suction nozzle and motive nozzle diameters. Effects of variable geometry on sub-component performance were shown to be significant, and compressor operating speed was an added cycle optimization variable that was assessed in conjunction with the ejector geometry. A clear optimum suction nozzle diameter was identified, and the cycle gas cooling pressure associated with the maximum COP was reached through modulation of the motive nozzle.

In addition to the fixed and variable geometry ejectors discussed above, multi-ejector technology has taken hold in the market and is becoming a leading solution for COP improvement in transcritical CO<sub>2</sub> cycles across a broad array of applications. The multi-ejector concept was developed by Hafner et al. [45,46] and entails the connection of several fixed geometry ejectors in parallel. Depending on the demand of the system and the operating conditions, a control scheme directs flow to one or multiple ejectors through the control of a solenoid valve upstream of each ejector. Haida et al. [47] experimentally validated the multi-ejector concept over a broad range of operating conditions and utilized ejectors of various geometry. While the multi-ejector cycle did not always achieve a higher COP than the referenced parallel compression cycle, the reduced COP was largely due to inefficient compressor operation. The authors have clearly identified a high-potential solution to expansion work recovery which has been proven in subsequent experiments and pilot applications since this preliminary analysis. A maximum COP increase of 8.1% was achieved with a corresponding ejector efficiency of 24%. Additionally, a maximum ejector efficiency of 33.4% was achieved. The concept of a controllable ejector has drawn the attention of major commercial developers, as shown by the development of the Danfoss Multi Ejector [48] and the Carel EmJ, or Electronically Modulating Ejector [49], the latter of which utilizes an actively-controlled motive nozzle to facilitate efficient operation over varying operating conditions. Reviews containing additional information on ejector technology and ejector refrigeration can be found in Elbel and Lawrence [50] and Besagni et al. [51], respectively. The former review focuses on advanced aspects of ejector design and performance, while the latter focuses on the application of ejec-

tors in a broad array of commercial applications. A summary of discussed methods of expansion work recovery, along with comments on their respective strengths and weaknesses, is provided in Table 1.2.

Modeling efforts regarding ejectors fall largely into two types: analytical and CFD. Li and Groll [52] developed a constant-area mixing section model for an ejector applied in a transcritical CO<sub>2</sub> refrigeration cycle and found that the cycle COP can be improved by more than 16% over a basic transcritical CO<sub>2</sub> cycle. Liu and Groll [53] furthered their 2012 work and developed polynomial efficiencies for increased accuracy without requiring significantly more computation time. To validate the component efficiency results, the calculated COP and cooling capacity values were within 8% and 12% of experimental data, respectively. Lucas et al. [54] proposed another polynomial correlation for ejector efficiency and driving mass flow rate, which agreed with experimental data within 10% and 5%, respectively. A review of ejector efficiencies can be found in Liu et al. [55], where the most common methods of quantifying ejector efficiencies in vapor compression cycles are discussed and any associated polynomials are provided. The modeling approach of applying efficiency polynomials to ejector components has therefore been validated to agree reasonably with experimental data at a low computational cost. Efficiency polynomials provide a valuable alternative to CFD, and highlight the need to balance model accuracy versus computational efficiency.

Many CFD efforts in ejector modeling operate using the Homogeneous Equilibrium Model (HEM). Palacz et al. [56] assessed the accuracy of both HEM and Homogeneous Relaxation Model (HRM) in a CFD analysis of a CO<sub>2</sub> ejector relative to experimental data. Discrepancies between the two models and the experimental data ranged from 0.3% to 43.3% and 0.7% to 42.0% for HEM and HRM, respectively, with the most significant inaccuracy occurring around the critical point. At lower pressures and temperatures, the HRM has a higher accuracy than the HEM, and the error with the HRM results was approximately 5% lower than the HEM results. Palacz et al. [57] performed CFD mixing section shape optimization of an ejector applied in a CO<sub>2</sub>



Table 1.2.  
Summary of select research on expansion work recovery methods.

Expansion Method	Reference System	COP Impr.(%)	Device Eff. (%)	Analysis	Ref.
Recip. Expander	Single-stage IHX	25	60	Th.	[30]
Recip. Expander	4-component	10.5	11	Exp.	[31]
Turbo Expander	2-stage with vap. inj. and IC	11	50	Th.	[32]
Rotary-Vane Expander	4-component	14.2	22.6	Exp.	[33]
Turbo Expander- Compressor	4-component	39	56	Exp.	[35]
Scroll Expander	Single-stage IHX, expander without IHX	46	60	Th.	[36]
Fixed Geometry Ejector	4-component	17	22	Exp.	[41]
Variable Geometry Ejector	4-component	7	14.5	Exp.	[42]
Multi-ejector	Parallel compression	8.1	24.4	Exp.	[47]

cycle using the HEM, and achieved a result that increased the ejector efficiency by 2%. In an effort to assess performance differences between fixed and variable geometry ejectors, He et al. [58] conducted an exergetic analysis on each design and provided key differences, as well as reasoning, between them. The effects of the needle in the variable geometry ejector were found to be notable, increasing the entrainment ratio by up to 11% depending on back pressure, due to the needle causing decreased expansion of the primary flow and thus decreasing the velocity differential between motive and suction flows. Exergy losses in the mixing section and diffuser, particularly in the critical case of a shock occurring at the diffuser inlet, are higher for the fixed geometry ejector than the variable geometry ejector as a direct result of the same decreased acceleration present in the variable geometry design. These counteracting effects result in the variable geometry achieving an exergetic efficiency only 0.5% below that of the fixed geometry design, but with a decreased divergence angle the separation of the shock wave losses in the fixed geometry design would decrease, thus increasing the gap in exergetic efficiency between the two designs. A common assumption made in the modeling of ejectors, as well as many other components, is that the component is adiabatic. Haida et al. [59] investigated the validity of the adiabatic assumption, and assessed its application to both the outer walls of the ejector as well as to internal components in several combinations. Whether or not the external walls were adiabatic was found to have little effect on the ejector performance, resulting in a decoupling of the ejector performance from ambient conditions. However, heat transfer between motive and suction nozzles had a notable effect, with a maximum degradation of entrainment ratio of 13%. The adiabatic assumption was experimentally validated to be a reasonable assumption by Mastrowski et al. [60], who assessed the effects of heat transfer on a fixed geometry ejector and capillary tube. Flow visualization within CO<sub>2</sub> expansion devices has proven to be challenging due to the inherently high pressures throughout the cycle. However, recently Haida et al. [61] have successfully developed a test stand to visualize two-phase flow within ejectors, facilitating assessment of various ejector shapes through the use of particle imaging velocimetry and high-

speed cameras. A summary of potential COP benefits from many of the papers from Section 1.2.1 is provided in Figure 1.3.

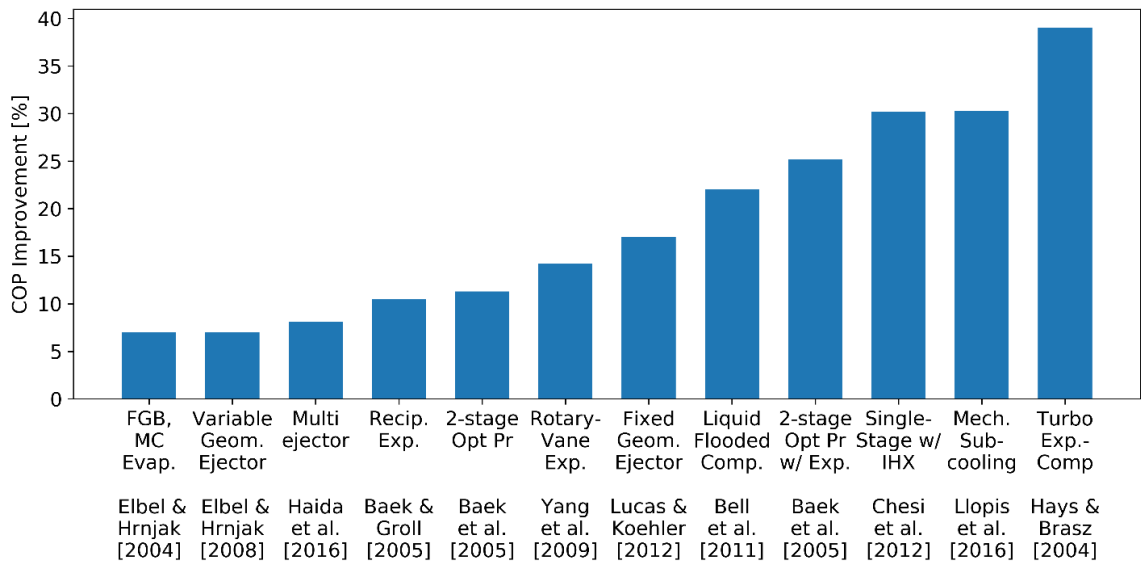


Fig. 1.3. Summary of potential COP improvements of modifications to transcritical CO<sub>2</sub> cycles relative to 4-component cycles.

### 1.2.2 Stationary Refrigeration Applications

The majority of stationary transcritical CO<sub>2</sub> applications and research focus on supermarkets in mild or moderate climates, but there have been studies on other applications as well. The most widespread application of stationary transcritical CO<sub>2</sub> refrigeration is in supermarkets and other food display cases. The non-flammability and general safety of CO<sub>2</sub> reduces concerns about the refrigerant being in contact with food or endangering humans in case of a significant leak. Furthermore, supermarket refrigeration systems generally require longer line lengths than most applications, necessitating significantly more charge. The leak rates and additional charge make the low cost, high volumetric heat capacity, and low-GWP of CO<sub>2</sub> particularly advantageous. The general complexity of supermarket systems also lends well to modifications that increase the efficiency of transcritical CO<sub>2</sub> cycles, as concerns about weight are

nonexistent and there are fewer space restrictions. Thermodynamically, the shape of the CO<sub>2</sub> vapor dome lends well to a significant enthalpy of evaporation at evaporator air inlet temperatures near 0 °C and -20 °C for refrigeration and freezing, respectively. Despite the favorably-shaped vapor dome, advanced transcritical CO<sub>2</sub> cycles in supermarket applications are often necessary to achieve COPs higher than the HFC DX systems they replace in high ambient temperature conditions. Much of the work discussed herein is aimed at how CO<sub>2</sub> systems can achieve a higher COP than a DX HFC system at high ambient temperatures, with notable success.

Literature has revealed that approximately 70% of multi-temperature vapor compression systems are found in supermarket refrigeration, transport refrigeration, and household refrigerators and freezers. The multi-stage technology required to operate multi-temperature vapor compression cycles efficiently is mature, with upcoming technologies such as ejector systems showing promise [62]. Multi-evaporator architectures in supermarket refrigeration systems are common because there are multiple areas and display cases that may not be located immediately next to each other, and display cases may also operate at different temperatures. In order to maintain a central refrigeration system, multiple evaporators stem from the same vapor compression cycle. Gullo et al. [63] provided a comprehensive review regarding transcritical CO<sub>2</sub> supermarket applications, including multi-evaporator systems. The review discussed key markets, unique aspects of transcritical CO<sub>2</sub> cycles in supermarket applications, control strategies, and the latest and most-innovative technologies in supermarket applications. Additionally, a summary providing further perspectives on CO<sub>2</sub> supermarket systems is provided in Gullo et al. [64], where a numerical comparison of several state of the art transcritical CO<sub>2</sub> systems to a DX R-404A system was conducted in the context of annual weather data from several European cities. Energy savings from 3.0% to 37.1% were observed, and it was also pointed out that CO<sub>2</sub>-only solutions for supermarket applications increased energy efficiency up to 25% while their equipment cost reduced 30% between 2008 and 2016.

While possible cycle architectures based on the multi-evaporator foundation can be numerous, one of the most common is the conventional booster system with flash gas bypass for supermarket applications. While state of the art systems being installed today may be increasingly based on more complex architectures, booster systems continue to have a strong presence, particularly in northern Europe [65]. An example of a booster system is provided in a thermodynamic analysis conducted by Ge and Tassou [66] and a schematic and pressure-specific enthalpy (P-h) diagram are provided in Figure 1.4(a) and Figure 1.4(b), respectively. In-depth numerical analyses of performance over varying ambient conditions were performed, including direct comparisons to an R-404A DX system in the same application. The COP of the CO<sub>2</sub> system exceeded that of the R-404A DX system at ambient conditions at and below 10 °C, but resulted in a maximum deficiency of 26% at an ambient temperature of 33 °C.

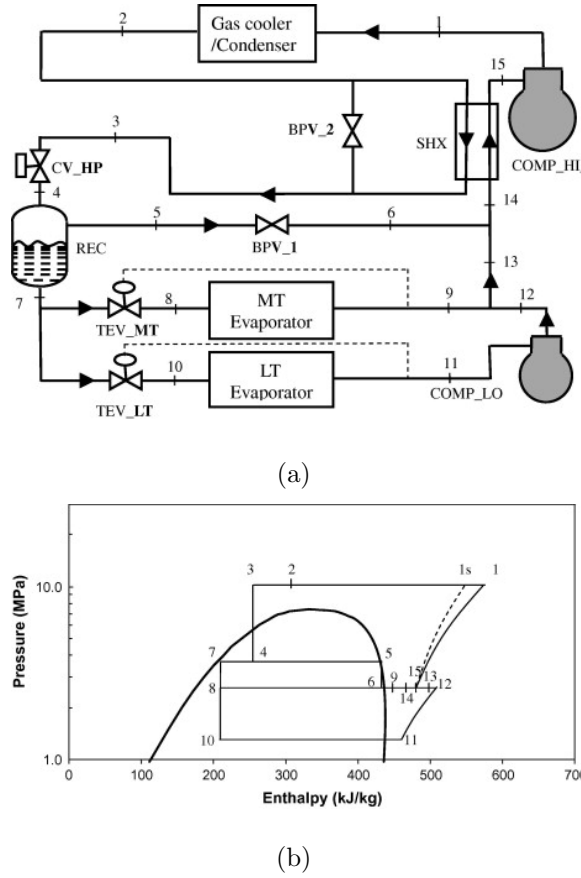


Fig. 1.4. (a) Schematic of a transcritical CO<sub>2</sub> booster cycle for supermarket application [66]; (b) State points of a transcritical CO<sub>2</sub> booster cycle operation for supermarket application on a P-h diagram [66].

The booster architecture is effective and among the simplest ways to achieve multiple evaporation temperatures, increasing initial cost-effectiveness and energy efficiency. A laboratory-scale CO<sub>2</sub> booster system was tested by Sharma et al. [67] over a range of ambient conditions, resulting in COP values of 3.3 to 1.4 at ambient conditions of 10.0 °C and 35.0 °C, respectively. The COP values achieved by the laboratory CO<sub>2</sub> booster system were then compared to another laboratory-scale R-404A DX system of similar scale by Fricke et al. [68], which concluded that the transcritical CO<sub>2</sub> system had, on average, a 15% greater COP over an ambient temperature range of 15.6 °C to 31.1 °C. Several centralized transcritical CO<sub>2</sub> supermarket systems were

numerically investigated by Sawalha [69] and compared to a DX R-404A system in Stockholm, Sweden. The researcher concluded that the CO<sub>2</sub> system would consume 4% - 12% less energy than the DX system, but warned that the system would not be an efficient replacement for HFC systems in countries with high average ambient temperatures. Field data for 4 to 18 months from three Swedish supermarkets using three transcritical CO<sub>2</sub> architectures was analyzed by Sawalha et al. [70]. The three older supermarket systems were installed in 2007 and utilized intercooling and sub-cooling, while the two newer systems were installed in 2010 and employed vapor injection via closed economization between the booster and high stage compressors. The newer systems achieved energy savings of 35% - 40% over the older systems, largely due to lower superheat and 10% - 15% more efficient booster compressors.

Despite the clear progress made with transcritical CO<sub>2</sub> booster systems, further advancement has been shown with the adoption of parallel compression systems for supermarket applications. A primary advantage of parallel compression is the ability of the cycle to efficiently handle a wide range of required cooling loads, meaning that there can be auxiliary compressors in parallel compression arrangements which can be utilized when additional capacity is needed. In addition to parallel compression, many of the common modifications discussed in Section 1.2.1 are applied to achieve even greater energy efficiencies. Sharma et al. [71] conducted a numerical analysis of eight complex supermarket cycles utilizing parallel compression, cascaded cycles, internal heat exchange, and secondary loops, among others, over one year of data for eight climate zones in the U.S. The transcritical CO<sub>2</sub> booster system with bypass compression consumed the least energy at ambient temperatures below 8 °C, and at higher temperatures the DX R-404A system consumed the least energy. Gullo et al. [72] performed exergetic analyses on a CO<sub>2</sub> booster system with parallel compression as well as on several supermarket refrigeration systems [73]. The former work identified the gas cooler/condenser, high stage compressors, and medium-temperature (MT) display cabinets to have the largest potential for improvement. The latter analysis found that the maximum ambient temperature where transcritical CO<sub>2</sub> cycles in

supermarket application could compete with a DX R-404A refrigeration systems was increased from 14 °C with first generation booster technology to 27 °C with more advanced parallel compression solutions.

The first application of the multi-ejector device in a commercial application was a supermarket in Switzerland. Practical aspects of the multi-ejector application are discussed in-depth in Schoenenberger et al. [74] and Hafner et al. [75]. Investigations of superheated outlet and flooded MT evaporators, as well as the optimal number of ejectors to use, were conducted. The energy consumption of the supermarket with the multi-ejector was compared to the average annual energy consumption of three supermarkets utilizing parallel compression with transcritical CO<sub>2</sub>. The annual power consumption of the multi-ejector system was found to be 14% lower. The ejector is one of the most prominent technologies to help move a theoretical line known as the CO<sub>2</sub> equator further south. This equator represents a geographical limit where transcritical CO<sub>2</sub> cycles can perform better than HFC systems over the course of a year, given that average ambient temperatures generally increase as one nears the equator. In the past few years this line has been identified as crossing the northern shores of the Mediterranean Sea [76]. In this spirit, Gullo et al. [77] conducted a theoretical study comparing annual performance of a multi-ejector CO<sub>2</sub>-only supermarket system to a number of other cycles utilizing various HFC and HC working fluids under temperature profiles of several cities below the CO<sub>2</sub> equator. Energy savings and reduction of the total equivalent warming impact (TEWI) of up to 26.9% and 90.9% were achieved over conventional HFC-based systems, respectively, including AC demand. Another experimental assessment of the multi-ejector concept was conducted by Abdin et al. [78] through instrumentation of the first transcritical CO<sub>2</sub> supermarket system in the Middle East, located in Amman, Jordan. The system was outfitted with a de-superheater, flash gas bypass, a multi-ejector, parallel compression, and flooded evaporators. Preliminary results show energy savings of over 30% relative to new HFC systems installed in the region, with no food waste due to consistent temperatures in the cabinets.



Another performance-enhancing technique often applied to supermarket systems utilizing parallel compression is evaporator flooding. Evaporator flooding entails controlling the flow rate through evaporators such that the evaporator outlet state is a high-quality two-phase flow as opposed to superheated vapor, thus allowing the system to operate at a higher evaporation temperature for a given heat source temperature. The two-phase outlet state enters an accumulator, which then separates the phases and only sends vapor to the compressor suction while sending the liquid back to the evaporator inlet. Evaporator flooding is often employed along with ejectors and parallel compression to be applied in supermarket refrigeration, which utilize the ejectors to pull the liquid from the accumulator via entrainment from the motive nozzle flow. An example of the evaporator flooding technique was conducted by Minetto et al. [79] and a schematic of the experimental cycle utilized is shown in Figure 1.5. The experimental cycle was successful in that the evaporators remained flooded and the ejectors facilitated adequate re-circulation of liquid, which also resulted in a 13% reduction in compressor power consumption due to increased evaporation pressures. Furthermore, the electronic expansion valve (EXV) operation was able to maintain flooded operation via an input of air temperature in the cooled area, and mal-distribution of superheat across the evaporators was nearly entirely eliminated, as validated by an infrared image.



store application. Both CO<sub>2</sub>-only cycles returned a higher COP than the cascade cycle at ambient temperatures from 2 °C to 14 °C, above which the cascade cycle performed better for the supermarket application. The ambient temperature where the CO<sub>2</sub>-only system achieved a higher COP than the cascade cycle increased to 26 °C in the convenience store application, suggesting that the convenience store capacity distribution between evaporators lends well to the specific combination of components utilized in the experimental analysis. Ballot-Miguet et al. [81] applied thermal storage and sub-cooling to a transcritical CO<sub>2</sub> supermarket system currently installed in France. Over the course of eight months, energy usage was reduced by 23 kWh, which was equivalent to 6% of the annual electricity bill dedicated to MT refrigeration. The researchers found sensitivity to scheduling and control over the course of a day, and suggested further investigation of operating scheduling for the work for increased efficiency benefit.

From a more traditional controls definition, several works have been conducted regarding fundamental control strategy types. A hierarchical control scheme applied to a two-evaporator two-stage booster transcritical CO<sub>2</sub> cycle was simulated by Beghi et al. [82], and utilized a supervisor and local controller control scheme, shown schematically in Figure 1.6. Within the supervisor and local controller scheme, MT and LT evaporator air temperatures, as well as both compressor suction pressures, were considered variables for local regulation, and several facets of reinforcement learning were assessed. The idea behind reinforcement learning is that a controller balances time between using what it already knows about maintaining a set point and searching the defined space for a more optimal solution. One reinforcement learning algorithm known as Q-learning was applied to a controller with unsupervised learning, as well as to a standard regulator which was fed information on the operating conditions a-priori. While both schemes worked reasonably well, the scheme with domain knowledge reached the optimal policy in approximately 50% as many learning episodes as the unsupervised scheme needed, as shown in Figure 1.7, both validating Q-learning as well as providing insights on its optimal implementation.

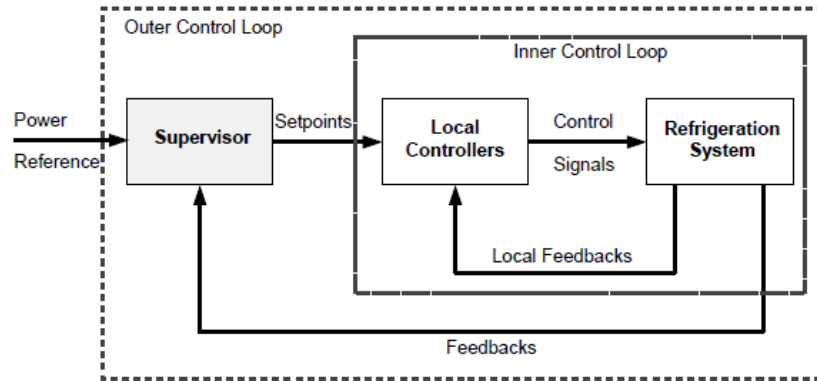


Fig. 1.6. Overview of a hierarchical control scheme applied in a multi-stage transcritical CO<sub>2</sub> refrigeration cycle [82].

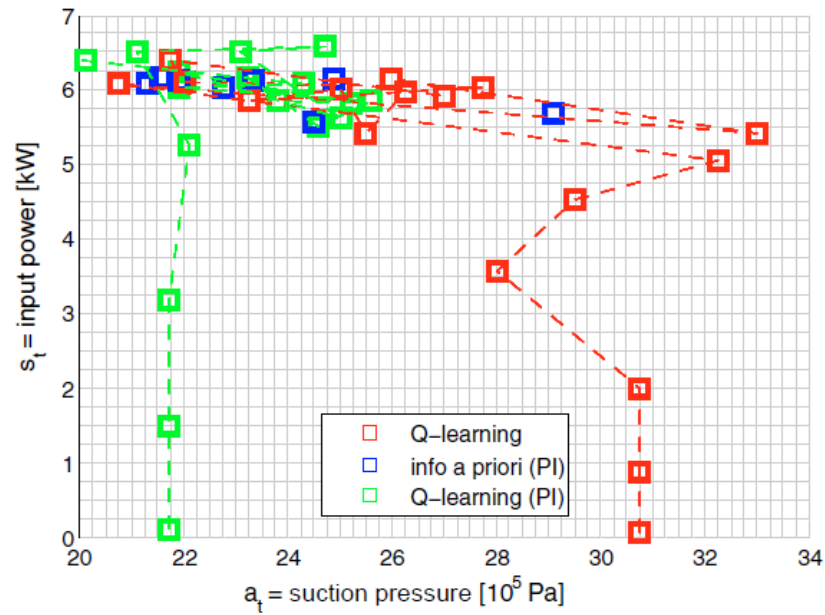


Fig. 1.7. Visual representation of Q-learning algorithm differences resulting from the analysis of a hierarchical control scheme applied in a multi-stage transcritical CO<sub>2</sub> refrigeration cycle [82].

Cortella et al. [83] instrumented a transcritical CO<sub>2</sub> cycle installed in a refurbished supermarket in northern Italy, and used the experimental data to validate a TRNSYS model. The TRNSYS model was intended to capture the dynamics of heating, ventilation, air conditioning, and refrigeration (HVAC&R) equipment, as well as their interrelations in more complex systems. The data and model allow the development of control strategies which targeted heat recovery through two HXs placed between compressor discharge and the gas cooler to reduce the overall energy consumption of the system. The heat recovery HXs were used for hot water heating and space heating, in order of closest to the compressor discharge. When no heating was needed, the control scheme modulated the high-side pressure as a function of ambient temperature. However, in a departure from traditional CO<sub>2</sub> supermarket control, when heating was demanded, two assessed schemes pushed the cycle into transcritical operation in order to ensure adequately high compressor discharge temperatures. The active transition into transcritical operation was shown to be less efficient than supplementing the heating capacity with an additional heat pump, but was an interesting aside that further proved the significant impact transcritical operation has on power consumption and that it should be avoided whenever possible. The same instrumented supermarket system was utilized to further develop the TRNSYS model in [84], where the model showed good agreement but under-predicted refrigeration capacity by up to 12% in some cases. This error was somewhat constant, and therefore attributed to a systematic inaccuracy of the modeling of the refrigerated display cabinet model. Regardless, the measurements and simulations were used to show that the system could provide the majority of space heating, water heating, and AC required by the supermarket while also providing a 7% reduction in global energy consumption. While several strategies were assessed, all but 6% of the heating demand, in addition to all of the cooling demand, could be met with an additional evaporator that increased system capacity, facilitating an all-in-one solution to heating and cooling needs without the need for additional heat pumps. A summary of the control strategies discussed in this section is provided in Table 1.3.

Table 1.3.  
Summary of reported control schemes.

Strategy	Finding	Analysis	Ref.
2-stage throttling via intermediate receiver	10% increase in power consumption over R-404A DX	Th., Exp.	[85], [86]
Liquid flooded evaporator with receiver	13% decrease in compressor power consumption	Exp.	[79]
Multi-ejector, intermediate pressure, and compressor speed	27% power savings, successful integration of multiple controls together	Th., Exp.	[87]
Real-time high-side pressure control	Reduced impact of errors in correlations, proved to be more robust	Th.,Exp.	[88], [89]
High-side and supplemental capacity control for cooling and both space and DHW heating	100% cooling and 94% of heating loads could be met with a standalone system	Th.,Exp.	[83], [84]
Hierarchical control scheme with reinforcement learning Q-learning algorithm	Unsupervised exploration converged, a-priori information reduced search time by 50%	Th.	[82]
Cloud-based control scheme for commercial refrigeration	Low-cost retrofit facilitated individualized control schemes, initial findings showed 20-50% reduction in energy consumption	Exp.	[90]

### 1.2.3 Transportation Refrigeration Applications

Transportation was one of the first uses of CO<sub>2</sub> as a refrigerant, where it was applied in marine cooling applications in the early 20th century. The low heat sink temperature provided by the ocean allowed subcritical operation with pressure differentials that were small enough to be manageable by compressor technology of that time. However, with the advent of CFCs and other synthetic refrigerants, transportation applications of CO<sub>2</sub> did not resurface significantly until the 1990s when Gustav Lorentzen sparked its revitalization as a natural alternative refrigerant [91]. Following the resurgence of CO<sub>2</sub> as a refrigerant, transcritical CO<sub>2</sub> transportation applications largely fell into two topics: automotive AC systems and cooling of shipping containers. The former context was largely driven by legislation and well-known leak rates of open-drive automotive AC systems, and the latter consisted of both civilian and military applications desiring increased environmental friendliness. This thesis focuses on the shipping container applications of transcritical CO<sub>2</sub> cycles in transportation.

Multiple evaporator systems are used in transportation applications that require the ability to independently cool separate compartments at different temperatures and capacities. Transportation refrigeration systems must be extremely reliable and also have the ability to operate efficiently over a broad range of operating conditions. System capacities for shipping containers generally fall at or under 10 kW, with varying distribution of this capacity between evaporators. For the cooling of food, refrigeration applications target temperatures for cooling and freezing of food to approximately 0 °C and between -18 °C and -35 °C, respectively. Elaboration on evaporator source conditions as well as a further review of emerging technologies for food refrigeration applications can be found in Tassou et al. [92]. While traditional food refrigeration technologies were discussed in this work, the majority of the content focused on up and coming technologies and their potential for this application, such as thermoacoustics, magnetic, and air cycles, among others.

Panozzo et al. [93] identified and discussed the shift in focus of international regulations on food transportation from solely consumer safety to include the global quality of goods. Increasingly efficient technology for cooling throughout the food chain was cited as a necessity, and multi-evaporator containers were recommended as a part of the solution to optimizing the logistics of the cold chain for environmental purposes. In an effort to meet the technological needs of the cold chain, a real-time control scheme that could maintain evaporator temperatures and capacities regardless of internal or external variations was recommended as a solution by the IIR [94]. Stack and Finn [95] experimentally and numerically assessed a dynamic model for a multi-evaporator vapor compression cycle in transportation applications. Evaporator loads were varied 50%, and the resulting evaporator load and outlet superheat were numerically predicted by the model within 10% of experimental results, along with the notable result of capturing the dynamics coupled from the use of more than one evaporator. Ibrahim [96] numerically investigated the effects of sudden changes in temperature and mass flow rate of the counter-flow fluid to an evaporator in a refrigeration system controlled by a thermostatic expansion valve (TXV). The researcher concluded that the system could retain evaporator outlet superheat with mass flow rate and temperature variation up to twice their initial values, but superheat was temporarily lost when the load and temperatures were decreased to 50% of their initial values. Additionally, irrecoverable system instability occurred with a further load reduction to 25%. Shah et al. [97] presented an open-loop step response dynamic modeling methodology for a transcritical CO<sub>2</sub> multi-evaporator AC system and compared the results to experimental data. The model was able to capture system dynamics well, with the specific observation that both evaporators reacted similarly to the compressor outputs. Additionally, differences between multi-input multi-output (MIMO) and single-input single-output (SISO) control strategies were discussed, and MIMO was found to be more applicable due to its ability to capture the coupled dynamic effects of various components within the system.



A multi-temperature container system in extreme ambient conditions was investigated by Lawrence et al. [98] for U.S. military applications. The project entailed a target of a COP of 1 at an ambient condition of 57 °C, while still maintaining a refrigeration compartment at approximately 3 °C and a freezing compartment at -20 °C. The researchers found that a COP of 0.96 could be achieved using an IHX and an ejector, resulting in COP improvements of 35.3% and 27.3%, respectively in independent applications. When applied together, the two aforementioned modifications can increase COP by up to 68.6% over the baseline cycle. In another assessment of a similar two-evaporator, multi-stage transcritical CO<sub>2</sub> transportation refrigeration system, Barta et al. [99] assessed the effects of varying ambient temperature and flash tank pressure relative to evaporation pressure on compressor suction superheat, flash tank liquid level, and system COP. It was concluded that the system COP was maximized for a given ambient condition when the flash tank pressure was as close to the evaporation pressure. This provided maximum potential pressure differential for expansion work recovery. However, when the flash tank pressure was as close to the evaporation pressure as possible, compressor superheat could become dangerously low, suggesting that a pressure differential should be retained, which will also maintain the liquid level in the flash tank at a high-enough level to not risk flash tank liquid starvation.

#### 1.2.4 Discussion, Challenges, and Future Prospects

Supermarkets and transportation refrigeration make up the majority of research, development, and applications of transcritical CO<sub>2</sub> cycles. There are many perspectives that could be used to explain the reasoning behind this distribution, but the simplest way to state it would be that the inherent disadvantages of transcritical CO<sub>2</sub> cycles do not have as high of a penalty in either supermarket or transportation applications. A myriad of performance-enhancing cycle architectures and components have been developed and largely proven for various applications. In addition, many of these components can be utilized in multiple applications. The environmental-

friendliness of CO<sub>2</sub> is undeniable, clear operating conditions where it can compete with or surpass HFC efficiency have been defined, and there are a significant number of components designed for CO<sub>2</sub> application in mass production. The primary challenges then become cost of installation and operation, as well as energy efficiency in moderate- to high-ambient climates. In cool to moderate climates, transcritical CO<sub>2</sub> technology today can compete with and out-perform HFC cycles without becoming notably complex, which places the operating cost of CO<sub>2</sub> systems below that of competing systems. Combine the potential for efficient operation with the cost of the actual working fluid, and the use of CO<sub>2</sub> systems in high-leak rate applications such as supermarkets become significantly less costly, both to the operator and the environment. CO<sub>2</sub> components are still more expensive than their HFC counterparts, but that gap is continuing to close as economies of scale and design optimization make an inevitable impact on component costs. Competitive efficiency in high-ambient climates has also been proven, but only in a small number of pilot installations requiring complex architectures. The pilot installations of advanced CO<sub>2</sub> technology need to be further proven before wider-spread acceptance of the technology in high-ambient environments can be achieved. However, it is a promising result and an excellent step in the right direction.

While tremendous progress has been made in applications of transcritical CO<sub>2</sub> cycles in both stationary and transportation refrigeration, several types of barriers stand between the state of the art and widespread acceptance. The first, and debatably most powerful, would be the legislation on the topic. While legislation is trending in the right direction with the HFC phase-down seen throughout the world, it will still take time for the HVAC&R industry as a whole to strictly rely on HFC/HFO blends, HC solutions, and natural refrigerants such as NH<sub>3</sub> and CO<sub>2</sub>. Once HFCs are completely phased-out, the most suitable low-GWP refrigerant will likely fall into its place with widespread adoption.

The next barrier would be availability and cost of components for transcritical CO<sub>2</sub> systems. This barrier shrinks every year, as existing components become more pop-

ular and technological developments help drive the introduction of new components into mass-production. This evokes economies of scale to push the cost of transcritical CO<sub>2</sub> systems closer to that of current HFC systems. Another aspect of the barrier associated with cost is the technician workforce that would service CO<sub>2</sub> systems. HVAC&R technicians are trained and focused on brazing copper tubing to build, repair, or replace systems. However, the use of stainless steel is common in CO<sub>2</sub> systems due to the high-pressures inherent of the cycle, so increased training on working with stainless steel and its fittings would be necessary. However, advancements in high-pressure copper alloys have resulted in a potential solution to this problem, with currently-available materials rated at pressures up to 120 bar.

Another of the major challenges with adoption of transcritical CO<sub>2</sub> technology is the complexity of the cycles necessary to compete with HFC cycles. While there has been tremendous headway made in the reliability of complex CO<sub>2</sub> cycles, it is a commonly-held opinion that simpler is generally more robust. This opinion has driven significant research into controls, field-testing, and safety mechanisms of transcritical CO<sub>2</sub> cycles. However, additional experimental and field studies are necessary for the adoption of the more-complex systems that have the potential to achieve a higher COP than an HFC system in a moderate or high ambient condition.

Future aspects of work on the topic of transcritical CO<sub>2</sub> refrigeration are continued experimental validation of existing transcritical CO<sub>2</sub> cycles, instrumented field tests of complex architectures to build consumer confidence, and optimization of applied components. The point of component optimization will likely bring about not only high-efficiency compressors and HXs optimized for use with CO<sub>2</sub>, but also further development of expansion work recovery devices. As has been shown, there is a significant amount of research and development being conducted on expanders, and even more on ejectors. The continued optimization of working principles, geometries, and transient operation over a broad range of operating conditions will undoubtedly push transcritical CO<sub>2</sub> cycles closer to widespread adoption. With increasing fidelity of modeling capabilities, designs that are deemed to have potential for further effi-

ciency improvement may either be outside of traditional manufacturing capabilities, or may be cost-prohibitive. Therefore, new and optimized components have potential for additive manufacturing, particularly with consideration of unique geometries of internal features such as ejector mixing sections, which could be extremely difficult to fabricate using a lathe or end mill with the small diameters characteristic of certain CO<sub>2</sub> system capacities. Given the significant efficiency benefits that have already been proven through the use of performance-enhancing devices, further development and increasingly-robust designs can only increase the potential COP benefit to transcritical CO<sub>2</sub> cycles.

Key takeaways are summarized in the following bullet points:

- While a significant amount of work has been done on development of individual components for modifications to transcritical CO<sub>2</sub> cycles, there is room for improvement in the efficiency and reliability of expansion work recovery devices. Furthermore, advanced design and analysis tools have gained popularity in assessing components for improving CO<sub>2</sub> cycle performance, thus providing new tools to reach previously-unattainable efficiencies.
- Supermarkets dominate the stationary industrial applications of transcritical CO<sub>2</sub> refrigeration, and the energy savings from experimental pilot installations become more impressive every year. With advanced architectures proving to outperform HFC cycles in nearly all climates, not just moderate and mild as was true in the past, supermarket applications seem to be here to stay. Furthermore, as simpler architectures, which can return higher efficiency in northern climates, become more robust, advanced CO<sub>2</sub> cycle applications should become more widespread in the coming years.
- Transportation refrigeration applications of transcritical CO<sub>2</sub> have been proven to be competitive in terms of efficiency, and shipping containers have been proven to be a common application in industry. However, there is relatively little published research on this particular application.

- Transcritical CO<sub>2</sub> cycles have been accepted in a broad array of applications, and are only growing in popularity. As HFCs continue to be phased out, research into further increasing efficiencies of previously-investigated applications as well as new applications is necessary to help continue popularity growth.

### 1.3 Research Focus and Open Questions

The open research questions this thesis aims to address are presented herein.

#### 1.3.1 Multi-Stage Two-Evaporator Carbon Dioxide Cycles

A vapor compression cycle with a second evaporating temperature and multiple compression stages leads to an increased number of possible cycle modifications. Furthermore, the increased complexity of cycle operation due to coupled evaporator dynamics and a higher number of mixing flows and compressors presents additional challenges. A question resulting from these inherent complexities is to determine the best way to balance cycle complexity with performance benefits over a range of ambient conditions. While numerical and experimental research has been conducted on the balance of complexity and performance, an exceedingly small number of publications address this balance with the same test stand that has consistent heat exchanger, compressor, and other system losses between comparisons. The second and third questions in this context both concern cycle stability and dynamic behavior. Assessing the ability of expansion work recovery to control a cycle is much less common than quantifying performance benefits at a design point. Less common yet is the comparison of expansion work recovery control methods to not only increase cycle performance, but also control the cycle with reliability and stability. On a broader level, the dynamics of complex architectures that have coupled dynamics between evaporators and multi-stage compression has not been a focus of research due to the trend of the literature to focus on sheer cycle performance benefits at steady state. While the value of the steady state perspective is undeniable and such analyses are

also conducted herein, both qualitative and quantitative descriptions of cycle dynamics that will aid in the development of robust control schemes are lacking in the literature.

### **1.3.2 System Design**

Designing a complex experimental setup can result in unforeseen challenges in terms of both measurement and performance. While the results of an experiment are generally what answers the open questions in the literature, there are many questions that can be answered from an in-depth description of the design, construction, and testing of an experimental test stand. Questions regarding test stand design are not a gap in the literature in the traditional sense, but information and lessons learned from efforts undertaken to develop complex test stands can aid in the development of other test stands which can push experimental research in the area of transcritical CO<sub>2</sub> refrigeration forward. In particular, design of a modular test stand to test multiple cycle architectures and transition between different architectures through strategic placement of ball valves is not common, and can aid in the development of test stands to provide increasingly meaningful comparisons of cycle architectures and associated dynamics.

### **1.3.3 Ejector Design**

While the amount of research on ejectors applied in transcritical CO<sub>2</sub> cycles is significant and continues to grow, there are several questions that are consistently overlooked in the literature. The first of these questions is regarding a clear methodology for ejector design. Many researchers investigate the nuances of the design of a particular section, perform optimization, and present the results with occasional dimensions, but there is seldom discussion on the actual design process behind the development of a prototype. Another of these overlooked questions would be the variation in internal geometry for ejectors applied in different operating conditions. Not only does the assessment of this geometry variation complement the design as-

pects of the first question, but it also quantifies and draws attention to the significant challenges associated with designing two-phase expansion components that can be reliably and efficiently operated over a broad range of conditions. Finally, the fact that an operating condition that results in the maximum COP for a cycle utilizing an ejector may not be the condition where the ejector performs at its highest efficiency has been proven repeatedly. However, any differences in the associated geometries for ejector designs focused on maximum ejector efficiency versus maximum cycle COP for the same condition have not been previously addressed.

#### **1.3.4 Dynamic Behavior**

In a four component vapor compression cycle, predictions of the effects of varying parameters such as the heat sink temperature, the heat source temperature, or the expansion valve orifice size on cycle behavior can be made reliably. However, such predictions become more challenging with each added flow path, valve, heat exchanger, and compressor. To further complicate matters, the beginning and end states of altering a system parameter are only part of the story, as understanding intermediary steps and their relative rates is vital to maintaining reliable cycle dynamics. For example, if the orifice diameter of an expansion valve upstream of an evaporator is decreased, the end result for the downstream evaporator will almost always be a lower evaporation temperature and a higher outlet superheat. However, the secondary implications of valve actuation would certainly affect the flash tank liquid level, the superheat values of different compressor suction ports, and also the temporary capacity of the refrigeration system. Understanding and quantifying the transient effects on system behavior and performance will allow the development of robust control schemes that can help reduce the impact of transient scenarios on cycle performance and reliability. While research and development of refrigeration cycles is not new, there is a lack of experimentally-validated dynamic models that can be ap-

plied to a broad range of dynamic scenarios to help develop control schemes without the need for experimental work at every iteration.

#### 1.4 Research Objectives and Approach

In an effort to address existing gaps in the literature, several contributions have been identified. In particular, four major aspects will be considered in the present work:

- To provide a meaningful and systematic experimental comparison between transcritical CO<sub>2</sub> cycle multi-evaporator architectures that can be applied in both supermarket and transportation refrigeration.
- To experimentally assess ejector control methods and the resulting impact on cycle performance and behavior.
- To create and validate a comprehensive ejector design tool that can be applied over a broad range of applications and working conditions.
- To develop and validate a detailed dynamic model of a multi-evaporator transcritical CO<sub>2</sub> cycle for control strategy development.

More specifically, the following cycle enhancements will be considered and investigated:

- Multi-stage compression with intercooling;
- Open economization and the associated evaporator flash gas bypass;
- Ejector expansion work recovery with a variable motive nozzle diameter;
- Application of a CO<sub>2</sub> pump between the gas cooler and ejector motive nozzle inlet.

A modular test stand has been developed to compare all of these cycle enhancements over a range of ambient conditions. With respect to expansion work-recovery, two control methods of a two-phase flow ejector will be assessed. In particular, the modulation of the motive nozzle diameter through an adjustable needle located in the



nozzle throat will be compared to the application of a CO<sub>2</sub> pump located between the gas cooler outlet and the motive nozzle inlet. Ejector control refers to the ability to actively modulate the motive nozzle inlet pressure in a way that results in a change in the ejector efficiency, pressure lift, or entrainment ratio. The two ejector cycles will be compared to cycles utilizing a flash tank at the evaporator inlet and a baseline cycle with no phase separation. While all of these performance-enhancing technologies besides the pump have been discussed individually or in a combination of one or two as reported in the literature review, there has not been a single, comprehensive experimental test stand able to test all of the proposed performance-enhancing technologies under the same operating conditions with the same components to the best knowledge of the author. The experimental test stand developed as part of this work serves the purpose of providing a direct comparison in expansion methods and components in an effort to bring more conclusive recommendations to the body of knowledge on transcritical CO<sub>2</sub> cycles as to which architectures have the highest COP and/or capacity over a range of operating conditions.

Ejectors have become the most widely-used method of expansion work recovery in vapor compression cycles, and as a result there is a significant amount of literature reported on their use. Despite the popularity, the majority of the literature containing physical and practical aspects on ejector design do so as a secondary contribution, thus lacking comprehensive nature. The ejector design tool presented in this thesis provides insights from fundamental fluid mechanics and thermodynamics to manufacturability, and enables the output of physical ejector dimensions in applications over a broad range of operating conditions with the potential to be applied in different working fluids.

The dynamic modeling literature is largely focused on gas-cooling pressure optimization, along with growing amounts of work on the area of intermediate-pressure optimization. With that being said, there is a significant gap in the literature concerning dynamic control scheme development focused on cycle optimization using both multi-stage compression and economization simultaneously. In addition to this gap,

the literature is lacking in experimental validation of transient models and discussion of any discrepancies in their behavior. The dynamic model presented herein provides insights on the development of an experimentally-validated dynamic model as well as two examples of utilizing the dynamic model for control scheme development.

## 1.5 Overview

The structure of this thesis to meet the previously mentioned objectives is as follows:

In Chapter 2, the design, structure, and instrumentation of the experimental test stand is explained. Chapter 3 provides an experimentally-validated ejector design tool and explanation of its use as well as potential applications. Chapter 4 presents an in-depth description of the dynamic model and the solution procedure within Dymola. The experimental parametric study, data reduction, test stand operating procedure, and results are provided in Chapter 5. Validation of the dynamic model with experimental data is reported in Chapter 6. Finally, Chapter 7 summarizes conclusions, lessons learned, challenges encountered, and future work identified for this research work.

## 2. SYSTEM DESIGN

The purpose of this chapter is to provide insights into the design and construction of the experimental system. In particular, the overall system architecture and the different cycle configurations are described in detail. Then, a thermodynamic model is employed to size the system and the necessary components and sensors are selected. Lastly, the system is assembled and commissioned. A photo of the final experimental system placed in a psychrometric chambers at the Ray W. Herrick Laboratories is shown in Figure 2.1.



Fig. 2.1. Photo of the completed transcritical CO<sub>2</sub> test stand inside of a psychrometric chamber.

## 2.1 System Design Introduction

As the concept and background for the need for systematic comparisons between modifications to transcritical CO<sub>2</sub> refrigeration cycles has been discussed thoroughly in Chapter 1, a brief introduction for context is provided here to provide additional motivation for the design and construction of the test stand described in this chapter. A number of studies on modifications of transcritical CO<sub>2</sub> cycles, as well as their focus and whether they were numerical or experimental in nature, are summarized in Table 2.1.

Given the supermarket context for applications of complex cycles transcritical CO<sub>2</sub> cycles, a gap can be found in the literature for a systematic comparison of more than two to three cycle comparisons performed with the same compressors and heat exchangers. This comparison will minimize the differences between the cycles and isolate the performance variation to the specific components or architectures being tested. Additionally, how these different cycles behave not only at steady state but also during transient conditions is yet to be explored experimentally for several different cycle architectures in a meaningful, direct comparison. The research presented herein concerns the development of a transcritical CO<sub>2</sub> test stand with the purpose of conducting comparisons between combinations of common cycle modifications discussed above, which could be applied in either supermarket or transportation applications. In particular, the developed test stand utilizes three stages of compression with intercooling between the second and third stages of compression, and two independently-controlled evaporators, each with a dedicated flash tank for open economization at each evaporation pressure. Additionally, the test stand is designed to be able to transition between EXV mode expansion to ejector mode expansion without the need to turn off the compressors. Furthermore, the multi-stage and open-economization combination with an ejector was informed by Ladd [107–110] with the intention of validating a particular multi-stage flashing refrigeration cycle. The design, assembly, and validation of energy balances under EXV and ejector modes with

Table 2.1.  
Summary of select cycle modification studies.

Author	Architecture or Modification	Type
Groll and Robinson [30]	Turbine expander, IHX	Num.
Elbel and Hrnjak [21]	Flash gas evaporator bypass	Exp.
Kim et al. [11]	Expansion work recovery	Num.
Baek et al. [31]	Reciprocating expander	Exp.
Agrawal et al. [20]	Two-stage comp., IC, closed econ.	Num.
Bertsch and Groll [100]	Two-stage comp., Vapor injection	Exp. and Num.
Elbel and Hrnjak [42]	Variable geometry ejector	Exp. and Num.
He et al. [101]	Turbo expander	Exp. and Num.
Wang et al. [102]	Open and closed economization	Exp.
Xu et al. [103]	Vapor injection	Exp.
Wang et al. [104]	Rotary expander	Num.
Liu and Groll [53]	Variable geometry ejector	Exp. and Num.
Zhang and Tian [105]	Turbo expander-phase separator	Num.
Hafner et al. [46]	Multi-ejector	Num.
Haida et al. [47]	Multi-ejector	Exp.
Barta et al. [106]	Turbo expander-phase separator	Exp. and Num.

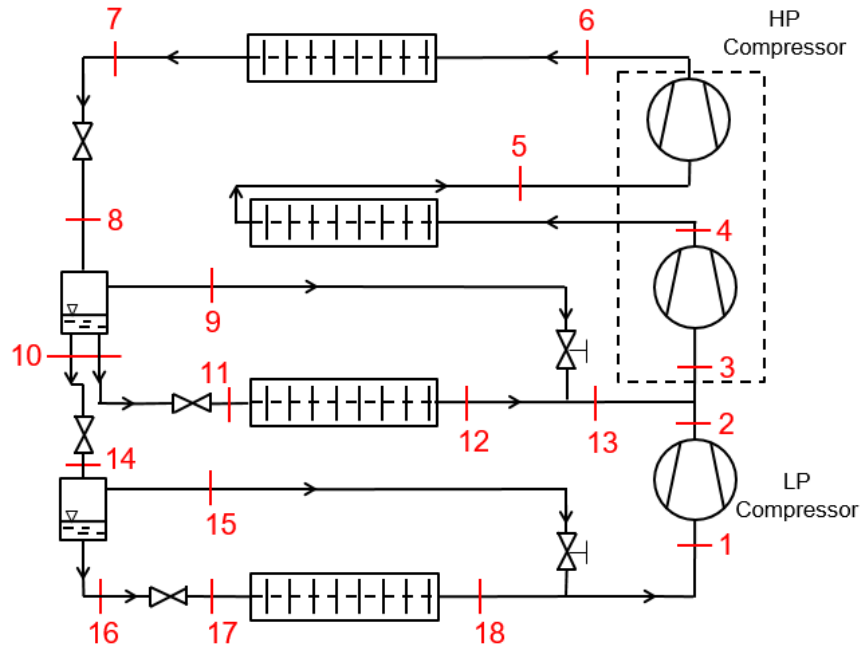
economization is presented in this work. In addition, deficiencies in the design and associated recommendations are provided, as is a description of future work intended for the test stand.

## **2.2 Cycle Design and Thermodynamic Modeling**

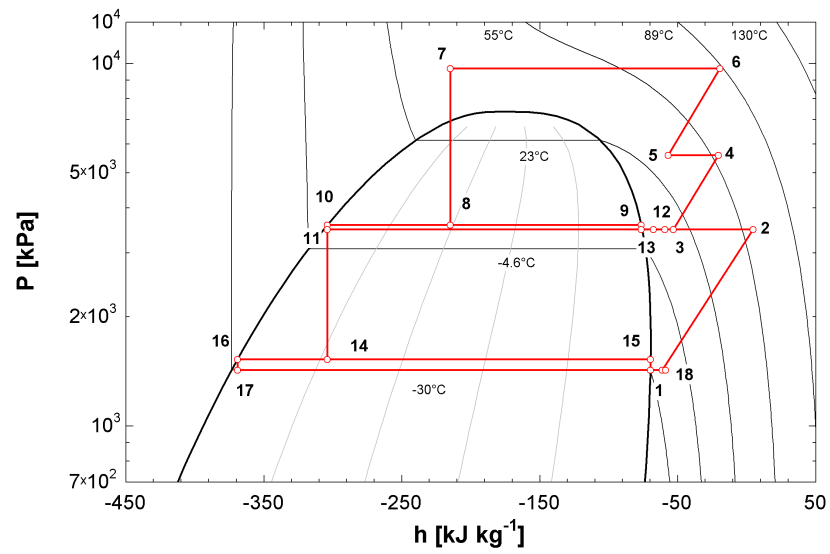
The design of the test stand is based on two primary cycle configurations that are based upon different expansion technologies. In particular, the cycle architecture employing EXVs with no phase separation is considered to be the baseline configuration. The second configuration features an ejector expansion device. This section provides a detailed description of the two architectures and their variations. Moreover, the thermodynamic modeling conducted to provide estimates of system capacity, pressure, and temperatures throughout to aid in component selection is outlined.

### **2.2.1 Cycle Design Overview**

The schematic of the baseline EXV mode cycle and the corresponding state points on a P-h diagram are provided in Figure 2.2(a) and Figure 2.2(b), respectively.



(a)



(b)

Fig. 2.2. (a) Schematic of the experimental CO<sub>2</sub> test stand in EXV mode; (b) Theoretical state points of the experimental CO<sub>2</sub> test stand in EXV mode on a P-h diagram.

An ejector operates by converting the high-pressure flow from the gas cooler (GC) outlet through a motive nozzle to a high-velocity flow which enters the receiving section. The low-pressure vapor from the evaporator outlet is entrained into the receiving section by the high-velocity motive flow. The two flows mix in a constant-area cylindrical mixing section before exiting the ejector through a diffuser. It is vital to observe that the pressure at the diffuser outlet is higher than the evaporation pressure, as the higher diffuser outlet pressure represents the ability of the ejector to harness the available expansion work to reduce the load on the compressor. A schematic and P-h diagram of the ejector cycle are provided in Figure 2.3(a) and Figure 2.3(b) respectively.



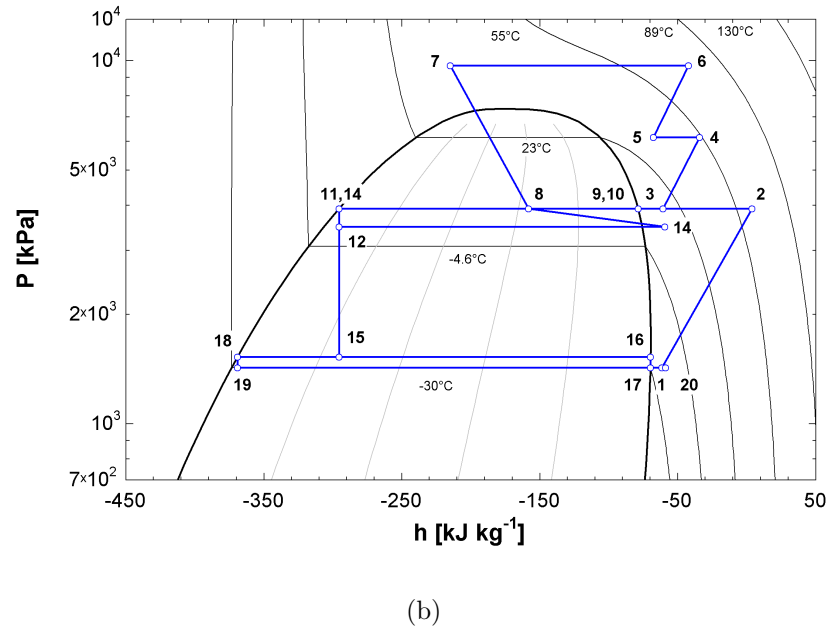
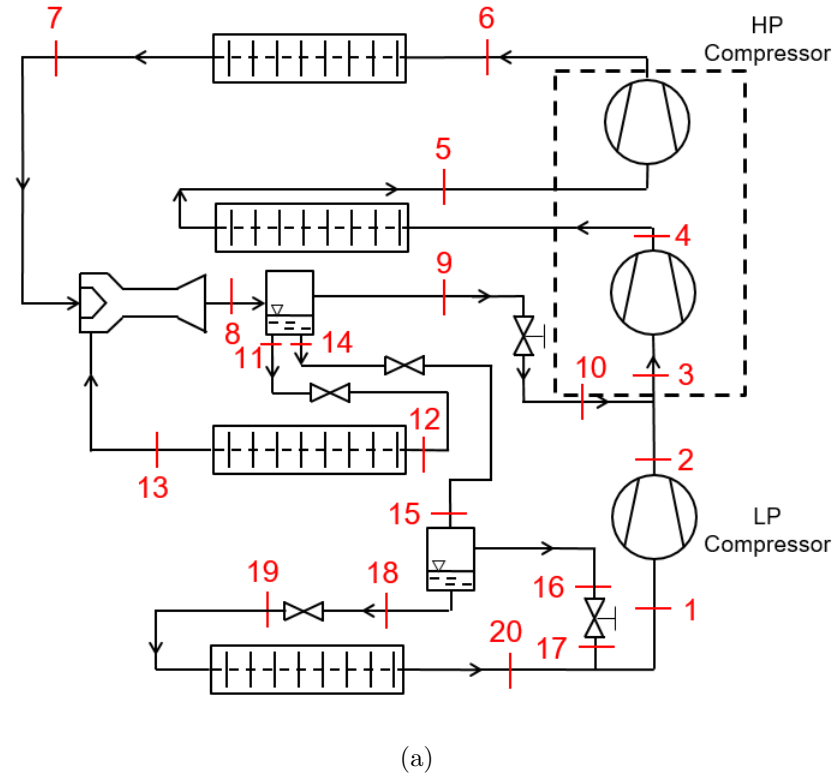


Fig. 2.3. (a) Schematic of the experimental CO<sub>2</sub> test stand in ejector mode; (b) Theoretical state points of the experimental CO<sub>2</sub> test stand in ejector mode operation on a P-h diagram.

The ejector installed in the test stand was developed by Liu and Groll [111]. The ejector was designed with variable geometry that allows variation of the motive and suction nozzle diameters, but only the motive nozzle diameter can be changed during operation. The motive nozzle diameter is modulated through a threaded needle that moves up and down the motive nozzle, varying its effective flow area. A photo and technical drawing of the ejector are shown in Figures 2.4(a) and 2.4(b), respectively.

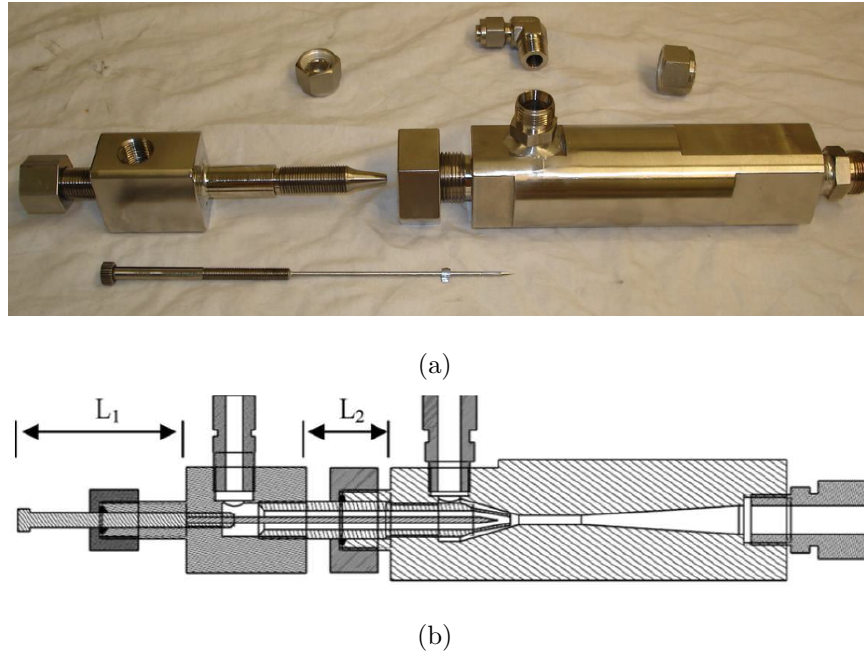


Fig. 2.4. (a) Photo of the adjustable ejector applied in the  $\text{CO}_2$  test stand; (b) Technical drawing of the adjustable ejector applied in the  $\text{CO}_2$  test stand.

In addition to the variation of the motive nozzle diameter, the use of a pump to control the motive nozzle inlet pressure was assessed. A high-pressure pump specified to handle suction pressures up to 80 bar was placed at the gas cooler outlet, and variation of the pump speed would result in control of the motive nozzle inlet state. The idea behind applying a pump was that it requires less work to increase the pressure of a liquid than a gas, due to the smaller change in specific volume associated with decreasing compressibility of a fluid for a given pressure rise. Therefore, the work

input by the pump would result in an increase in ejector pressure lift that would decrease the work input required by the compression process by a larger amount of power than was required by the pump, thus increasing the cycle COP. The pump employs three cylinders that are 20 mm in diameter with a stroke of 30 mm. The suction chamber is separated from the crank case through Tungsten-Carbide plungers and piston rings with tight tolerances, so force is transmitted via coupling of the pistons from the crank case to the bottom of the plungers. A photo of the pump installed in the test stand is shown in Figure 2.5.

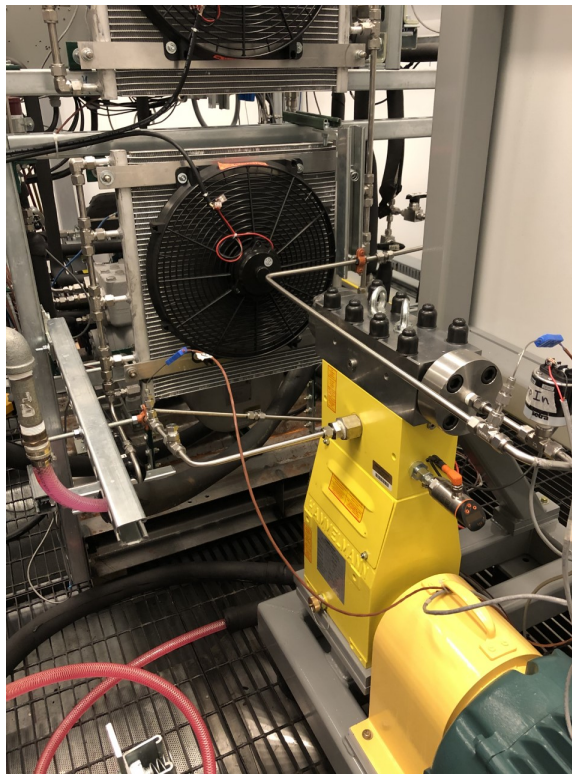


Fig. 2.5. Photo of the CO<sub>2</sub> pump installed in the test stand.

A table outlining all six possible cycle architectures is provided in Table 2.2, with HP and LP referring to high pressure and low pressure, respectively.

Table 2.2.  
Possible cycle architectures for the CO<sub>2</sub> test stand.

Number	Expansion	Economization
1	EXV	None
2	EXV	MT evaporator
3	EXV	LT evaporator
4	EXV	MT and LT evaporators
5	Ejector	MT evaporator
6	Ejector	MT and LT evaporators

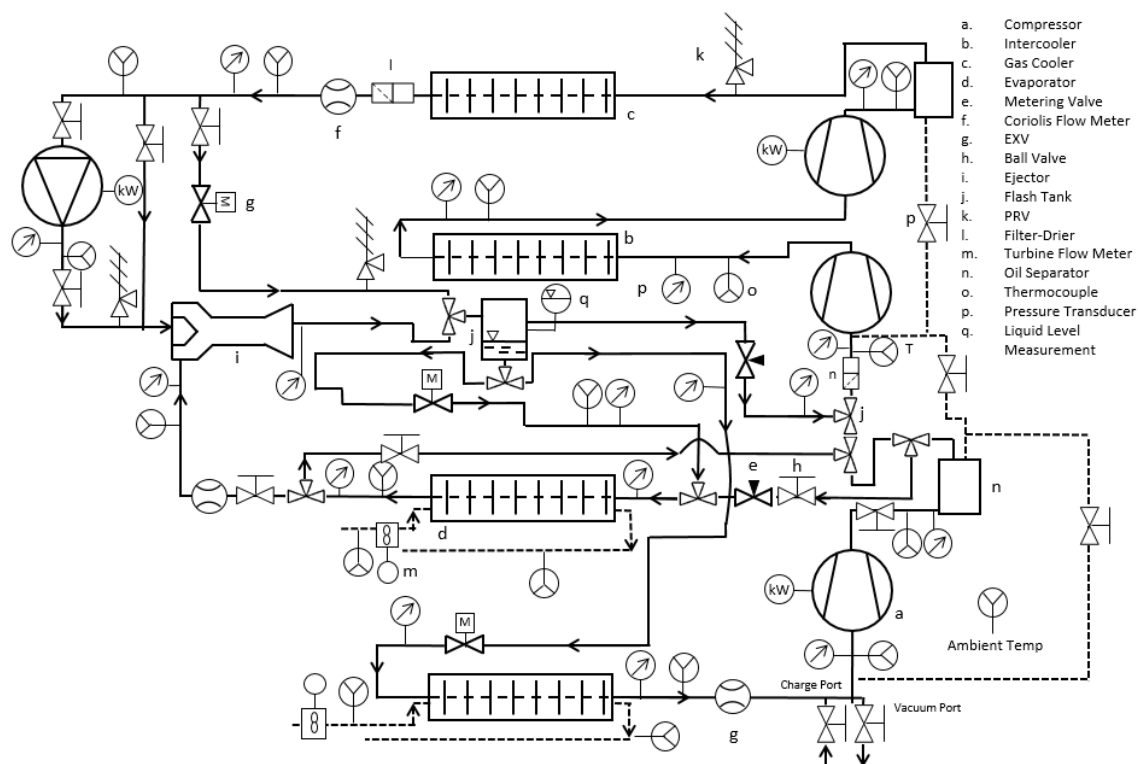


Fig. 2.6. Detailed P&ID schematic of the CO<sub>2</sub> test stand.

A detailed piping and instrumentation diagram (P&ID) for the test stand that was built to assess these cycles and their derivatives is provided in Figure 2.6. Oil management was conducted through dedicated oil separators installed at the discharge of each compressor with a metering valve (MV)-actuated return line to the compressor oil sump. Tubing was installed between the compressor sumps and controlled with a ball valve (BV) for equalization of oil levels between compressors, which can be actuated once a given test has concluded. In practice, the oil bypass valves can be partially opened to allow the cycle to retain a similar pressure differential, in which case the oil bypass should be left open for longer but the cycle will return to its original conditions faster. alternatively, the bypass valves could be opened to expedite the oil return but sacrifice cycle operating conditions.

Two techniques for monitoring liquid level in the flash tanks were implemented for redundancy. The first is visual liquid level monitoring and the second is capacitive liquid level sensing. The EXVs immediately upstream of each evaporator are used for evaporator outlet superheat control, while the EXV between the two flash tanks is used for charge distribution control between the two tanks. If the liquid level rises in a flash tank, the upstream EXV will reduce its effective diameter, and vice-versa if the liquid level decreases in a flash tank. Simultaneously, the vapor bypass valves at the outlet of each evaporator will be employed to ensure that enough vapor is bypassed to allow complete phase separation within the flash tanks while also matching the pressure drop on the evaporator-side, thus allowing a constant liquid level to be achieved. Otherwise, the vapor bypass will receive more flow and risk flash tank flooding. Conversely, if the EXV at the flash tank outlet drives more flow than the bypass valves, the flash tank could drain all of the liquid, thus significantly reducing evaporator capacity. A physical photo of the instrumented and insulated flash tanks is shown in Figure 2.7.



Fig. 2.7. Photo of liquid level measurements in the CO<sub>2</sub> test stand.

Measurement devices and the reasoning for their placement will be discussed in-depth in Section 2.3. Valves were placed strategically throughout the test stand, as shown in the form of a thorough schematic in Figure 2.6 as well as in a simplified schematic in Figure 2.8, in order to facilitate a safe transition between EXV and ejector operating modes without turning off the compressors. The green lines represent refrigerant flow that will be utilized throughout all cycles, while the red, yellow, and blue lines represent refrigerant flow paths unique to ejector, ejector and pump, and EXV modes, respectively. As can be seen, the heat exchangers, compressors, and the majority of the tubing will be common throughout the designs, suggesting a solution that comes as close to meeting the test stand goals as possible. While the transitions between combinations of economization can be conducted with MV actuation, namely MV 1 and MV 2, the transition between EXV and ejector mode for high-side expansion requires four steps. The transition to ejector operation entails first actuating ball valve BV 8 to direct flow to the motive nozzle inlet, closing BV 1 to divert 100% of the GC outlet flow to the ejector motive nozzle, opening BV 4 to send flow

from the evaporator outlet to the ejector suction nozzle inlet, and finally closing BV 3 to divert 100% of the evaporator outlet flow to the ejector suction nozzle, shown by steps 1 through 4, respectively, in Figure 2.8.

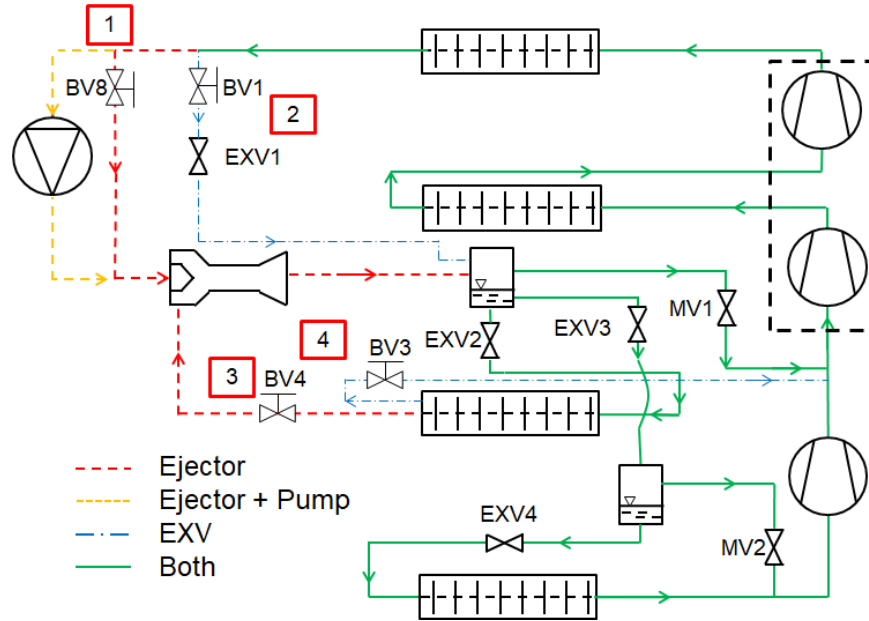


Fig. 2.8. Summary of the EXV to Ejector transition in the CO<sub>2</sub> test stand.

### 2.2.2 Thermodynamic Model Overview

The purpose of the thermodynamic modeling was to develop a model for the purpose of component sizing and selection. As such, simplifying assumptions were made surrounding the system and primary components. Compressor performance was quantified via 10-coefficient ARI maps [112], which have been obtained through a combination of testing on a hot-gas bypass test stand and manufacturer data, and were corrected for a suction superheat of 10 K. Pressure drop in heat exchangers was neglected, and the heat exchanger outlet state was solved as function of a fixed pinch of 5 K between the refrigerant outlet and secondary fluid inlet temperature. The flash

tank phase separation was assumed to be ideal, and expansion through EXVs was assumed to be isenthalpic. Heat loss and pressure drop in the lines were neglected.

The ejector model was based off of a constant-area cylindrical mixing section model by Li and Groll [52] with a modified numerical approach that provided a solver to quickly solve the entire cycle for a range of operating conditions. Conservation of mass in the mixing section is solved by iterating on the mixing pressure as shown in Equation 2.1, and is confirmed again between the diffuser outlet quality and the flash tank into which it diffuses.

$$\frac{(a_{\text{mb}} + a_{\text{sb}})u_{\text{mix}}}{v_{\text{mix}}} = 1 \quad (2.1)$$

where  $a$  is the area per ejector mass flow rate,  $u$  is the flow velocity and  $v$  is the specific volume. The relationship between entrainment ratio, defined in Equation 2.2, and diffuser outlet quality is found through solving the thermodynamic definitions of quality and entrainment ratio to arrive at an expression of quality as a function of the entrainment ratio, as well as other mass flow rates throughout the system depending on system complexity.

$$w = \frac{\dot{m}_{\text{suction}}}{\dot{m}_{\text{motive}}} \quad (2.2)$$

where  $x_d$  is the diffuser outlet quality,  $w$  is the entrainment ratio, and  $\dot{m}$  is the mass flow rate. A flowchart for the ejector solver is shown in Figure 2.9. In particular, the inlet conditions from the GC and evaporator outlet are inputs during the initialization phase, along with initial guesses for  $w$  and mixing section pressure,  $P_{\text{mix}}$ . Next, the ejector solves each component sequentially, using the outputs from the motive and suction nozzle calculations as inputs for the mixing section, before the diffuser utilizes outputs from the mixing section as its inputs. Once the component solutions are calculated, conservation of mass is checked at two places. The first check occurs at the mixing section outlet, where the mixing section pressure is iterated upon until convergence. Next, the diffuser outlet quality is used along with the input entrainment ratio and other system mass flows to check for conservation of mass with respect to the



entire cycle, and the entrainment ratio is iterated upon until the conservation of mass criterion is satisfied. After satisfying conservation of mass, the solver is complete and has also been automatically integrated within the rest of the cycle given its consideration of system conservation of mass. It is worth noting that, despite the first conservation check occurring before the diffuser, the diffuser is solved anyway because it is inside of the first loop and is a function of independent, intensive properties only.

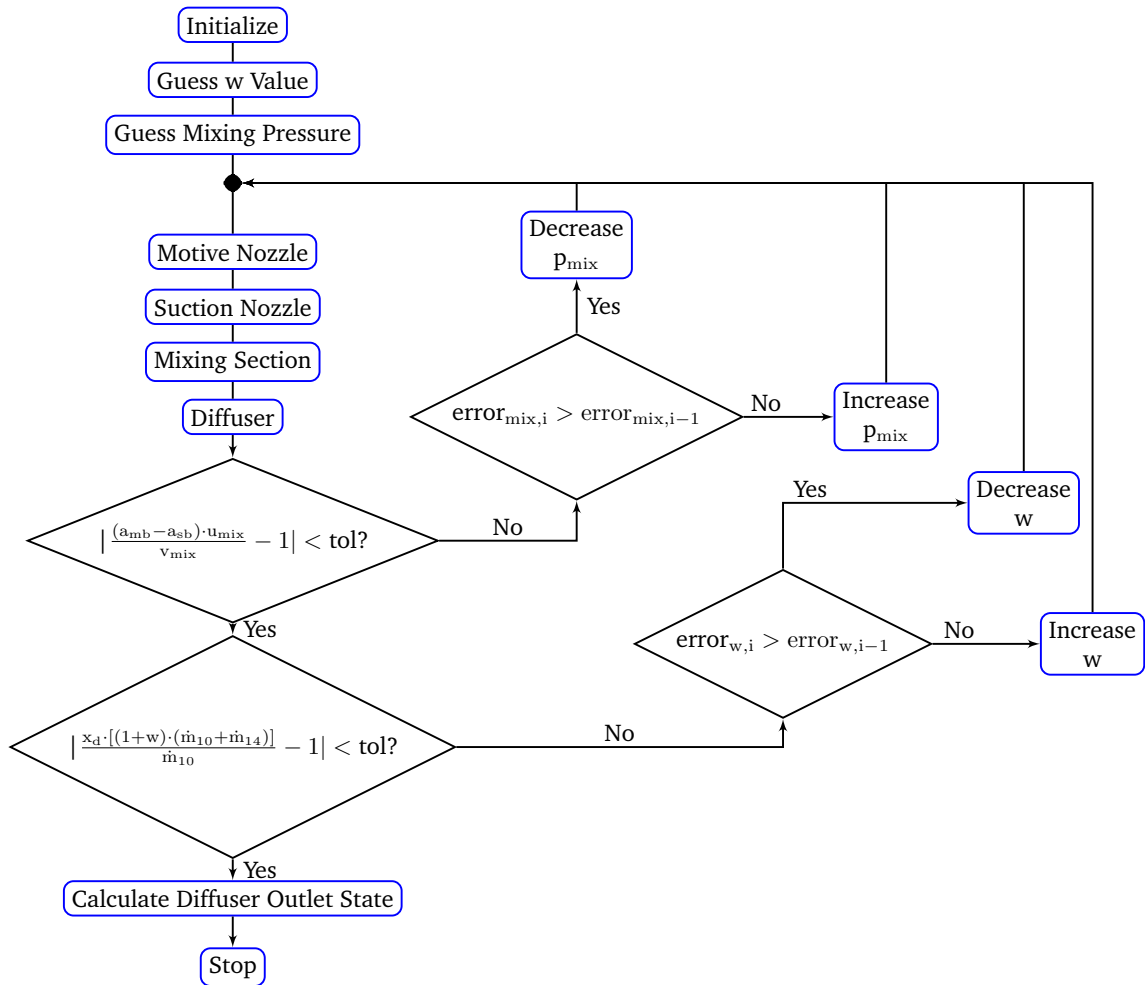


Fig. 2.9. Flowchart of the ejector solver integrated into the CO<sub>2</sub> test stand model shown in Figure 2.3(b)

Motive and suction nozzle efficiencies were assumed to be 0.9, and the diffuser efficiency was assumed to be 0.8 from the literature, as summarized in Liu [55]. Nozzle and diffuser efficiency calculations are provided in Equations 2.3 and 2.4, respectively, and operate under an adiabatic assumption.

$$\eta_{\text{nozzle}} = \frac{h_{\text{in}} - h_{\text{out}}}{h_{\text{in}} - h_{\text{out},s}} \quad (2.3)$$

$$\eta_{\text{diffuser}} = \frac{h_{\text{out},s} - h_{\text{in}}}{h_{\text{out}} - h_{\text{in}}} \quad (2.4)$$

where  $h$  is the specific enthalpy and the  $s$  subscript denotes the outlet if the process were isentropic.

Once the thermodynamic state points had been identified, line size was varied and the velocity at states throughout the test stand was calculated. Per the ASHRAE Refrigeration Handbook [113], Table 2.3 outlines the ranges of flow velocities throughout the test stand. The lower bound is set to prevent significant oil entrapment, and the upper bound is set to avoid high pressure drops and excess noise throughout the system.

The three inlet conditions to the ejector motive nozzle were sub-cooled liquid, super-critical liquid, and super-critical fluid. These three design states are summarized in Table 2.4, including ambient temperature, GC pressure, and projected evaporator cooling capacities for each condition. The evaporator conditions at all tested states were air inlet temperatures of 3.3 °C and -20.6 °C for the MT and LT evaporators, respectively, with an assumed pinch point of 5 K. LP compressor suction and MT evaporator outlet superheats were set to 10 K.

Table 2.3.  
Recommended design velocities throughout a refrigeration system [113].

Location	Velocity (m s <sup>-1</sup> )
Suction Line	2.5 - 20
Discharge Line	10 - 18
Liquid Line, Condenser to Receiver	< 0.5
Liquid Line, Receiver to Evaporator	< 1.5

Table 2.4.  
Summary of chosen design points for the CO<sub>2</sub> test stand.

State	$T_{\text{Amb}}$ (°C)	$P_{\text{GC}}$ (kPa)	$\dot{Q}_{\text{MT}}$ (kW)	$\dot{Q}_{\text{LT}}$ (kW)
Sub-cooled Liquid	23	7000	7.7	3.1
Super-critical Liquid	25	8000	7.8	3.1
Super-critical Fluid	30	10000	9.9	3.1

The test stand was placed in a psychrometric chamber to enable control of the ambient temperature and humidity. For control of evaporation conditions, two separate constant-temperature Water-Ethylene Glycol (EG) baths were implemented to serve as evaporator heat sources. the independent bath configuration allowed separate control of evaporator temperatures and loads, enabling a broader range of test conditions. As such, both evaporators are plate heat exchangers (PHX) installed in vertically in counter-flow orientation. The MT evaporator temperature can supply fluid from -16 °C to 37 °C and the LT temperature bath can reach temperatures down to -35 °C. Both are operated at target a flow rate of 10 liters per minute to maxi-

mize temperature differential for accurate measurement while also retaining accurate measurements from the turbine flow meter

### 2.2.3 Design Constraints and Results from Modeling

A simplified charge inventory model was developed with conservative estimates for line lengths and component internal volumes. For the HXs, the density from the lower temperature port was taken as the density throughout the HX, leading to an overestimate. The conservative charge estimate was made with the intention of the flash tanks also being oversized, and thus being able to absorb any additional charge necessary. The low cost of CO<sub>2</sub> was also considered in the decision to oversize the flash tanks. The system model utilized the specific volume from each state point and the estimated volume of the system components to calculate the system charge, which resulted in a charge estimation of 6 kg. For each of the three design operating conditions, internal optimization was used to solve for the GC outlet pressure that led to the highest COP at the given operating condition. Therefore, key system attributes such as pressure, mass flow rate, and temperatures for components reflected the cycle operation at an operating condition that resulted in the highest COP at that condition. The largest components were associated with the lowest ambient temperature, and were chosen as the target design point to ensure the system was not undersized. The resulting design points used for evaporator design were driven largely by compressor map outputs and are provided in Table 2.5.

Table 2.5.  
Summary of evaporator design points for the CO<sub>2</sub> test stand.

MT Evaporator					LT Evaporator				
CO <sub>2</sub> Side			Glycol Side		CO <sub>2</sub> Side			Glycol Side	
$T_{\text{in}}$	$\dot{m}$	$\dot{Q}_{\text{cool}}$	$T_{\text{in}}$	$\dot{m}$	$T_{\text{in}}$	$\dot{m}$	$\dot{Q}_{\text{cool}}$	$T_{\text{in}}$	$\dot{m}$
(°C)	(g s <sup>-1</sup> )	(kW)	(°C)	(g s <sup>-1</sup> )	(°C)	(g s <sup>-1</sup> )	(kW)	(°C)	(g s <sup>-1</sup> )
3.7	42.6	9.83	13.0	1350	-30.0	9.53	3.0	-15.0	1350

The EXV sizing was based on results from the modeling described Section 2.2 and was limited by three attributes, being maximum pressure, maximum operating pressure differential (MOPD), and inlet volumetric flow rate. Because the valves were designed for transcritical CO<sub>2</sub> operation, the design MOPD of 9 MPa and maximum operating pressure of 14 MPa were both greater than the values from the model prediction for test stand behavior. The inlet states dictated the maximum pressure and volumetric flow rate, and a combination of inlet and outlet states provided conditions for the operating pressure differential. The chosen EXV met the required specifications well, and three different valve models were selected to best match the four EXV applications. The  $k_v$  values, defined as the volumetric flow rate through an area resulting in a 100 kPa pressure drop with water at 15.6 °C, for each of the four EXVs installed in the test stand are provided in Table 2.6 to show justification for the choice, following nomenclature from Figure 2.8.

Table 2.6.  
EXV operating conditions and valve selections for the CO<sub>2</sub> test stand.

<i>Danfoss CCMT Ranges</i>		
Valve	$k_v$	
(-)	(m <sup>3</sup> hr <sup>-1</sup> )	
CCMT 2	0.17	
CCMT 4	0.45	
CCMT 8	0.8	
<i>Test Stand EXV Ranges</i>		
EXV #	$k_v$	CCMT Selection
(-)	(m <sup>3</sup> hr <sup>-1</sup> )	(-)
1	0.49	8
2	0.18	4
3	0.05	2
4	0.03	2

## 2.3 Component Selection and Test Stand Construction

This section discusses application of the design constraints obtained from initial modeling in Section 2.2 to the selection of available componentry for the test stand. Details of component and measurement device selection and placement are provided, as is an overview and final result of the test stand construction process.

### 2.3.1 Primary Component Selection

The selection of key components within the cycle was driven by the use of compressors that were available at the research facility. The selected components, along

with any important comments, will be discussed herein. The LP compressor used in the setup is a two-cylinder reciprocating compressor with a total displacement of 16.7 cm<sup>3</sup>. The HP compressor is a two-stage transcritical compressor with two cylinders dedicated to the first stage and a third cylinder dedicated to the second stage with total displacements of 33.3 cm<sup>3</sup> and 20.0 cm<sup>3</sup>, respectively.

The chosen air to refrigerant HXs were micro-channel HXs (MCHX), with stainless steel construction and aluminum louvers between passes. Given that each MC heat exchanger has a nominal capacity of 5 kW, one MCHX was selected to perform as the intercooler (IC) between the two compression stages of the HP compressor and three MCHXs were used in series for the GC portion of the cycle. Initial model results showed up to 5 kW of heat rejection at the IC and between 10 kW and 15 kW during gas cooling. Because the nominal capacity of the MCHXs that were available was 5 kW, one was applied for intercooling and three were applied in series for the gas cooling process. The fans mounted on the surface were rated at 3420 m<sup>3</sup> hr<sup>-1</sup> each, with one installed on each HX. In order to facilitate independent control of each evaporator via temperature bath, a PHX design was selected for both evaporators. Because the HXs were to be subjected to the high system equilibrium pressures that could reach 5 MPa, high-pressure stainless-steel PHXs were needed. 24 plate and 26 plate PHX designs were chosen for the LT and MT evaporators, respectively, due to the larger predicted capacity of the MT evaporator.

A three-port pressure vessel was selected for the flash tank. The inlet was chosen to be the port in the middle, while the liquid and vapor outlet ports were chosen to be the bottom and top ports, respectively. A high-pressure pressure relief valve (PRV) was installed at the third stage compressor discharge, and an intermediate-pressure PRV was installed at the inlet to the MT flash tank. The intermediate-pressure PRV was installed to ensure the resting pressure of the system does not exceed the pressure rating for the flash tanks and their liquid level measurement devices. The operating pressure for the flash tanks is below their maximum pressure ratings, but since the resting pressure of the test stand could exceed 5 MPa, the installation of

the intermediate-pressure PRV was deemed prudent. To connect the EXVs to the system, a stainless-steel tube was welded to the housing for connection to the rest of the system via swage fittings. Manual control of the valves was achieved through the use of a controller and display, which allowed the input of settings such as number of steps, maximum rate of valve steps, and voltage input range, among others. The valves were then mated to the LabVIEW visual interface for manual control via analog voltage input.

The detailed physical description and performance characterization of the ejector installed in the test setup can be found in Liu and Groll [114]. In particular, the ejector features a variable geometry motive nozzle, allowing the variation of the nozzle diameter via a threaded needle, as well as a motive receiving section diameter to enable off-design point operation.

### 2.3.2 Selection of Measurement Devices

The test stand cycle architectures have been discussed in depth in Section 2.2. Specifically, Figure 2.6 shows all installed measurement devices in the experimental setup. To correctly estimate thermo-physical properties at each state point throughout the cycle, both in-line temperature and pressure are measured at single-phase points. For states that fell within the vapor dome, an assumption of isenthalpic expansion is used in combination with often-redundant temperature and pressure to back out specific enthalpy of the state point. Mass flow rate measurements are made with Coriolis-effect mass flow meters, while the EG-side volumetric flow rates are measured with turbine flow meters. Power consumption of both compressors is measured independently by means of watt transducers placed upstream of the variable frequency drives installed on both compressors. The complete list of measurement instrumentation is provided in Table 2.7 as is the accuracy, model, and manufacturer.



Table 2.7.  
Summary of sensors and corresponding uncertainties for the CO<sub>2</sub> test stand.

Measurement	Description	Model	Accuracy
Temperature	Ungrounded TC	Omega T-Type	$\pm 0.5$ K
Pressure (HP side)	PT, 0-20684 kPa	Setra 206	$\pm 26.9$ kPa
Pressure (LP side)	PT, 0-6895 kPa	Setra 206	$\pm 9.0$ kPa
Mass flow ( $\dot{m}_{\text{motive}}$ )	Coriolis mass flow meter	Micromotion CMFS050	$\pm 0.1\%$ Rdg.
Mass flow ( $\dot{m}_{\text{suction}}$ )	Coriolis mass flow meter	Micromotion F025	$\pm 0.2\%$ Rdg.
Mass flow ( $\dot{m}_{\text{LTE}}$ )	Coriolis mass flow meter	Micromotion F025	$\pm 0.2\%$ Rdg.
Volume flow ( $\dot{V}_{\text{EG}}$ )	Turbine volume flow meter	Omega FTB-1424	$\pm 0.1\%$
Liquid Level	Capacitive liquid sensor	SWI CS02	0.2% Rdg./0.4% FS
Compressor Power	Watt transducer	Ohio Semitronics GW5-015E	0.5% Linearity
Fan Power	Watt transducer	Ohio Semitronics PC8-001	1.0% FS

The uncertainties of calculated variables were determined using the accuracy of instrumentation and Equation 2.5 [115].

$$U_Y = \sqrt{\sum_i \left( \frac{\partial Y}{\partial X_i} U_{X_i} \right)^2} \quad (2.5)$$

where  $Y$  is the calculated quantity,  $X$  is the measured quantity, and  $U$  is the uncertainty.

A photo of the completed test stand assembly from the back of the psychrometric chamber is shown in Figure 2.10.

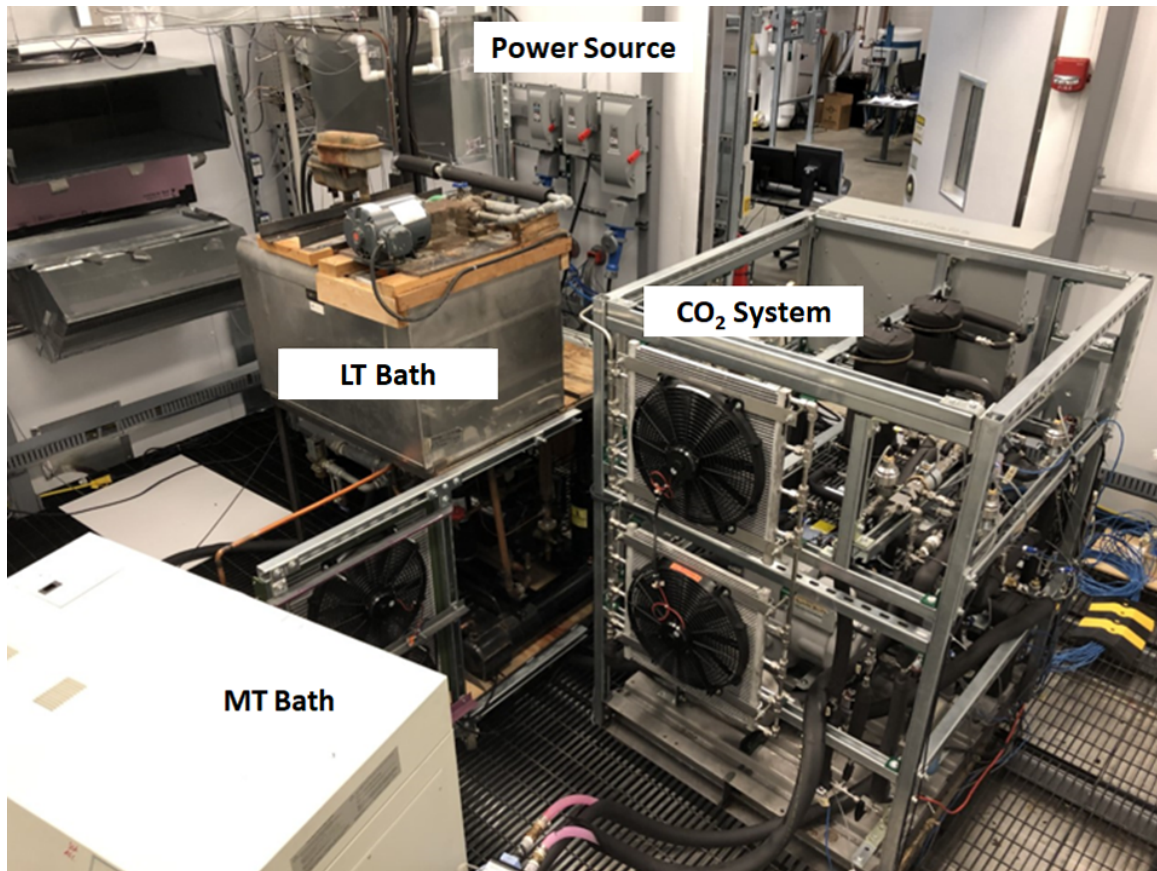


Fig. 2.10. Rear view of the CO<sub>2</sub> test stand placed inside of a psychrometric chamber.

The fan power consumption is measured by a watt transducer, but due to the high start-up current draw of over 5 A for each fan and budgetary constraints, two separate 20 A power supplies were required to power all four fans. Therefore, the outputs each power supply were combined upstream of the watt transducer to be measured together. As the supplied power continued through the watt transducer, four individual DC lines split off to feed each fan. A wiring diagram of the system power measurement is provided in Figure 2.11. The pump power measurement was added to this wiring scheme, but follows the same wiring as the two GW5 transducers

shown. Furthermore, both compressors and the pump were eventually modified to be controlled by an individual variable frequency drive (VFD) for maximum control.

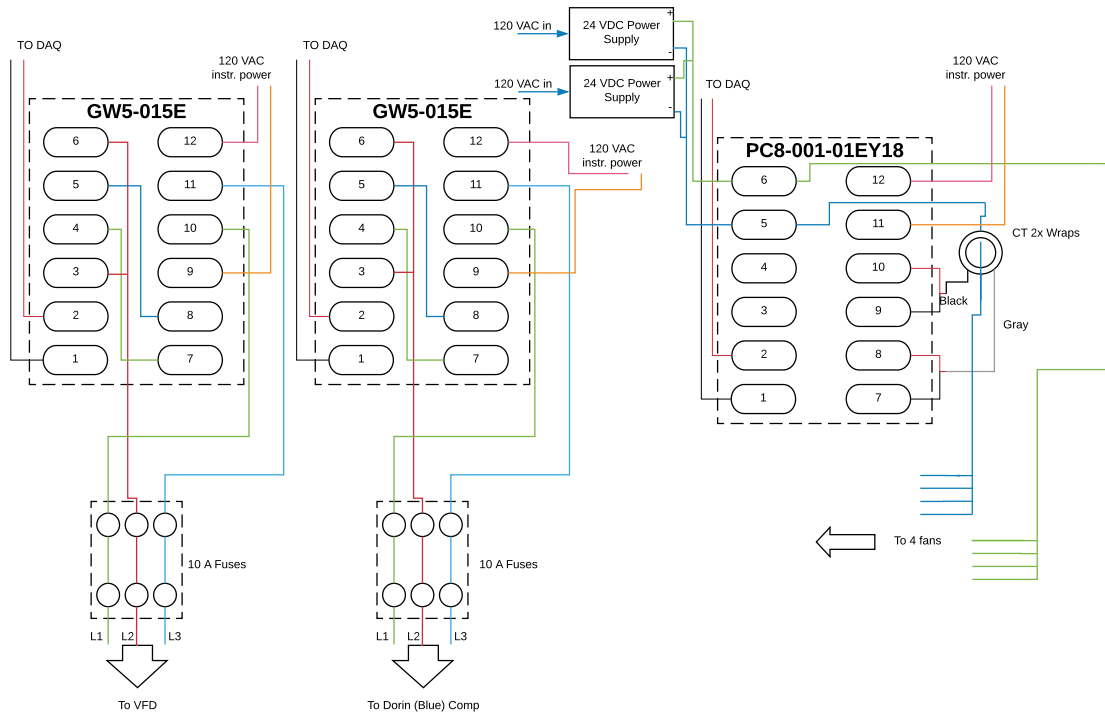


Fig. 2.11. Power measurement wiring diagram for the CO<sub>2</sub> test stand.

While the test stand consumes a significant amount of power, and thus requires planning for physical disconnects, wire sizes, and fuses, both compressors operate on 460 VAC. Therefore, the current draw for each compressor is less than 10 A. However, the two temperature baths required to facilitate cycle establishment operate on 208 VAC draw 31.5 A and 21.6 A for LT and MT baths, respectively. The wiring sizes and disconnects were selected carefully to ensure safe and reliable system operation. A schematic showing the nominal current draw, denoted as RLA, and the locked-rotor

current draw (LRA) for all components is provided in Figure 2.12. Additionally, the cable sizes, disconnect sizes, and fuses applied are included in the schematic.

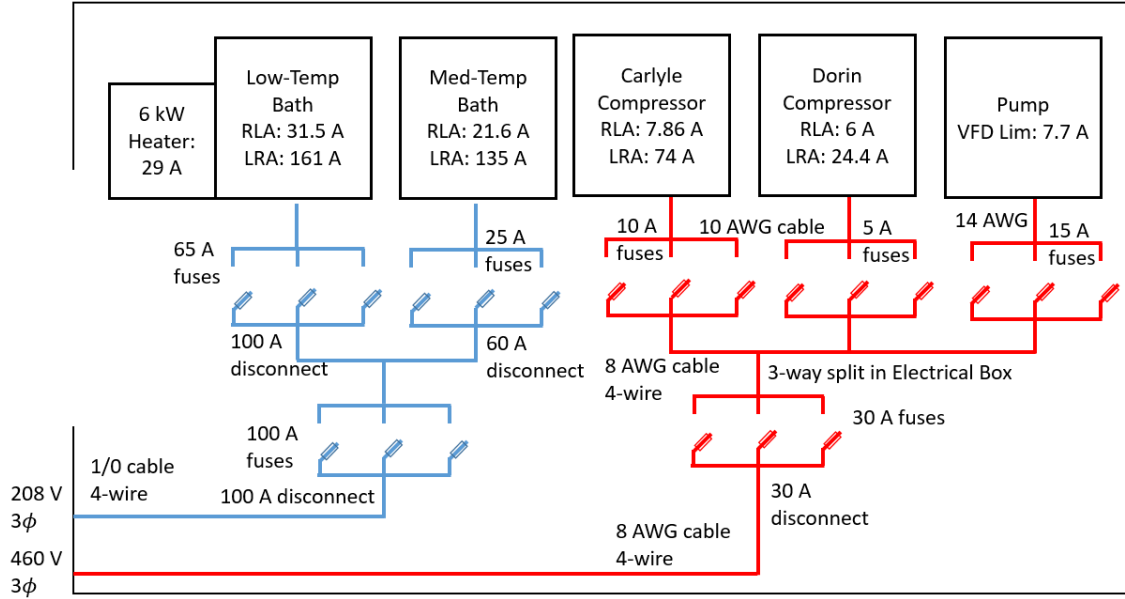


Fig. 2.12. CO<sub>2</sub> test stand power supply schematic.

## 2.4 Experimental Operation and Validation

In order to validate the operation of the test stand, two energy balances were assessed. The first is the evaporator energy balance between the refrigerant and the EG heat source loop. Once the specific heat,  $c_{p,EG}$ , and density,  $\rho_{EG}$ , of the EG mixture are known, the cooling capacities for each secondary loop are calculated and compared to the refrigerant-side cooling capacity. Equations governing the calculation of the secondary loop cooling capacity, refrigerant-side capacity, and the comparison of the relative error,  $RE$ , between the two are provided in Equations 2.6, 2.7, and 2.8, respectively.

$$\dot{Q}_{cool,secondary} = \dot{V}_{EG} \rho_{EG} c_{p,EG} (T_{in,EG} - T_{out,EG}) \quad (2.6)$$

$$\dot{Q}_{\text{cool,ref}} = \dot{m}_{\text{ref}}(h_{\text{evap,out}} - h_{\text{evap,in}}) \quad (2.7)$$

$$RE_{\text{capacity}} = \frac{\dot{Q}_{\text{cool,ref}} - \dot{Q}_{\text{cool,secondary}}}{\dot{Q}_{\text{cool,ref}}} \quad (2.8)$$

where  $\dot{Q}$  is heat transfer rate,  $\dot{V}$  is volumetric flow rate,  $\rho$  is density,  $c_p$  is specific heat at constant pressure, and  $\dot{m}$  is mass flow rate.

The second energy balance was on the refrigerant-side to determine how well the sensors and post-processing procedure could account for all energy entering and exiting the system. The energy balance is shown in Equation 2.9, and the error of the energy balance is calculated relative to the amount of power input into the system, shown analytically in Equation 2.10 and schematically in Figure 2.13. The pump was not utilized in initial testing, therefore its power consumption and heat loss is not considered in energy balance analyses until Chapter 5.

$$\begin{aligned} E_{\text{bal}} = & \dot{W}_{\text{comp,LP}} + \dot{W}_{\text{comp,HP}} + \dot{Q}_{\text{cool,ref}} - \dot{Q}_{\text{reject,IC}} - \dot{Q}_{\text{reject,GC}} \\ & - \dot{Q}_{\text{loss,comp,LP}} - \dot{Q}_{\text{loss,comp,HP}} + \dot{Q}_{\text{gain,Amb}} - \dot{Q}_{\text{loss,Amb}} \end{aligned} \quad (2.9)$$

$$RE_{\text{E-bal}} = \frac{E_{\text{bal}}}{\dot{Q}_{\text{cool,ref}} + \dot{W}_{\text{comp,LP}} + \dot{W}_{\text{comp,HP}}} \quad (2.10)$$

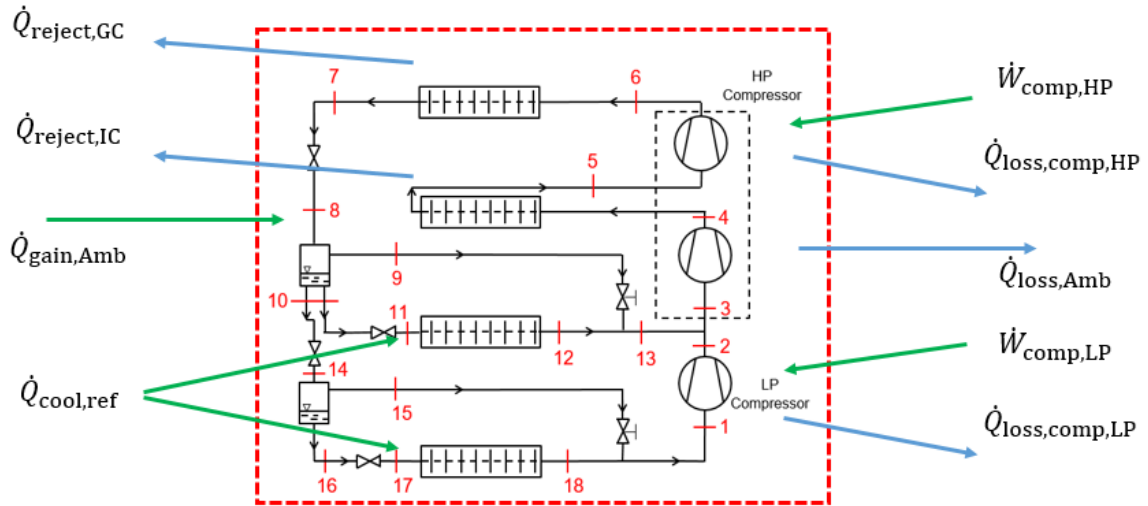


Fig. 2.13. CO<sub>2</sub> test stand energy balance in schematic form.

While the power consumed by both compressors as well as all fans dedicated to rejecting heat from the system is measured, the evaporators utilize the pumps within their respective temperature baths to supply the fluid velocity for the internal forced convection. However, the evaporator portion of the cycle was designed in order to facilitate independent control of each evaporator. True application of this refrigeration system would utilize air as the fluid to provide heat to the evaporators and thus, cool a refrigerator or freezer compartment. Therefore, the fan power that would be associated with an air-source evaporator needed to be extrapolated from data taken on a similar system, both in design and capacity, by another research team to simulate the power consumption at a constant speed. The data showed a fan power consumption of approximately 250 W per evaporator. Therefore, 500 W is conservatively assumed to be the evaporator fan power consumption of the experimental setup. All of these measurements and assumptions are applied in the calculation of COP, shown in Equation 2.11. Fan power is considered to be the sum of the measured fan power for heat rejection and the 500 W assumed for the evaporator fan power consumption. While the assumed 500 W fan power is considered in the

COP calculation, only the measured fan power is reported in the final results to retain meaning of the uncertainty associated with its measurement.

$$COP = \frac{\dot{Q}_{MT} + \dot{Q}_{LT}}{\dot{W}_{HP,Comp} + \dot{W}_{LP,Comp} + \dot{W}_{Fans}} \quad (2.11)$$

The following experimental results were obtained with varying charge levels, depending on the architecture. Without phase separation, charge was set with the goal of balancing compressor suction superheat and GC outlet states, as is done in standard vapor compression cycles, with an approximate charge of 5.7 kg. However, for architectures using the flash tanks, charge was added until approximately 30% of the flash tank was full of liquid in order to ensure saturated liquid and saturated vapor exited the bottom and top ports, respectively. While the additional charge can vary due to the capacity of the flash tank to hold several kg of charge, 8 kg was used in the tests presented here. The valves used for EXV 1 and EXV 2 were switched after initial testing showed that high-side pressure control was limited with the larger valve, and that the MT evaporator could be controlled with the larger valve. It should be noted that the selected valves were found to be oversized due to initial misunderstanding of  $k_v$  versus inlet volumetric flow rate, but recalibration of the valve openings through the LabVIEW visual interface still enabled control of the cycle. Another challenge that was observed was that the Coriolis mass flow meters placed at the evaporator outlets were found to be unreliable, the likely sources of which were the appearance of two-phase flow as well as oil in the meter.

Therefore, the EG-side capacity from the MT evaporator was used after validation using simpler cycles and the mass flow meter at the outlet of the gas cooler. The evaporator heat transfer rate measurement validation is shown in Figure 2.14, where an MAE of 3.2% of the energy balance error outlined in Equation 2.8 was achieved with eight tests. Finally, actual pinch values between the gas cooler outlet and ambient air were found to reach as low as 3.5 K. All further results shown herein utilize the EG-side capacity for both evaporators, and the resulting refrigerant-side energy balances agreed within 3.5%. Target evaporator inlet source temperatures for the

MT and LT evaporators are 3 °C and -20 °C, respectively, and are meant to simulate operating conditions for refrigeration and freezing, respectively.

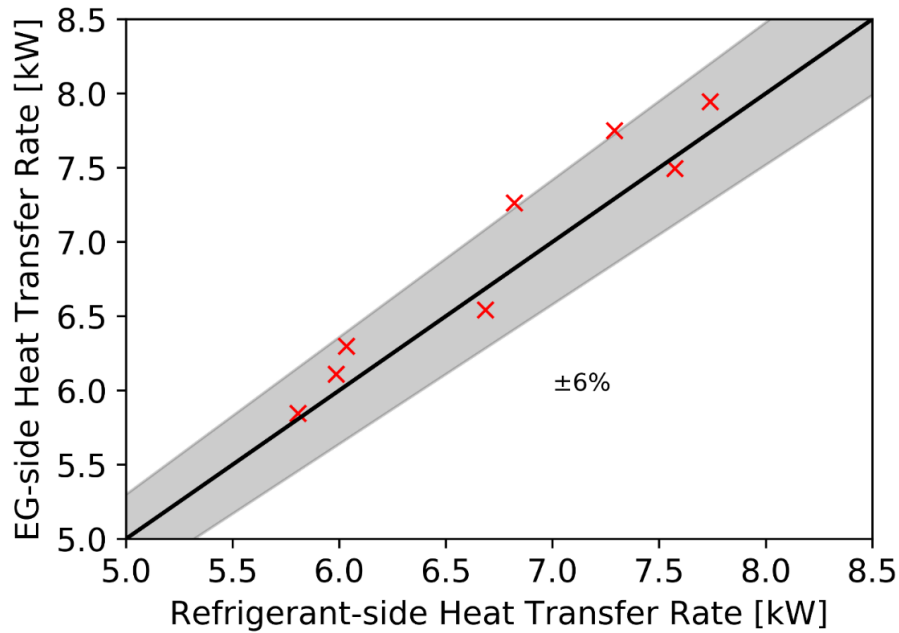


Fig. 2.14. MT evaporator energy balance: Comparison of heat transfer rates between refrigerant- and EG-sides.

First, the EXV expansion cycle using MT evaporator bypass, cycle 2, is shown at steady state in Figure 2.15, with operating parameters and energy balance results for all reported cycles provided in Table 2.8. The test of cycle 2 resulted in steady operation and a steady liquid level in the flash tank, thus validating its use. Furthermore, cycle 3 was utilized as a test to assess pressure drop in the flash tank as well as standard operation, shown in Figure 2.16. In-line thermocouples were installed at the liquid and vapor outlets, then compared to the saturation temperature associated with the pressure measured at the tank inlet. The liquid outlet temperature was found to be within 0.5 °C of the inlet saturation temperature, suggesting negligible pressure drop. However, the vapor outlet temperature was approximately 7 °C higher than the saturation temperature, which led to the conclusion that the flash



tank and suction line absorbed approximately 35 W from the ambient at a saturation temperature of  $-30\text{ }^{\circ}\text{C}$ . Next, MT economization was applied with the ejector to achieve cycle 5, shown in Figure 2.17. The cycle 5 test showed that the ejector and phase separation could both reach steady and controllable operation. The cycle architectures that utilized both flash tanks simultaneously are not reported due to rapid charge migration from the MT flash tank to the LT flash tank after opening of MV 2 to enable phase separation. The rapid charge migration could be mitigated through nearly closing EXV 3, but closing EXV 3 had the adverse effect of decreasing the LT evaporation temperature below  $-45\text{ }^{\circ}\text{C}$  and increasing suction superheat for both compressors to over 30 K. This extremely low evaporation temperature led to unsafe operation, and charge migration strategies to solve the challenge of the LT flash tank are in the future work as a result.

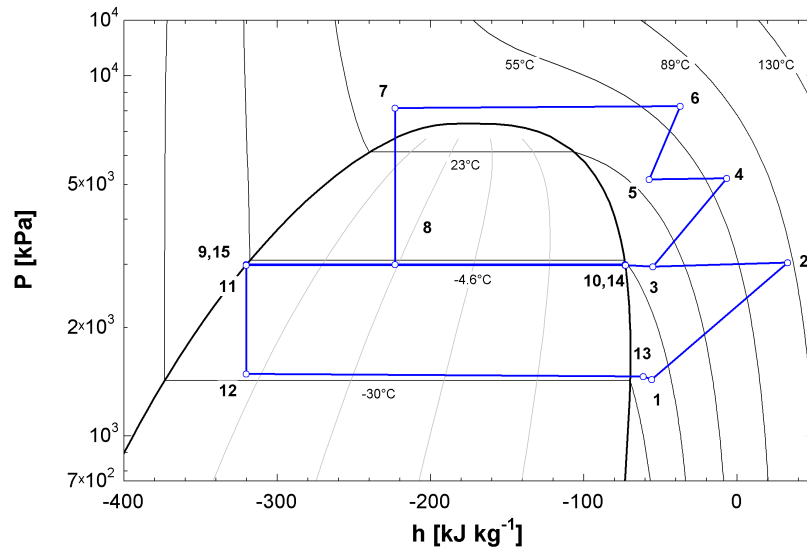


Fig. 2.15. P-h diagram of the experimental cycle achieved with the  $\text{CO}_2$  test stand using MT evaporator economization, cycle 2.

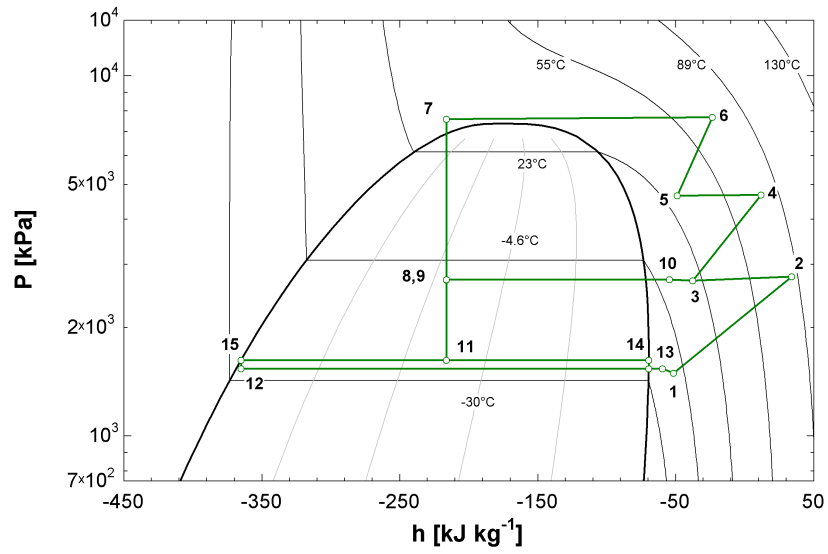


Fig. 2.16. P-h diagram of the experimental cycle achieved with the CO<sub>2</sub> test stand using LT evaporator economization, cycle 3.

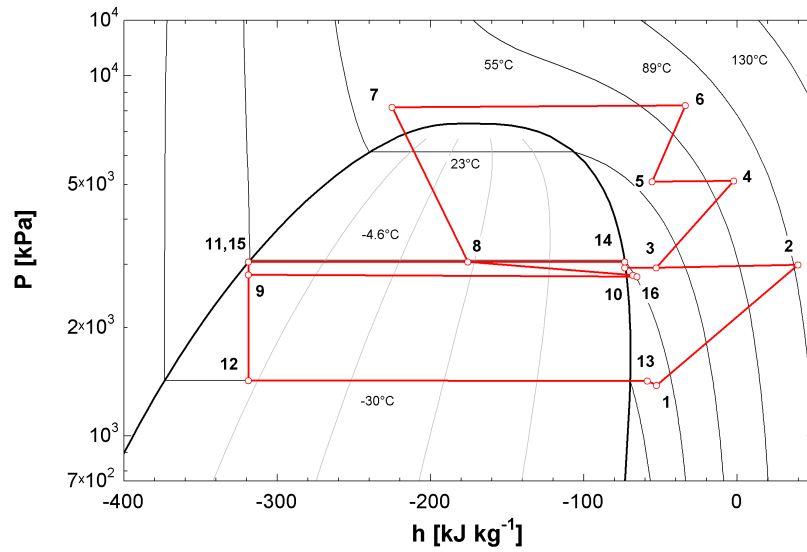


Fig. 2.17. P-h diagram of the experimental cycle achieved with the CO<sub>2</sub> test stand using an ejector, cycle 5.

Table 2.8.  
Experimental results from preliminary CO<sub>2</sub> test stand operation.

Cycle (-)	COP (-)	$\dot{Q}_{\text{MT,Evap}}$ (kW)	$\dot{Q}_{\text{LT,Evap}}$ (kW)	$\dot{W}_{\text{HP,Comp}}$ (kW)	$\dot{W}_{\text{LP,Comp}}$ (kW)	$\dot{W}_{\text{Fans}}$ (kW)	$T_{\text{MT,Evap}}$ (°C)	$T_{\text{LT,Evap}}$ (°C)	$T_{\text{Amb}}$ (°C)
2	$1.20 \pm 0.05$	$4.90 \pm 0.24$	$2.48 \pm 0.21$	$3.86 \pm 0.032$	$1.20 \pm 0.032$	$0.57 \pm 0.006$	$-5.7 \pm 0.25$	$-28.8 \pm 0.25$	$24.0 \pm 0.25$
3	$1.04 \pm 0.06$	$3.94 \pm 0.23$	$2.14 \pm 0.22$	$3.57 \pm 0.032$	$1.19 \pm 0.032$	$0.57 \pm 0.006$	$-9.1 \pm 0.25$	$-27.8 \pm 0.25$	$23.7 \pm 0.25$
5	$1.20 \pm 0.05$	$5.23 \pm 0.23$	$2.20 \pm 0.21$	$3.85 \pm 0.032$	$1.26 \pm 0.032$	$0.57 \pm 0.006$	$-8.0 \pm 0.25$	$-30.0 \pm 0.25$	$23.8 \pm 0.25$

Experimental validation of transitioning between EXV and ejector operation is provided in Figure 2.18, which shows an annotated plot of primary system pressures over time while the process shown in Figure 2.8 is applied. Compressor suction superheat was retained above a minimum safe operating value of 5 K during the entirety of the transition from EXV to ejector mode. The increase in gas cooling pressure in the middle section was achieved by slowly decreasing the diameter of the motive nozzle,  $d_{\text{motive}}$ .

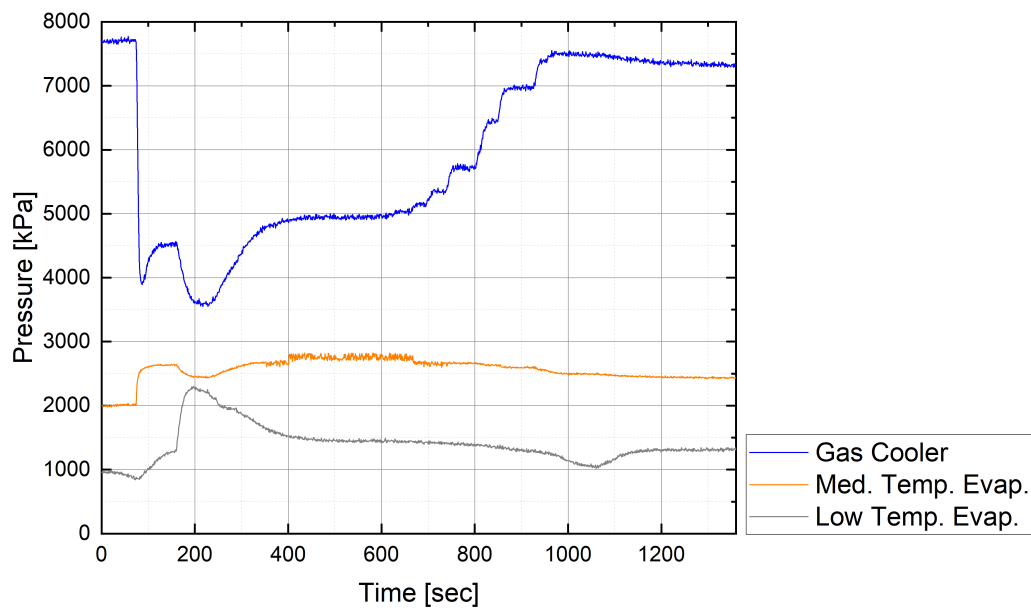


Fig. 2.18. System pressure variation over time during the transition from EXV to ejector mode in the CO<sub>2</sub> test stand.

From a system dynamics perspective, system stability was robust and allowed a reasonable amount of adjustment. However, secondary effects of adjustments must be considered in order to effectively control the stand. For example, if the EXV opening at the GC outlet is closed, the superheat at both evaporator outlets will increase, and the evaporation pressures will decrease. The increase in evaporator outlet superheat

and decrease in evaporation temperature can then be mitigated by opening the EXVs at the inlet to the respective evaporators, but care needs to be taken so that the liquid level in the flash tank does not disappear as a direct result. The varying liquid level drives tuning of the MVs, which are used to balance the vapor bypass pressure drop and flow rate but also have an effect on the evaporation pressure. Such dependent effects, coupled with the fact that both EG baths, the psychrometric chamber, and the system itself all need to achieve steady state operating conditions to take reliable data, can make cycle operation a challenge. However, once a reasonable condition is achieved in all of the aforementioned thermal systems, the same thermal inertia that made achieving steady state challenging becomes an advantage, and slight variations in the system condition, such as a sweep of GC pressures, can be absorbed by the system reasonably well, allowing the systems to return to steady operation somewhat quickly. The overview of responses discussed is something that would ultimately be taken care of by EXV proportional integral (PI) controllers, but during initial test stand development cycle control was monitored by the user manually until system dynamics are reliably modeled in the future work.

## 2.5 System Design Conclusions

This chapter presented the design and commissioning of a novel test stand to assess the performance of multiple common cycle architectures for transcritical CO<sub>2</sub> cycles. The test stand consists of two evaporators, three stages of compression, a flash tank upstream of each evaporator, and the possibility to switch between ejector and EXV expansion methods. A design overview was given, as were particulars on the component selection and design. Control strategies and measurement details were discussed. Then, the most complex architectures using EXV and ejector expansion methods were validated experimentally.

The test stand was proven to be able to close energy balances on the refrigerant-side as well as with the secondary fluid used as a heat source in both evaporators.

Challenges regarding phase separation transients were remedied through fine-tuning of the evaporator vapor bypass rate and redundant flash tank liquid level measurements. Additionally, lessons learned from the test stand design and instrumentation were discussed.

### 3. EJECTOR DESIGN

This chapter presents the development and validation of a design tool for an ejector applied in a transcritical CO<sub>2</sub> vapor compression cycle. Fundamental equations are presented, as is the process to convert an intensive thermodynamic model to physical dimensions along with validation using experimental data. Additionally, parametric studies on the impact of sub-component efficiencies and system operating conditions on performance and geometry are discussed. Finally, a comparison between ejector design and operation for maximum COP and ejector efficiency is conducted.

The author would like to acknowledge Parveen Dhillon for his assistance in developing the numerical solution schemes and the integrated cycle model presented herein.

#### 3.1 Ejector Design Introduction

Growing global energy consumption and environmental concerns, such as global warming, are primary drivers in the development of efficient and natural refrigeration solutions that utilize fluids such as CO<sub>2</sub>. When CO<sub>2</sub> is applied in vapor compression cycles, such cycles often reject heat above the critical pressure, causing transcritical operation. Typically, transcritical cycles consume more compressor power than comparable subcritical cycles at the same heat source and heat sink conditions due to cycle thermodynamics. However, the high pressure differential across the system also provides an increased potential for expansion work recovery relative to most other working fluids, making a transcritical CO<sub>2</sub> cycle a promising application for an ejector.

Variable geometry ejectors, fixed geometry ejectors, and multi-ejectors have all proven to recover expansion work effectively. Elbel and Hrnjak [42] experimentally

tested a variable geometry ejector applied in a transcritical CO<sub>2</sub> refrigeration system, achieving increases in COP and cooling capacity of 7% and 8%, respectively. Furthermore, they tested diffuser angles of 5°, 7.5°, and 10°, and concluded that the 5° design performed best. A maximum ejector efficiency of 14.5% was achieved. Banasiak et al. [116] conducted experimental and numerical assessments of different geometries of nozzle, mixing section, diffusing, and discharge sections of the ejector, achieving a maximum COP increase of 8% over a DX cycle. A diffuser expansion angle of 3° was numerically found to be the best, but experimentally a 5° angle was applied, which resulted in a higher ejector efficiency relative to the 7.5° and 10° diffusers tested. Key geometry ratios throughout the ejector can be calculated from the reported absolute geometric values, and pressure profiles throughout the ejector are provided for different geometries, lending significant insight into the internal operation of the device. Lucas and Koelher [41] also conducted experimental and numerical analyses into ejector design, ultimately achieving an ejector efficiency of 22% and a COP increase of 17%. As one of the earlier research efforts on this topic, the experimental work led to the insight that the motive nozzle throat became choked in transcritical operation, and also provided a simple but effective numerical modeling strategy. Li and Groll [52] introduced another numerical approach for ejectors applied in a transcritical CO<sub>2</sub> cycle, providing guidance on the modeling of both individual components and systems. Most notably, the integration of the component and cycle models provided relationships between outlet quality and entrainment conservation of mass at the ejector outlet, and utilized the relationship as an optimization parameter through the introduction of a compressor suction bypass to facilitate additional control and stability of the cycle. Liu and Groll [53] utilized a variable geometry ejector and experimental data to derive polynomials for individual ejector components as a function of ejector operating conditions. The efficiency polynomials provided significant insight not only into the potential efficiencies achievable by ejector components, but also showed their variation with operating conditions.

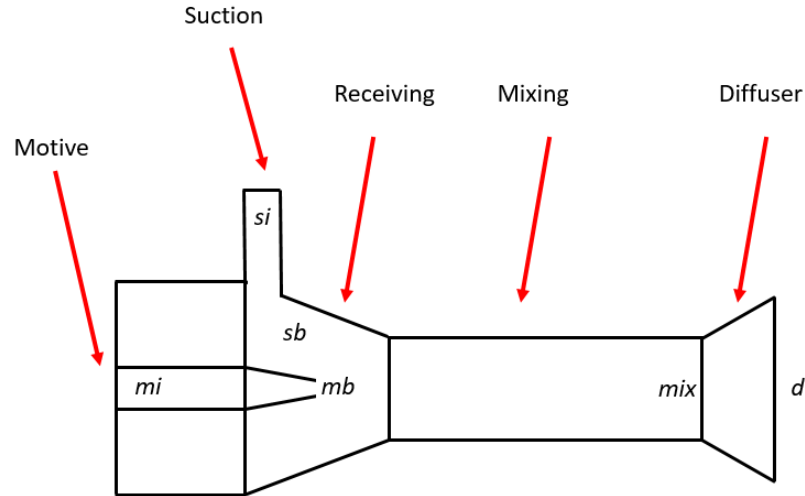


Hafner et al. [46] introduced the multi-ejector concept as another answer to the question of ejector control over varying operating conditions. Multi-ejector technology has been commercialized, and several initial studies to validate its performance quickly showed its promise. Haida et al. [47] built a full-scale test stand to simulate supermarket refrigeration conditions, and utilized a multi-ejector block with four different ejector sizes in parallel. Two different low-side refrigeration conditions and loading scenarios were assessed over a range of ambient conditions, with a maximum COP increase of 7% compared to the baseline parallel compression system. The operation of the ejector notably varied the load distribution between compressors, which had a detrimental impact on compressor efficiency for the given design. Therefore, if compressor operating conditions were optimized to work with the multi-ejector, the performance benefit would likely be even greater.

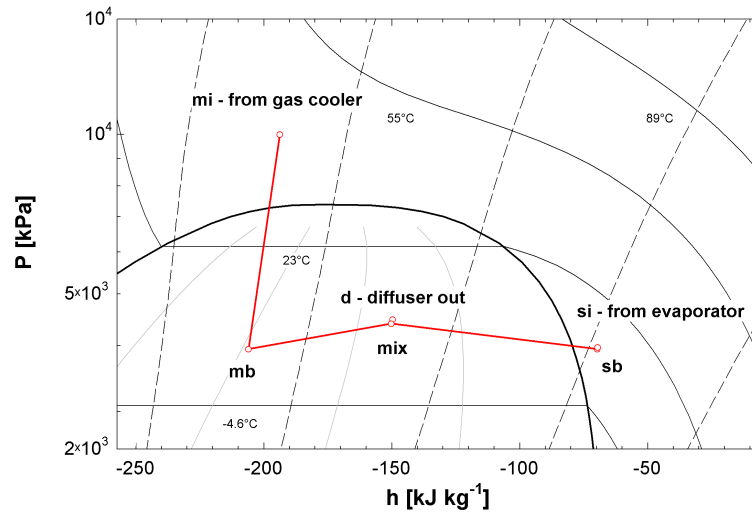
Despite the amount of quality design, validation, and performance assessment work that has been conducted on ejectors applied in refrigeration cycles, the specific ejector designs utilized are often secondary to the analysis conducted. Furthermore, there is limited work in the literature regarding the explicit design of an ejector using first-principle analytical models. The effects of component efficiencies and operating conditions on geometry, which can be valuable for those interested in investigating ejectors applied in vapor compression cycles, is also lacking in the literature. This chapter presents an ejector design tool that has been experimentally validated for a transcritical CO<sub>2</sub> vapor compression cycle but can be extended to other working fluids. The design tool was integrated into a full system model to assess the relative effects of individual component efficiencies as well as operating conditions on overall ejector efficiency and ejector geometry. Differences in ejector geometry and efficiency when optimizing the ejector versus the entire cycle are presented. Lastly, potential model improvements and perspectives on future work are discussed.

### 3.2 Approach and Sub-Models

This section describes the sub-models, governing equations, and overall system design used throughout this chapter. For visualization, the internal processes of an ejector are shown schematically in Figure 3.1(a) and in a P-h diagram for a trans-critical CO<sub>2</sub> cycle in Figure 3.1(b). Ejector operation begins at the motive nozzle inlet, *mi*, where the high-pressure flow from the gas cooler outlet is accelerated to the motive nozzle throat, *mb*. The high-velocity motive flow then entrains low-pressure vapor from the evaporator outlet into the suction nozzle inlet, *si*. The suction nozzle slightly accelerates the vapor from the evaporator outlet into the throat of the suction nozzle, *sb*. The outlets of both nozzle throats then send the two flows into the receiving section. Following the receiving section, the two flows enter the suction chamber and begin to mix at the entrance to the circular, constant-area mixing section, where the mixed flow then increases in pressure due to the mixing process as it reaches the end of the mixing section, *mix*. Finally, the flow enters the diffuser where the flow pressure is further increased until exiting the ejector at a two-phase state, *d*.



(a)



(b)

Fig. 3.1. (a) Ejector components and internal states; (b) Ejector process applied in transcritical  $\text{CO}_2$  operation shown on a  $P$ - $h$  diagram.

### 3.2.1 Sub-Component Modeling Strategy

Four primary sub-component models are utilized in the overall ejector model. They are the motive nozzle, suction nozzle, mixing section, and diffuser. The funda-

mental equations are based off of a combination of those utilized by Li and Groll [52] and Liu and Groll [53]. The maximum velocity at the outlet of the motive nozzle is limited by choked flow, which is achieved when the average flow velocity reaches the speed of sound in a converging nozzle. The two-phase speed of sound can be estimated by employing different approaches [14, 117, 118], depending on assumptions. The most simplified method of characterizing two-phase flow is to assume that the flow is homogeneous, is in thermodynamic equilibrium, and has a slip ratio of unity. The homogeneous model was chosen because literature has shown that the complexity and computational cost associated with more complex two-phase flow models within ejectors outweighs the small benefit in accuracy. Additionally, the homogeneous assumption was applied in the development of the polynomials applied for experimental investigation. The method for estimating the speed of sound applied herein is adapted from Attou and Seynhaeve [117] and is shown in Equation 3.1.

$$V_c = \sqrt{\frac{v_{mb}^2(h_g - h_f)}{(v_g - v_f)(h'_{mb} - v_{mb}) - v'_{mb}(h_g - h_f)}} \quad (3.1)$$

Where  $V$  is velocity,  $v$  is specific volume,  $h$  is specific enthalpy,  $g$  denotes saturated vapor,  $f$  denotes saturated liquid,  $v'$  is defined in Equation 3.2, and  $h'$  is defined in Equation 3.3.

$$v' \equiv x \frac{\partial v_g}{\partial P_{sat}} + (1 - x) \frac{\partial v_f}{\partial P_{sat}} \quad (3.2)$$

$$h' \equiv x \frac{\partial h_g}{\partial P_{sat}} + (1 - x) \frac{\partial h_f}{\partial P_{sat}} \quad (3.3)$$

It is worth noting that the expression for the two-phase speed of sound shown in Equation 3.1 trends towards a lower speed of sound as the quality decreases. The trend towards a lower speed of sound with quality is relevant to ejector design because as the condenser or gas cooler outlet specific enthalpy decreases, the nozzle outlet quality will also decrease. Therefore, choked flow will be achieved at significantly varying pressure levels depending on the motive nozzle inlet state and isentropic

efficiency. When the motive nozzle model tries to achieve choked flow at pressures significantly below that of the evaporation pressure for a given application, it can restrict ejector performance if the pressure rise from the mixing section and diffuser cannot bring the mixed flow pressure up past the evaporation pressure. Exceedingly low motive nozzle throat pressures have not proven to be a significant issue with CO<sub>2</sub> ejector applications, given the amount of motive flow acceleration possible due to the high pressure differential across the system. However, low motive nozzle throat pressures can become an issue if the two-phase speed of sound model is applied as a convergence criterion in models utilizing other working fluids with less available expansion work. If the model predicts a motive nozzle outlet pressure significantly below the evaporation pressure, then the nozzle convergence criterion should switch to a sub-sonic nozzle design with the outlet state defined as some pressure offset below the evaporation pressure. Another challenge in the motive nozzle outlet state characterization aspect of the work comes from when the outlet state of the nozzle reaches the saturated liquid line or passes into the sub-cooled liquid region, which could happen with a low gas cooler outlet temperature or during subcritical operation. Along the saturated liquid line the differences in correlations for critical flow in two phase become a numerical hindrance. Models which do not consider metastability, and thus delayed evaporation effects, can result in a discontinuity [119] at the saturated liquid line.

All components are assumed to be adiabatic and operate at steady state, steady flow, with the nozzle work being zero. Additionally, the inlet velocity to both nozzles and the outlet velocity of the diffuser are assumed negligible, given the small impact those respective velocities would have on the first law of thermodynamics. Gravitational effects are also assumed to be negligible. The equations applied for the isentropic efficiency of a nozzle and the subsequent calculation of the outlet velocity, are shown in Equations 3.4 and 3.5, respectively. These equations are applied to both the suction and motive nozzles.

$$\eta_{\text{is,nozzle}} = \frac{h_{\text{in}} - h_{\text{out}}}{h_{\text{in}} - h_{\text{out,is}}} \quad (3.4)$$

$$V_{\text{out}} = \sqrt{2(h_{\text{in}} - h_{\text{out}})} \quad (3.5)$$

The convergence criterion for the choked flow motive nozzle model is the comparison of the speed of sound and the velocity resulting from the energy balance. For the suction flow, the same isentropic efficiency and velocity equations used in the motive nozzle calculations are applied, but in this instance conservation of mass is used to ensure the outlet velocity is correct. The conservation of mass is applied using Equation 3.6, and the area portion of the calculation is calculated using a fixed ratio of throat diameter relative to the motive nozzle. The suction nozzle area calculation is achieved through the introduction of a pseudo-mass flow rate that is used to develop ratios throughout. For example, assuming a motive mass flow rate of  $1 \text{ kg s}^{-1}$ , the entrainment ratio is then used to solve for the suction mass flow rate, shown in Equation 3.7. Finally, using Equation 3.8, a diameter for the motive nozzle is applied to determine the proposed suction nozzle diameter. With both an area and a mass flow rate known, Equation 3.6 is used to calculate an outlet velocity from the conservation of mass to be compared to the outlet velocity from the energy balance to form the convergence criterion.

$$\dot{m} = \rho AV \quad (3.6)$$

$$w = \frac{\dot{m}_{\text{suction}}}{\dot{m}_{\text{motive}}} \quad (3.7)$$

$$\frac{d_{\text{mb}}}{d_{\text{sb}}} = \text{Constant} \quad (3.8)$$

Mixing section losses are primarily due to fluid flow friction in the mixing section and have the effect of decreasing the outlet velocity and the potential pressure lift

across the ejector. Since conservation of mass and energy are satisfied with both motive and suction nozzle calculations, the difference in velocity outputs of momentum and energy balances is used as the convergence criterion for the mixing section. For the former, conservation of momentum is manipulated to produce an expression for outlet velocity, shown in Equation 3.9. The energy balance is conducted by defining both nozzles and the mixing section as the control volume and utilizing both nozzle inlet states as the inputs, shown in Equation 3.10. Defining the control volume as the mixing section outlet to both nozzle inlets minimizes the propagation of error through the nozzle outlet velocity calculations.

$$V_{\text{mix}} = \sqrt{\frac{1}{\rho_{\text{mix}}} \frac{a_{\text{mb}}(P_{\text{mb}} + \eta_{\text{mix}}\rho_{\text{mb}}V_{\text{mb}}^2) + [a_{\text{mix}}(1 + w) - a_{\text{mb}}](P_{\text{sb}} + \eta_{\text{mix}}\rho_{\text{sb}}V_{\text{sb}}^2)}{a_{\text{mix}}(1 + w)} - P_{\text{mix}}} \quad (3.9)$$

$$V_{\text{mix}} = \sqrt{2\left[\left(\frac{h_{\text{mi}} + wh_{\text{si}}}{1 + w}\right) - h_{\text{mix}}\right]} \quad (3.10)$$

where  $a$  represents the inverse of mass flux, calculated as the ratio of specific volume to velocity. The inverse mass flux value provides the bridge from intensive thermodynamic properties to physical dimensions. Because the units are area by mass flow rate, multiplying the inverse mass flux value by a given mass flow rate returns the area necessary for the applied mass flow to occur.

The diffuser performance is calculated as presented by Liu and Groll [53], with the only difference being the area ratio is calculated by a series of constant diameter ratios and angles. The diffuser lift coefficient is calculated through Equation 3.11, with the corresponding pressure lift calculated by Equation 3.12. The overall ejector efficiency is calculated using Equation 3.13 from Koehler et al. [43], and the angles and ratios used in the ejector for experimental validation are provided in Table 3.1. It should be noted that the two ratios involving motive and suction nozzle diameters were varied between tests used for validation based on the ratios applied for the experimental data point being assessed. The values presented in Table 3.1 represent

ratios used during tests conducted by Liu and Groll [114] that yielded some of the highest ejector efficiency values observed during testing. The use of these ratios, angles, and the inverse mass flux is the key to transitioning these governing equations from an analysis to a design tool, as all that is necessary to go from an intensive property to an area is multiplication of  $a$  at each key point by the mass flow rate through that portion of the ejector. Then, the ratios and angles from Table 3.1 are applied to find the remaining lengths.

$$C_t = 0.85\rho_{\text{mix}}[1 - (\frac{A_{\text{mix}}}{A_d})^2][\frac{x_{\text{mix}}^2}{\rho_{\text{g,mix}}} + \frac{(1 - x_{\text{mix}})^2}{\rho_{\text{f,mix}}}] \quad (3.11)$$

$$C_t = \frac{P_d - P_{\text{mix}}}{0.5\rho_{\text{mix}}V_{\text{mix}}^2} \quad (3.12)$$

$$\eta_{\text{ej}} = w \frac{h(P_d, s_{\text{si}}) - h_{\text{si}}}{h_{\text{mi}} - h(P_d, s_{\text{mi}})} \quad (3.13)$$

### 3.2.2 Cycle Description

A schematic of the cycle used in the system analysis is shown in Figure 3.2. The two primary differences between the cycle used herein and a four component vapor compression cycle are the ejector between state points 3, 7, and 4, and the phase separator between states 4, 5, and 1. The phase separator is necessary because the diffuser outlet state will be two-phase, necessitating phase separation so that the compressor receives saturated vapor and avoids two-phase flow in the suction port. Theoretical models generally fix state point 1 as saturated vapor at the ejector diffuser outlet pressure. However, in reality, many transcritical  $\text{CO}_2$  cycles utilize a semi-hermetic reciprocating compressor, where the suction flow enters the compressor and flows over the motor before entering the compression chamber. The refrigerant flow cools the motor and superheats the vapor before it enters the compression chamber, which makes the cycle architecture shown in Figure 3.2 more robust in actuality than



Table 3.1.  
Ratios and angles applied in the ejector design model.

Ratio	Description	Value
$\frac{A_{\text{mix}}}{A_{\text{d}}}$	Ratio of mixing section area to diffuser outlet area	0.111
$\frac{L_{\text{d}}}{L_{\text{mix}}}$	Ratio of diffuser length to mixing section length	2.525
$\frac{L_{\text{mix}}}{d_{\text{mix}}}$	Ratio of mixing section length to diameter	6.5
$\frac{d_{\text{mb}}}{d_{\text{sb}}}$	Ratio of motive and suction nozzle throat diameters	0.33
$\frac{d_{\text{mb}}}{d_{\text{mix}}}$	Ratio of motive nozzle throat diameter to mixing section diameter	0.45
$\Theta_{\text{m}}$	Motive nozzle angle	10°
$\Theta_{\text{s}}$	Suction nozzle/receiving section angle	16°
$\Theta_{\text{d}}$	Diffuser expansion angle	3.5°

it may appear. Additionally, the bypass from state 1 to state 6 is there to provide additional control should instabilities arise during ejector operation.

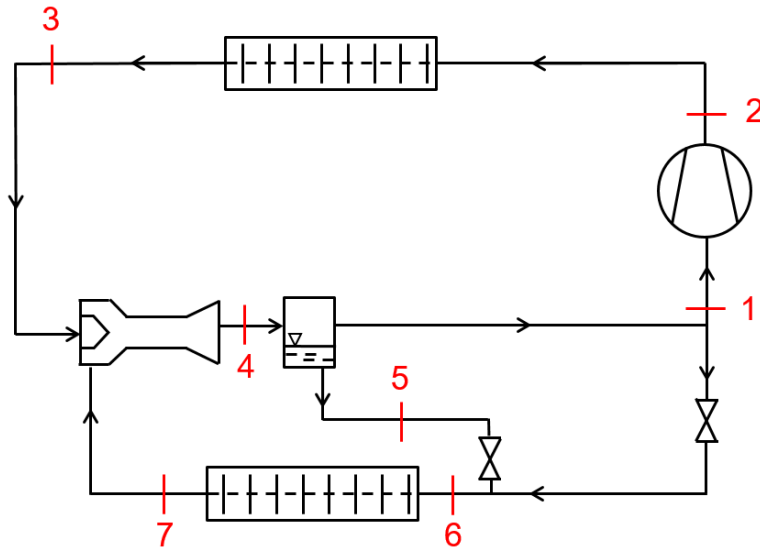


Fig. 3.2. Schematic of the CO<sub>2</sub> ejector cycle used in the optimization studies.

### 3.3 Numerical Description and Solution Schemes

Two general numerical strategies are discussed herein. The first strategy is used in the validation of the numerical model with experimental data and physical geometry, while the second is the numerical strategy of applying the same fundamental model as a design tool.

The overall solution scheme receives inputs of the two inlet states, characterized by temperature and pressure due to their single-phase state, and the outlet state, defined by pressure and an entrainment ratio. The entrainment ratio is calculated through the ratio of suction to motive mass flow rates, shown in Equation 3.7, which then allows the calculation of geometry throughout. The flowchart utilized for both validation and design is shown in Figure 3.3. Both solution schemes solve the motive

nozzle, suction nozzle, mixing section, and diffuser outlet states sequentially, in that order. The two main differences between the two solution schemes are the convergence criteria and the component efficiencies used.

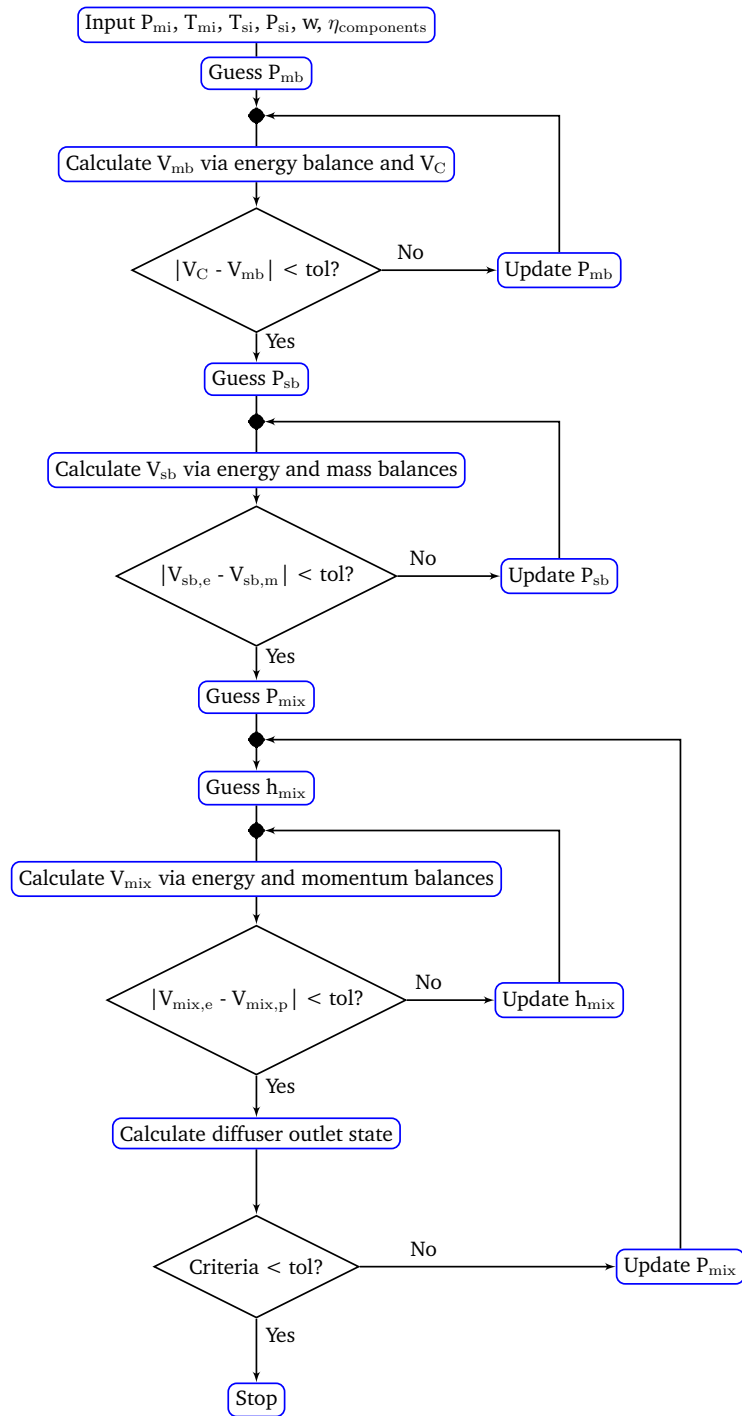


Fig. 3.3. Flowchart for the ejector solver utilized for ejector design and validation.

### 3.3.1 Numerical Strategy for Validation

The validation solution entails employing governing equations, experimentally-derived efficiency polynomials, and experimental data from Liu and Groll [53] to output geometry used to achieve a given efficiency for a given condition. The experimental data used in this validation was the same used for the development of these polynomials, and was taken from Liu and Groll [114]. The criteria for validation are key geometric parameters that would be used to produce a given thermodynamic result. Using the solution scheme shown in Figure 3.3, the inlet states and the outlet pressure are matched as close as possible to experimental data for validation. In the validation portion of this work the convergence criterion is shown in Equation 3.14. Then, the mass flow rates used in the experimental data are passed through the model to produce the four primary diameters of concern, being the diameters of the motive nozzle throat, the suction nozzle throat, the mixing section, and the diffuser outlet.

$$|P_{d,calc} - P_{d,data}| < tol? \quad (3.14)$$

### 3.3.2 Solution Scheme for Design

The design solution scheme convergence criterion is defined by the relationship between the diffuser outlet quality and the ejector entrainment ratio, shown in Equation 3.15. This convergence criterion allowed the minimum amount of compressor suction bypass flow shown in Figure 3.2, resulting in an ejector design that makes the most use of the two flow rates it receives. This bypass serves as a system stabilizer against experimental instabilities, and also eases numerical solutions by offering an additional convergence criterion. The overall numerical structure of the design scheme shares the solution scheme shown in Figure 3.3. With respect to component efficiencies, it has been shown that the polynomials used in the validation scheme are more accurate than constant efficiency assumptions, given the logical conclusion that a nozzle, mixing section, and diffuser performance will vary for different operating conditions and

entrainment ratios. However, the polynomials used in Section 3.3.1 were derived from data from AC testing, limiting them to somewhat high evaporation temperatures.

This model utilizes the same governing equations regardless of applying constant or variable component efficiencies. The use of fundamental equations broadens the model applicability to most vapor compression cycles. Furthermore, the relationship between the ejector outlet quality and entrainment ratio can be modified to fit more complex cycles. For example, if the phase separation process at the diffuser outlet has more than the standard two outlets, as long as the fundamental definitions of quality and entrainment ratios are satisfied, then more complex expressions can replace the final convergence criterion and the target mixing section pressure will still be reached. An example of a more complex relation between ejector entrainment ratio and outlet quality was provided in Figure 2.9 in Chapter 2.

$$|x_d(1 + w) - 1| < tol? \quad (3.15)$$

### 3.3.3 Cycle Analysis and Optimization

To study the effects of operating conditions, individual component efficiencies and design parameters on the overall system and ejector performance, the ejector solver model described in Section 3.3 is integrated into an overall system model. Furthermore, this model formulation can be used to perform optimization on design parameters for a target system performance based on the user application. Figure 3.4 shows a flowchart to solve the system shown in Figure 3.2 with an integrated ejector for an array of operating conditions and design parameters. The idea behind the numerical solution scheme is to solve the different components either sequentially or simultaneously with additional constraints to ensure convergence at different component interface states. An example interface would be the outlet of the evaporator to the suction nozzle inlet. Here, in addition to ejector internal states shown in Figure 3.3, diffuser outlet pressure,  $P_d$ , and entrainment ratio,  $w$ , are iterated over simulta-

neously to find a solution which satisfies the convergence criteria for the ejector as well as different component and cycle models.

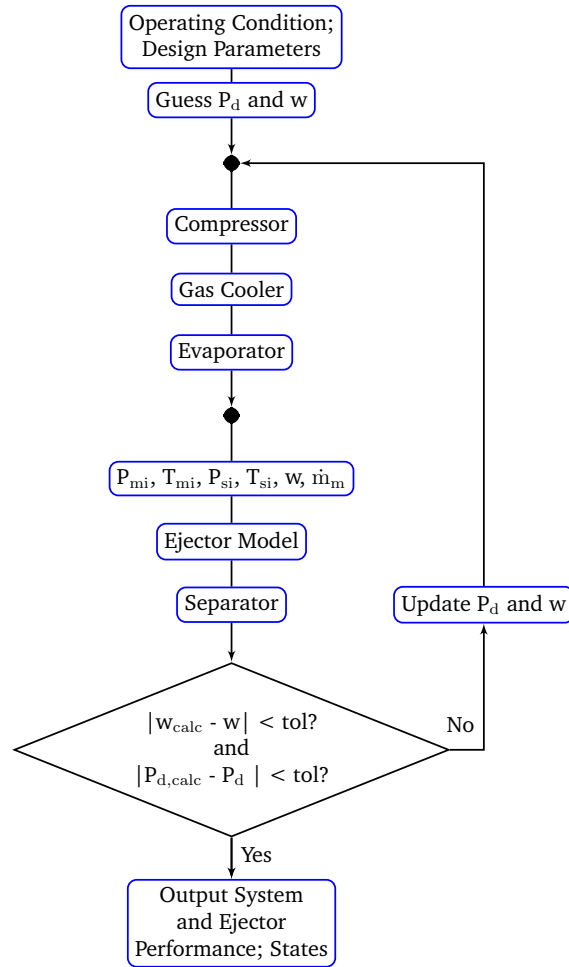


Fig. 3.4. Flowchart for analysis of the ejector cycle used in the optimization studies.

In this study, an ARI 10-coefficient compressor map [112] shown in Equation 3.16 and developed using data from the manufacturer was utilized to model a fixed speed compressor with a volumetric displacement rate of  $1.75 \text{ m}^3 \text{ hr}^{-1}$  at 60 Hz. Pressures were used in place of condensing and evaporating temperatures more commonly seen in 10-coefficient maps due to transcritical operation decoupling the high-side temperature and pressure, as proposed by Hubacher and Groll [120]. Table 3.2 shows

the corresponding compressor map coefficients for volumetric, isentropic, and overall efficiency. The volumetric efficiency was used to solve for the mass flow rate, the isentropic efficiency was used to solve for the discharge temperature, and the overall efficiency was used to solve for the power consumed by the compressor. In this work, the primary focus was to study the system performance with an ejector, as well as how different operating conditions and ejector geometric design parameters affect the overall system and ejector performance. Therefore, a simple heat exchanger model was considered for the evaporator as well as the gas cooler with an assumption that the heat exchangers are sized properly to have constant pinch point, subcooling and superheat values with no pressure drop. However, the user can implement a more detailed model based on their application and design purpose.

$$\eta = a_0 + a_1 P_1 + a_2 P_1^2 + a_3 P_1^3 + a_4 P_2 + a_5 P_2^2 + a_6 P_2^3 + a_7 P_1 P_2 + a_8 P_1 P_2^2 + a_9 P_1^2 P_2 \quad (3.16)$$

where the pressure is in Pa. Mass flow rate and compressor power consumption corrections for superheat relative to the 10 K at which the map was developed are calculated with Equations 3.17 and 3.18, respectively,

$$\frac{\dot{m}_{\text{new}}}{\dot{m}_{\text{data}}} = 1 + F \left( \frac{\rho_{\text{suc,new}}}{\rho_{\text{suc,data}}} - 1 \right) \quad (3.17)$$

$$\frac{\dot{W}_{\text{new}}}{\dot{W}_{\text{data}}} = \frac{\dot{m}_{\text{new}}}{\dot{m}_{\text{data}}} \frac{\Delta h_{\text{is,new}}}{\Delta h_{\text{is,data}}} \quad (3.18)$$

where  $F$  is a correction factor assumed to be 0.75,  $\rho$  is density, *suc* denotes suction, *new* represents the corrected superheat state, *data* is the state from the experimental data, and *is* denotes the outlet state of an isentropic process.



Table 3.2.  
Compressor map coefficients applied in the ejector system model.

Coefficient	$\eta_{\text{volumetric}}$	$\eta_{\text{isentropic}}$	$\eta_{\text{overall}}$
$a_0$	1.03	$5.70 \cdot 10^{-1}$	$5.63 \cdot 10^{-1}$
$a_1$	$7.08 \cdot 10^{-8}$	$-2.19 \cdot 10^{-7}$	$-2.32 \cdot 10^{-7}$
$a_2$	$-1.67 \cdot 10^{-14}$	$-5.45 \cdot 10^{-14}$	$-5.48 \cdot 10^{-14}$
$a_3$	$2.53 \cdot 10^{-22}$	$-5.03 \cdot 10^{-21}$	$-2.59 \cdot 10^{-21}$
$a_4$	$-1.53 \cdot 10^{-7}$	$1.45 \cdot 10^{-7}$	$1.07 \cdot 10^{-7}$
$a_5$	$6.60 \cdot 10^{-15}$	$-6.19 \cdot 10^{-14}$	$-5.29 \cdot 10^{-14}$
$a_6$	$-2.53 \cdot 10^{-23}$	$5.85 \cdot 10^{-21}$	$4.89 \cdot 10^{-21}$
$a_7$	$3.80 \cdot 10^{-14}$	$1.39 \cdot 10^{-13}$	$1.42 \cdot 10^{-13}$
$a_8$	$-1.67 \cdot 10^{-21}$	$-1.52 \cdot 10^{-20}$	$-1.36 \cdot 10^{-20}$
$a_9$	$-1.92 \cdot 10^{-21}$	$1.10 \cdot 10^{-20}$	$7.53 \cdot 10^{-21}$

### 3.4 Results and Discussion

This section provides a summary and discussion of the primary findings from the presented analysis strategies. Validation is covered first, followed by a component sensitivity analysis. A parametric study showing component geometry variation with ambient and low-side conditions is then presented. Finally, a comparison of ejector efficiency, system COP, and geometric parameters observed as a result of ejector efficiency and cycle efficiency optimizations is presented.

#### 3.4.1 Experimental Validation

Validation of the model against experimental data was taken in two steps. First, individual component models were compared against experimental data, then the entire model was assembled and integrated with the numerical solution. Data was

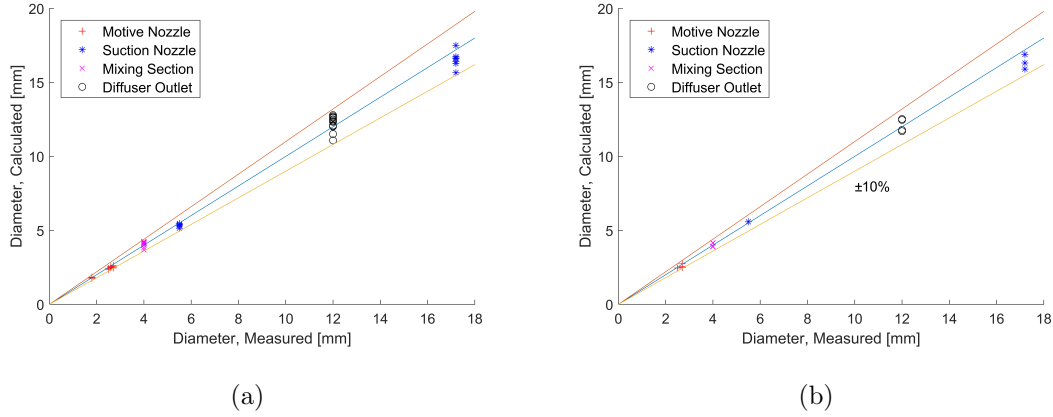


Fig. 3.5. Ejector model validation with: (a) Nozzle data input simulation; and, (b) Fully numerical simulation.

taken at only two suction nozzle diameters of 5.5 mm and 17.2 mm due to the need to remove the ejector from the experiment to vary the suction nozzle diameter, while the motive nozzle diameter could be actively varied during cycle operation. Mixing and diffuser models were validated simultaneously, using experimental data for the motive and suction nozzles, including geometric inputs to ensure that their geometries and flow outlets were as accurate as possible. The application of data to calculate nozzle outlet states in this portion of the validation allowed assessment of the mixing section and diffuser geometry calculations. Validation for all four assessed diameters with nozzle data input is shown in Figure 3.5(a).

Once confidence grew in the sub models, the entire model was run numerically. The model received only temperatures and pressures at the two nozzle inlets, pressure at the diffuser outlet, and the suction and motive mass flow rates. The model predictions for the four primary component diameters, being the motive nozzle throat, suction nozzle throat, mixing section, and diffuser outlet, were determined and are shown relative to the physical dimensions in Figure 3.5(b). Results of MAE for all validation simulations are provided in Table 3.3.

Table 3.3.  
MAE obtained during validation of component diameters throughout the ejector.

Simulation	Parameter	MAE (%)
Motive nozzle throat diameter validation	Motive nozzle throat diameter	3.7
Suction nozzle throat diameter validation	Suction nozzle throat diameter	3.7
Mixing and diffuser section validation	Mixing section diameter	3.7
	Diffuser outlet diameter	3.9
Completely numerical validation	Motive nozzle throat diameter	4.0
	Suction nozzle throat diameter	4.0
	Mixing section diameter	3.1
	Diffuser outlet diameter	3.1

### 3.4.2 Trends of Component Efficiency and Geometry

When designing an ejector, it is vital to understand the relative impact of individual component efficiencies on the overall ejector efficiency and the ejector geometry. Figure 3.6(a) shows the effects of varying three primary component efficiencies, being motive nozzle, suction nozzle, and mixing section efficiencies, on the overall ejector efficiency for transcritical CO<sub>2</sub> system operation. Here, only one of the component efficiencies was varied at a time while the other two were held constant at 0.75. Choked flow in the motive nozzle throat was also set as a convergence criterion for the model

to consider the dependence on the two-phase speed of sound. Furthermore, operating conditions were kept constant with a gas cooler outlet pressure of 90 bar and outlet temperature of 30 °C. This gas cooler outlet temperature represents a range of ambient temperatures between 25 °C and 27 °C depending on the approach temperature between air and refrigerant. The evaporation temperature was held constant at a temperature of -5 °C with a 10 °C outlet superheat. The compressor was modeled to run at a fixed speed of 1750 revolutions  $\text{min}^{-1}$ . For ejector geometric parameters, the ratios of motive to suction nozzle throat diameter and mixing section area to diffuser outlet area were also kept constant as per Table 3.1. The range of efficiencies was motivated by the literature [55] as well as experimental data utilized in this investigation. COP is defined as the ratio of cooling capacity to compressor power, as fan power was neglected.

It can be seen that the mixing section losses have the most significant impact on the overall ejector efficiency with an almost-linear direct trend. On the other hand, changes in motive and suction efficiencies at lower values have a substantial effect on overall ejector efficiency. However, as these component efficiencies increase, the added benefit to overall ejector efficiency decreases, which provides a designer an opportunity to prioritize maximizing the efficiency of the components with the most significant effect on overall ejector efficiency. Figure 3.6(a) also highlights that the mixing section efficiency has a greater impact on the ejector efficiency than any other single ejector component. This corroborates the increase in research focused on mixing section optimization aspects of ejector design research.

Figure 3.6(b) shows the variation of mixing section diameter with component efficiencies for the same parametric study used to produce Figure 3.6(a). With respect to the mixing section diameter, the effects of the two nozzle efficiencies and mixing section efficiency can be related to the diameter through consideration of two-phase density. The actual *mix* state is the outlet of the mixing section, which is the portion of the section that is at the highest pressure because overall ejector pressure rise occurs primarily in the mixing and diffuser sections. Therefore, for a given mass flow

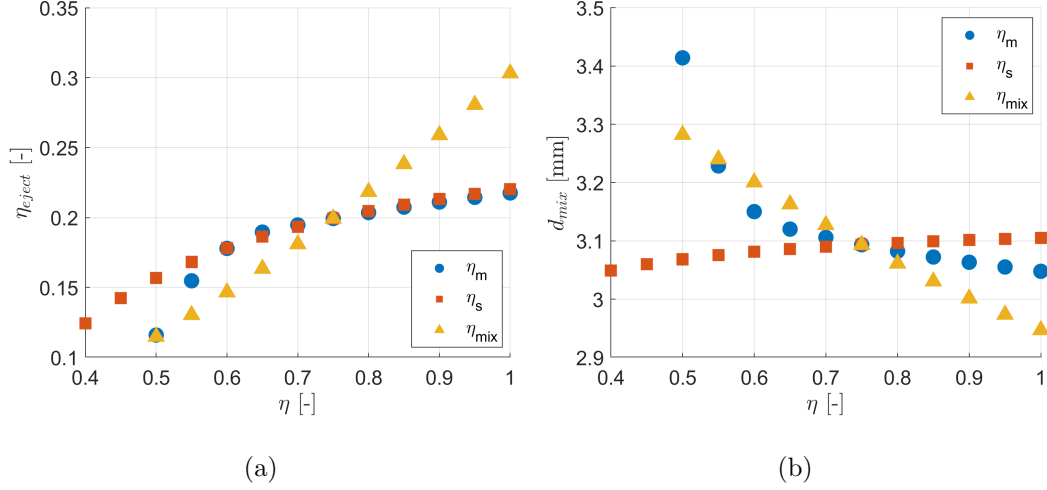


Fig. 3.6. Through variation of the efficiency of one component at a time, with the other two component efficiencies held constant at 0.75, the assessment of: (a) Ejector efficiency variation with component efficiency; and, (b) Ejector mixing section diameter variation with component efficiency.

rate, the outlet of the mixing section has the lowest density and thus, represents the smallest area which would satisfy conservation of mass for a given flow rate. With the relationship between density and area in mind, Figure 3.6(b) shows that the mixing section efficiency has an inverse relationship with mixing section diameter. This inverse relationship is logical, given that the mixing section efficiency primarily represents the adverse effects of friction in the mixing section, as shown in Equation 3.9. Therefore, the mixing section outlet velocity, pressure, and density are directly proportional to the mixing section efficiency and inversely proportional to the mixing section outlet diameter.

With respect to traditional fluid dynamics, the simultaneous increase of pressure and velocity could be counter-intuitive in that the relationship between velocity and pressure rise generally represents a tradeoff. A decrease in velocity would therefore lead to an increase in pressure. While the mixing section does decrease velocity to increase pressure, a portion of the decreased velocity in the mixing section would also be due to frictional losses. However, the governing equations for the mixing

section outlet state shown in Equations 3.10 and 3.9, in conjunction with the flow chart shown in Figure 3.3, reveal that the interrelations of pressure and velocity in the mixing section are more complex. The mixing section pressure is varied in order to facilitate both conservation of mass and energy, but must also satisfy momentum dissipation considerations imparted through the mixing section efficiency. Therefore, in satisfying conservation of mass, momentum, and energy, the solution suggests that an increase in mixing section efficiency increases the pressure rise, showing that additional velocity has been converted. However, the final result that the outlet velocity also increased shows that the mixing section efficiency increase resulted in a velocity increase that was significant enough that, even with additional pressure rise, the outlet velocity still grew proportionally to mixing section efficiency. The decrease in outlet quality with increasing mixing section efficiency had minimal impact on the mixing section outlet pressure because the observed quality decrease was on the order of 1%.

The motive nozzle efficiency shares a similar relationship to mixing section diameter because of its direct relationship to motive nozzle outlet velocity. The higher the motive nozzle outlet velocity is, the more effective the entrainment process is and the more kinetic energy can be converted to pressure across the ejector. Additionally, a higher motive nozzle isentropic efficiency expanding from supercritical flow to subcritical flow would result in a higher outlet density, allowing more mass flow rate through the ejector for a given area, or a smaller area for a given mass flow rate.

The only component whose efficiency varies directly with mixing section diameter is the suction nozzle. At first glance, the direct relationship between suction nozzle efficiency and diameter may appear to hurt performance, as the previous two component efficiencies would suggest that a smaller suction nozzle diameter is correlated with increased ejector efficiency. Because the suction nozzle area is solved as a ratio to the motive nozzle area in this model, that ratio is held constant when the suction nozzle efficiency is varied. Therefore, the outlet pressure must be varied to reach an outlet state that satisfies both conservation of mass and conservation of energy, shown

in Equations 3.6 and 3.5, respectively. In the case of the suction nozzle, the variation of the outlet pressure results in a suction nozzle outlet pressure that increases with suction nozzle efficiency. While the relationship between pressure and efficiency in the suction nozzle appears to be counter-productive given the purpose of a nozzle is to accelerate flow, the overall ejector performance needs to be considered. An increased pressure at the outlet of the suction nozzle results in a higher density fluid. The higher density allows more mass flow to be entrained when all other parameters are held equal and thus, increases the entrainment ratio shown in Equation 3.7. While the change in specific enthalpy across the suction nozzle may decrease with increasing efficiency due to an increased outlet pressure, the overall ejector efficiency increases because the increased entrainment ratio outweighs any decrease in the change in specific enthalpy, shown in Equation 3.13. Furthermore, an increased entrainment ratio results in more mass flow rate passing through the evaporator and less mass flow needing to be compressed by the compressor, resulting in an increased COP in conjunction with increased ejector efficiency. When considering relative magnitudes of specific enthalpy changes through each component, Figure 3.1(b) can offer a visual reference.

A similar study was conducted for the motive nozzle throat diameter sensitivity to component efficiencies. It was concluded that the motive nozzle throat diameter is most sensitive to motive nozzle efficiency with an exponentially decreasing effect. The suction nozzle and mixing section efficiencies were found to have negligible effects on the motive nozzle throat diameter, which is primarily due to the choked condition at the throat of the nozzle.

The performance implications of sub-component efficiencies are much more significant than the geometric implications. While analyzing the variation in mixing section diameter with various sub-component efficiencies offers a background for insights on the fluid dynamics phenomena resulting from sub-component efficiency variation, the practical impact on design and manufacturability is minimal. To quantify this state-

ment, varying the mixing section efficiency from 0.5 to 1.0 results in a decrease in mixing section diameter from 3.33 mm to 3.05 mm, as shown in Figure 3.6(b).

### 3.4.3 Effects of Operating Condition on Geometry

A vapor compression cycle is often required to operate over a wide range of operating conditions. Therefore, it is important to understand the effects of operating conditions on the overall system and ejector performance, as well as on ejector geometric parameters. A parametric study was performed for different operating conditions of a transcritical CO<sub>2</sub> system based on the numerical scheme outlined in Section 3.3.3. The gas cooler pressure was varied from 80 bar to 110 bar and evaporating temperature was varied from -15 °C to 20 °C to simulate both refrigeration and AC system operation. The evaporator outlet superheat was kept constant at 10 °C. The gas cooler outlet temperature was fixed at 30 °C, with the compressor running at a fixed speed, similar to the study in Section 3.4.2. The number of parameters and conditions varied was limited to isolate the effects of varying certain parameters on ejector performance and geometry. The ratios of motive to suction nozzle throat diameter and mixing section area to the diffuser outlet area were kept constant as per Table 3.1. Furthermore, the ejector component efficiencies were kept constant at nominal values with the motive nozzle at 0.7, suction nozzle at 0.65, and mixing section at 0.85, as motivated by the literature [55].

Figure 3.7(a) illustrates the variation of ejector efficiency with gas cooler pressure and evaporating temperature. In general, ejector efficiency increases as the gas cooler pressure increases with a varying degree at different evaporating temperatures until almost becoming constant at an upper value. It would appear that this nearly-constant value is an optimum with a fairly broad plateau, after which the ejector efficiency decreases at a slow rate, as shown by the -15 °C evaporation temperature line. However, a broader gas cooler range would need to be applied to confirm the plateau of ejector efficiency. The reason for the chosen gas cooler pressure upper limit



is the outlet state of the motive nozzle would approach, and occasionally cross, the saturated liquid line, striking a numerical discontinuity as discussed in Section 3.2.1. The gas cooling pressure at which the optimum occurs is directly proportional to the evaporation temperature.

Figure 3.7(b) shows the ejector system COP difference compared to a four component system. To isolate the effect of the ejector being applied in the vapor compression cycle, the performance of the system with an ejector is compared to a standard four component system operating with the identical compressor at the same gas cooler and evaporator conditions. The COP benefit of the ejector has a maximum value associated with a certain gas cooling pressure, which is a result of the combined effects of change in the compressor and ejector performance at different conditions. As the gas cooler pressure increases past this maximum, the added benefit of the ejector on the system COP decreases. This explanation of ejector applications builds on the standard trend of transcritical  $\text{CO}_2$  cycles achieving a maximum COP at a gas cooler pressure that balances increasing system capacity with increasing compressor power. Moreover, the ejector system performs poorer than the normal four component system at higher evaporating temperature conditions. The observation of the diminishing benefit of an ejector with increased evaporation temperature for a given motive nozzle inlet condition agrees with the well-reported concept of ejectors being beneficial in systems with higher temperature lift due to additional available expansion work. However, the gas cooler pressure does not have any drastic effect on the difference in cooling capacity provided by the ejector system relative to the four component system. At a fixed gas cooler pressure, as the evaporating temperature decreases, the relative performance of the system with the ejector comparatively increases. Four test points at low evaporation temperatures and high gas cooling pressures were outside the bounds of the compressor map utilized and hence were removed from this study.

Variation of the motive nozzle throat and mixing section diameters with gas cooler pressure and evaporating temperature is shown in Figures 3.8(a) and 3.8(b), respec-

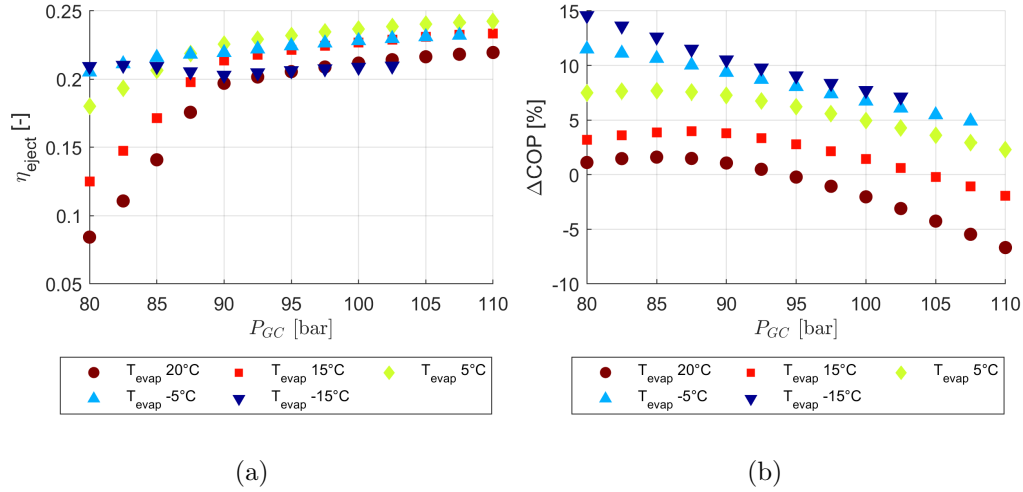


Fig. 3.7. (a) Ejector efficiency variation with gas cooler pressure and evaporating temperature; and, (b) Variation of ejector system COP difference relative to a four component system with gas cooler pressure and evaporating temperature.

tively, for the same parameters used for Figure 3.7(a) and Figure 3.7(b). As the gas cooler pressure increases, the motive nozzle throat diameter decreases with more sensitivity to the variation at lower gas cooler pressures, which can be mainly attributed to the change in motive nozzle inlet conditions and its mass flow rate due to the compressor volumetric efficiency change. The change in mixing section diameter shows a similar behavior at higher evaporating temperatures. However, at the lower evaporating temperatures the variation in mixing section diameter with gas cooler pressure is less significant. One reason for the reduction in variation of mixing section diameter is the relatively small variation in motive nozzle mass flow rate, which is also the compressor mass flow rate, with a change in gas cooler pressure at lower evaporating temperatures. The connection between mixing section diameter and compressor mass flow rate highlights that the characteristics of other components in a system can greatly affect the ejector design and the need to carefully consider these characteristics in the design process in order to have an optimum system performance at various operating conditions. A similar study can be extended to other operating

conditions, such as ambient temperature, and with a more detailed heat exchanger model or variable speed compressor.

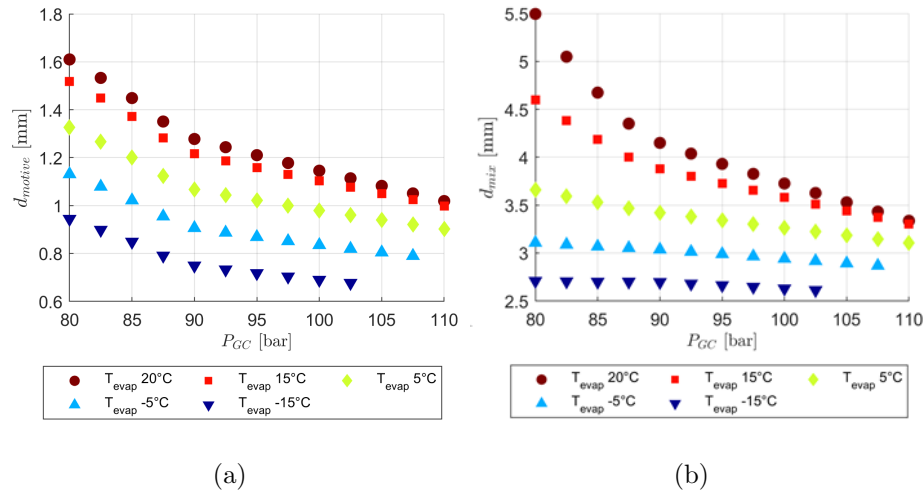


Fig. 3.8. Resulting diameters of the: (a) Ejector motive nozzle throat with varying gas cooler pressure and evaporating temperature; and, (b) Ejector mixing section with varying gas cooler pressure and evaporating temperature.

### 3.4.4 Effects of Cycle Efficiency Optimization on Geometry

In Section 3.4.3, the geometric parameter ratios of motive to suction nozzle throat diameters and mixing section to diffuser outlet diameters were kept constant. In this section, the effect of these two ratios on both ejector and system performance are studied. First, a parametric study at a single operating condition is conducted. The ejector component efficiencies were kept constant at the same nominal values used in Section 3.4.3. For the parametric study, only one geometric ratio was varied while the other was held constant at 0.33. The variation in system COP and ejector efficiency with the ratios of motive to suction nozzle diameters and mixing section to diffuser outlet diameters is shown in Figures 3.9(a) and 3.9(b), respectively.

The ratio of motive nozzle throat to suction nozzle throat diameter does not have a significant impact up to a certain value, but increasing the ratio beyond that suddenly decreases the system and ejector performance drastically. The sudden decrease in ejector performance with increasing the ratio of the motive nozzle to suction nozzle throat diameters is due to the decrease in suction nozzle mass flow rate and decrease in pressure rise between the ejector diffuser outlet pressure and evaporating pressure. Increasing the mixing section to diffuser outlet diameter ratio decreases both the system and the ejector performance in an almost quadratic correlation because of the corresponding decrease in the diffuser pressure lift coefficient.

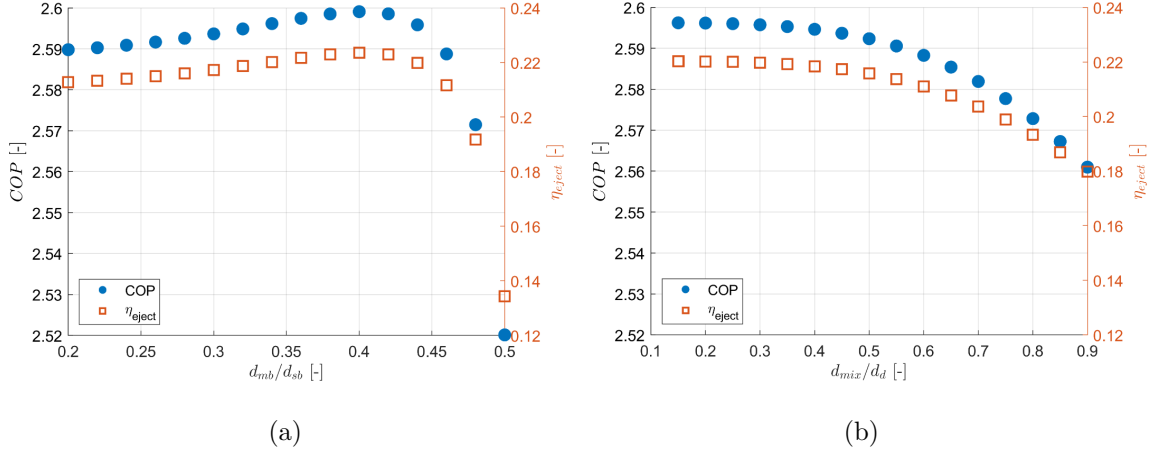


Fig. 3.9. Ejector efficiency and COP variation with ratios of: (a) Ejector motive to suction nozzle diameters; and, (b) Ejector mixing section to diffuser outlet diameters.

Next, to study the effect of optimization for a target performance parameter on geometric parameters, two different optimizations were run over a range of operating conditions similar to those used in Section 3.4.3. The objective of the first optimization was to maximize the ejector efficiency and the objective of the second optimization was to maximize the system COP. For both target parameters, a constrained optimization was performed at each operating condition using the Sequential Quadratic Programming algorithm due to the non-linearity of the problem. The ratio

of motive to suction nozzle throat diameters was constrained to vary from 0.2 to 0.5 and the ratio of mixing section to diffuser outlet diameters was constrained to vary from 0.15 to 0.9 based on the literature and experimental data used in this work. Figure 3.10(a) shows the variation of optimized geometric ratios at different operating conditions to maximize the ejector efficiency. The ratio of mixing section to diffuser outlet diameters converges to the lower constraint limit because the smaller the ratio is, the higher the diffuser lift coefficient which increases the diffuser efficiency and in turn increases the ejector efficiency. However, the ratio of motive to suction nozzle throat diameters decreases as the gas cooler pressure increases, and increases with the rise in evaporating temperature, converging at the upper constraint limit for some operating conditions with low gas cooler pressure and high evaporating temperatures. The reason for the ratio converging to the numerical upper limit is that the system is trying to keep the suction nozzle diameter constant or increase it slightly as the gas cooler pressure decreases in order to maximize ejector efficiency through maximizing the entrainment ratio.

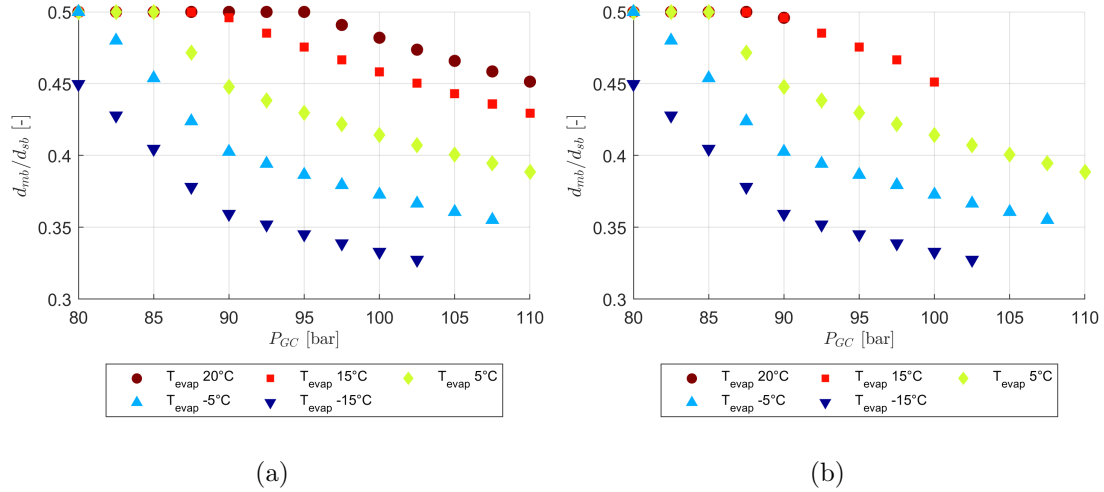


Fig. 3.10. Motive to suction nozzle throat diameter ratio variation with gas cooler pressure and evaporating temperature for the case of: (a) Ejector efficiency optimization; and, (b) System COP optimization.

Figure 3.10(b) shows the variation of optimized geometric ratios for the case of system COP optimization. As can be seen, the results are similar to the case of ejector efficiency optimization except for some conditions with high evaporating temperatures. At the higher evaporating temperature conditions, the cycle has a higher COP without an ejector than with an ejector, so these geometric ratios are omitted from Figure 3.10(b) because they are not meaningful. The omitted operation conditions correspond to conditions where the COP of a system with an ejector is lower than the simple four component system such that an ejector does not have any added benefit at these operating conditions. Figure 3.11(a) shows the variation of ejector pressure rise, defined as the difference between the diffuser outlet pressure and evaporating pressure, and Figure 3.11(b) shows the ejector efficiency with different operating conditions for the system COP optimization case. The higher evaporation temperature points trending towards zero at higher gas cooling pressures are a result of the cycle optimization trying to eliminate the impact of the ejector on the cycle for conditions where the application of an ejector would reduce cycle COP. The resulting behavior is in part also due to the compressor performance characteristics used in this study. With a different compressor and other system components, optimization may result in different geometric parameters.

In this section, optimization was performed on only two geometric ratios. The limited breadth of the assessed parameters was mainly due to the ejector model formulation used. However, using the outlined approach, a designer can extend the optimization study further by utilizing a more detailed model formulation that could account for the effects of additional geometric parameters on the ejector performance, such as the mixing section length to diameter ratio and the diffuser section length. Also, the ejector components efficiencies were kept constant in the present study but the effect of ejector geometric parameters on its component efficiencies can also be included by using efficiency curves for a particular system derived either from experimental data or more detailed theoretical models, such as those using CFD.

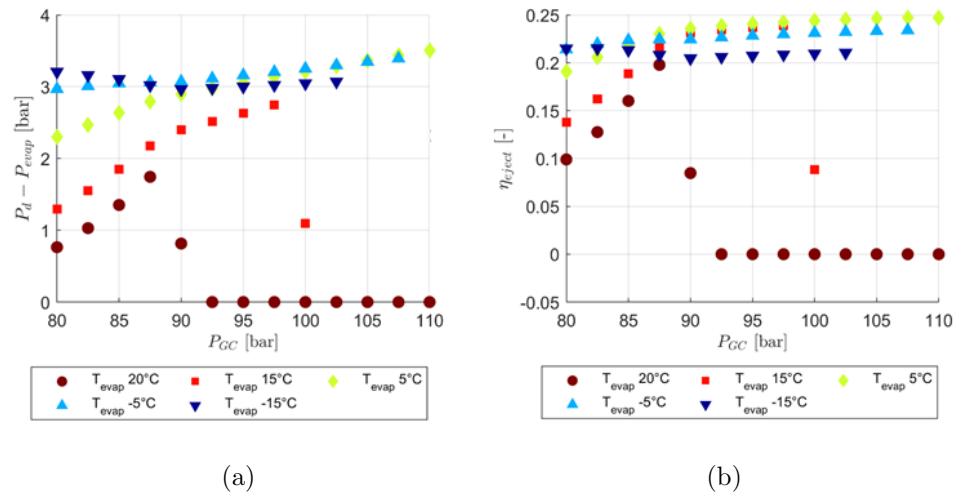


Fig. 3.11. Variation with gas cooler pressure and evaporating temperature of: (a) Ejector pressure rise for the case of system COP optimization; and, (b) Ejector efficiency for the case of system COP optimization.

### 3.5 Practical Considerations

The  $\text{CO}_2$  ejector analyzed in the ejector numerical design chapter and experimentally-tested in Chapter 5 is a robust design. It was able to vary both the motive and suction nozzle diameters effectively, and the device performance was reasonable. With that being said, stainless steel straight threads had a tendency to gall with only slight interference. Furthermore, some of the fittings designed to mate with the test stand tubing were soldered instead of welded. As long as the solder had a high silver content, the choice of solder was acceptable. However, a weld would be more robust. After years of use, the threads began to experience galling, and one of the soldered joints was compromised. Therefore, the threads were re-tapped and the solder was removed and replaced with a weld through Purdue Research Machining Services. A photo of the broken solder and galling is shown in Figure 3.12, and photos of the refurbished ejector with clean threads and welds are shown in Figures 3.13(a) and 3.13(b), respectively. A final photo of the refurbished ejector is shown in Figure 3.14.



Fig. 3.12. CO<sub>2</sub> ejector with broken solder joint and galled threads.



(a)

(b)

Fig. 3.13. CO<sub>2</sub> ejector with: (a) Tapped threads; and, (b) Tapped threads and clean welds.

Leak paths can be a significant challenge with any variable geometry component operating in a pressurized environment. The initial design of the CO<sub>2</sub> ejector relied on nylon washers and compression from a nut forcing the washer against a tapered lip to deform the washer such that it formed a tight seal around the outer diameter of the nozzle. The same sealing concept was applied for both the motive nozzle needle and the motive nozzle assembly, and can be effective. However, multiple



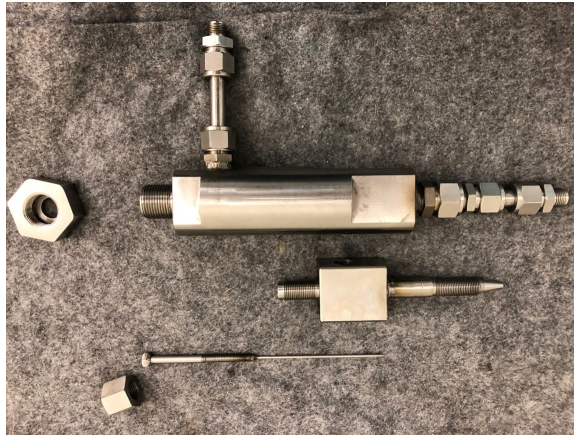


Fig. 3.14. CO<sub>2</sub> ejector with clean welds and tapped threads.

leaks occurred over the course of testing that required re-tightening of the nut and occasional replacement of the seal. In order to decrease the chances of leaks occurring in future designs, a cue from a high-pressure ball valve design was taken through application of a double o-ring design on the outer diameter of the shaft in addition to the nut-driven deformation relied upon in the initial design. A CAD image of the double o-ring concept is shown in Figure 3.15.

The final practicality aspect would be the manufacturability of the ejector as a whole. The design for the CO<sub>2</sub> ejector was developed between 2005 and 2008, which was a time when additive manufacturing was not nearly as widespread as it is today. Therefore, the initial design was developed with a cylindrical piece of stainless steel then had the ejector internal geometry machined inside of it using a combination of lathes and end mills. While the traditional fabrication strategy is just as sound today as it was upon conception, if the size of the ejector or ratios of diameters to lengths were to change significantly, some internal geometries would be a challenge to fabricate. The difficulty of machining certain internal geometries would be particularly relevant in the diffuser due to the exceedingly small diffuser angle. One solution to fabricating this challenging angle would be additive manufacturing, which would be able to fabricate components with large length-to-diameter ratios.

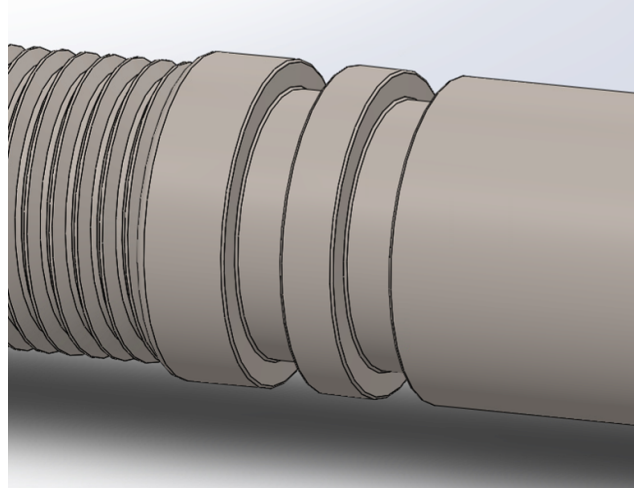


Fig. 3.15. Proposed double o-ring design for additional leak protection on variable nozzle outer diameters.

However, if additive manufacturing was to be considered, then the design starting with a cylinder of stainless steel no longer makes sense due to the amount of raw stainless steel needed, which is often in powder form depending on the specific type of additive manufacturing. With the desired type of manufacturing in mind, redesigning the exterior of the ejector to match the internal contour would be one solution to decrease overall mass, cost, and manufacturing time. An example modification was assessed using a derivative of the  $\text{CO}_2$  ejector introduced in Chapter 2, and the design that was optimized for additive manufacturing required less than 25% of the mass of the original design. CAD renderings of the original design and the design optimized for additive manufacturing are shown in Figures 3.16(a) and 3.16(b), respectively.

### 3.6 Ejector Design Conclusions

This chapter presented a design tool for two-phase flow ejectors applied to vapor compression cycles. Governing equations were presented and discussed. Additionally, sub-model validation of calculated values for the motive and suction nozzle throat diameters, the mixing section diameter, and the diffuser outlet diameter against ex-

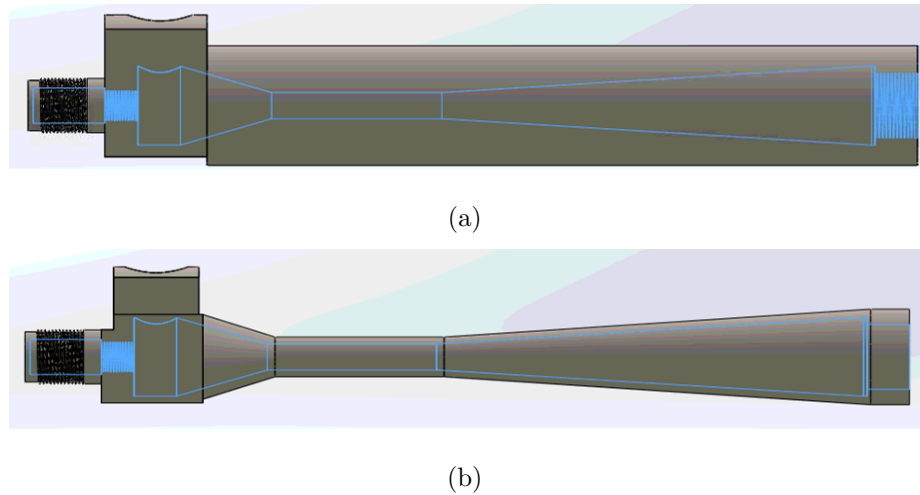


Fig. 3.16. (a) CAD rendering of ejector design for traditional manufacturing; (b) CAD rendering of ejector design for additive manufacturing.

perimental data resulted in an MAE of 3% to 4% for all diameters assessed. The ejector model was then applied in a cycle model where the effects of varying ejector component efficiencies and operating conditions on ejector performance and geometric parameters were assessed. Reasonable trends were achieved, and physical explanations were provided. The gas cooling pressure where the maximum COP benefit from an ejector relative to a four component cycle occurred was found to be lower than the gas cooling pressure where the maximum ejector efficiency occurred. Also, it was found that applying an ejector in higher evaporation temperature applications in low ambient temperature conditions could result in a lower cycle COP than could be achieved with a four component cycle.

Finally, optimization of geometric ratios of the four primary system diameters was conducted with the objectives of maximizing ejector efficiency and maximizing cycle COP. During the ejector optimization, reducing the ratio of mixing section diameter to diffuser outlet diameter resulted in an increased ejector efficiency through the smaller ratio facilitating maximum diffuser pressure lift. However, diminishing returns for

minimization of the ratio of mixing section to diffuser outlet diameters were observed. To provide an example with the ejector parameters resulting from system modeling in Section 3.4.3, increasing the ejector efficiency from 19.9% to 20.8% would require a diffuser length increase of 5.1 mm, whereas a further increase in ejector efficiency from 20.8% to 21.7% would require a diffuser length increase of 17.1mm. While the absolute values used in this example are not massive, the relative size of the length increase for increasing efficiency is the key takeaway. Therefore, the intended application and manufacturing technique should be considered when deciding the ratio of mixing section to diffuser outlet diameters for a design. Additionally, a ratio of motive nozzle to suction nozzle diameters was shown to reach a clear optimum value, but it should be noted that this value will decrease with increasing gas cooler pressure and decreasing evaporation temperatures.

Future work is to develop more comprehensive sub-models that can capture efficiency variation over a broad range of operating conditions, as well assess the results of the model using various two-phase speed of sound definitions to broaden model applicability. Additionally, experimentally validating optimized designs through testing of a prototype is a next step in this work.

## 4. DYNAMIC MODELING

This chapter provides an overview of the dynamic model developed to predict transient and performance of the test stand developed in Chapter 2. An overview of the dynamic modeling environment is provided, including solution schemes, boundary conditions, and cell types within the model. Component sub-models and how their parameters were modified to represent the experimental cycle are presented in-depth. In particular, heat exchanger, compressor, and valve sub-models are described in an effort to increase the robustness of the model and minimize inputs from the user. Finally, two case studies showing potential applications of the dynamic model are assessed.

### 4.1 Dynamic Modeling Introduction

As transcritical CO<sub>2</sub> cycle architectures increase in complexity, control of these cycles becomes a greater challenge. Optimization opportunities are one aspect of controlling transcritical CO<sub>2</sub> cycles, including a free high-side pressure, impactful pressure differentials between evaporators and flash tanks, and vapor injection pressure. However, optimization is secondary to ensuring the system operates reliably. Particularly when phase separation and flooded evaporators are utilized, the transients associated with quality variation with pressure and the risk of drying out the evaporators must be addressed with robust solutions. Controlling superheat at the evaporator outlet via a TXV or EXV upstream of the evaporator is a standard and robust method of cycle control. However, as transcritical CO<sub>2</sub> cycles become increasingly complex, additional control methods and tools to develop them are needed. As dynamic modeling efforts and programs have developed over the past several decades [121], two definitive types of dynamic models have become apparent and

widely-used. The first is lower-fidelity that relies largely on linear relationships and is used primarily for large time scale problems, such as simulations on the order of years. The second type is a higher-fidelity, physics-based modeling approach [122]. These models consist of algebraically-coupled differential equations, and have been implemented in several different coding languages, some examples of which have been mentioned in Chapter 1 [123–125].

A dynamic simulation of a 1:1 scale laboratory transcritical CO<sub>2</sub> supermarket system was conducted by Pardinas et al. [87] using Dymola [126] and TIL libraries [127]. The researchers assessed several architectures utilizing parallel compression, phase separation, and evaporator flooding, then tested control strategies to ensure safe transitions when varying the number of compressors in operation based on required loads. In particular, it was found that parallel compression led to a reduction in power consumption of 19% at 30 °C relative to a standard booster system, and that implementing ejectors in the cycle made an additional 8% power reduction possible. The authors proposed application of a variable speed drive to at least one compressor within a block of parallel compressors to ease transitions when bringing them online to supplement capacity, and also applied a high-pressure EXV in parallel with the multi-ejectors. While the idea behind the multi-ejector setup is that solenoid valves open and close upstream of each ejector to modulate system capacity and high-side pressure through increasing or decreasing the ejector effective flow area, the addition of an EXV is a prudent safety mechanism. The motive nozzle of both ejector blocks is fed by the gas cooler outlet flow, but the suction nozzle of one set of ejectors was fed by the MT cabinets while another was fed by the AC evaporator. The separate sources for the suction nozzle necessitated a tradeoff in control priorities between either optimizing the AC load and risking upsetting the gas cooling pressure or using both ejector blocks to optimize the gas cooling pressure and risking reaching a limit on AC capacity. Finally, the intermediate receiver pressure availed itself as a control variable and it was proposed to actively control this pressure through compressor power minimization as a function of ambient temperature just as is done with high-

side pressure control. Cabello et al. [88] compared experimental measurements of the optimum high-side pressure in a transcritical CO<sub>2</sub> cycle to four correlations for COP optimization in the literature. The researchers concluded that very slight errors in the calculation of the optimum gas cooling pressure resulted in significant COP reduction. In response, a number of researchers proposed the application of real-time control strategies of optimum high-side pressure, which Cecchinato et al. [89] concluded was a more robust solution than the application of correlations from the literature.

This section focuses on the development of a detailed model of the test stand introduced in Chapter 2. The significantly larger amount of published literature on steady state performance of multi-evaporator vapor compression cycles relative to dynamic models was a motivator for the development of the model presented herein. Additionally, efforts to experimentally-validate dynamic models are fewer yet, adding to the potential impact of this chapter. Details on modified sub-component models are discussed, and two case studies for application of the model to develop control schemes are proposed. An overview of the numerical environment used for this model is provided, and the application described herein is conducted in the Modelica language [128], utilizing the Dymola environment [126] and TIL Suite library developed by TLK-Thermo [127].

## 4.2 Model Overview

Developed in 1997, Modelica is an object-oriented, multi-domain, declarative language that allows component-oriented modeling of complex systems. One of the benefits of utilizing a language like Modelica is that it enables the user to convert continuous and discrete components into a system of hybrid differential-algebraic equations that are transformed by a simulation environment. An example of a simulation environment that is compatible with Modelica is Dymola, which was utilized for the work conducted herein. Furthermore, within the Dymola environment, a number

of libraries exist that are focused on thermal systems modeling. One such example is the TIL Suite, which contains pre-loaded thermo-physical properties for a broad array of common refrigerants and organic substances. Within the TIL Suite, TIL Media allows the quick and efficient calling of these thermo-physical properties through custom high-performance equations of state, tabulated bi-cubic spline interpolation, as well as an interface to the refrigerant property database REFPROP [129]. Furthermore, the library offers numerous examples of thermal system simulations, both vapor compression cycle and otherwise, along with a vast array of components, fluid choices, and unique boundary conditions. A high-level description of the Modelica environment and physics-based dynamic modeling relative to other techniques can be found in Desideri [122]. Within the TIL Suite the structure available to the user is shown in Figure 4.1. Additionally, an overview of possible fluid types within the TIL Library [127] and their associated parameters is provided in Figure 4.2. A diagram of the developed cycle model in Dymola is provided in Figure 4.3.



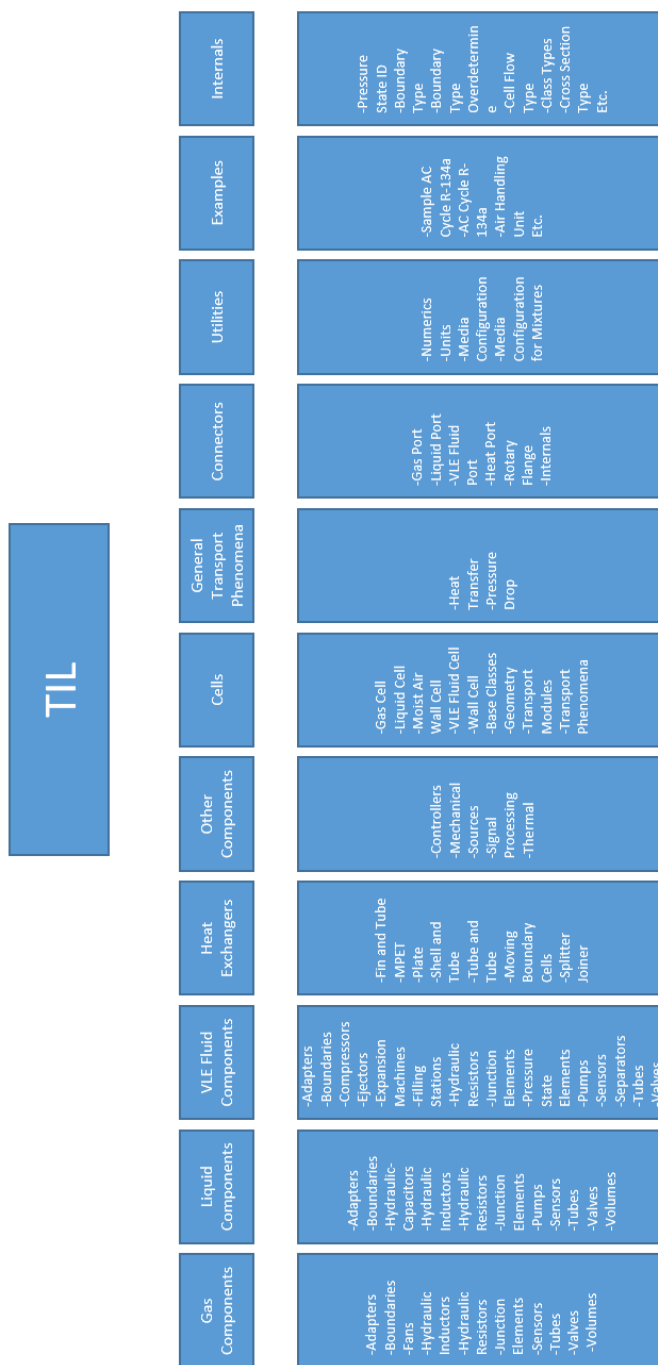


Fig. 4.1. TIL library structure [127].


Name	Content		Symbol
GasPort	p	Pressure at the port	orange 
	m_flow	Mass flow rate (flow)	
	h_outflow	Enthalpy leaving the port (stream)	
	xi_outflow	Mass fraction leaving the port (stream)	
LiquidPort	p	Pressure at the port	blue 
	m_flow	Mass flow rate (flow)	
	h_outflow	Enthalpy leaving the port (stream)	
	xi_outflow	Mass fraction leaving the port (stream)	
VLEFluidPort	p	Pressure at the port	green 
	m_flow	Mass flow rate (flow)	
	h_outflow	Enthalpy leaving the port (stream)	
	h_limit	Minimum enthalpy leaving the port (stream)*	
HeatPort	T	Temperature at the port	red 
	Q_flow	Heat flow rate (flow)	
RotatoryFlange	phi	Absolute rotation angle of flange	grey 
	tau	Cut torque in the flange	
ElectricPin	v	Potential voltage at pin	blue/white 
	i	Electric current (flow)	

Fig. 4.2. List of possible fluid types and connectors available within the TIL library [127].

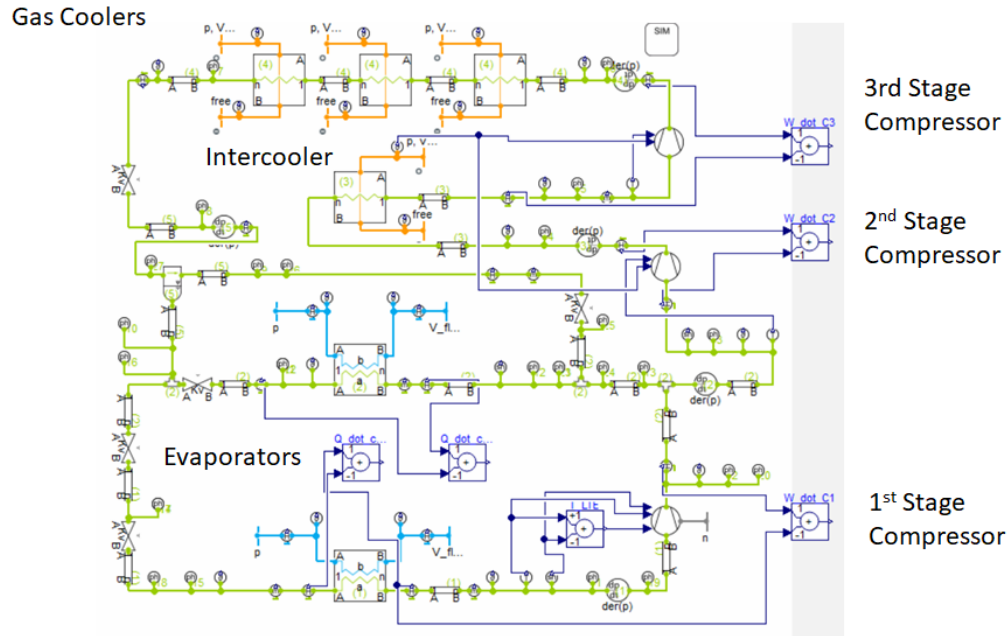


Fig. 4.3. Cycle assessed in the Dymola environment [127].

### 4.3 Boundary Conditions and Solution Schemes

The cycle solver within Modelica converges based on continuity between coupled algebraic equations within a given tolerance between all components and flows within the cycle. All fluid-types specified in Figure 4.2 have connectors that are specific to each fluid type. At each boundary or connection throughout the system, conservation of mass, momentum and energy are checked, and convergence will not be allowed until system attributes, such as temperatures and pressures, are iterated upon to a point of satisfaction for all three conservation equations. Each type of cell interacts with a port when connecting to a boundary or another component. A summary of ports is provided in Figure 4.2.

In this simulation,  $\text{CO}_2$  is considered the *VLE Fluid*, or vapor liquid equilibrium fluid, the moist air used to cool the GCs is *Gas*, and the EG is *Liquid*. Each of these cell types has a unique range of properties associated with it in order to fully define

the thermodynamic state. Accordingly, unique conservation equations are associated with each fluid cell type. Tables 4.1 provides a summary of the cell type and the associated conservation equations for VLE Fluid, Moist Air Wall, and Liquid cells.

Table 4.1.  
Map for the three cell types utilized in the TIL Suite [127].

<i>Mass Balance</i>
<i>Energy Balance</i>
<i>Momentum Balance</i>
<b>VLE Fluid</b>
$\frac{d\xi}{dt} = \frac{\dot{m}_{\text{flow,A}} \cdot (\xi_{\text{flow,A}} - \xi_{\text{VLEFluid}}) + \dot{m}_{\text{flow,B}} \cdot (\xi_{\text{flow,B}} - \xi_{\text{VLEFluid}})}{\dot{m}_{\text{VLEFluid}}}$ $\frac{dh}{dt} = \frac{\dot{m}_{\text{flow,A}} \cdot (h_{\text{flow,A}} - h_{\text{VLEFluid}}) + \dot{m}_{\text{flow,B}} \cdot (h_{\text{flow,B}} - h_{\text{VLEFluid}}) + \dot{Q}_{\text{flow}} + \text{Volume} \cdot \frac{dp}{dt}}{\dot{m}_{\text{VLEFluid}}}$ $p_A - p_B = \Delta p$
<b>Moist Air Wall</b>
$0 = \dot{m}_{\text{flow,A}} + \dot{m}_{\text{flow,B}} - \dot{m}_{\text{flow,Condensate}} + \dot{m}_{\text{flow,Evaporate}}$ $0 = \dot{Q}_{\text{flow}} + \dot{m}_{\text{flow,A}} \cdot h_A + \dot{m}_{\text{flow,B}} \cdot h_B + h_{\text{film}} \cdot (\dot{m}_{\text{flow,Evaporate}} - \dot{m}_{\text{flow,Condensate}})$ $p_A - p_B = \Delta p$
<b>Liquid</b>
$\dot{m}_{\text{flow,A}} + \dot{m}_{\text{flow,B}} = \beta \cdot \rho_{\text{Liquid}} \cdot \frac{dT_{\text{Liquid}}}{dt} \cdot \text{Volume}$ $\frac{dT_{\text{Liquid}}}{dt} = \frac{\dot{m}_{\text{flow,A}} \cdot (h_{\text{flow,A}} - h_{\text{VLEFluid}}) + \dot{m}_{\text{flow,B}} \cdot (h_{\text{flow,B}} - h_{\text{VLEFluid}}) + \dot{Q}_{\text{flow}}}{c_p \cdot \dot{m}_{\text{Liquid}}}$ $p_A - p_B = \Delta p$

where  $\xi$  is mass ratio,  $t$  is time,  $\dot{m}$  is mass flow rate,  $h$  is specific enthalpy,  $\dot{Q}$  is heat transfer rate,  $p$  is pressure,  $T$  is temperature,  $\beta$  is the convective mass transfer coefficient, and  $c_p$  is specific heat at constant pressure.

Given the dynamic nature of modeling a vapor compression cycle in Dymola, particularly when used with cycles as complex as the test stand cycle, initial guess values and boundary conditions are very important to achieve convergence. At the

highest level,  $(dp/dt)$  nodes represent starting pressure values and are placed at each point in the cycle where a unique pressure level will occur. For example, the third stage of compression outlet meets a pressure node with an initial pressure guess value. The GCs are also associated with this same pressure node, despite the pressure drop that will occur within them. Mathematically, these nodes impart the assumption that the time derivative of pressure will remain constant along the direction of flow for all components at a given system pressure level. The constant time derivative of pressures effectively increases the model time constants, thus improving simulation performance. To better illustrate how the constant time derivative of pressure is applied, Figures 4.4(a) and 4.4(b) show the pressure differential across a flow path and the pressure node applied in the Dymola environment, respectively. Additionally, Table 4.2 provides the initial pressure values for each node to help define the unique pressure levels within the test stand.

Table 4.2.  
Pressure node initial values used in the dynamic test stand simulation.

Node	Description	Unit	Value
1	LT Evap	(kPa)	1000
2	MT Evap	(kPa)	2200
3	IC	(kPa)	4700
4	GC	(kPa)	7500
5	FT	(kPa)	3000
6	EXV 3-4 Line	(kPa)	2000

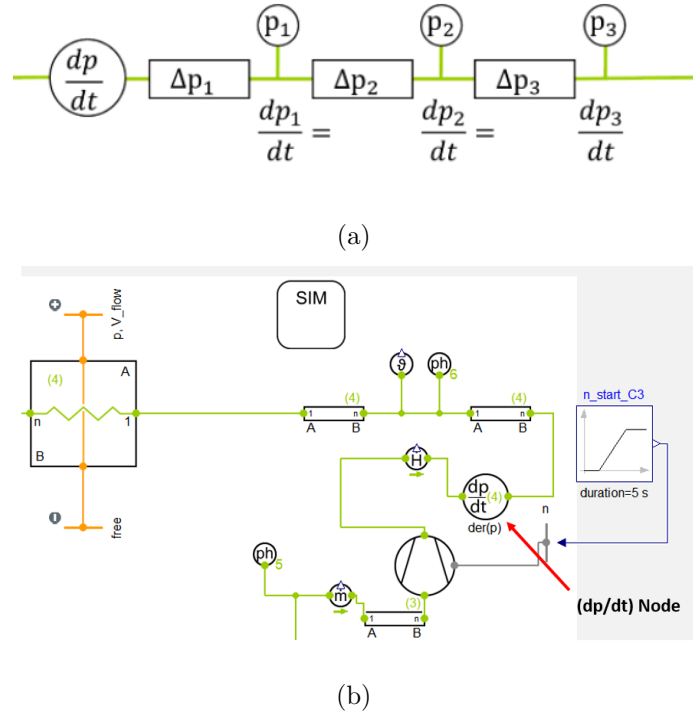


Fig. 4.4. (a) Example of using the  $(dp/dt)$  module provided within the TIL library [127]; (b) Pressure node in Dymola environment [127].

Each major component is then associated with one of the aforementioned pressure nodes, and many components have the ability to receive further initial guesses. For instance, tee junctions where flow streams mix allow to specify an estimated mixture specific enthalpy, and flash tanks require an initial liquid level and inlet quality as initial values.

The initial guess values for the HXs are considerably more complex. Firstly, there are conditions for both the counter/cross-flow fluid-sides as well as the refrigerant-side. In situations where humid air is used as the secondary fluid as is the case with the heat sink applied in this model, the humidity ratio guesses need to be provided. In addition, reasonable HX wall temperatures, outlet specific enthalpies for the refrigerant-side, and mass flow rate guesses are also required to facilitate and ease the convergence of the simulations. A reasonable set of initial values is of particular

importance when HXs with a more complex geometry are considered as well as when pressure drops and heat transfer correlations are selected instead of constant values for heat transfer coefficients and pressure drop across components. Nevertheless, once meaningful initial values are input, the cycle converges consistently and repeatably.

Relative to all components in a vapor compression cycle, the HX dynamics have been shown to govern the transient behavior of a cycle. Thermal system transients are often governed by HX dynamics because of the longer time scales necessary for these dynamics, particularly in two-phase applications, relative to pressure propagation or the mechanical dynamics of a compressor. As such, particular attention is paid to the modeling and solution scheme surrounding the HXs in the system. The two most common techniques for modeling HXs are moving boundary and finite-volume analyses. The moving boundary analysis entails separating the HX into general regions as a function of phase of the working fluid, then applying the appropriate correlations to solve to heat transfer and pressure drop through the respective sections. Finite-volume breaks the HX into a number of elements of equal volume, then solves for the heat transfer and pressure drop behavior of each respective section as governed by conservation of mass, momentum and energy. The phase of the working fluid in each volume element is assessed, and the appropriate correlations are applied. Because this model uses CO<sub>2</sub> as the working fluid, the heat rejection portion of the cycle can operate either sub-critically or transcritically, depending on ambient temperatures and the heat rejection pressure. In low-ambient condition operating conditions heat rejection will occur with two-phase fluid due to sub-critical operation, and in higher ambient conditions the heat rejection will occur in the supercritical state. Both HX modeling techniques are used often, but as a general rule the moving boundary method is more efficient but less accurate than the finite-volume method. At the time when this model was developed there was not a moving-boundary MCHX GC available in the TIL Suite, so the two techniques were not able to be compared for validity or numerical robustness. Therefore, all HXs in the model utilize the finite-volume solution scheme, shown schematically in Figure 4.5.

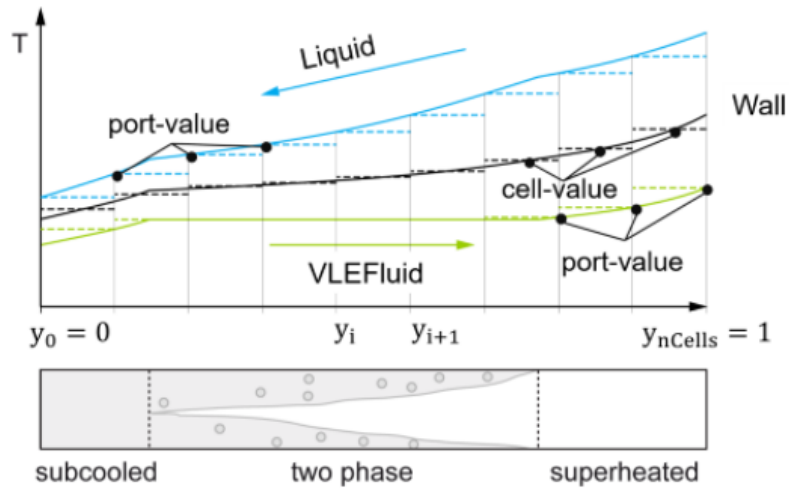


Fig. 4.5. Dymola finite-volume heat exchanger analysis method overview [127].

Boundary conditions were implemented for the counter-flow secondary fluids exchanging heat with the refrigerant in the MT and LT evaporator PHXs and enabled the user to set the operating temperatures for the cycle. For the air-side which cools the MCHX IC and GC through cross-flow, inlet temperature, volumetric flow rate, humidity ratio were input. The volumetric flow rate was scaled to match that of the fans installed on the MCHXs, and the air inlet temperature and relative humidity were set to be equal given their placement in the same ambient air flows. The GC that appears as a single HX in system schematics such as Figure 2.6 is split into three identical units in series to replicate the experimental setup, as shown in Figure 4.3 and explained in Section 2. The boundary conditions for each evaporator were selected as a function of the fluid temperature of their respective temperature levels, such as freezer or refrigerator temperature levels, along with both the concentration and volumetric flow rate of their respective constant-temperature baths.

Dymola features a number of predefined solvers which can be selected by the user depending on the complexity of the simulation. In addition, step size, step rate, and convergence tolerance can be specified. The default solver within the TIL Library is



DASSL, a numerical solver algorithm for the systems of implicit differential algebraic equations [130]. DASSL is used for solving differential algebraic equations in the form shown in Equations 4.1, 4.2, and 4.3.

$$F(t, y, y') = 0 \quad (4.1)$$

$$y(t_o) = y_o \quad (4.2)$$

$$y'(t_o) = y'_o \quad (4.3)$$

In particular, DASSL can be used to solve two types of problems that ordinary differential equation solvers cannot: (i) when  $y'$  is not possible to solve for explicitly and (ii) when there is a solution for  $y'$  but it is not practical to do so due to potentially encountering a sparse matrix which would make solving the original form much easier. DASSL uses Newton's method and a kth order backwards differentiation formula to transition between time steps. In practice, the solver is meant to be easy to use while maintaining flexibility to solve a broad array of problems. If the function  $F$  from Equation 4.1 is known and receives a consistent set of initial values, the solver will work most effectively. This solution structure and applicability is logical to be applied to the differential algebraic equations and initial values produced by cycles developed in Dymola, and thus has remained the solver utilized herein.

#### 4.4 Component Models

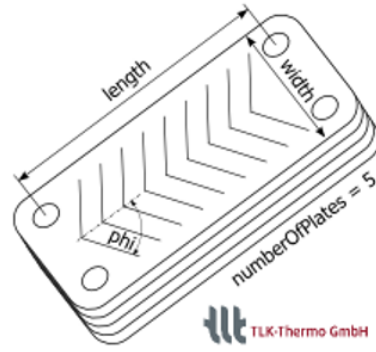
For the model development process, the test stand cycle model initially contained many basic components in an effort to satisfy energy and mass balances and establish meaningful boundaries as well as guess values for the solver. The process of implementing component models intended to represent the components applied in the test stand is described herein. Given that heat rejection is performed with MCHX GCs to air, and evaporation occurs in PHXs from EG, different sets of correlations are used

for both types of HX, and individual geometries are input. The solution for each HX is solved with the following elements:

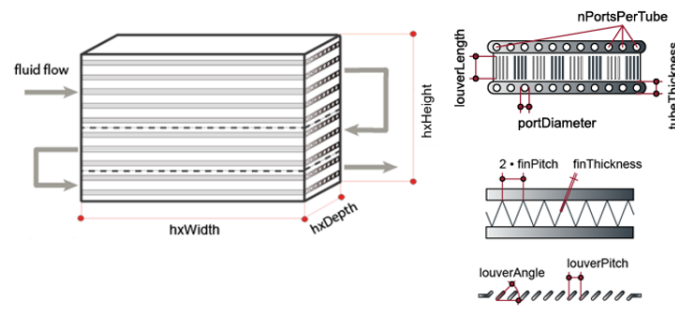
- Geometry
- Pressure drop
- Heat transfer
- By finite-volume analysis

#### **4.4.1 Heat Exchangers**

The two types of HXs utilized in the test stand are a stainless-steel PHX and a stainless-steel MCHX with aluminum fins. TIL facilitates geometry inputs for both of these HX types. Possible inputs and associated geometric diagrams for PHX and MCHX are provided in Figure 4.6(a) and Figure 4.6(b), respectively. Geometric values for the PHX and MCHX installed in the test stand are provided in Tables 4.3 and 4.4, respectively.



(a)



(b)

Fig. 4.6. (a) PHX schematic with examples of modifiable parameters in TIL Library [127]; (b) MCHX schematic with examples of modifiable parameters in TIL Library [127].

Table 4.3.

PHX geometric parameters input to the dynamic test stand model.

Parameter	Unit	Value
Number of Plates	(-)	26 (MTE), 24 (LTE)
Length	(mm)	329
Width	(mm)	120
phi	(°)	75

Table 4.4.  
MCHX geometric parameters input to the dynamic test stand model.

<i>Overall Geometric Parameters</i>		
<b>Parameter</b>	<b>Unit</b>	<b>Value</b>
Height	(mm)	508
Width	(mm)	438
Depth	(mm)	16
N Tubes per Pass	(-)	52
<i>Tube Side Geometry</i>		
N Ports per Tube	(-)	8
Cross Section Type	(-)	Circular
Port Diameter	(mm)	0.54
Tube Thickness	(mm)	0.5
<i>Fin Side Geometry</i>		
Fin Thickness	(mm)	0.15
Fin Pitch	(mm)	1.67
Louver Pitch	(mm)	2.0
Louver Length	(mm)	2.13
Louver Angle	(°)	20

Once the geometry and material specifications are input, the second fluid used in the HX needs to be specified. As mentioned above, the MCHXs are used in heat rejection to ambient air in cross-flow, therefore moist air is used as the secondary fluid. The counter-flow fluid in MT bath is Dowtherm SR-1, which is 95.5% EG and 4.5% performance additives by mass. An equivalent concentration of pure EG of 34.4% by mass was calculated and used in subsequent calculations. The LT bath utilized a 50% by mass concentration of EG and water.

The MCHX refrigerant-side heat transfer used for GCs utilize a combined algorithm from TLK comprised of Gnielinski, Dittus and Boelter [131] for single-phase flow, which was particularly recommended for supercritical CO<sub>2</sub>. Correlations by Cavallini [132] and Kondou and Hrnkjak [133] were experimentally validated for use with subcritical CO<sub>2</sub> condensation, and were therefore chosen for the condensation correlation in the case of subcritical heat rejection. Heat exchange within the MCHX was calculated with geometry-based conduction and the selection of stainless steel as the material. Refrigerant-side pressure drop was calculated from Konakov [134] with a smooth-pipe assumption. A constant-fin efficiency model was used for the fin calculations, assuming aluminum material composition and a constant efficiency of 90%. For the MCHX air-side heat transfer Chang and Wang [135] was utilized with the consideration of moist air. Kim and Bullard [136] was utilized for the air-side pressure drop correlations.

In the PHX evaporators, refrigerant-side heat transfer was calculated utilizing Longo [137] due to its applicability in PHXs in particular, and refrigerant-side pressure drop was calculated utilizing a correlation optimized for chevron plates from Holger [138]. The EG-side heat transfer and pressure drop were calculated with PHX correlations specifically for chevron plates from Holger [138]. Heat exchange within the PHX was solved using geometry-based conduction.

#### 4.4.2 Compressors

The first stage compression in the test stand is performed by a single-stage reciprocating compressor and the second and third stages of compression are performed by a two-stage compressor with intercooling between stages. Both compressors were initially tested on a hot-gas bypass compressor load stand, and were tested further in the multi-stage test stand presented in Chapter 2. Empirical correlations for both compressors were developed through several iterations that were dictated by the compressor operating range during testing in the multi-stage test stand. The evapora-

tion temperatures tested with the hot-gas bypass test stand were higher than those encountered during testing with the multi-stage test stand. Therefore, the initial compressor data could not be mapped empirically to accurately predict compressor performance at the operating conditions where they operated in the multi-stage test stand. Therefore, additional data from the multi-stage test stand needed to be utilized for development of a compressor map that was applicable over a broader range of compressor operating conditions.

Because the first stage compressor was being applied as a booster compressor between evaporation pressures despite being rated for transcritical operation, it was operated near the bottom limit of its envelope, shown in Figure 4.7. Operation near the lower limits of the compressor envelope offers an explanation for the first stage compressor achieving an isentropic efficiency below 40% for many data points.

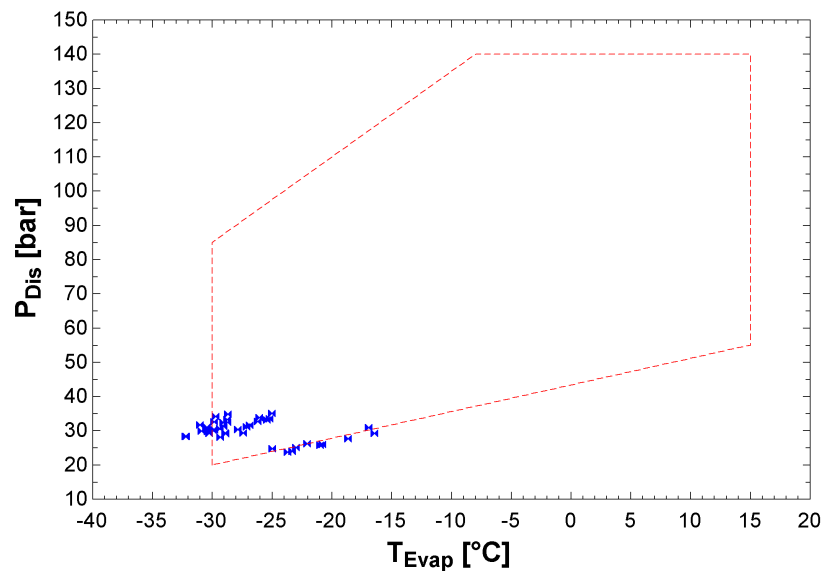


Fig. 4.7. First stage compressor operating envelope with experimental operating data of the experimental campaign in the CO<sub>2</sub> test stand.

Initially, a 10-coefficient ARI compressor map [112] was developed to empirically characterize the single-stage compressor performance. However, the 10-coefficient cor-

relation became an issue with the two-stage compressor because it had an IC between the stages. Therefore, a traditional single-stage map would not be reliable because the IC outlet temperature was a function of more than just first stage compressor suction superheat and pressure ratio. The IC and two-stage compression led to the decision to apply a dimensionless correlation technique based on the Buckingham Pi Theorem proposed by Mendoza-Miranda et al. [139], which could take into account heat loss to the ambient as well as variable compressor suction superheat, among other parameters. An overview of the Pi groups is provided in Table 4.5.

Table 4.5.  
Summary of applied Pi groups for the mapping of the compressors in the CO<sub>2</sub> test stand [139].

$\pi_i$	Volumetric Efficiency	Isentropic and Overall Efficiencies
$\pi_1$	$\eta_v$	$\eta_{is}$ or $\eta_o$
$\pi_2$	$\frac{P_d}{P_s}$	$\frac{P_d}{P_s}$
$\pi_3$	$(\frac{\rho_s}{P_s})^{1.5} N^3 V_G$	$\frac{N_r}{N}$
$\pi_4$	$\frac{N_r}{N}$	$\frac{N^3 V_G}{\Delta h_{is}^{1.5}}$
$\pi_5$	$\frac{M_{R-134a}}{M_{alt}}$	$\frac{\Delta h_{is} \rho}{P_s}$
$\pi_6$	-	$(\frac{T_s + T_{d,is}}{2} - T_{Amb})^{-1}$
$\pi_7$	-	$\frac{M_{R-134a}}{M_{alt}}$

Relevant Pi numbers to calculate three compressor efficiencies were determined through a parametric sensitivity study conducted in Mendoza-Miranda et al. [139]. The sensitivity study entailed removing Pi numbers from the calculation of an efficiency and observing the effects. If the removal of a particular Pi number had a minimal impact on the accuracy of the efficiency calculation over the range of the assessed experimental data, that Pi term was removed from the correlation for that particular efficiency in an effort to balance complexity with accuracy. The three

compressor efficiencies quantified were volumetric, isentropic, and overall efficiency, shown in Equations 4.4, 4.5, and 4.6, respectively.

$$\eta_{\text{vol}} = \frac{\dot{V}}{\dot{V}_{\text{max}}} = \frac{\dot{m}v_{\text{suc}}}{V_{\text{disp}}N_{\text{comp}}} \quad (4.4)$$

$$\eta_{\text{is}} = \frac{h_{2s} - h_1}{h_2 - h_1} \quad (4.5)$$

$$\eta_o = \frac{\dot{m}(h_{2s} - h_1)}{\dot{W}_{\text{Elec}}} \quad (4.6)$$

The parametric sensitivity resulted in expressions for volumetric, isentropic, and overall compressor efficiency provided in Equations 4.7, 4.8, and 4.9, respectively. The exponents were all developed using experimental data from an R-134a reciprocating compressor, but could be applied to various compressor types and working fluids, hence the inclusion of the  $\Pi$  terms that consider a ratio of molar mass of the working fluid relative to the molar mass of R-134a.

An additional coefficient,  $a_1$ , was applied to increase the fit of the data to the  $\text{CO}_2$  data from the test stand introduced in Chapter 2 and is tabulated for all three compressor stages mapped in Table 4.6.

$$\eta_{\text{vol}} = a_{1,v}\pi_2^{-0.2678}\pi_4^{-0.0106}\pi_5^{0.7195} \quad (4.7)$$

$$\eta_{\text{is}} = a_{1,\text{is}}\pi_2^{0.0753}\pi_3^{0.2183}\pi_4^{0.0015}\pi_6^{0.0972} \quad (4.8)$$

$$\eta_o = a_{1,o}\pi_2^{-0.1642}\pi_3^{0.2050}\pi_6^{0.0659}\pi_7^{0.7669} \quad (4.9)$$



Table 4.6.

Summary of scaling coefficients  $a_1$  applied to expressions for efficiencies of the compressors in the CO<sub>2</sub> test stand, shown in Equations 4.7, 4.8, and 4.9.

Compressor Stage	$a_{1,v}$	$a_{1,is}$	$a_{1,o}$
1	0.467	0.633	0.338
2	0.4131	1.3	0.501
3	0.475	0.485	0.237

Modeling the two-stage compressor with intercooling ultimately resulted in separate correlations for both compressor stages. However, because the power input measurement was only measured upstream of the compressor VFD, the heat loss distribution between compressor stages needed to be assessed through an alternative means. The two stages of compression are shown graphically in a P-h diagram shown in Figure 4.8.

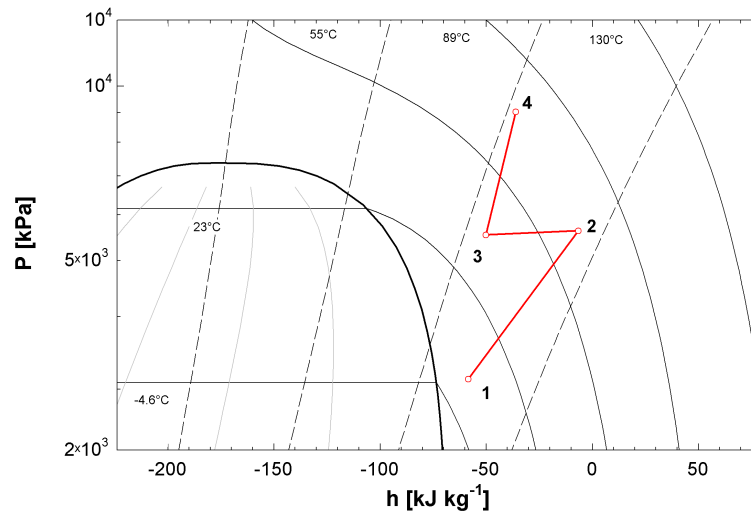


Fig. 4.8. P-h diagram of a two-stage compression process using a trans-critical CO<sub>2</sub> compressor with intercooling.

Given the single power measurement taken for a two-stage compressor, Equation 4.10 shows that only the total heat loss rate from both stages can be calculated. Therefore, an assumption on how to distribute the heat loss between the compressor stages needs to be made.

$$\dot{W}_{\text{Elec}} = \dot{m}[(h_2 - h_1) + (h_4 - h_3)] + \dot{Q}_{\text{loss,total}} \quad (4.10)$$

Figure 4.8 shows that the two stages of compression have drastically different slopes, suggesting a larger discrepancy in efficiencies of the two stages than should physically occur. Therefore, two heat transfer paths are considered within the compressor to explain and characterize the difference in slopes. First, because the compressor is semi-hermetic, the suction flow, state 1 in Figure 4.9, travels over the compressor motor for motor cooling. The heat transfer from the motor further superheats the refrigerant before it is compressed from state 1 to state 2. After being discharged from the compressor at state 2, the flow enters an air-source IC where heat is rejected to the ambient before the flow enters the second stage of compression at state 3. From state 3, the flow is compressed to the highest discharge pressure at state 4. The two-stage compression process, as well as the location of the motor heat transfer, is shown in Figure 4.9.

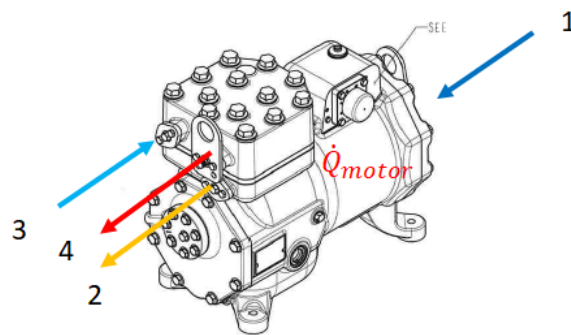


Fig. 4.9. Schematic of heat and mass flow within a two-stage compressor.

If a motor efficiency of 10% is assumed and 100% of the heat from the motor is assumed to be absorbed by the refrigerant, Equation 4.11 can be used to approximate the superheat of the flow after cooling the motor. Once the approximate amount of heat transfer into the refrigerant from the compressor motor is known, an updated state of the refrigerant, *new*, entering the first stage compression chamber can be calculated with Equation 4.11. From the updated compressor suction chamber inlet state, the outlet specific enthalpy from an isentropic compression process,  $h_{2s}$ , can be calculated. The superheat increase resulting from the motor superheat is shown relative to the measured compressor suction superheat upstream of the motor at state 1 as a function of compressor pressure ratio in Figure 4.10.

$$\dot{Q}_{\text{motor}} = 0.1\dot{W}_{\text{elec}} = \dot{m}(h_{1,\text{new}} - h_1) \quad (4.11)$$

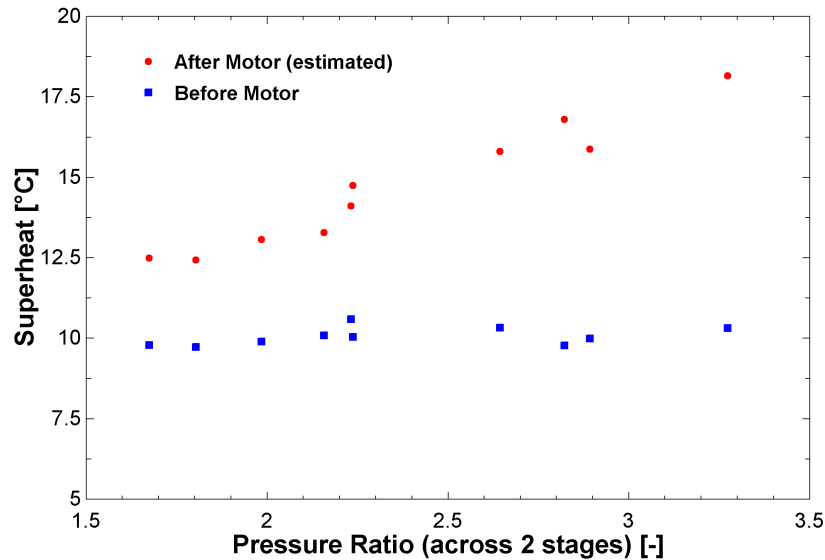
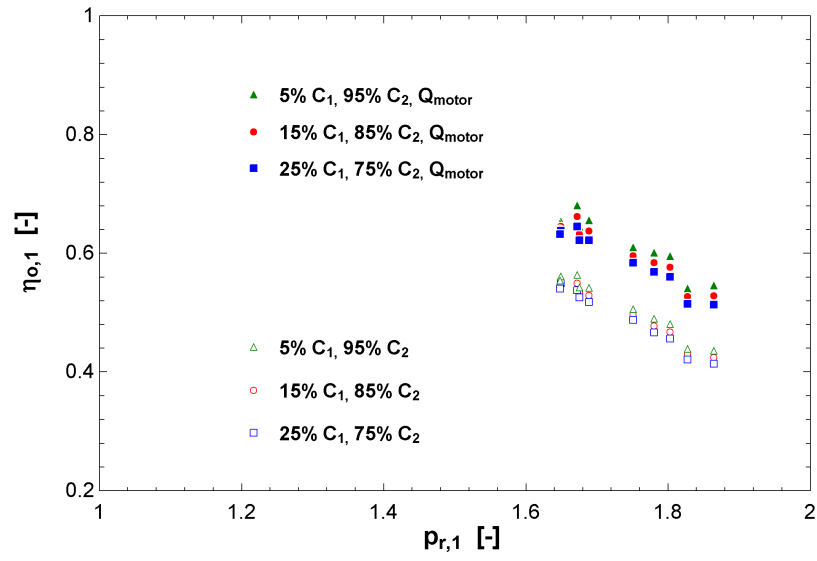


Fig. 4.10. Refrigerant superheat before and after cooling the motor of a semi-hermetic CO<sub>2</sub> compressor.

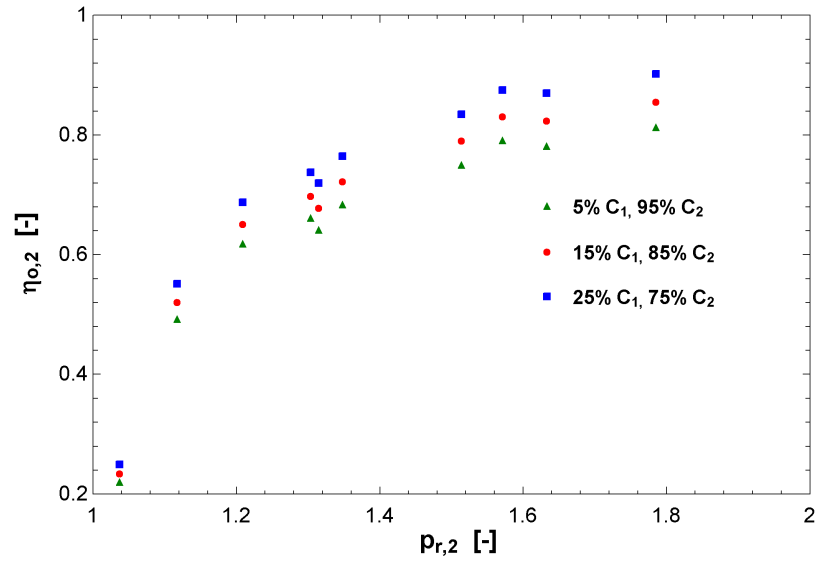
The increased superheat due to motor cooling increases the efficiency of the first stage of compression due to the increased specific enthalpy of the fluid entering the

first stage compression chamber. Due to the fixed discharge state, the heat transfer from the motor decreases the change in specific enthalpy across the first stage of compression process, which then increases the isentropic efficiency of the first stage of compression as calculated in Equation 4.5 and shown in Figure 4.10. However, the heat transfer from the motor does not solve the problem of the heat loss distribution between compressor stages. Given that the second stage compressor efficiency is significantly higher than the first stage, heat loss distributions of between 75% and 95% from the second stage were assessed.

The combination of considering the heat transfer from the motor as well as attributing the majority of the heat loss to the second stage of compression results in a significant reduction in the difference in efficiencies between compressor stages. A final decision was made to distribute 85% of the heat loss to the second stage of compression to balance efficiency agreement with physical feasibility.



(a)



(b)

Fig. 4.11. (a) First stage CO<sub>2</sub> compressor overall efficiency with motor superheating and varying heat loss distribution between stages; (b) Second stage CO<sub>2</sub> compressor overall efficiency with varying heat loss distribution between stages.

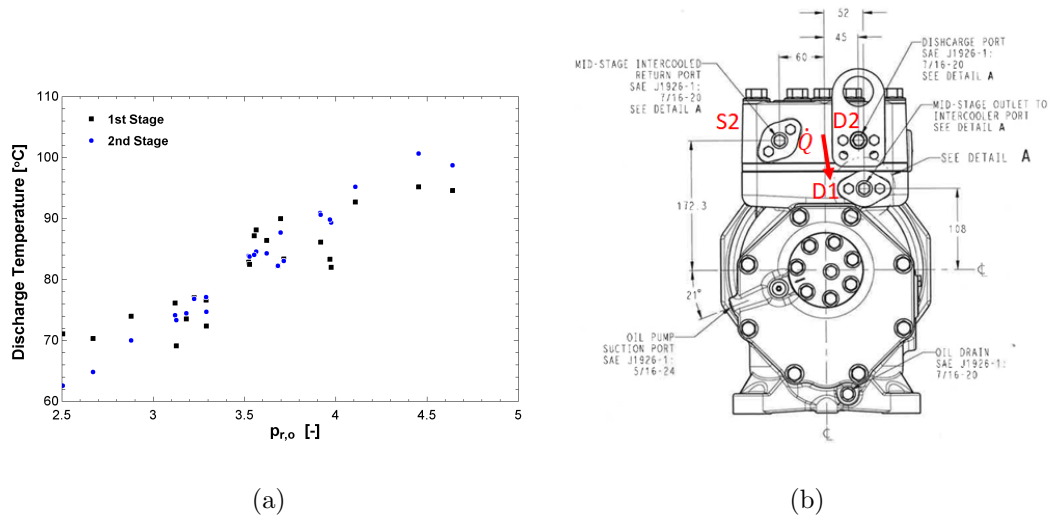


Fig. 4.12. (a) Experimental discharge temperatures from both compression stages of the two-stage compressor in the  $\text{CO}_2$  test stand; (b) Heat transfer path between compressor stages.

To further assess the physical feasibility of the proposed heat transfer path between compressor stages, the discharge temperatures from both compression stages were compared and the physical locations of the discharge ports were assessed. Figure 4.12(a) shows that the discharge temperatures from both compressor stages are nearly identical over a broad range of experimental operating conditions. Furthermore, Figure 4.12(b) shows that the discharge ports of the compressor are situated immediately next to each other, providing a short conductive heat path to facilitate the significant heat transfer from the second stage of compression to the first stage of compression.

#### 4.4.3 Expansion Valves, Flash Tanks, and Tubing

The four EXVs were sized to match the capacity relative to the percent opening curves shown in Figure 4.13, and the capacity of both the fine and coarse MVs were shown to be linear as a function of number of turns up to six turns from closed, per

the manufacturer data sheet. To assist in replicating the experimental geometries of the valves for a given condition, the experimental setup writes the voltage input to all four EXVs as well as the valve position of the MV to the data output file. The data analysis script then converts the voltage to a flow coefficient value,  $k_v$  in  $\text{m}^3 \text{hr}^{-1}$ , that can then be input into the Dymola model.

The flow coefficient calculation is performed using Figure 4.13, where a polynomial relating the valve opening percentage to the valve flow coefficient. The 0 - 10 V range of the valve input voltage was related to opening percentage directly, where 10 V is 100% open and 0 V is 0% open. The valve capacity calculation is shown in Equation 4.12, where  $k_{v,\text{max}}$  represents the maximum volumetric flow rate of the EXV being assessed which were tabulated in Table 2.6. Equation 4.13 can then be applied to convert the input  $k_v$  values into effective flow areas.

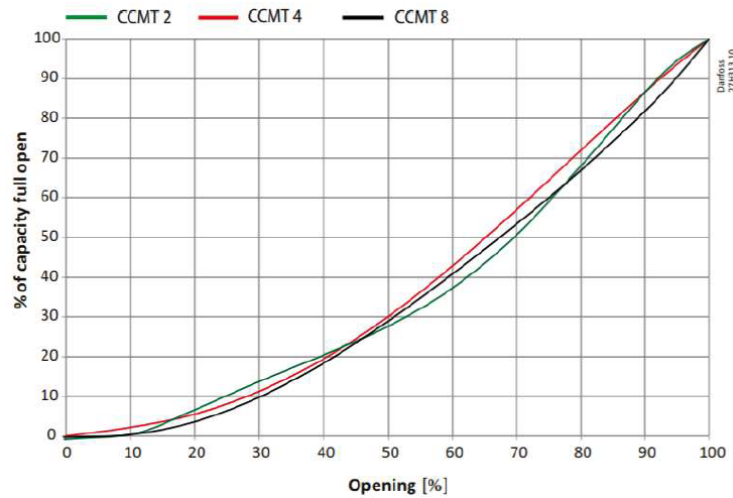


Fig. 4.13. Curves of CCMT EXV capacities over the range of opening percentages.

$$k_{v,\text{EXV}} = \frac{\%_{\text{capacity}} k_{v,\text{max}}}{100} \quad (4.12)$$

$$A_{\text{Eff,kv}} = k_v \sqrt{\frac{1000(\frac{kg}{m^3})}{2 \cdot 1bar}} \quad (4.13)$$

The calculation of the effective flow area from data,  $A_{\text{Eff,data}}$ , was performed using a more generalized form of Equation 4.13, which was derived from the Bernoulli incompressible flow relations and is shown in final form in Equation 4.14.

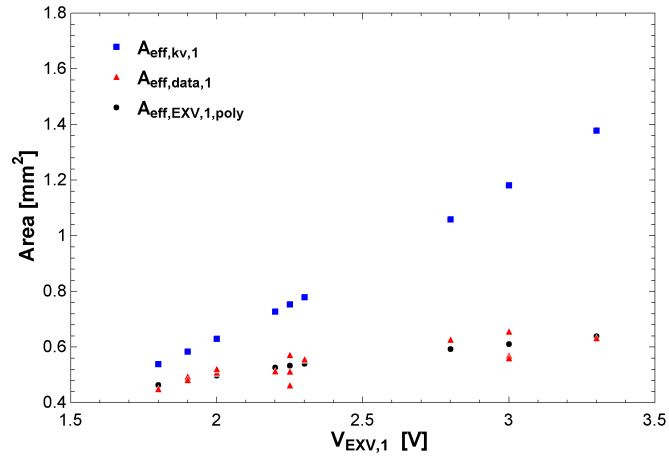
$$A_{\text{Eff,data}} = \frac{\dot{m}}{\sqrt{(P_1 - P_2)2\rho}} \quad (4.14)$$

The flow areas calculated from the  $k_v$  value,  $A_{\text{Eff,kv}}$ , with Equation 4.14 were then compared to the effective flow areas calculated from experimental data,  $A_{\text{Eff,data}}$ .

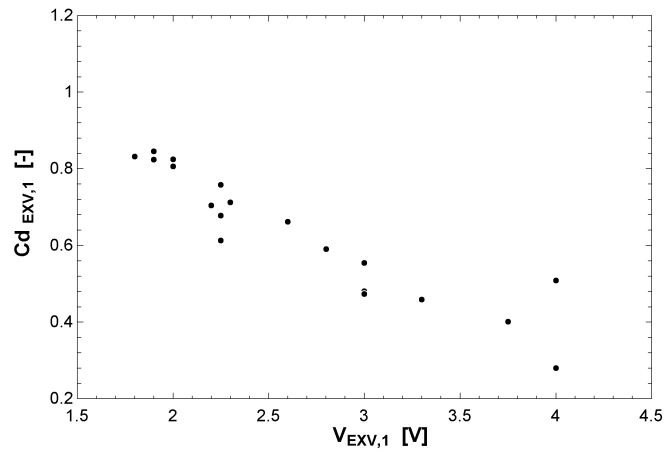
The two effective flow areas are plotted in Figure 4.14(a). The resulting factor was identified as the valve discharge coefficient,  $C_d$ , as identified by Li and Braun [140], and was calculated with Equation 4.15 and plotted for EXV 1 in Figure 4.14(b). Equation 4.15 pulls the two out of the square root and into the coefficient, which was not done in Figures 4.14(a) and 4.14(b) for clarity surrounding the derivation of the expression. In practice,  $C_d$  acts as a factor defined by the ratio of  $A_{\text{Eff,data}}$  to  $A_{\text{Eff,kv}}$ , and is fit to a polynomial for direct calculation from EXV input voltage, the results of which is also reflected in Figure 4.14(a).

$$C_d A_{\text{Eff,data}} = \frac{\dot{m}}{\sqrt{(P_1 - P_2)\rho}} \quad (4.15)$$





(a)



(b)

Fig. 4.14. (a) Comparison of effective flow areas calculated for EXV 1; (b) Resulting EXV discharge coefficient calculation,  $C_d$ , from EXV 1 data.

As shown in Figure 4.14(b), the  $C_d$  for EXV 1 varied significantly with voltage. The remaining EXVs did not experience this same behavior, which is likely due to a choked flow condition occurring in EXV 1. Therefore, the  $C_d$  for EXV 1 was calculated as a polynomial shown in Equation 4.16, while the  $C_d$  for EXV 2 was set as 0.6 and the  $C_d$  for EXV 3 and EXV 4 for was set to 0.5 because they are the same valve model.

The constant  $C_d$  values were chosen based on calculations with experimental data and, in the case of EXV 2, a value that resulted in more accurate system behavior within Dymola due to challenges in experimental valve characterization that are discussed further in Chapter 6.

$$C_{d,1} = 1.77 - 0.63V_{\text{EXV}_1} + 0.07V_{\text{EXV}_1}^2 \quad (4.16)$$

The refrigerant line lengths were measured by hand and have a consistent nominal diameter of 9.53 mm. Corresponding lines were placed within the Dymola model and both conductive heat transfer and pressure drop correlations were applied, similar to simplified versions of the heat exchangers. Convection to the environment was not included due to the significant computational time necessary for consideration of this phenomenon given the ambient environment heat port connection required. Additionally, the test stand was insulated with the intention of minimizing heat transfer to and from the environment. Conduction within the tubing was considered, and the same pressure drop and heat transfer correlations used in the MCHX were applied in the tubes, with Gungor and Winterton [141] being used for evaporation due to its applicability of characterizing evaporation in circular flow paths. The flash tank in the cycle was simply modeled as a volume, with the eventual possibility of implementing separation efficiency curves. A volume of  $0.5 \text{ m}^3$  was used for the flash tank based on the dimensions of the physical flash tank installed in the test stand.

The final physical component utilized were the junctions. Instead of simply mating a line that joins an existing line at a tee, the TIL library requires an internal volume of the junction as well as initial estimates of relative flow rates of the mixture components and an estimated specific enthalpy after mixing.

## 4.5 Model Application for Controls Development

A primary motivation for the development of a high-fidelity system model for the system that is dynamic in nature as opposed to static is the desire to understand

system responses and develop a control strategy accordingly. Namely, the control schemes assessed will focus on two primary goals:

1. Reliable and safe system operation.
2. Operation without sacrificing unnecessary cooling capacity.

The safe and reliable operation of this system is defined as operation while maintaining safe suction superheat, greater than 3 K with a target of 10 K, to all three stages of compression. With that being said, the suction port of the third stage of compression was placed after an IC and was at much higher pressures. Given the shape of the vapor dome for CO<sub>2</sub>, the third stage compressor port is very unlikely to experience two-phase, even if the suction port to the second stage compressor was subjected to two-phase flow.

Given the complex nature of the cycle, anticipated responses from the modulation of an EXV are not nearly as predictable or straightforward as in a four component vapor compression cycle. In addition, the modulation of one EXV could have one result, then if that same modulation were to occur at the same time as modulation of another EXV in the system, the effects could be entirely different. As such, the focus of the controls considerations is utilize the dynamic nature of the test stand cycle dynamic model to quantify, and ultimately anticipate, the relative rates of the effects of valve modulation. Furthermore, the observations drawn from experimental testing of the system provide insights for control scheme development. In order to display the ability of the dynamic model to meet these goals, two test scenarios are implemented following steady state and transient validation of the model with experimental data. The purpose of the order of these steps is to prove the accuracy of the model, then show how it could be used.

The first simulated scenario is evaporator pull down. Evaporator pull down is when the set point for an evaporator is reduced and the vapor compression cycle needs to react to be able to accommodate the change in desired source temperature. In the case presented herein, both the MT and LT evaporator are initially operating

with source temperatures of  $3.3\text{ }^{\circ}\text{C}$ , meaning that both are operating at refrigeration conditions. When the transient simulation begins, the source temperature for the LT evaporator is decreased by  $24.3\text{ }^{\circ}\text{C}$  down to a source temperature of  $-21\text{ }^{\circ}\text{C}$  over the course of 180 seconds to simulate a transition to freezing operation. For the second scenario, an evaporator disturbance is simulated. An evaporator disturbance could take the form of the door to the freezer compartment being opened widely in a high ambient climate. The door would then be shut, and the freezing compartment would slowly return to its original set point. The evaporator disturbance scenario was simulated through an increase in the LT evaporator source temperature of  $15\text{ }^{\circ}\text{C}$  over 30 seconds, followed by a return to the original set point of  $-21\text{ }^{\circ}\text{C}$  over 360 seconds. These variations were simulated through the use of ramps within the dynamic simulation, shown structurally in Figure 4.15(a) and in application in Figure 4.15(b).

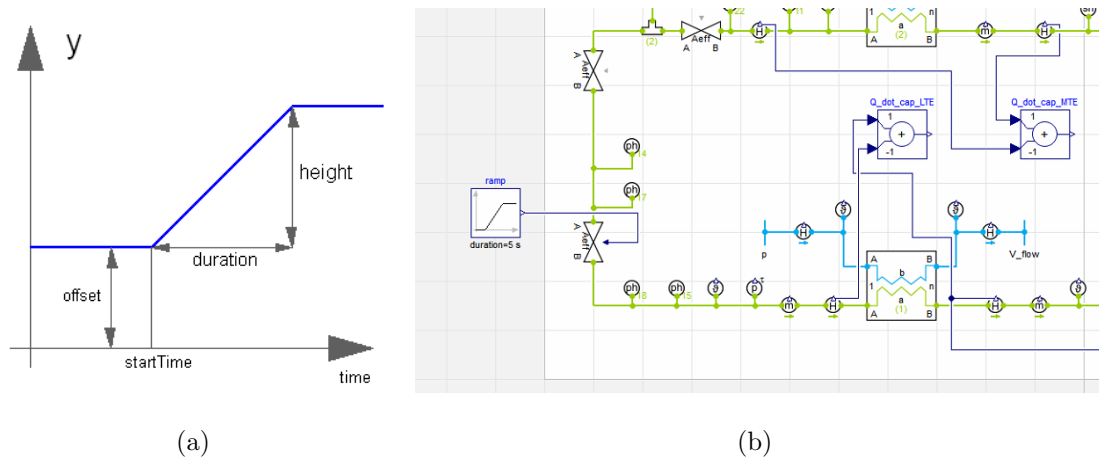


Fig. 4.15. Visualization of the: (a) Ramp structure in the Dymola environment [127]; and, (b) Ramp connected to an EXV in the Dymola environment [127].

All other sink and source temperatures were held constant, and only the two EXVs directly upstream of each evaporator were actuated. The control of the two EXVs took the form of a PI controller that was given a set point for compressor suction

superheat values of 10 K. Upper and lower bounds for the flow areas were input to the controller to provide a reasonable range of operation, and both the proportional gain and time constant were iterated on over the course of the simulation development. The gas cooler outlet EXV was not varied in these tests due to the desire to isolate the impact of the transient scenarios on the coupled dynamics of the evaporators, and also because gas cooler pressure optimization in simulations has been heavily investigated by researchers.

#### 4.6 Dynamic Modeling Conclusions

This chapter presented the development of a dynamic model of the experimental test stand described in Chapter 2. The overall structure of the numerical environment, boundary conditions, and solution schemes were discussed. Fluid types and how their respective cells contribute to the numerical solution scheme were presented, as were the details of the integration of several sub-components. In particular, heat exchanger geometry and correlations, valve effective flow areas, and compressor characterization were explained. Two scenarios to assess the ability of the dynamic model to develop control schemes were proposed. Future work for this model is increased accuracy of compressor and valve characterization sub-models. In particular, the exponents for the first two compressor stage correlations should be updated to correct for the lower evaporation temperatures where the first two compressor stages are operated, and additional experimental data with pressure transducers immediately upstream and downstream of the EXVs should be conducted for more accurate valve characterization. Finally, the communication between the visual interface and the EXV controller should be refined to ensure that every voltage change requested by the user results in a shift in the EXV stepper motor, which failed to occur approximately 5% of the time depending on the change in voltage input.

## 5. EXPERIMENTAL TESTING

This chapter will discuss the experimental testing aspect of the work presented in this thesis. In particular, the instrumentation measurement selection and justification provided in Chapter 2 will be elaborated upon, followed by a description of the experimental setup as well as the uncertainty of measurement devices. The test matrix is outlined, and experimental results from both EXV and ejector operating modes are presented and compared.

### 5.1 Experimental Testing Introduction

A significant number of cycle modifications have been proposed to increase the COP of transcritical CO<sub>2</sub> cycles, and, within the topic of cycle modifications, expansion work recovery has proven to have significant potential. The same increased pressure differential the compressor must provide for the cycle to achieve adequate heat rejection during transcritical operation makes expansion work recovery a promising modification that has garnered significant attention by researchers. One of the most widely-used methods of expansion work recovery is an ejector, which was first introduced via a patent by Gay [38]. The past decades have brought about a large amount of research on ejectors devices, both numerically and experimentally [39–41,44]. However, the primary purpose of an expansion device in a vapor compression cycle is to control the cycle over the range of operating conditions associated with its proposed application. As such, active control of the ejector has become a research focus. A variable diameter motive nozzle applied in an ejector was investigated by Elbel and Hrnjak [42], resulting in COP and cooling capacity improvements of 7% and 8%, respectively, as well as proving the device control could be used to vary the gas cooling pressure of the cycle to achieve a maximum COP. Another strategy for ejector control

is the multi-ejector, introduced by Hafner et al. [46] and experimentally-investigated by Haida et al. [47]. In the latter work, COP and exergetic efficiency benefits of 7% and 13.7%, respectively, were obtained and cycle stability was validated through variation of both ambient temperature and flash tank pressure. The multi-ejector concept operates by placing several fixed geometry ejectors in parallel and utilizing valves upstream of the ejectors to modulate flow depending on the desired capacity and operating condition. Zhu and Elbel [142] found that introducing a tangential flow upstream of a converging-diverging nozzle to impart a swirl could be an effective method to control nozzle performance. The researchers successfully varied the mass flow rate necessary to achieve choked flow by 42% at the same operating conditions. The associated implications of the swirl on nozzle performance are discussed in-depth, and this work proves that a fixed geometry nozzle performance can be actively controlled through imparting a swirl through tangential flow.

Multi-evaporator cycles are commonly applied in both supermarket and transport refrigeration due to the need to maintain cooling compartments at different temperatures while using a central vapor compression cycle. Additionally, many cycle modifications are applied in supermarket refrigeration cycles due to the large physical footprints and energy consumption of the installations. The cycle architectures applied in transcritical CO<sub>2</sub> supermarket applications vary in complexity in order to achieve a performance benefit over the HFC cycles they seek to replace depending on the proposed ambient conditions [65]. On the complex end of the cycle architecture spectrum, Minetto et al. [79] experimentally investigated parallel compression, ejector expansion work recovery, and flooded evaporation in a multi-evaporator architecture, reducing compressor power consumption by 13% at an ambient temperature of 16 °C. Gullo and Hafner [73] assessed several existing supermarket systems and found that first generation booster technology could achieve higher COP values than a direct expansion R-404A system at ambient temperatures up to 14 °C. In contrast, the maximum temperature where the efficiency of an R-404A supermarket refrigeration system is lower than that of a CO<sub>2</sub> system increased to 27 °C with more

advanced parallel compression system designs. A summary of the state-of-the-art of supermarket refrigeration cycles can be found in Gullo et al. [63], which provides numerous examples of multi-evaporator architectures, expansion work recovery, and phase separation. Lawrence et al. [98] numerically assessed the performance of a multi-temperature refrigerated transportation container system using a transcritical CO<sub>2</sub> with an ejector and internal heat exchanger, resulting in a COP of 0.96 at an extreme ambient temperature of 57 °C. Barta et al. [34] also investigated a multi-temperature refrigeration container system numerically, applying an expander and a flash tank upstream of the MT evaporator, achieving a COP of 1.28 at an ambient temperature of 57.2 °C. These papers numerically displayed the ability of complex cycles to be applied to multi-evaporator transportation container refrigeration systems in an effort to achieve COP values equal to or over unity, motivating further experimental investigation.

This chapter presents a comprehensive experimental comparison of modifications to a multi-stage two-evaporator transcritical CO<sub>2</sub> refrigeration cycle. The multi-stage and open-economization combination with an ejector was inspired by Ladd [107–110] with the intention of validating a particular multi-stage flashing refrigeration cycle as well as use of a pump to increase the performance of the ejector and the cycle. Among the cycle comparisons are two methods for ejector control. The first control method is a variable motive nozzle and the second is the addition of a variable speed pump located at the gas cooler outlet to vary the ejector motive nozzle inlet pressure. The results of a comprehensive comparison parametric study are presented, as is an assessment of the effectiveness of both proposed control methods. Lessons learned and next steps are presented following the discussion of results.



## 5.2 System Overview

This section outlines the experimentally-assessed cycles, the associated test matrix, and metrics of performance quantification applied during post-processing of the experimental data.

### 5.2.1 Overall Design

The experimental test stand utilized in this work is comprised of two evaporation temperatures, three stages of compression, intercooling between the second and third compression stages, a flash tank at the MT evaporator inlet, and either an EXV or an ejector for expansion. An ejector harnesses expansion work by accelerating the high-pressure flow from the gas cooler outlet via a motive nozzle into a motive flow which entrains low-pressure flow from the evaporator outlet through a suction nozzle. The two flows then mix and diffuse at a pressure higher than the evaporation pressure, thus reducing the amount of pressure lift required of the compressor. Open economization is conducted with a flash tank, which is a large vessel that two-phase flow enters and flashes into separate phases as a result of the sudden increase in volume. Gravity then further separates the phases such that the saturated vapor flows out the top of the tank to bypass the evaporator while the saturated liquid exits the bottom of the tank to enter the evaporator at a lower specific enthalpy than the evaporator inlet would receive without phase separation. This application of phase separation can result in an increased cooling capacity if the impact of the larger change in specific enthalpy across the evaporator outweighs the adverse impact of the reduction of the mass flow rate passed through the evaporator as a result of the vapor bypass.

In the test stand utilized herein, the flow from the outlet of the gas cooler can be directed through an EXV, directly to the ejector motive nozzle inlet, or through a pump before entering the motive nozzle inlet. In the latter two scenarios, the flow from the MT evaporator is routed to the suction nozzle of the ejector instead of to the second stage compressor suction. The ambient conditions are controlled with the

psychrometric chamber where the test stand is located, and both evaporators are controlled by independent EG baths. The MT EG-side evaporator inlet temperature target was approximately 3 °C to simulate refrigeration applications, and the LT EG-side evaporator inlet temperature target was approximately -21 °C to simulate freezer applications. Ambient relative humidity was set at 30% in order to minimize frost formation on the ejector. A P&ID of the test stand is shown in Figure 2.6 and a detailed overview of the test stand design is provided in Chapter 2.

### 5.2.2 Analyzed Cycles

Four cycle architectures were assessed over a range of operating conditions. The first cycle was treated as the baseline and consists of isenthalpic expansion through an EXV with no flash tank phase separation. Next, a flash tank was applied upstream of the MT evaporator to facilitate open economization. The saturated liquid exits the bottom of the flash tank where it is throttled slightly through an EXV before entering the MT evaporator, while the saturated vapor bypasses the evaporator through a metering valve and mixes with the flow from the MT evaporator outlet and first stage compressor discharge before entering the second stage compressor suction port. The third cycle utilizes an ejector with motive flow from the gas cooler outlet and suction flow from the MT evaporator outlet. The ejector diffuser outlet flow then enters the flash tank where the saturated vapor exits through the top of the flash tank to mix with the first stage compressor discharge flow before entering the second stage compressor suction port. The saturated liquid flow exits the bottom of the flash tank to enter the EXV upstream of the MT evaporator. Finally, a pump was added between the gas cooler outlet and the motive nozzle inlet in order to achieve two goals. The first goal was to modulate the motive nozzle input state to provide control of the ejector efficiency, pressure lift, and entrainment ratio. The second goal was to increase the cycle efficiency by providing additional pressure differential across the motive nozzle, and thus additional potential work for expansion work recovery. The

idea behind applying a pump was that it requires less work to increase the pressure of a liquid than a gas, due to the smaller change in specific volume for a given pressure rise associated with less-compressible fluid states. Therefore, the work required by the pump would result in an increase in ejector pressure lift, thus decreasing the work input required by the compression process. The ejector utilized in this work was developed and tested in Liu et al. [44], and the motive nozzle diameter was varied manually during testing through rotation of a threaded needle with a wrench to move the needle in and out of the motive nozzle throat, thus varying the effective motive nozzle diameter.

Steady state results were collected for each of the proposed test stand architectures over a range of ambient conditions. For each ambient condition and architecture, the gas cooler pressure was varied in order to find the pressure that resulted in the maximum COP. The test matrix is provided in Table 5.1.

Table 5.1.  
Overview of the tests conducted with the CO<sub>2</sub> test stand.

Test	Description	Ambient Temperature (°C)
1	EXV, No Economization	14
2		19
3		24
4		28
5	EXV, MT Economization	14
6		19
7		24
8		28
9	Ejector, MT Economization	14
10		19
11		24
12		28
13	Ejector, MT Economization, Pump	14
14		19

Additional details on measurement devices and associated uncertainties is provided in Table 2.7 in Chapter 2. For the results presented herein, the COP calculation is an updated version of the calculation provided in 2.11 that includes the pump power consumption, shown in Equation 5.1.

$$COP = \frac{\dot{Q}_{\text{cool,MT}} + \dot{Q}_{\text{cool,LT}}}{\dot{W}_{\text{comp,HP}} + \dot{W}_{\text{comp,LP}} + \dot{W}_{\text{pump}} + \dot{W}_{\text{fans}}} \quad (5.1)$$

Ejector entrainment ratio,  $w$ , and ejector efficiency,  $\eta_{\text{ejector}}$ , are two common methods of ejector performance quantification, shown in Equations 5.2 and 5.3, respec-

tively. Both equations are the same as those used in Chapter 3, but are also repeated here for convenience.

$$w = \frac{\dot{m}_{\text{suction}}}{\dot{m}_{\text{motive}}} \quad (5.2)$$

where *suction* refers to the flow traveling through the evaporator into the suction nozzle and *motive* refers to the flow that travels through the second and third compression stages as well as the gas cooler before entering the motive nozzle of the ejector.

$$\eta_{\text{ej}} = w \frac{h(P_d, s_{\text{si}}) - h_{\text{si}}}{h_{\text{mi}} - h(P_d, s_{\text{mi}})} \quad (5.3)$$

where  $h$  is specific enthalpy,  $P$  is pressure,  $s$  is specific entropy, *si* denotes the suction nozzle inlet, *mi* denotes the motive nozzle inlet, and *d* denotes the ejector diffuser outlet. The pressure lift achieved by the ejector is defined as the difference in pressure between the ejector diffuser outlet and the MT evaporator outlet.

### 5.3 Parametric Comparison Between Architectures

The results of this study are comprised of 58 steady state data points consisting of between five and ten minutes of steady measurement for each point. Statistics of parameters concerning the consistency and comparability of the tests are provided in Table 5.2. A target compressor suction superheat of approximately 13.5 °C was chosen to increase the chance of measureable superheat being present at the evaporator outlets. This was prioritized because of cycle instabilities that resulted when the evaporator outlet state transitioned from superheated vapor to a high-quality two-phase flow. The instabilities were exacerbated by the lack of a mixing chamber at both compressor suction ports and occurred when a lower compressor suction superheat was targeted. Charge was held constant at a value of 7.9 kg for all tests utilizing the flash tank. The baseline cycle architecture did not have the flexibility of the flash tank acting as charge storage to allow adequate compressor suction superheat and

condenser outlet sub-cool for sub-critical operation over varying ambient conditions. Therefore, the charge for the baseline tests varied between 4.6 kg and 5.1 kg for different ambient conditions to maximize the range of operating conditions that could be achieved. Error bars are included in all plots, but horizontal error bars with the gas cooling pressure were excluded because their value of  $\pm 26.9$  kPa is small relative to the pressure values measured and the bars made the plots less clear. Any sub-critical data points had measured sub-cool of at least 1.8 K, and all but two points had sub-cool greater than 4 K. The overall system energy balance was within 6% for all tests, and the EG-side heat transfer rates were taken as the cooling capacity values for both evaporators due to the discovery that two of the three Coriolis mass flow meters in the refrigerant line were not reliable because of their placement at the outlet of both evaporators. Placement at the evaporator outlets subjected the Coriolis flow meters to oil and occasional two-phase flow conditions, rendering their measurement less reliable. The third mass flow meter at the gas cooler outlet was reliable due to a consistent single-phase state. For the conditions that only required one of the two unreliable Coriolis flow meters to complete the cycle analysis, the LT evaporator EG heat transfer rate was taken as an input into the post-processing script and the resulting EG and refrigerant-side heat transfer rates in the MT evaporator were found to agree within 10% for all points presented. P-h diagrams of each cycle are provided in Figure 5.1, Figure 5.2, Figure 5.3, and Figure 5.4. The P-h diagrams represent the gas cooling pressure which achieved the highest COP for each ambient condition tested.

Table 5.2.

Statistical parameters regarding the consistency of test conditions for the reported experimental results.

Parameter	Average Value	Standard Deviation
(-)	(°C)	(°C)
LT Evaporator EG Inlet Temperature	-20.7	0.4
MT Evaporator EG Inlet Temperature	2.6	0.7
First Stage Compressor Suction Superheat	14.4	1.4
Second Stage Compressor Suction Superheat	13.1	1.5

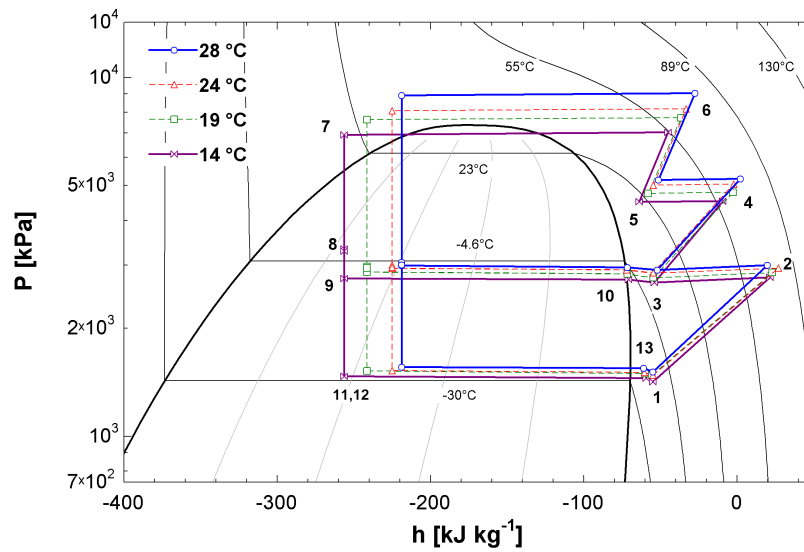


Fig. 5.1. P-h diagram of experimental test stand data from the baseline cycle at four ambient temperatures.

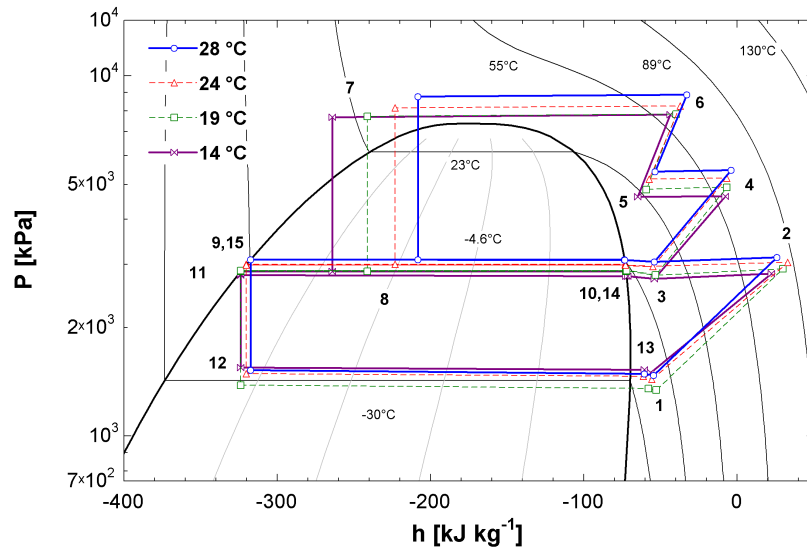


Fig. 5.2. P-h diagram of experimental test stand data from the MT economization cycle at four ambient temperatures.

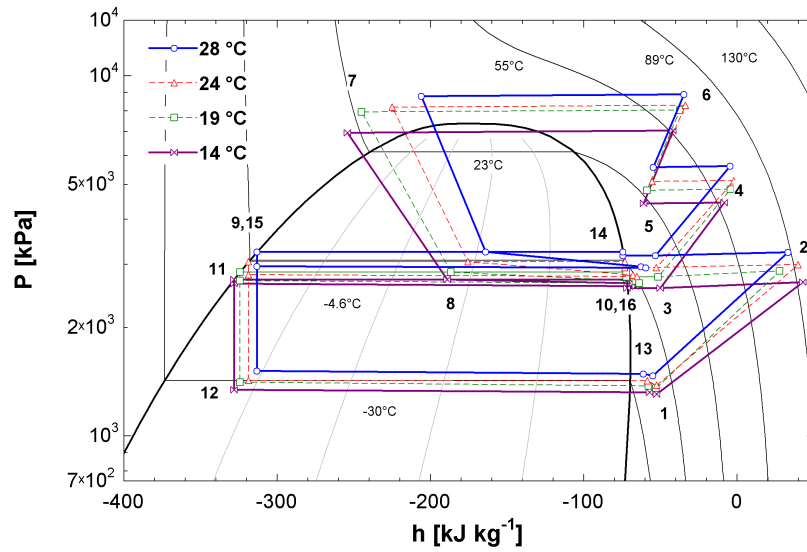


Fig. 5.3. P-h diagram of experimental test stand data from the ejector cycle at four ambient temperatures.



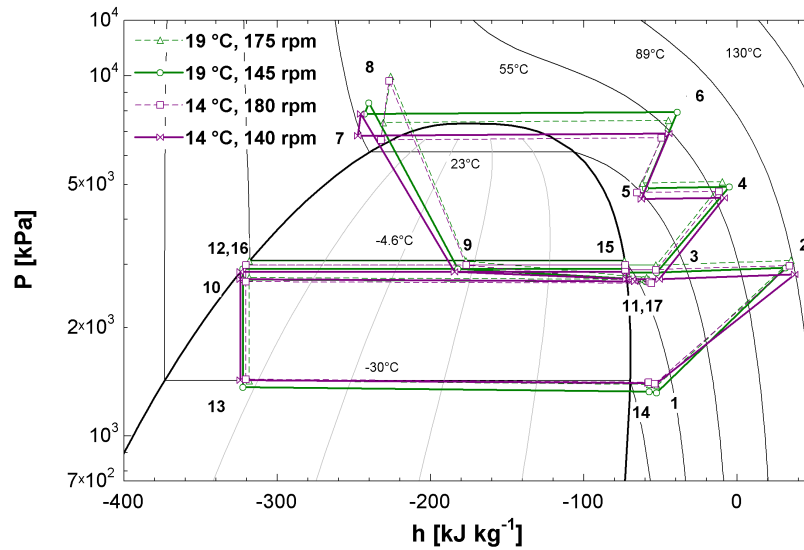


Fig. 5.4. P-h diagram of experimental test stand data from the ejector and pump cycle at four ambient temperatures.

The ejector was originally sized for a 15 kW AC system, and was therefore oversized for the test stand at refrigeration conditions, which had an approximate total capacity of 8 kW. The motive nozzle was still able to be modulated to provide adequate control of the gas cooling pressure. The suction nozzle diameter was set to approximately 6.4 mm and the motive nozzle diameter ranged from 0.3 mm to 0.8 mm for the tests presented herein. The suction nozzle diameter was set near the minimum value of the ejector to allow for a small diameter while leaving additional room for modulation if ejector efficiencies were found to be unreasonably low. The lower bound of the motive nozzle diameter was dictated by ejector design while the maximum motive nozzle diameter was limited by a diameter that would keep the motive nozzle inlet state in a single-phase state. The pump design maximum inlet temperature is 25 °C. Therefore, it was only applied at the 14 °C and 19 °C ambient conditions. The maximum speed the pump was operated at was limited to a speed that would keep the pump discharge pressure below the maximum design discharge pressure of 100 bar. The two stage compressor that performed the second and third

stages of compression proved to be another limiting factor in test stand operation due to being undersized, resulting in the inability to reach a gas cooling pressure corresponding to a maximum COP at the 28 °C condition because of the motor current draw limit.

The high-side EXV was modulated to vary across a range of gas cooling pressures in search of the maximum COP for each cycle and condition that did not employ the ejector, bounded by the aforementioned experimental limitations. Pressures corresponding to the maximum COP were identified at all ambient conditions except the 28 °C condition, and for all cycles except the cycle with the pump. In the case of the pump cycle, the COP decreased with increasing pump speed for all points tested. The lowest COP corresponded to the highest pump speed. The ejector motive nozzle was at the minimum motive diameter for both conditions where the pump was applied in order to minimize the chance of cavitation in the pump suction chamber due to the suction state entering the vapor dome. The resulting COP values with gas cooling pressure variation for all four ambient conditions are shown in Figure 5.5, Figure 5.6, and Figure 5.7 for the baseline, MT economization, and ejector cycles, respectively.

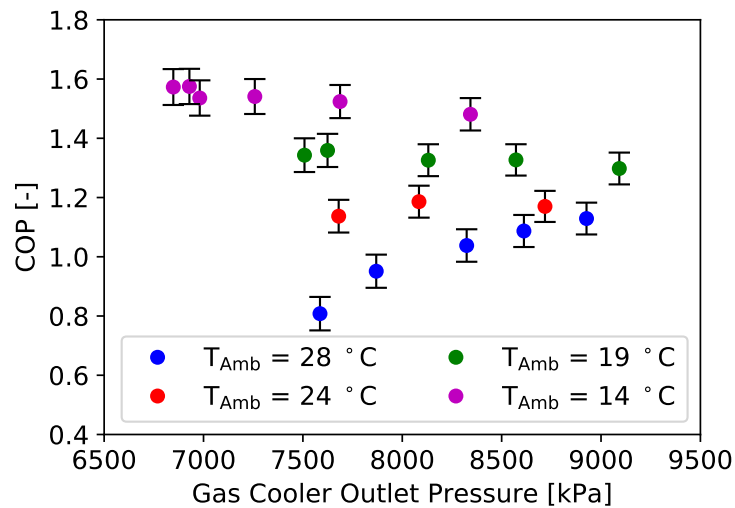


Fig. 5.5. Baseline cycle COP with gas cooling pressure variation at four ambient temperatures.

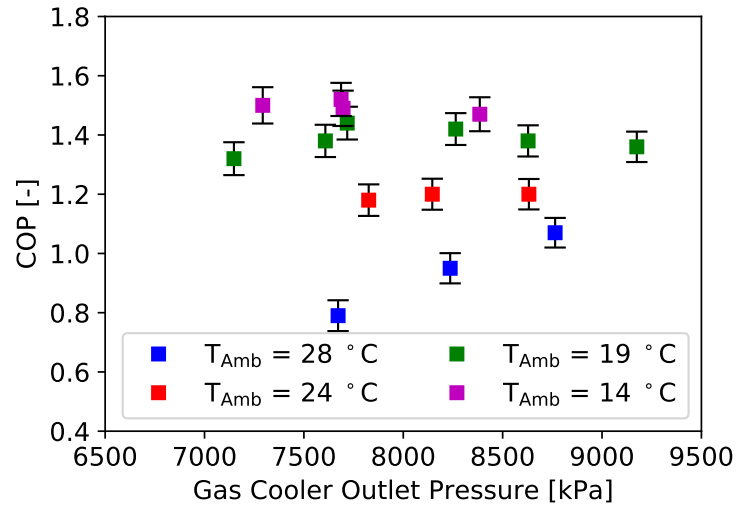


Fig. 5.6. MT economization cycle COP with gas cooling pressure variation at four ambient temperatures.

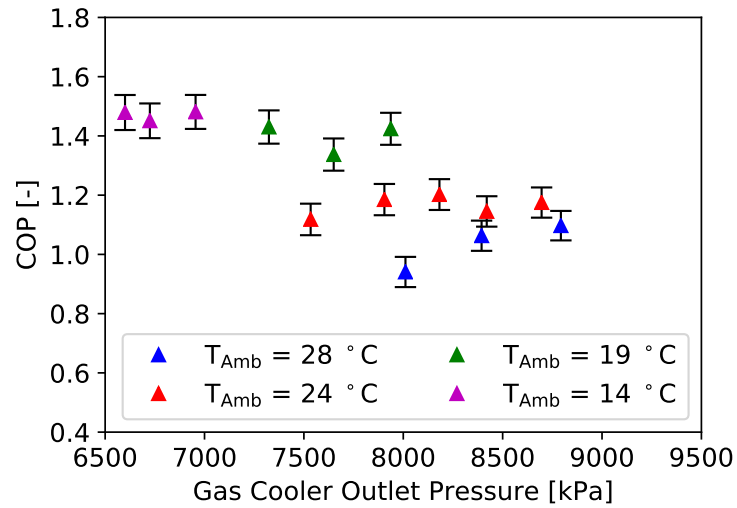


Fig. 5.7. Ejector cycle COP with gas cooling pressure variation at four ambient temperatures.

The COP trends followed the expected result of attaining a maximum value for a given ambient condition at a higher pressure with increasing ambient temperature.

The maximum COP values for each cycle at each ambient temperature tested are plotted at the corresponding gas cooler outlet pressure in Figure 5.8 for an overall comparison. The two pump points are plotted showing the highest speed tested. For comparison, the nozzle position where the pump is utilized corresponds to the highest gas cooling pressure shown in Figure 5.7 for a given ambient condition. Therefore, as the pump speed increases the COP ranges from the ejector-only COP at the same ambient condition to the value shown in 5.8. A summary of COP, gas cooler outlet pressure, cooling capacities, and power consumption for all points shown in Figure 5.8 is provided in Table 5.3.

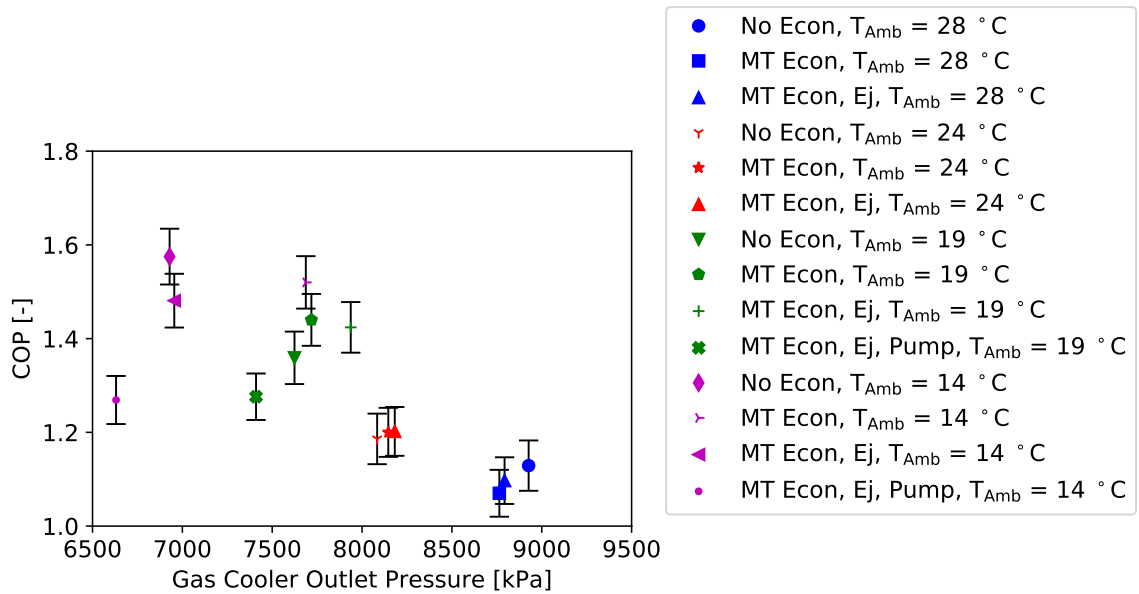


Fig. 5.8. Summary of maximum COP values at the corresponding gas cooler outlet pressures over a range of ambient temperatures for all cycles tested.

Table 5.3.

Summary of the obtained data at maximum COP gas cooler outlet pressures over a range of ambient temperatures for all reported steady state tests.

$T_{\text{Amb}}$ (°C)	Architecture (-)	$P_{\text{GC,out}}$ (kPa)	COP (-)	$\dot{Q}_{\text{cool,LT}}$ (kW)	$\dot{Q}_{\text{cool,MT}}$ (kW)	$\dot{W}_{\text{comp,LP}}$ (kW)	$\dot{W}_{\text{comp,HP}}$ (kW)
28	Baseline	8927±26.9	1.13±0.05	1.81±0.22	5.22±0.25	1.07±0.032	4.08±0.032
	MT Econ.	8764±26.9	1.07±0.05	2.60±0.20	4.06±0.23	1.10±0.032	4.07±0.032
	Ejector	8793±26.9	1.10±0.05	2.14±0.20	4.73±0.23	1.12±0.032	4.08±0.032
24	Baseline	8084±26.9	1.19±0.06	1.78±0.21	5.40±0.24	1.16±0.032	3.82±0.032
	MT Econ.	8146±26.9	1.20±0.05	2.48±0.21	4.90±0.24	1.20±0.032	3.86±0.032
	Ejector	8182±26.9	1.20±0.05	2.20±0.21	5.23±0.23	1.26±0.032	3.85±0.032
19	Baseline	7624±26.9	1.36±0.06	1.94±0.21	5.92±0.24	1.06±0.032	3.65±0.032
	MT Econ.	7718±26.9	1.44±0.06	2.65±0.20	5.81±0.24	1.08±0.032	3.71±0.032
	Ejector	7937±26.9	1.42±0.05	2.39±0.20	6.14±0.24	1.14±0.032	3.77±0.032
	Ejector & Pump	7410±26.9	1.28±0.05	2.40±0.20	5.91±0.24	1.17±0.032	3.59±0.032
14	Baseline	6929±26.9	1.58±0.06	2.18±0.21	6.64±0.24	1.03±0.032	3.47±0.032
	MT Econ.	7687±26.9	1.52±0.06	2.06±0.20	6.82±0.25	1.03±0.032	3.69±0.032
	Ejector	6955±26.9	1.48±0.06	2.06±0.20	6.37±0.25	1.10±0.032	3.50±0.032
	Ejector & Pump	6631±26.9	1.27±0.05	2.47±0.20	5.52±0.24	1.14±0.032	3.32±0.032

Cooling capacities for all steady state tests for the baseline, MT evaporator, ejector, as well as the ejector and pump cycles are shown in Figures 5.9(a), 5.9(b), 5.9(c), and 5.9(d), respectively. The general trends show a decreased capacity with increasing ambient temperature, as well as an increased capacity with increasing gas cooling pressure for all cycles except the ejector and pump cycle. The capacity decreases with ambient temperature due to the curvature of the isotherms near the critical point such that, even at a gas cooling pressure that results in the highest COP for a given condition, the specific enthalpy at the expansion inlet will increase, resulting

in an increased expansion outlet quality. The same isotherm curvature surrounding the critical point is also the reason the cooling capacity increases with gas cooling pressure. For a given ambient temperature, a higher gas cooling pressure will move the expansion inlet state up and left along the isotherm, thus resulting in a decreased expansion outlet quality. As the gas cooling pressure increases and the expansion inlet state continues to climb up the isotherm, there is a point of diminishing returns such that the compressor power needed to achieve the gas cooling pressure increases more than the resulting increase in cooling capacity. This is why there is a gas cooling pressure that results in a maximum COP for transcritical CO<sub>2</sub> cycles, above which the COP decreases. Another important observation regarding cooling capacity variation over ranges of ambient conditions and gas cooling pressures is that the MT evaporator cooling capacity varies significantly more than the LT evaporator cooling capacity. This is due to the LT evaporator mass flow rate being approximately four times lower than that of the MT evaporator, such that the absolute change in cooling capacity with operating condition will be much smaller for the LT evaporator than for the MT evaporator. In the case of the ejector and pump cycle, the cooling capacity decreases directly with the pump outlet pressure, denoted as the motive nozzle inlet pressure in Figure 5.9(d). The decreased capacity with increasing pump discharge pressure can be justified by observing the direct relationship of ejector diffuser outlet quality with pump discharge pressure on the P-h diagram provided in Figure 5.4.

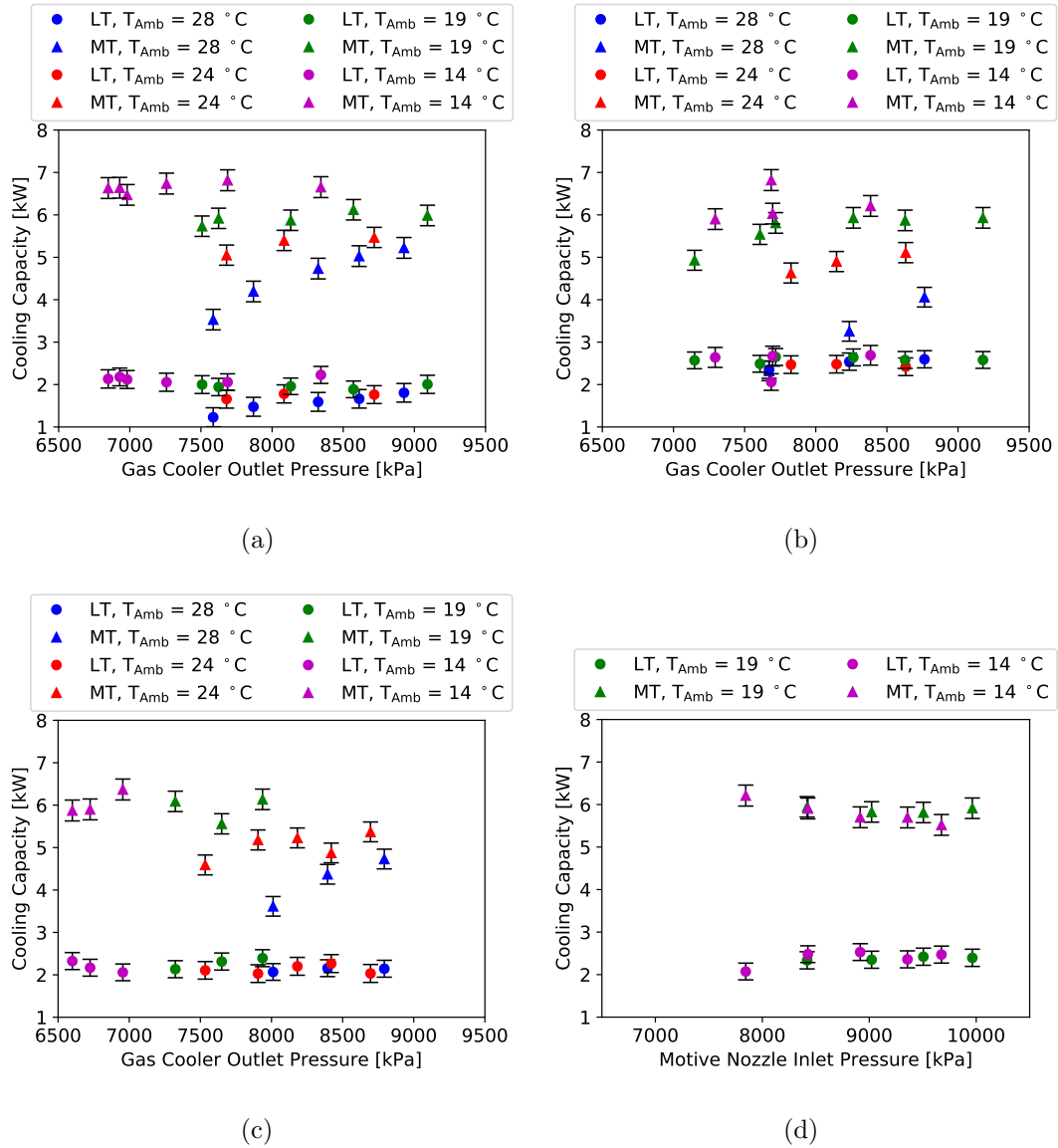


Fig. 5.9. Summary of cooling capacities over a range of ambient temperatures for all reported steady state tests for each cycle: (a) Baseline; (b) MT Economization; (c) Ejector; and, (d) Ejector and pump.

Maximum COP improvements of 6% and 5% over baseline were obtained with the MT economization and ejector cycles, respectively, at the  $19^{\circ}\text{C}$  ambient condition. Smaller COP improvements from the MT economization and ejector cycles were obtained at the  $24^{\circ}\text{C}$  condition. The P-h diagram in Figure 5.3 justifies why the

ejector COP benefit did not increase with ambient temperature at the 24 °C ambient condition by showing that the ejector motive nozzle inlet pressure did not increase significantly past the cycle shown at the 19 °C ambient condition. The small increase in gas cooling pressure at the 24 °C ambient condition suggests that there may have been a slightly higher pressure that would have optimized the cycle further, despite Figure 5.7 appearing to have achieved a maximum COP for the 24 °C ambient condition. Both the MT economization and ejector cycles resulted in lower maximum COP values at the 14 °C and 28 °C conditions. The lower COP at the 14 °C condition is largely due to the low evaporator inlet quality achieved with the baseline cycle due to the low condenser outlet temperature. In the case of low-ambient temperatures, the benefit of an increased change in specific enthalpy across the evaporator is less significant such that the detrimental effect of the reduced mass flow rate through the evaporator due to phase separation on the cooling capacity outweighed the benefit of the lower evaporator inlet quality. A similar explanation can be given for the decrease in COP of the cycle utilizing the ejector, as the reduction in mass flow rate through the evaporator was not outweighed by the decreased compressor input power required. Insufficient reduction in compressor input power is a result of the ejector being unable to increase the compressor suction pressure enough due to a smaller amount of available expansion work. Both the MT economization and ejector cycles would likely achieve higher maximum COP values than baseline, but the compressor was not able to reach a gas cooling pressure associated with a maximum COP for any of the cycles tested at the 28 °C condition.

#### 5.4 Ejector Control and Performance Assessment

Two methods of ejector control were assessed in this chapter. The first was a variable diameter motive nozzle and the second was a variable speed pump located between the gas cooler outlet and motive nozzle inlet. The motive nozzle diameter variation was used to search for the gas cooling pressure corresponding to the maxi-



imum COP in Figure 5.7, validating motive nozzle diameter modulation as an effective means of gas cooling pressure variation. Contrary to many expansion work recovery device control methods, the variation in motive nozzle diameter did not significantly impact the ejector efficiency, as shown by Figure 5.10. The slight variation in ejector efficiency in the middle of the 14 °C and 19 °C conditions and at the second-highest pressure at the 24 °C condition was due to increased MT evaporator outlet superheat. An MT evaporator outlet superheat of 5 °C was targeted during testing, but there was some variation on the order of 3 °C to 5 °C above and below the target superheat. The three peaks in ejector efficiency show that ejector efficiency will increase with superheat at the suction nozzle inlet, but the increased superheat at the suction nozzle inlet results in a decreased cycle COP because the evaporation temperature needs to be lower to accommodate heat transfer to the refrigerant from the secondary fluid. The trend of increased evaporator outlet superheat increasing ejector efficiency but decreasing cycle COP is consistent with the COP values reported in Figure 5.7, with the peaks in ejector efficiency corresponding to local minima of COP.

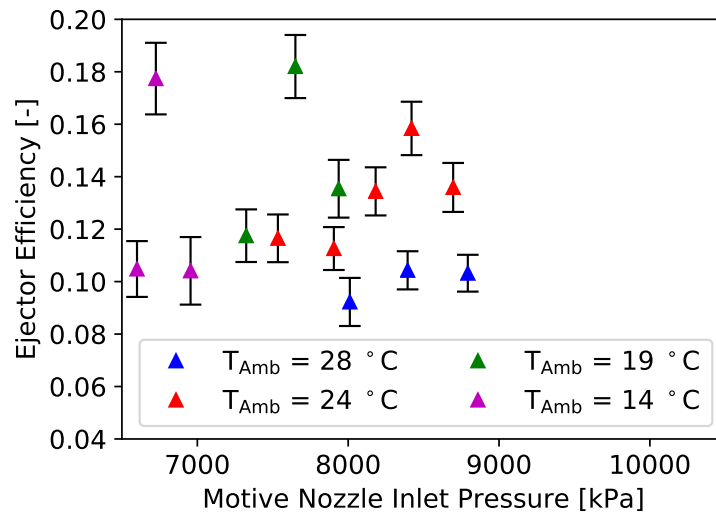


Fig. 5.10. Ejector efficiency variation with motive nozzle modulation at four ambient temperatures.

Due to the generally direct relationship of cooling capacity to COP, a higher ejector entrainment ratio often results in an increased COP because the numerator of the entrainment ratio calculation is the mass flow rate through the MT evaporator, shown in Equation 5.2. The ejector cycle cooling capacity variation shown in 5.9(c) confirms the direct relationship of entrainment ratio with cooling capacity. Measured entrainment ratios from ejector operation are shown in Figure 5.11 and follow the same trends observed with COP in Figure 5.7. The direct relation of ejector lift with gas cooling pressure for different ambient conditions is shown in Figure 5.12. While some trends associated with ejector pressure lift and gas cooling pressure can be related to other plots, the ejector pressure lift cannot be directly associated with trends observed in reported plots of ejector efficiency, entrainment ratio, or cycle COP. As noted in the description of the ejector efficiency trend, the ejector suction nozzle inlet superheat varied slightly over the conducted tests. For a constant evaporator outlet superheat, ejector pressure lift would be directly proportional to the pressure differential across the motive nozzle. Conversely, for a constant motive nozzle inlet state and pressure differential, an increased evaporator outlet superheat would lead to increased ejector pressure lift. However, when both suction nozzle superheat and the motive nozzle inlet condition vary, it is challenging to identify a single cause of the ejector pressure lift variation, thus both the evaporation condition and ejector motive inlet pressure are cited as causes of the ejector pressure lift behavior observed in Figure 5.12.

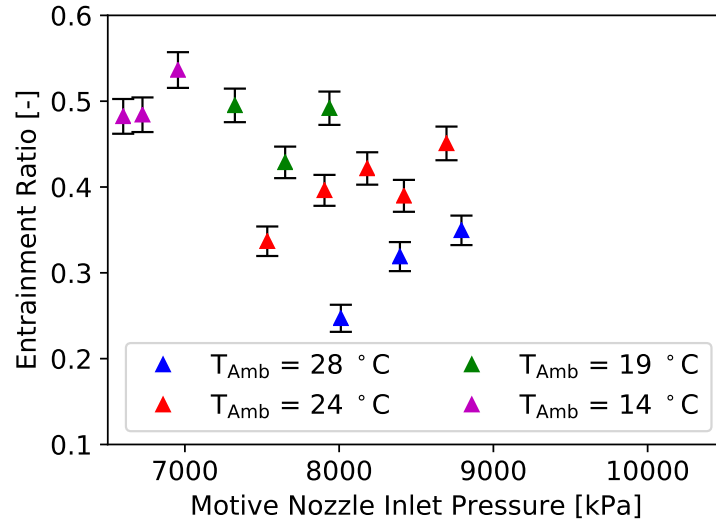


Fig. 5.11. Ejector entrainment ratio variation with motive nozzle modulation at four ambient temperatures.

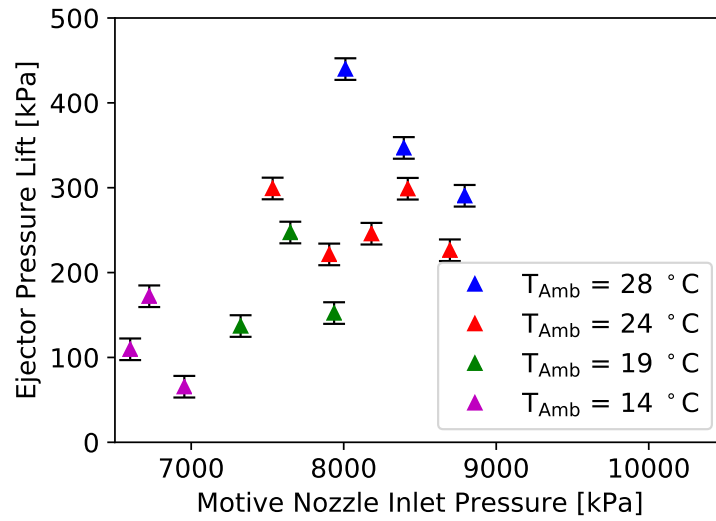


Fig. 5.12. Ejector pressure lift variation with motive nozzle modulation at four ambient temperatures.

Applying a pump to compress the sub-cooled liquid, where the temperature and pressure of the refrigerant are below their respective critical values, or supercritical

liquid, where the fluid pressure is above the critical pressure but the temperature is below the critical temperature, resulted in consistent trends and reliable operation. Ejector efficiency varied directly with pump speed and thus, pump outlet pressure, as shown in Figure 5.13. There appears to be a peak ejector efficiency at the 14 °C ambient condition, but the variation between this perceived local maximum and the points on either side of it is well within experimental uncertainty. Additionally, the significant sensitivity of ejector efficiency to operating condition variation further motivates the conclusion that a broader array of pump and ejector testing would be needed to confidently identify a maximum ejector efficiency corresponding to a particular pump outlet pressure. Despite the increased ejector efficiency, the entrainment ratio of the ejector decreased with increasing pump outlet pressure. The P-h diagram of the pump cycle shown in Figure 5.4 offers visual support for the trend of a decrease in entrainment ratio with increasing pump discharge pressure through an increase in the ejector diffuser outlet quality with increasing pump outlet pressure. While the relationship of diffuser outlet quality and ejector entrainment ratio is further complicated by the multi-evaporator architecture, the diffuser outlet quality does dictate the ratio of vapor mass flow rate that bypasses the evaporators and can therefore be used as an indicator for cooling capacity trends. Despite the increasing ejector outlet quality, the total system cooling capacity did not vary more than 0.4 kW over the range of all pump conditions tested. At the 14 °C ambient condition, the distribution of cooling capacity between evaporators shifted to the LT evaporator with increasing pump pressure. This resulted in an increase of the LT evaporator capacity by 19% while the MT evaporator capacity was reduced by 11%. However, the COP of the cycle decreased with use of the pump, as shown in Figure 5.8.

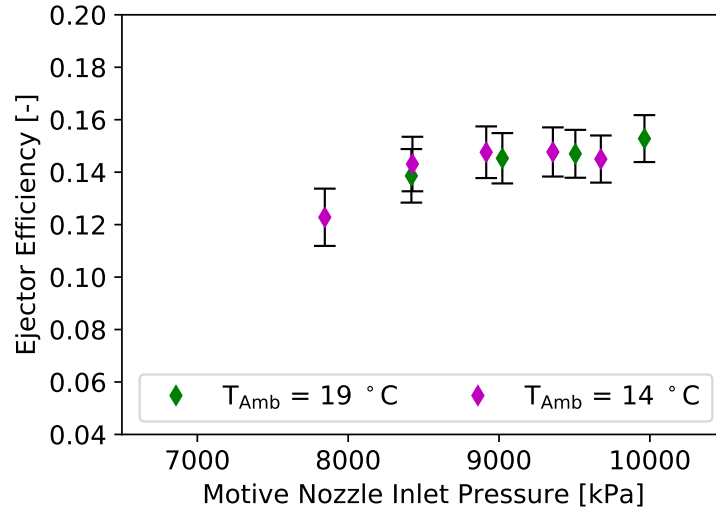


Fig. 5.13. Ejector efficiency variation with pump outlet pressure modulation at two ambient temperatures.

As discussed was discussed with respect to cooling capacity, the ejector entrainment ratio decreased with increasing pump discharge pressures, shown in Figure 5.14. The pump was therefore validated as a means to control ejector efficiency, pressure lift, and entrainment ratio. Despite the increased pressure lift achieved through the additional pressure differential across the motive nozzle applied by the pump, shown in Figure 5.15, the application of the pump did not decrease the compressor input power enough to offset the power required to operate the pump. Over the range of applied pump speeds, the pump suction pressure decreased slightly despite the motive nozzle diameter remaining constant over the course of the pump tests. To provide added context to the relationship between ejector and pump pressure lift, the pump inlet pressure decreased from 68 to 66 bar for the 14 °C ambient tests and from 78 bar to 74 bar for the 19 °C ambient condition as the pump speed increased. Therefore, while pump efficiency increased at lower ambient temperatures, the ratio of pump pressure differential to ejector pressure differential was significantly smaller at the 19 °C ambient condition. This was likely due to the inability of the ejector motive nozzle to increase the pump suction pressure further. However, the discrepancy in

pump suction pressure offers a notable perspective on pump performance that can be achieved through speed modulation when it is noted that the extra 5 rotations per minute applied to the pump speed at the 14 °C ambient test made up for the 8 bar difference in suction pressure to achieve a similar discharge pressure as the 19 °C ambient test.

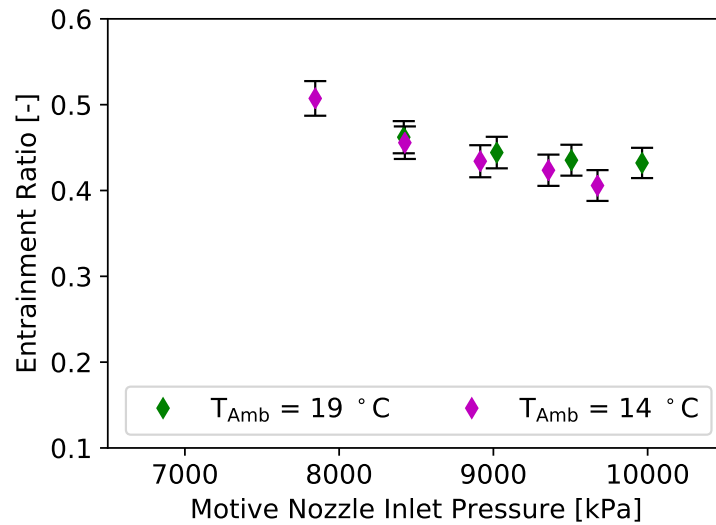


Fig. 5.14. Ejector entrainment ratio variation with pump outlet pressure modulation at two ambient temperatures.

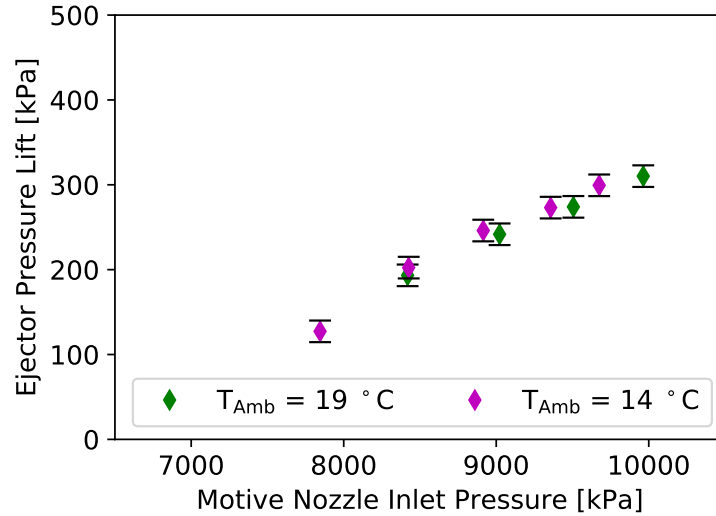


Fig. 5.15. Ejector pressure lift variation with pump outlet pressure modulation at two ambient temperatures.

The overall pump efficiency varied from 8% to 29% during the tests used reported in Figures 5.13, 5.14, and 5.15. The low pump efficiency was due to the maximum pump operating speed being approximately 40% of the design speed of the pump. The pump was intentionally oversized, but the data used in the initial calculation of the required pump volumetric flow rate was from this same test stand operating at higher evaporating conditions than tested herein. Increased pump efficiency would decrease the COP discrepancy between the cycle utilizing the ejector and the cycle utilizing the ejector and the pump, but preliminary numerical results analyzing the COP benefit of a higher pump efficiency showed that the ejector efficiency would also need to increase in order to approach the COP of the cycle without the pump.

When the design tool from Section 3 is applied to the experimental operating conditions achieved in the test stand using assumptions from Section 3.4.4, recommendations for ejector design improvements for application in this test stand can be made. Ejector operation with and without the pump resulted in slightly different designs, both of which were closer to each other than to the design of the ejector

that was applied in experimental testing. In particular, the mixing section diameter should be reduced from 4 mm to either 3.6 mm or 3.2 mm for ejector or ejector with pump operation at the maximum pump discharge pressure, respectively. If this change were to be made, the current variable diameter motive nozzle design could be retained, as the recommended motive throat diameter of approximately 1.2 mm falls within the range of achievable motive nozzle diameters with the existing variable geometry ejector. The differences in recommended motive nozzle diameters differed by less than 0.05 mm between the ejector and ejector with pump input states. The desired suction nozzle diameter would be very near that of the mixing section, on the order of between 3.5 and 4.0 mm, therefore the suction nozzle diameter would need to be decreased from the current design. Finally, the length of the diffuser in the current ejector would result in a decreased ratio of mixing section to diffuser outlet diameter ratios. This decreased ratio would result in an increased ejector efficiency without an increased length due to the decreased mixing section diameter. Given the observation of diminishing returns on ejector efficiency increase with a decreasing ratio of mixing section diameter to diffuser outlet diameter, if the current diffuser length of approximately 65 mm was retained with the updated mixing section diameter, the ejector efficiency would come within 0.2% of the efficiency obtained with a mixing section diameter to diffuser outlet diameter ratio of 0.1. Because 0.1 was set as the lower bound for the parametric analysis of the impact of the ratio of mixing section to diffuser outlet diameters shown in Figure 3.9(b), the ejector efficiency obtained at ratio value of 0.1 was accepted as the maximum for that particular parameter. Given the conservative component efficiencies assumed in Section 3, the design tool estimated that this design could increase ejector efficiency from the 10% to 18% observed in testing, with the majority of points falling between 10% and 16% efficiency, to between 19% to 21%, with further improvement possible with sub-component optimization.



## 5.5 System Behavior

This section is included in order to give an overview of system dynamics considerations, as well as to give context to the results observed during testing. General controls are overviewed to shed light on how steady state conditions were achieved, and insights into system transients are shared to provide background into the quantification of system dynamics presented in Chapter 6.

This section outlines the techniques used to control the test stand. Control of the physical CO<sub>2</sub> system will be discussed in-depth. However, it needs to be noted that stable operation of the test stand requires steady operation of not a single vapor compression cycle, but the stable operation of four vapor compression cycles. As the test stand is located in a psychrometric chamber, the room vapor compression and heater controls need to reach steady state within the room environment. Efforts to achieve steady conditions in the psychrometric chamber can be upset by the variation of loads produced by any of the other three cycles associated with the test stand and located within the chamber, but the chamber also has approximately five times the capacity of the other cycles in the experimental setup, so it can absorb thermal transients well. The two EG baths also have internal vapor compression cycles which need to stabilize, a processes that is assisted by the thermal buffer provided by the EG secondary loops between these two cycles and the CO<sub>2</sub> test stand. Once the three cycles in charge of fixing simulated heat source and heat sink conditions are stable, the CO<sub>2</sub> test stand can then pursue stability.

### 5.5.1 Cycle Control and Liquid Level Management

The first priority with system control must be maintaining safe system operation. Safe operation is primarily defined by pressures and superheat values. The test stand was designed with stainless steel and components intended for transcritical CO<sub>2</sub> on the high-side of the system so that the system can be safely operated at maximum pressures of over 100 bar. The flash tanks and liquid level sight glasses are rated for

HFC pressures, which is still more than adequate at normal evaporation conditions for the test stand. However, at operating points that require significant throttling of EXVs 2 through 4, the flash tank pressure can be pushed above safe levels, which needs to be considered during test stand operation. Compressor suction superheat is a concern at all times, and ideally remains above 5 K. While the evaporator outlet needs to be superheated in order to accurately calculate a refrigerant-side cooling capacity, validated EG-side capacities can provide an estimation of evaporator capacity as well.

Once the ambient conditions are steadied by the psychrometric chambers and both evaporator temperatures and loads are stabilized through the EG secondary loops, the test stand operation can then be manipulated. Referring to the simplified nomenclature of Figure 5.16, EXV 1 is used to control the high-side pressure of the system. The EXVs upstream of both evaporators, EXV 2 and EXV 4 for MT and LT, respectively, are used to control superheat at the outlet of their respective evaporators. MV 1 and MV 2 are used to initiate and manage phase separation in the MT and LT flash tanks, respectively.

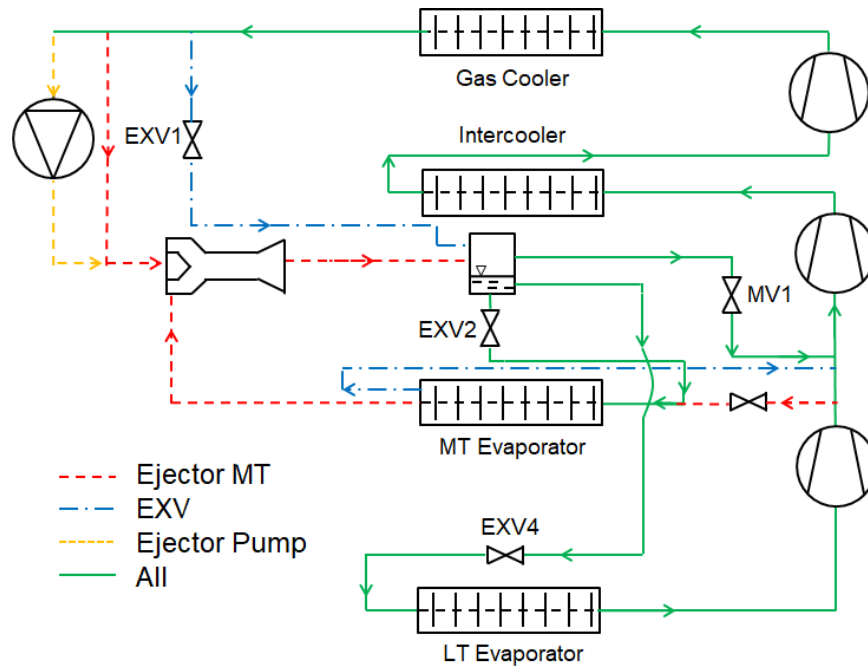


Fig. 5.16. CO<sub>2</sub> test stand schematic with valve labels.

Once initialized, the MV bypass is utilized in conjunction with the flash tank outlet EXV to maintain efficient system operation and a stable liquid level in the flash tank. A stable liquid level is maintained through balancing pressure drop across the MV and EXV, effectively manipulating flash tank outlet port which drives the outlet flow of a particular phase of fluid. The MV used for vapor bypass can be closed to throttle the refrigerant traveling through the vapor outlet more in an effort to increase the liquid level if the liquid level begins to decrease. The EXV can be used in the same way to achieve the opposite effect. Locally, the flash tank liquid level should be maintained in order to prevent liquid from being sent to the compressor suction or drying out the evaporator, which result from filling or emptying the flash tank of liquid, respectively. However, variation of flash tank liquid level should be viewed as adding or releasing charge from a system dynamics perspective. Therefore, decreasing the liquid level in the system increases the charge in the rest of the cycle components, which has a more significant impact on system performance. When a

system receives more charge, the general trend is that the pressures throughout the system increase, or from a visual perspective, the P-h diagram moves up and to the left. If the vapor compression cycle without the flash tank is considered to be the system, the trends in system behavior with increasing charge are due to the system having a fixed internal volume, and the draining of the flash tank effectively increases the amount of mass that the system contains. Therefore, the specific volume needs to decrease throughout the system to accommodate the changing mass in the system and satisfy conservation of mass. From an evaporator standpoint, increased charge results in lower evaporator outlet superheats and higher evaporation temperatures. On the high-side, the condenser outlet sub-cool increases if operating in sub-critical operation, and the gas cooling pressure increases in transcritical operation. The opposite occurs when increasing the liquid level in the flash tank. Understanding the liquid level effects is vital to controlling the system as well as achieving a target operating condition and compressor suction superheat.

A final comment must also be made regarding secondary effects of changes made during vapor compression cycle operation. In actuality, there are often ripple effects from a single valve actuation that can be seen throughout nearly every facet of the vapor compression cycle. The presence of additional effects of varying a cycle parameter is especially true with more complex cycles that have largely coupled dynamics between components. For example, while closing an EXV between a flash tank and an evaporator will decrease the evaporation temperature, it does so by decreasing the pressure at the valve outlet as well as the mass flow rate. Depending on the shape of the vapor dome for the working fluid being assessed, the rate of superheat increase facilitated by the decrease in mass flow rate can vary. Furthermore, closing an EXV upstream of an evaporator will increase the pressure of the flash tank upstream of the EXV. The same idea can be observed with the EXV at the gas cooler outlet, which is widely accepted to be an effective means of controlling the gas cooling pressure, and is a common strategy for optimization in transcritical CO<sub>2</sub> cycles. However, variations in the EXV opening will also vary mass flow rates downstream, thus changing evapo-

rator outlet superheats, and can also effect the amount of liquid entering a flash tank. The liquid level variation is more evident in sub-critical operation, where sub-cooled liquid at the outlet of the condenser can be passed at higher or lower rates into the flash tank.

When operating in ejector mode, gas cooler pressure control can be imparted through controlling the diameter of the motive nozzle via a threaded needle shown in Figure 3.14, and while this specific ejector was designed for a slightly larger system, control via modulation of the motive nozzle diameter method was still found to be possible, albeit with less fine tuning available relative to the high-side control resolution possible with EXVs. The scenarios discussed in this section are only a few examples of the extenuating effects of system dynamics that need to be considered upon analysis and consideration of the different time scales observed in thermal systems.

### 5.5.2 Pump Operation

The primary concern surrounding pump operation was preventing cavitation in the suction chamber. With the high pressure levels present in a CO<sub>2</sub> system, a significant amount of head is available. The more likely culprit of cavitation would be with the pump suction state entering the vapor dome, which was more likely than initially anticipated due to the undersized ejector motive nozzle and the unforeseen charge migration effects of engaging the pump. Pump engagement entailed calculation of the pump speed that would match the gas cooler outlet mass flow rate as closely as possible. The matching of these mass flow rates was achieved by using the the pump displacement volume and inlet specific volume to calculate the pump speed that would equal the system mass flow rate. The speed resulting from this calculation was used as the starting point to minimize system fluctuations. Once the initial speed was identified, two actions needed to occur simultaneously. First, the pump bypass, which took the form of a ball valve situated between the gas cooler outlet and motive

nozzle inlet, needed to be closed to prevent flow circulation to the pump suction port. Second, the pump needed to be started via entering the calculated speed and engaging the VFD. These two steps need to be taken nearly simultaneously. Once the startup sequence occurred, the system temporarily sent an increased amount of mass into the flash tank. While there are a number of nuances associated with the mass flow transients of the test stand, the initial increased flash tank level due to pump engagement had the effect of reducing the charge in the rest of the cycle momentarily, thus temporarily decreasing the pump inlet pressure. The mass was redistributed through the system within two to three minutes, but the decrease in pump suction pressure needed to be anticipated. This anticipation motivated a target margin of three to five bars of pressure between the pump suction port and the vapor dome before engagement.

Once the pump was running, the system remained very stable and operated reliably. The pump speed could then be increased incrementally to achieve higher motive nozzle inlet pressures. An increased pump speed led to a decreased pump suction pressure, but the suction pressure decreased significantly less than the discharge pressure increased for a given change in pump speed. Therefore, the maximum pump discharge pressure of 100 bar was often reached before the decreased suction pressure approached the vapor dome. Pump shutdown followed the startup process in reverse.

### 5.5.3 Relative Timescales of System Dynamics

The testing conducted consisted of the need to control several aspects of the experiment effectively, many of which operated on different time scales. The first, and slowest to react, was the control of the psychrometric chambers where the test stand was located. While getting the test chamber to the target operating condition took a significant amount of time, once conditions were reached the room was able to absorb varying internal loads and leverage its significant thermal mass to retain a steady operating condition. Also within the scope of environmental control was

management of the heat sources. As discussed in Chapter 2, both evaporators were controlled by independent EG baths. Both baths had an internal vapor compression cycle for cooling and a resistance heater for heating. At high-capacity conditions, the MT bath was not able to heat the EG enough to retain a constant temperature for several hours of high-capacity tests. While the resulting EG source temperature variation was not significant enough to be noted as an unstable condition during steady state testing, the test stand needed to transition to a reduced capacity to allow the MT bath to regain one or two Kelvin in order to return to the set point. The reduced capacity cycle was often conducted through sending oil back to the compressor oil sumps between test points via the bypass from the oil separator at the discharge of each compressor.

Within the test stand itself, there are three primary dynamics that need to be considered. The three dynamics are charge distribution, temperature, and pressure, in order from slowest to fastest. It was important to keep these dynamics in mind, particularly during operation of cycles that utilized the flash tank. When an EXV was actuated, system pressures immediately surrounding that valve would react within several seconds. However, the ensuing changes in temperatures could take on the order of 15 to 30 seconds to reach a more predictable trend, and possibly on the order of 15 minutes to stabilize, assuming the sink and source temperatures were held constant. Understanding these relative timescales is relevant because the combination of the relative rates of pressure and temperature reactions coupled with the shape of the vapor dome for the fluid being used could result in the temporary loss of compressor suction superheat. For example, if a cycle is operating at a compressor suction superheat of approximately 5 K and the evaporator inlet EXV is closed by a significant margin in anticipation for an upcoming change in set point or source temperature, the evaporation pressure may drop at a rate that is faster than the evaporator outlet superheat will increase such that the compressor suction port temporarily enters the two-phase region. While gradual changes are generally recommended in the operation of any thermal system, scenarios with rapid variation in system parameters can occur

with poorly-tuned valve controls or significant excitations, and should therefore be understood and considered by designers of system controls.

## 5.6 Experimental Testing Conclusions

This chapter presented an experimental analysis comparing two ejector control methods and four cycle architectures applied in a two-evaporator transcritical CO<sub>2</sub> refrigeration cycle with an approximate cooling capacity of 8 kW. In particular, the two ejector control mechanisms assessed were motive nozzle diameter variation via an adjustable needle located in the motive nozzle throat and motive nozzle inlet pressure modulation through a variable speed pump placed between the condenser/gas cooler outlet and the ejector motive nozzle inlet. The assessed cycles were (1) no economization, (2) flash tank economization applied upstream of the MT evaporator, (3) ejector and MT economization, and (4) ejector, MT economization, and a pump upstream of the motive nozzle inlet. The comparison was conducted over a range of four ambient temperatures ranging from 14 °C to 28 °C. The gas cooler outlet pressure was varied at each ambient condition for each cycle in an effort to identify the gas cooling pressure that resulted in the maximum COP. Ejector parameters such as entrainment ratio, efficiency, and pressure lift were also assessed.

The gas cooling pressure where the maximum COP occurred for each cycle decreased as ambient temperature decreased. Maximum COP increases of 6% and 5% were achieved at the 19 °C ambient condition with the MT economization cycle and ejector cycle respectively. The ejector efficiency was not adversely affected through modulation of the motive nozzle diameter. In fact, cycle parameters such as suction nozzle inlet superheat had a larger impact on ejector efficiency than variation of the motive nozzle diameter. The pump was able to increase ejector efficiency by approximately 41%. Therefore, both methods of ejector control were validated in their ability to control the ejector. However, all tests utilizing the pump resulted in a lower COP than the ejector cycle without the pump.



Future work is to optimize both ejector and pump designs for the operating conditions and capacity of this test stand to increase the COP benefit of both cycles. Additionally, the first stage compressor needs to be optimized for booster operation, and the capacity of the compressor performing the second and third stages of compression needs to be increased in order to achieve higher gas cooling pressures at high ambient conditions. An SLHX should also be considered at the outlet of the flash tank in order to provide sub-cooled liquid to facilitate a more accurate mass flow reading from a Coriolis mass flow meter. Placement of another SLHX should be considered between the gas cooler outlet and pump inlet to facilitate pump operation at higher ambient conditions

## 6. DYNAMIC MODEL VALIDATION AND EVALUATION

This chapter focuses on the results of the dynamic model development described in Chapter 4. First, steady state validation of both the compressor sub-model and the system model is presented, followed by validation of the ability of the model to characterize transient behavior of the test stand. Finally, the dynamic model is exercised in two test cases to display the ability of the model to develop control schemes.

### 6.1 Steady State Validation

#### 6.1.1 Compressor Sub-Model

The two compressors utilized in the test stand were ultimately characterized as three separate compressors through splitting the two-stage compressor into two separate correlations that captured the heat loss distribution between stages and the varying IC outlet states, as discussed in Section 4.4.2.

Validation of modeling the first stage of compression, performed by the single-stage compressor, is presented first. The three metrics assessed for accuracy with this compressor model are mass flow rate, power consumption, and discharge temperature. Comparison of the model calculation of these three metrics to experimental data is presented in the form of parity plots, and was conducted using 41 data points. Predictions of the mass flow rate through the single-stage compressor resulted in an MAE of 3.7%, shown in Figure 6.1(a). The first stage discharge temperature was predicted with an MAE of 5.7 K, and the power consumption was predicted with an MAE of 12.1%, shown in Figures 6.2(a) and 6.3(a), respectively.

The power consumption was under-predicted at lower power consumption states and over-predicted at higher power consumption operating points. This is consistent with the trends observed by the authors of the Mendoza-Miranda correlation [139] when applying the correlation to test data taken below the evaporation temperatures where the correlation was tuned. While the error imparted by the low evaporation temperatures was reduced through applying scaling factors, listed in Table 4.6, the slope of the power prediction should be increased through further modification of the exponents associated with the overall compressor efficiency given in Equation 4.9. The slope discrepancy was likely due to the combined effects of  $\pi_2$  and  $\pi_6$ , defined in Table 4.5, given their impact on the overall efficiency and consideration of the suction state. Therefore, a suction evaporation temperature below the intended application of the correlation would result in a less accurate correlation prediction due to the product of  $\pi_2$  and  $\pi_6$  raised to their respective exponents. Mathematically, the multiplication of two terms raised to different exponents would make tuning challenging and thus, necessitate recalculation of the exponent applied to each Pi term to better fit the tested operating conditions.

The validation of the two-stage compressor was conducted with 58 data points. The mass flow rate through the first and second stages of the two-stage compressor was predicted with an MAE of 1.8% and 1.3%, respectively, shown in Figure 6.1(b). The first stage discharge temperature was predicted with an MAE of 6.5 K, while the second stage discharge temperature was predicted with an MAE of 0.7 K, shown in Figure 6.2(b). Finally, the compressor power consumption by the first and second compressor stages was predicted with an MAE of 9.9% and 8.7%, respectively, shown in Figure 6.3(b).

The second compression stage of the two-stage compressor agreed with the experimental data slightly more than the first stage stage prediction did for the same reason the single-stage compressor power consumption prediction was less accurate. Of all compressor stages which were characterized with the Mendoza-Miranda correlation [139], the second stage of the two-stage compressor operated with the highest

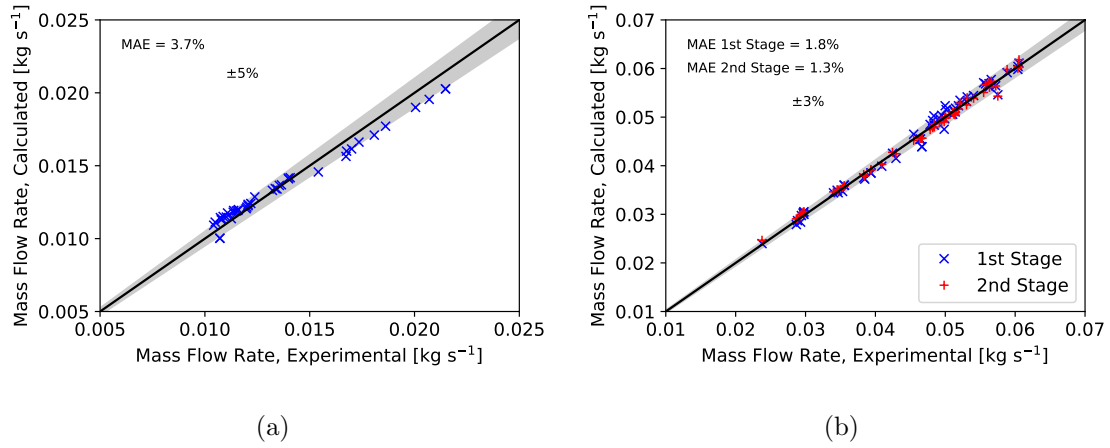


Fig. 6.1. Compressor map mass flow rate validation for: (a) Single-stage compressor; and, (b) Two-stage compressor.

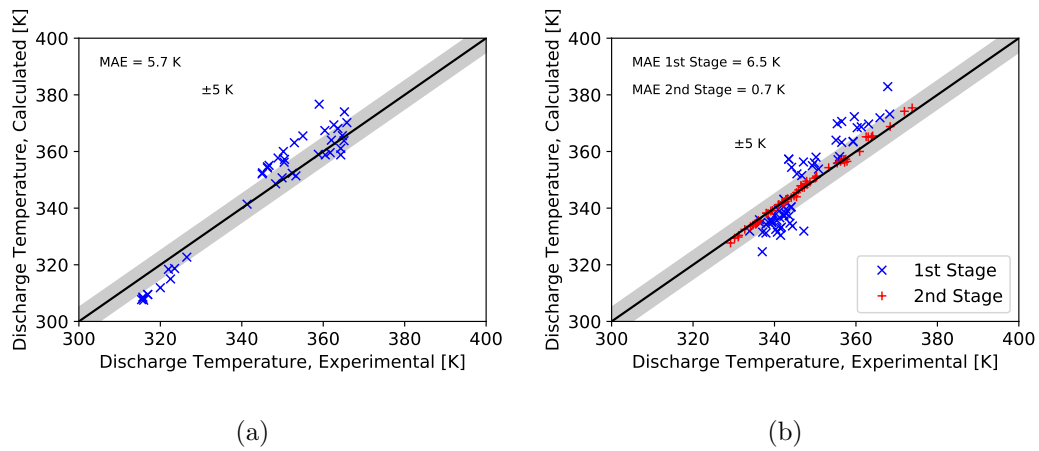


Fig. 6.2. Compressor map discharge temperature validation for: (a) Single-stage compressor; and, (b) Two-stage compressor.

suction pressure. This higher suction pressure equated to an equivalent higher evaporation temperature for that stage of compression, which best the conditions for applicability of the correlation, resulting in the most accurate predictions. A future remedy for the discrepancy in compressor performance prediction would be either re-tuning of the Pi group exponents or application of another compressor mapping

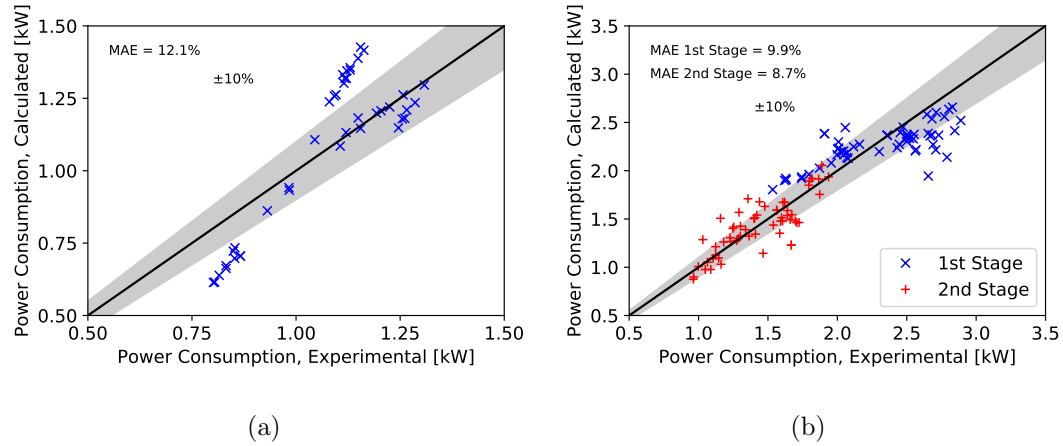


Fig. 6.3. Compressor map power consumption validation for: (a) Single-stage compressor; and, (b) Two-stage compressor.

technique, such as the AHRI 10-coefficient applied in Chapter 3. The latter suggestion would likely be the better path, as primary motivation for application of the Mendoza-Miranda correlation [139] was to capture the intercooling effects, and thus was only pertinent to the stage of compression with the IC outlet state as its suction state. During further development of compressor characterization, numerical robustness must be kept in mind. The compressor maps presented herein were less accurate than preliminary models. This is because the data points used for correlation development included a larger number of points over a broader range of operating conditions. The motivation for the broader range of operating conditions was that when dynamic models are working to initialize and bring the cycle to a reasonable set of operating conditions before predicting transients, the pressures and temperatures surrounding the compressor can be significantly outside of the intended operating range. While this challenge can be eased with thorough initial conditions, numerical variation is inevitable with modeling a cycle of this complexity. If the compressor sees a condition outside of its intended operating range and its performance map is strictly for a narrow range of conditions, the compressor sub-model will return unreasonable mass flow rate values that will make convergence of the cycle much more challenging.

Therefore, accuracy was knowingly sacrificed for numerical robustness in the case of the compressor maps presented in this chapter.

### 6.1.2 Cycle Performance

Before seeking dynamic model validation, the ability of the model to predict steady state cycle behavior needs to be assessed. The system model developed aims to predict the performance and behavior of the cycle with the flash tank upstream of the MT evaporator. Focusing on the MT flash tank cycle provided the chance to assess the ability of the model to capture phase separation and other system transients associated with a complex architecture. It was decided to model the MT flash tank cycle first before advancing to modeling the cycle with the expansion work recovery or the pump to balance complexity with ensuring the model was predicting reasonable results. In order to achieve steady state predictions, the dynamic model was run for a period of 20 minutes with inputs from the experimental model, after which steady state was reached. Model inputs from experimental data consisted of:

- EXV  $A_{\text{eff}}$  from post-processing script that receives input voltage from raw data
- MV position
- Compressor speeds
- Heat sink (air) temperature, relative humidity, and volumetric flow rate
- Heat source (EG) temperatures, concentrations, and volumetric flow rates (for each evaporator)

16 steady state points from experimental testing over all four ambient conditions assessed in Chapter 5 were used for validation. Both compressors were operated at a constant speed of 60 Hz. Parameters selected for validation were cooling capacity, evaporation temperature, compressor power consumption, gas cooling pressure, and gas cooler outlet temperature. These parameters were chosen given that they represent the values that are most impactful on cycle efficiency, capacity, and overall behavior. Parity plots of the LT and MT evaporation temperature predictions are

provided in Figures 6.4(a) and 6.4(b), respectively. Saturation temperatures for both the LT and MT evaporators were slightly under-predicted, but resulted in MAE values of 5.0 K and 3.3 K, respectively. One source of error that contributed to this discrepancy is due to the presence of a flash tank upstream of the LT evaporator inlet EXV that is not accounted for in the model and imparts additional pressure drop. The MT evaporation temperature under-prediction is due to two physical aspects of the valve in the test stand that made it difficult to characterize the valve accurately. The first of these aspects is the lack of pressure transducers on either side of the EXV, and the second is the fact that the EXV at the MT evaporator inlet is the largest of all the EXVs in the system. Initially, the largest EXV was placed at the gas cooler outlet. However, this EXV was found to be oversized, which had a more detrimental impact on the ability to control the gas cooler pressure than control the MT evaporator outlet superheat. Therefore, the oversized valve was placed upstream of the MT evaporator. The lack of pressure transducers coupled with the lower pressure drop associated with the oversized valve results in the need to estimate at discharge coefficient,  $C_d$ , based on the other valve sizing and tuning with simulation results.

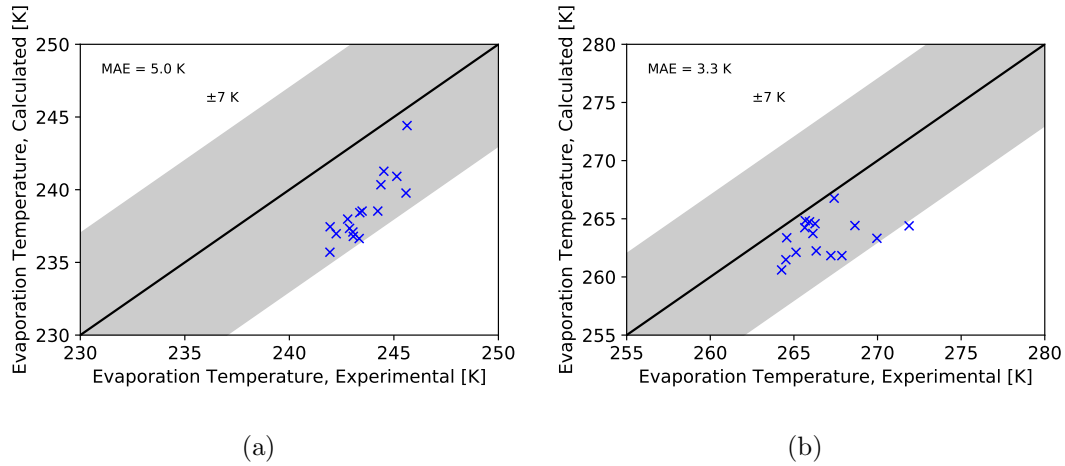


Fig. 6.4. Test stand system model steady state validation of: (a) LT evaporation temperature; and, (b) MT evaporation temperature.

The evaporator cooling capacities followed the same trend as the evaporation temperatures, offering further support for the conclusion that the model predicted over-throttling of flows upstream of both evaporators. The under-prediction of MT evaporator capacity is particularly noticeable at the lower capacity operating points, where the model under-predicts significantly due to propagation of error through sub-models that were designed for higher capacity operation.

Parity plots for the LT and MT cooling capacity predictions are shown in Figures 6.5(a), and 6.5(b). MAE values for the LT and MT evaporator capacity predictions were 12.3% and 18.7%, respectively.

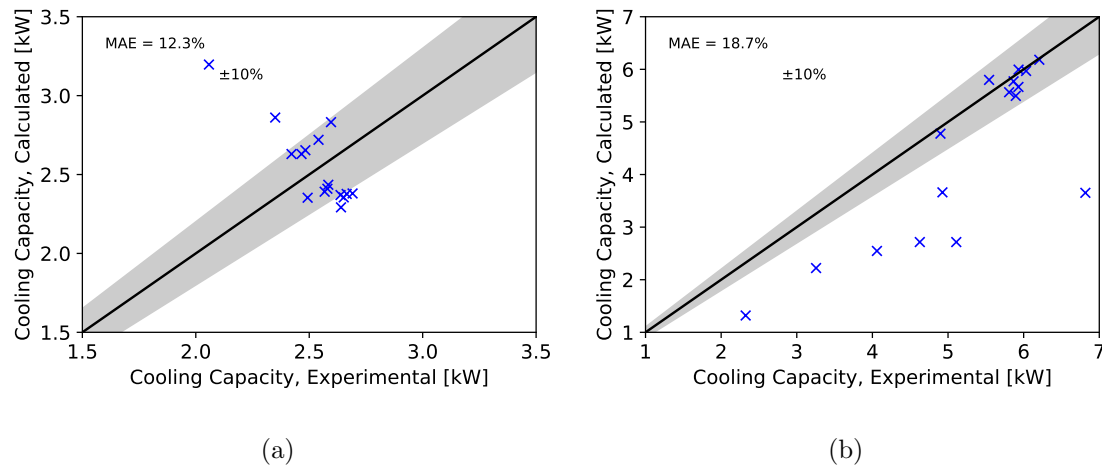


Fig. 6.5. Test stand system model steady state validation of: (a) LT evaporator cooling capacity; and, (b) MT evaporator cooling capacity.

The model predicted the compressor power consumption well given the error imparted from the compressor map validation in Section 6.1.1. The first stage compressor power consumption is validated in Figure 6.6(a), and the sum of the power consumed by the second and third compressor stages, representing the two-stage compressor, is validated in Figure 6.6(b). MAE values of 6.0% and 11.9% were achieved for the first stage and the summation of the second and third compression stage power consumption values, respectively. The continued trend of under-prediction can be at-



tributed to the decreased mass flow rate through each compressor. While the overall pressure ratio across the compressors was higher due to over-throttling, the decreased mass flow rate had a more significant effect on power consumption and thus, resulted in continued under-prediction.

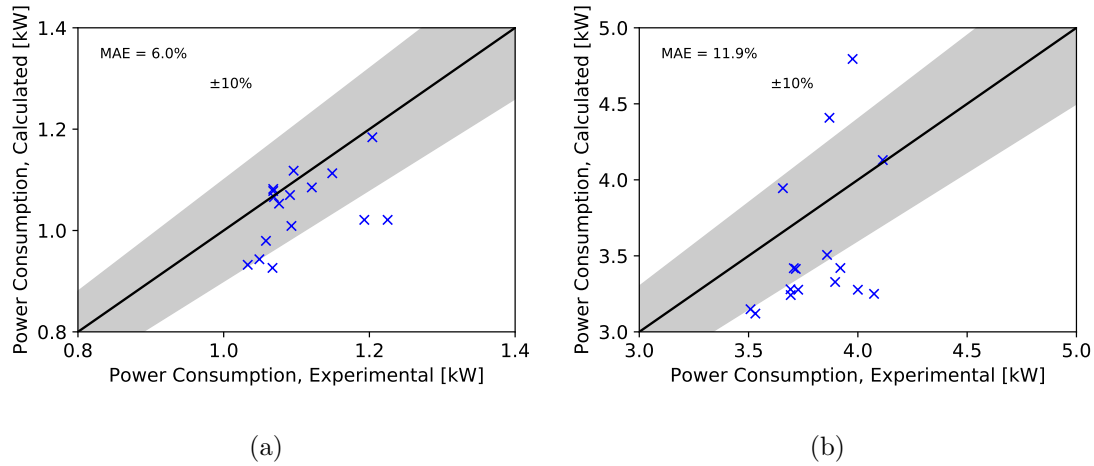


Fig. 6.6. Test stand system model steady state validation of: (a) First stage power consumption; and, (b) Second and third stage compressor power consumption.

To assess the heat rejection in the gas cooler and thus, the EXV inlet state, validation of the gas cooling pressure and gas cooler outlet temperature is shown in Figures 6.7(a) and 6.7(b), respectively. The gas cooling pressure was predicted with an MAE of 8.5% and the gas cooler outlet temperature was predicted with an MAE of 0.9 K. This shows a strong ability for the gas cooling process to capture heat exchange with ambient air, as well as the ability of the multi-stage compressor model to receive the varying IC outlet state and still capture the discharge pressure reasonably accurately.

Overall, the steady state validation of the compressors and cycle parameters showed reasonable agreement with the experimental data. Over-throttling was a consistent trend, but the majority of the predicted trends were correct. Additionally, sources of error were discussed and action to rectify the inaccuracies was identified.

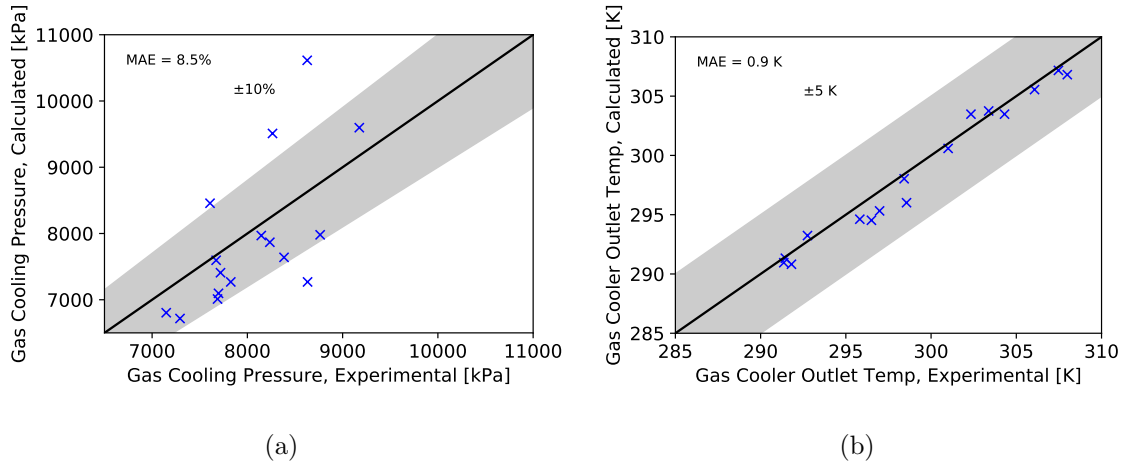


Fig. 6.7. Test stand system model steady state validation of: (a) Gas cooling pressure; and, (b) Gas cooler outlet temperature.

## 6.2 Transient Validation

### 6.2.1 Validation Strategy

To perform transient validation of a complex cycle, the ability of the model to capture transient effects of varying the position of one valve at a time needs to be assessed. Otherwise, identifying any weaknesses or sources of error would be more challenging. As such, four case studies are investigated and validated:

1. MT evaporator MV bypass valve opened from its original position at two turns from closed to six turns from closed.
2. MT evaporator inlet EXV closed from 3.5 to 2.75 Volts.
3. LT evaporator inlet EXV closed from 3 to 2.5 Volts.
4. Gas cooler outlet EXV opened from 2 to 2.5 Volts.

To validate the four scenarios, the transient experimental data was averaged over five second intervals and passed through the same post-processing system of equations

applied in Chapter 5. The only difference between the transient and steady state data analysis scripts was that the system of equations used to solve the cycle and output thermodynamic properties and cycle performance quantification was placed within a time loop instead of averaging all of the raw data. Structuring the initial data analysis script in a time loop allowed the selection of how many seconds the data would be averaged over to represent one point in the transient response. Five seconds was chosen in order to balance resolution of the transient response and a reasonable number of variables for EES to solve. The EES memory limit of 12,000 variables was reached at a time step of approximately 2.5 seconds, so in order to retain reasonable computational speed five seconds was chosen as the time step for transient data analysis. Comparisons between experimental data and the transient simulation were conducted with time on the x-axis and several performance parameters on the y-axis. Plotting parameters with respect to time allows the assessment of the ability of the model to follow the simulation on a similar timescale as well as whether or not a constant offset is maintained due to steady state error. If the error between the simulation and experimental results varies, the error variation can also provide insights into aspects of the model that need to be improved. The cycle cooling capacity, evaporation temperatures, compressor suction superheat, and compressor power consumption are the primary values assessed. These parameters not only reflect the ability of the model to predict the cycle performance, but also to retain evaporation temperatures and compressor suction superheat values that will allow safe operation of the compressors. A final comment on the transient simulation setup would be that the model is exactly the same as was validated in Section 6.1, except that the refrigerant line between the MT evaporator inlet EXV and the MT evaporator inlet were deleted due to being the sole source of consistently non-converging solutions despite repeated efforts to add constraints and initial conditions. Further investigation and reapplication of these lines is noted in the future work. The length of the lines was approximately two meters, which is not negligible but would not have a significant impact on the model accuracy.

### 6.2.2 Charge Migration

Before further system parameters are assessed for each transient case study, the ability of the simulation to predict charge migration is assessed. Charge migration is assessed by analyzing the flash tank liquid level variation with time. This is a vital observation because transient charge migration was found to be slower than both temperature and pressure propagation throughout the test stand. Therefore, if the rate of mass transfer throughout the test stand is predicted to be faster than it would be in reality, this would result in nearly all subsequent transients occurring faster in the simulation than in the experimental data. Furthermore, the additional components in the physical test stand which allow assessment of other architectures increased the test stand volume significantly relative to the single architecture used in this dynamic simulation. The resulting lower charge value in the simulation also contributed to the smaller inertia of the system dynamics relative to the experiment by nature. A comparison of simulated flash tank liquid level to measured flash tank liquid level with time for case study 1, 2, 3, and 4 is shown in Figures 6.8(a), 6.8(b), 6.8(c), and 6.8(d), respectively.

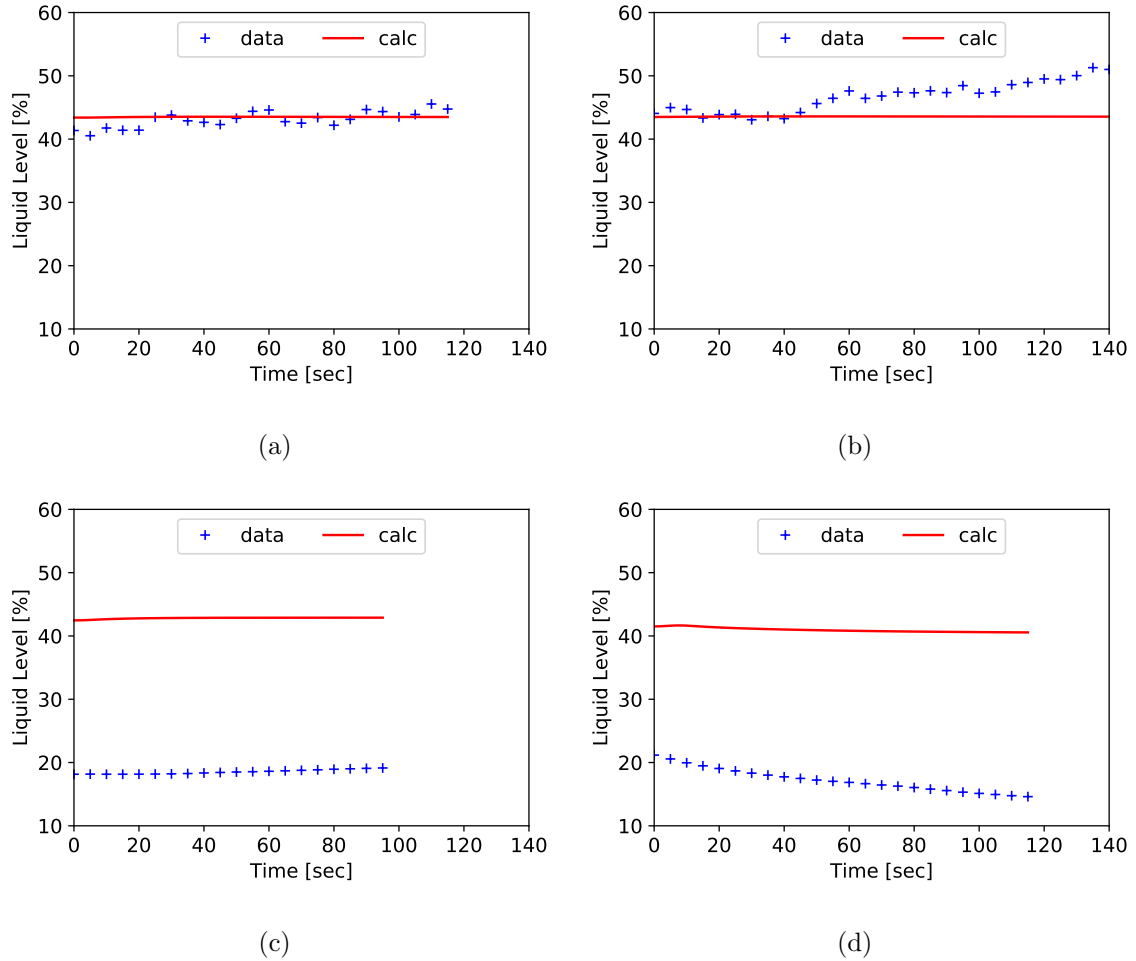


Fig. 6.8. Comparison of simulated and experimental flash tank liquid level variation in: (a) Case study 1; (b) Case study 2; (c) Case study 3; and, (d) Case study 4.

As the flash tank liquid level comparison showed, the simulation under-predicts the magnitude of the transients associated with all four case studies. This is evident in the significantly smaller variation in simulated flash tank liquid level than the measured variation, which confirms that the model mass transfer predictions are not capturing the inertial effects of charge migration well enough. In Dymola, the mass is a secondary calculation that is conducted after a state is fixed with two independent, intensive properties. These properties are defined through conservation

of mass, momentum, and energy presented in Table 4.1 in Chapter 4. Therefore, the final states are calculated through the results of isentropic efficiencies or heat transfer parameters. The only way to force charge as a parameter is through the use of a component called Filling Station within the TIL Library.

To assess the ability of the dynamic model to capture the impact of forcing charge variation on the model, an example is presented from preliminary modeling of a multi-stage cycle that is similar to the focus of this chapter. Using the same ramp concept in Dymola as was introduced in Chapter 4, Filling Station was applied. Filling Station is simply a port that breaks into the model conservation of mass system of equations to add or decrease charge at a given point in the cycle. The model was run for 40 minutes without charge variation to achieve steady state, then 0.75 kg of charge was added over a two minute period. This condition was then given an additional 38 minutes to reach steady state for 40 minutes in total, before 1.5 kg of charge was removed over 240 seconds and allowed to run for an additional 36 minutes, for a 120 minute simulation in total. A P-h diagram with all three plots overlaid on top of each other is shown in Figure 6.9.

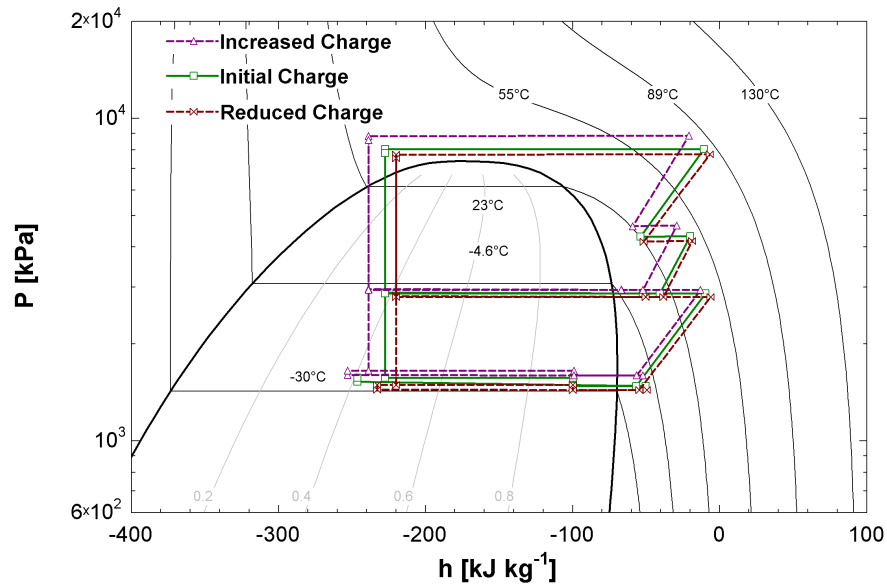


Fig. 6.9. Comparison of simulated charge variation effects on the test stand operating in LT economization mode.

Qualitatively, the system responds as would be expected. When charge is added, the system pressures increase in general. When charge is removed, the opposite occurs. To ensure that the mass flow rate and system capacity followed suit, Table 6.1 provides system parameters that are impacted by charge to compare all three charge operating conditions.

Table 6.1.

Results from simulated variation of the test stand charge in LT economization mode.

Cycle (-)	$\dot{Q}_{\text{MT,Evap}}$ (kW)	$\dot{Q}_{\text{LT,Evap}}$ (kW)	$T_{\text{MT,Evap}}$ (°C)	$T_{\text{LT,Evap}}$ (°C)
Initial Charge	5.32	1.97	-6.6	-28.2
Increased Charge	5.65	2.22	-6.0	-26.4
Decreased Charge	4.82	1.78	-7.8	-29.7

Following the qualitative results, the quantitative results provided validate the ability of TIL to capture charge variation. However, with charge held constant as was the case in the experimental testing, the model was not able to capture these same dynamics through liquid level variation in the flash tank. This is a fundamental challenge that should be remedied through additional modeling of the flash tank to result in more significant charge variation and increased accuracy of the dynamic response with transient phase separation. Addressing the charge migration transients is in the future work.

### 6.2.3 Model Validation Results

Transient validation plots of the cooling capacity, evaporation temperature, compressor suction superheat, and compressor power consumption for the first case study are shown in Figures 6.10(a), 6.10(b), 6.10(c), and 6.10(d), respectively. The gas cooling pressure was slightly under-predicted as a result of error due to valve characterization, which contributed to the reduced cooling capacity predictions. While the result of all assessed parameters showed similar trends between the model and experimental data, the simulated evaporator cooling capacity arrived at a stable operating condition faster than the experimental cooling capacity. Despite this, all other



simulated parameters varied on similar timescales to the experiment. Due to the previously-discussed under-prediction of rate of mass transfer effects in the model, it can be concluded that the evaporator capacities were more impacted by the mass transfer rate discrepancy than other parameters. The simulated flash tank liquid level shown in Figure 6.8(a) matched that of the experiment best in case study 1, which supports why the remaining parameters had similar dynamic responses.

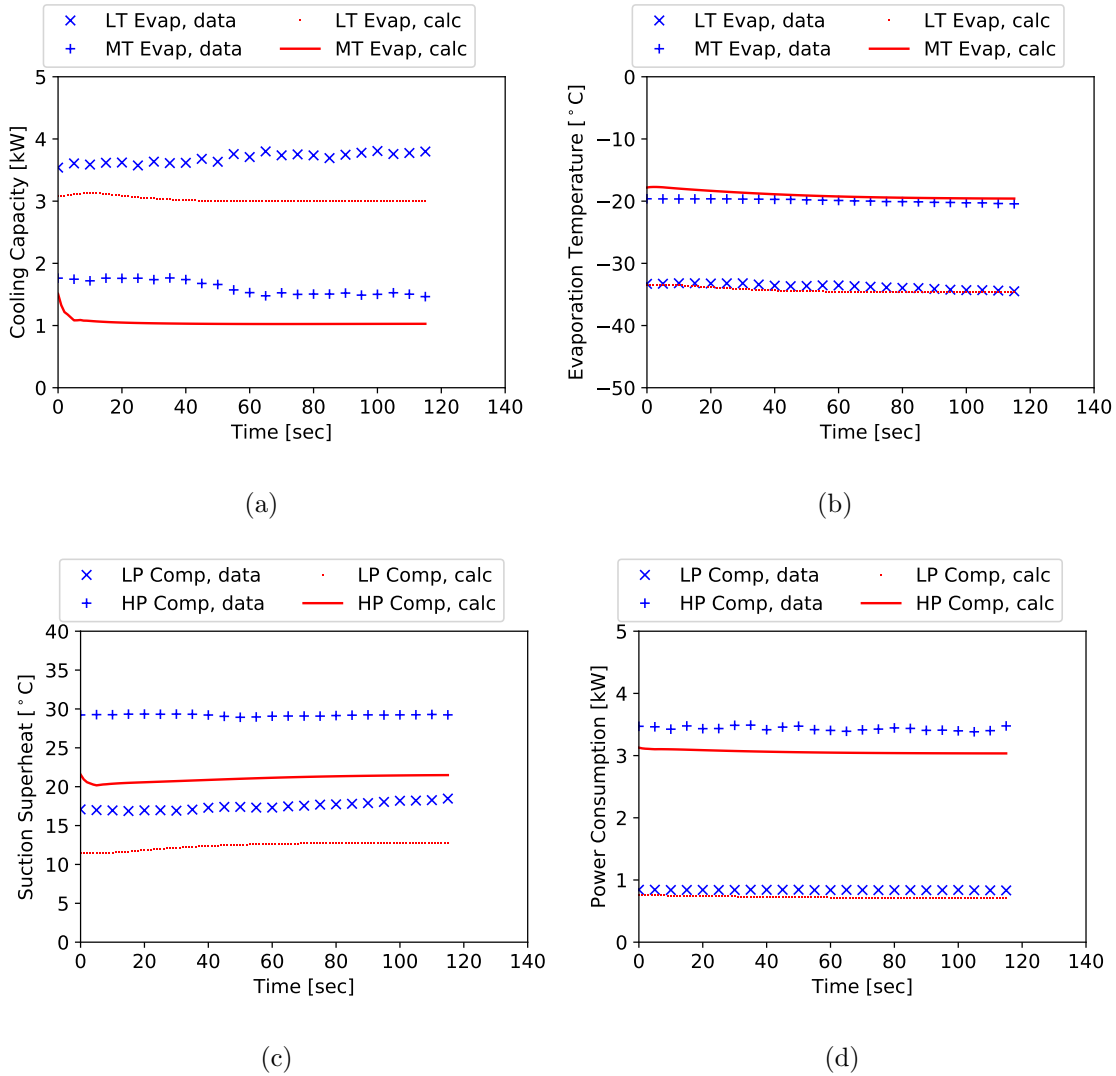


Fig. 6.10. Transient case study 1, MV actuation, comparison of experimental and simulated values: (a) Cooling capacities; (b) Evaporation temperatures; (c) Compressor suction superheat; and, (d) Compressor power consumption.

The closing of the MT evaporator inlet EXV in case study 2 also produced a rapid initial cooling capacity reaction. Transient validation plots of the cooling capacity, evaporation temperature, compressor suction superheat, and compressor power consumption for the second transient case study are shown in Figures 6.11(a), 6.11(b), 6.11(c), and 6.11(d), respectively. In case study 2 the simulated MT evaporator

cooling capacity decreased rapidly, then seemed to stabilize for the remainder of the simulation, while the experimental data decreased more slowly. The simulated LT evaporator capacity seemed to be more shielded from the variation of the MT evaporator state than the experimental data shows it should have been, resulting in a much smaller variation in simulated capacity than experimental capacity. The theme of the simulation reacting more quickly than the experiment was consistent through evaporator outlet superheat and evaporation temperature assessments as well. Additionally, the simulation predicted a smaller decrease in evaporation temperature than the data showed, thus resulting in a smaller rise in compressor suction superheat for the simulation than the data. While the connection of smaller changes in evaporation temperature resulting in smaller variation in compressor suction superheat is consistent with experimental trends, the simulated valve beginning and end states were not as different as they needed to be to match the experimental result. The experimental result of an increased compressor suction superheat and a decrease in evaporation temperature is consistent with the behavior of a vapor compression cycle that has decreasing charge. This result is corroborated by Figure 6.8(b), which shows a rising liquid level and thus, a lower effective charge in the cycle itself. Therefore, if the discrepancy in liquid level variation is taken into account, the simulation and experiment both behave reasonably. Finally, the simulated compressor performance was consistent with the experimental compressor performance in that neither varied significantly due to the reasonably small variation in compressor suction state and overall pressure ratio.

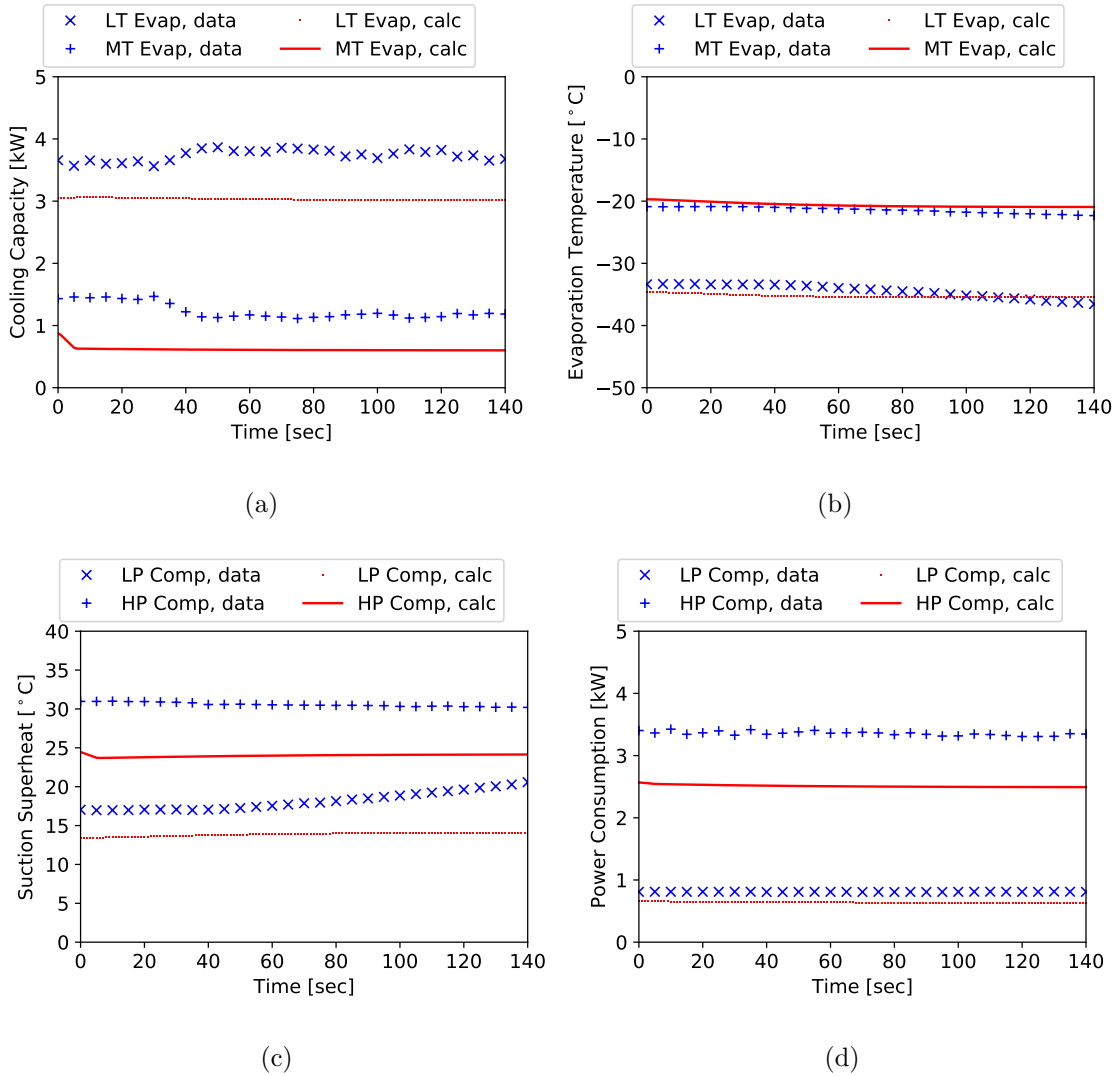


Fig. 6.11. Transient case study 2, MT EXV actuation, comparison of experimental and simulated: (a) Cooling capacities; (b) Evaporation temperatures; (c) Compressor suction superheat; and, (d) Compressor power consumption.

Case study 3 resulted in the LT evaporator behaving as would be expected with the closure of the EXV at its inlet for the first portion of the simulation. Transient validation plots of the cooling capacity, evaporation temperature, compressor suction superheat, and compressor power consumption for the third transient case study are shown in Figures 6.12(a), 6.12(b), 6.12(c), and 6.12(d), respectively. The model

captured the behavior associated with LT evaporator EXV actuation well, and on a similar time scale, for the first 20 to 30 seconds of the simulation of case study 3. However, in the remainder of the assessed time period, the simulated LT evaporator temperature followed the experimental until it reached an evaporation temperature of approximately  $-38^{\circ}\text{C}$ , after which time the simulated LT evaporator temperature stabilized and the experimental evaporation temperature continued to drop.

While Figure 6.4(a) shows that the simulation under-predicted the evaporation temperature, this was likely a result of the presence of a second flash tank located upstream of the LT evaporator inlet EXV that was not utilized during the testing of the MT flash tank architecture. In the first two transient case studies this error contributed to an offset, but instabilities from the lack of vapor bypass from the LT evaporator inlet flash tank could have impacted the significant drop in LT evaporation temperature observed in the experimental data. In addition to these observations, the envelope for the first stage compressor provided in Figure 4.7 shows that most test points conducted were very near, if not below, the minimum evaporation temperature for the first stage compressor. When the compressor envelope shown in Figure 4.7 is compared to the transient validation plot for evaporation pressure it can be seen that closing the LT evaporator inlet EXV resulted in compressor operation far below the compressor minimum design evaporation temperature of  $-30^{\circ}\text{C}$ . Furthermore, the many tests that were conducted controlling the LT evaporation temperature resulted in stable control of the evaporation temperature, and the only time a significant drop in evaporation temperature that was disproportionate to the EXV closure change occurred was at evaporation temperatures of approximately  $-40^{\circ}\text{C}$ . It can then be concluded that the eventual discrepancy in evaporator temperature observed in case study 3 was in part due to operation of the first stage compressor well outside of its operating envelope and in part due to the un-used flash tank located upstream of the LT evaporator. Therefore, the first portion of case study 3 should be taken as more representative of the cycle dynamics than the remaining time. While the predicted and experimental flash tank liquid levels were offset from each other in Figure 6.8(c),

their relative rates and directions of change matched well in case study 3. This does not suggest that the simulated liquid level was more accurate than previous case studies as much as that the experimental liquid level variation was small enough that simulated discrepancies did not have as significant of an impact. The offset appeared to be a numerical solution, as the cycle was impacted more by the change in liquid level than the absolute liquid level itself. In fact, the cycle behaved similarly across a large range of charges once there was a measurable liquid in the flash tank while charging the system during experimental testing.

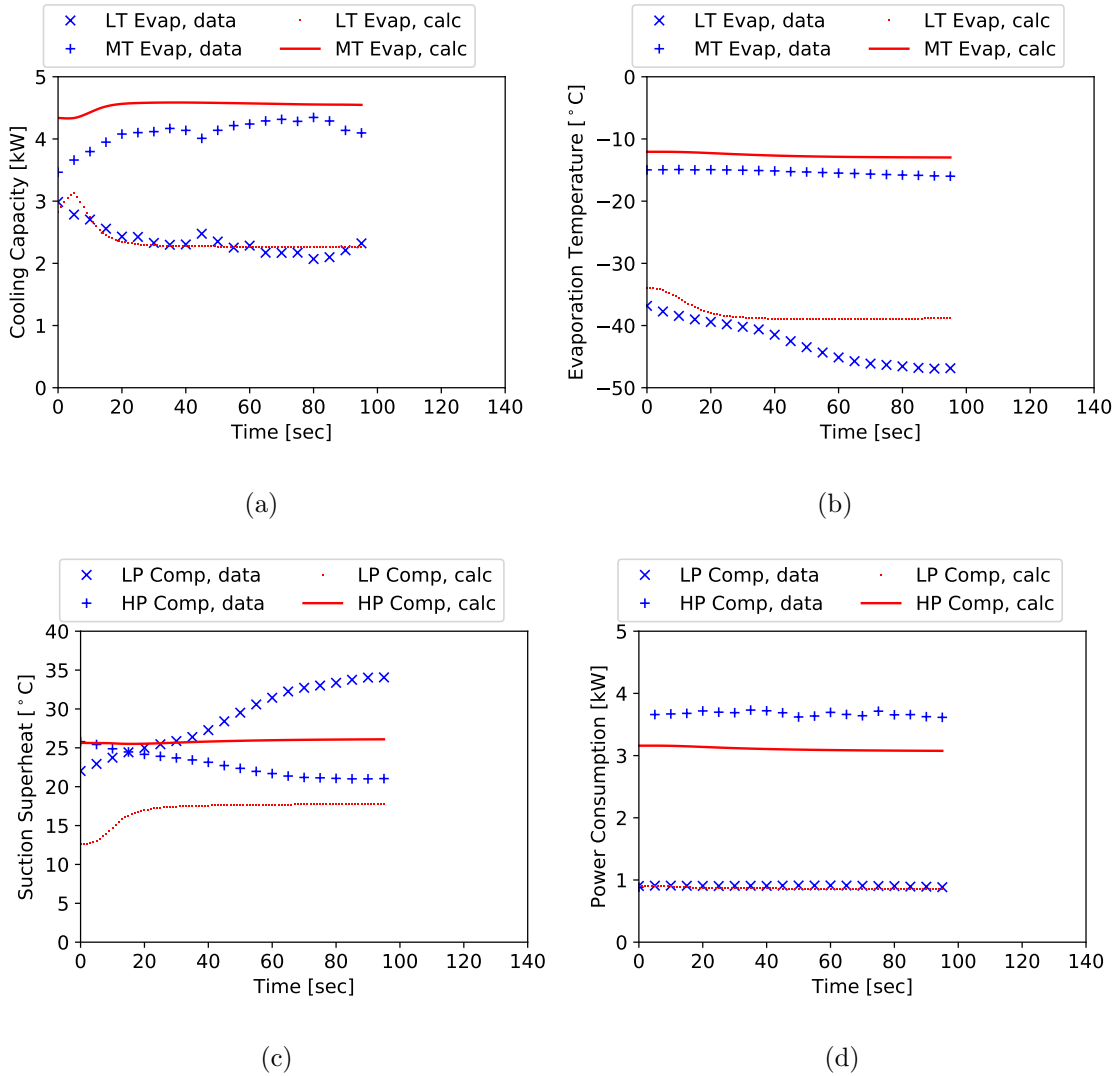


Fig. 6.12. Transient case study 3, LT EXV actuation, comparison of experimental and simulated: (a) Cooling capacities; (b) Evaporation temperatures; (c) Compressor suction superheat; and, (d) Compressor power consumption.

Finally, case study 4 assessed the ability of the model to capture transients surrounding opening of the gas cooler outlet EXV. Case study 4 is the only study that actuates a valve which 100% of the system mass flow passes through. Therefore, the impact of its actuation is significant and reaches all assessed parameters of cycle performance to varying degrees. Transient validation plots of the cooling capacity,

evaporation temperature, compressor suction superheat, and compressor power consumption for transient case study 4 are shown in Figures 6.13(a), 6.13(b), 6.13(c), and 6.13(d), respectively.

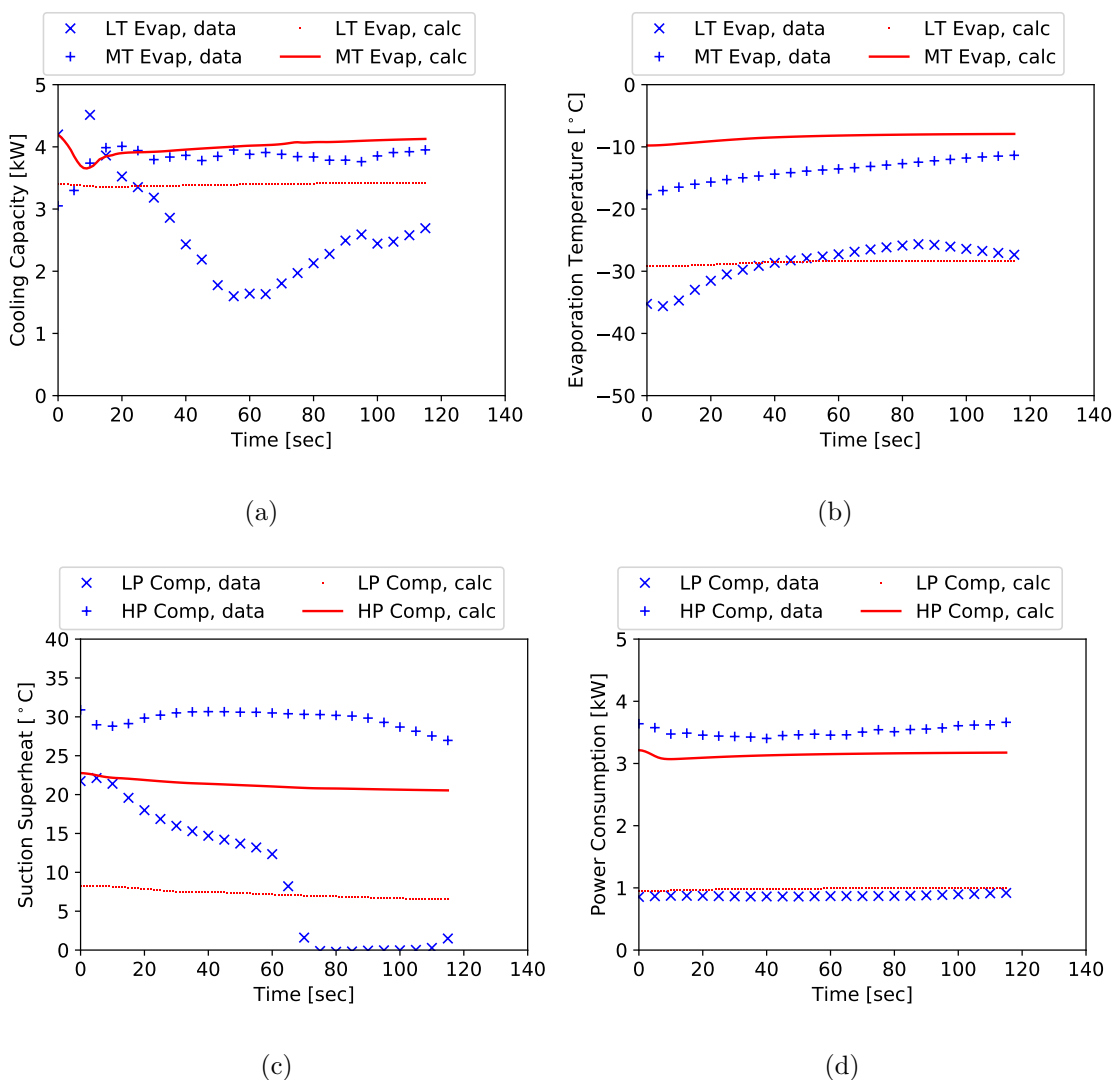


Fig. 6.13. Transient case study 4, GC outlet EXV actuation, comparison of experimental and simulated: (a) Cooling capacities; (b) Evaporation temperatures; (c) Compressor suction superheat; and, (d) Compressor power consumption.



First, the general path taken by the simulation was similar to that of the experimental data. However, the simulation plots the cycle contraction path at a significantly faster rate than all three previous case studies. The cycle would be expected to contract, resulting in a lower gas cooling pressure and higher evaporation pressures, and eventually stabilize. The discrepancy in reaction time is likely due to two transient phenomena that the model is not fully taking into account. The first is the inertia associated with mass transfer through the system. With all other valve positions, sink, and source conditions being held constant, the influx of mass flow associated with the opening of the gas cooler outlet EXV would take time to distribute through the system and stabilize. The impact of the mass distribution inertia is supplemented by the thermal inertia of the system. While the simulated refrigerant lines and flash tanks were input to closely match those of the experimental test stand and considered conduction and pressure drop, the lack of consideration of convective heat transfer to the environment effectively severs an anchor of inertia. To more-accurately capture the significant transient event imparted on the cycle through the opening of the gas cooler outlet valve, heat ports to simulated ambient conditions should be added to each line segment and flash tank in the model, as opposed to just the IC and gas cooler inlet states.

A notable aspect of this case study is the dip in MT evaporator cooling capacity. This is due to the gas cooler outlet state entering the vapor dome temporarily, which occurs because the gas cooling pressure drops faster than the gas cooler outlet temperature. As result, the MT flash tank inlet quality increases significantly and thus, the mass flow rate that travels to the evaporator decreases rapidly. The discrepancy of the timing of mass transfer through the system matches this well and also explains the thermal result. The impact on the first stage compressor suction superheat is due to inaccuracy of the EXV characterization, resulting in more extreme beginning and end states for the experimental cycle than the simulated, as has occurred in earlier test cases.

Aside from the response timing, the behavior of the simulation was similar to that of the experimental data. Opening the gas cooler outlet valves results in a contraction of the cycle, thus raising the evaporation temperatures for both evaporators. The increased evaporation temperatures then result in higher mass flow rates produced by the compressors and aided by the larger effective flow area in the gas cooler outlet EXV. Furthermore, the increased mass flow rate results in a decreased compressor suction superheat as well as a higher evaporator cooling capacity.

In contrast to case study 2, the flash tank liquid level decreased significantly over the course of case study 4, shown in Figure 6.8(d). This appears to be counter-intuitive in that the opening of the gas cooler outlet often results in an increased liquid level. However, the gas cooler outlet state was at a pressure just above the critical pressure and a temperature just below the critical temperature at the initial state of the simulation. Given the rapid change in properties near the vapor dome, the contraction of the cycle resulted in a significant enough increase in flash tank inlet quality that the rate of vapor mass flow resulting from the flashing overtook that of the liquid. Because the diameters of the two outlet valves on the flash tank were held constant, the liquid level began to decrease and thus, increased the effective charge in the vapor compression cycle. This further supports the increase in experimental evaporation temperature and decrease in compressor suction superheat.

### 6.3 Control Scheme Exploration and Case Study Validation

This section aims to exercise the validated dynamic model to provide two examples of how the model can be used to develop effective control schemes for transient scenarios introduced in Chapter 4. The first scenario is the pull down of the LT evaporator, where the evaporator source temperature is reduced from refrigeration to freezing, and the second is the application of an excitation to the LT evaporator to simulate a door opening in a high-ambient climate. For clarity, LP refers to the first stage compressor and HP refers to the second stage compressor.

The upper and lower bounds on the range of effective flow areas for the valves are input based on the range of values applied in Section 6.1.1, and EXV tuning for the MT evaporator inlet EXV and LT evaporator inlet EXV were iterated upon in the simulation. A summary of EXV PI control parameters is provided in Table 6.2. All other aspects of the cycle were held constant.

Table 6.2.  
EXV PI controller parameters applied in control scheme simulations.

EXV	$K_c$ (-)	$\tau_i$ (sec)	$A_{\min}$ (mm <sup>2</sup> )	$A_{\max}$ (mm <sup>2</sup> )
2	$1 \cdot 10^{-8}$	10	0.1	5
4	$1 \cdot 10^{-8}$	10	0.075	1

Similar to the transient validation data visualization, cooling capacity, evaporation temperature, and compressor suction superheat values are plotted over time in order to capture the ability of the control scheme to retain measurable, and preferably stable, compressor suction superheat. In addition, implications on system capacity can be assessed. The LT evaporator source temperatures were also plotted with respect to time for both simulations to provide context to the variation.

The source temperature, evaporation temperatures, compressor suction superheat values, and cooling capacities for the pull down scenario are plotted against time in Figures 6.14(a), 6.14(b), 6.14(c), and 6.14(d), respectively. Given the more gradual nature of the pull down scenario, the cycle reacted well with maximum compressor suction superheat variation of 5 °C and 4 °C for the LP and HP compressors, respectively. Furthermore, there was no rapid reaction by either EXV, such that the cooling capacity followed a stable and predictable trend. With the decrease in the LT evaporator source temperature, the LT evaporator outlet superheat decreases due to the reduction in thermal gradient between the refrigerant and the EG. Accordingly, the LT evaporator inlet EXV reduces its effective flow area in order to increase the

LP compressor suction superheat and thus, reduces the LT evaporation temperature. At this point the coupled dynamics of the evaporators come into play. Because the MT evaporator bypass valve was held at a constant  $k_v$  value, the majority of the impact of variation of the EXVs upstream of the evaporators can be isolated to mutual impact between the evaporators. This is most evident in Figure 6.14(c), which shows the first reaction taking place due to reduction of compressor suction superheat upon the initial decrease of the source temperature. The reduction in compressor suction superheat results in the LT evaporator inlet EXV reducing its opening, which then reduces the mass flow rate passed to the LT evaporator in an effort to increase the LP compressor suction superheat. Because the dynamics have not reached the compressor suction ports at a large enough magnitude, the full system mass flow rate is constant for several seconds following initial contraction of the LT evaporator inlet EXV. This results in a larger portion of the total mass flow rate being diverted to the MT evaporator because the EXV upstream of its inlet has not reacted yet. This is the reason for the initial reduction in HP compressor suction superheat that follows the initial decrease in LP compressor suction superheat. The EXV upstream of the MT evaporator quickly overreacts, resulting in an HP compressor suction superheat above 10 K until the magnitudes of the relative effects of the actuating EXVs reduce enough to return to a stable condition following the LT evaporator source temperature reaching its target condition. The cooling capacities follow this trend at a more reasonable rate of fluctuation, but the eventual result of the LT evaporator EXV ending with a smaller opening than it began the scenario with in order to facilitate safe LP compressor suction superheat at the updated lower source temperature agrees with the decreased LT evaporator cooling capacity over the course of the simulation. Conversely, the MT evaporator capacity would increase because, even with the slightly decreased MT evaporator temperature, a larger portion of the total system mass flow rate is passing through the MT evaporator at the final state.

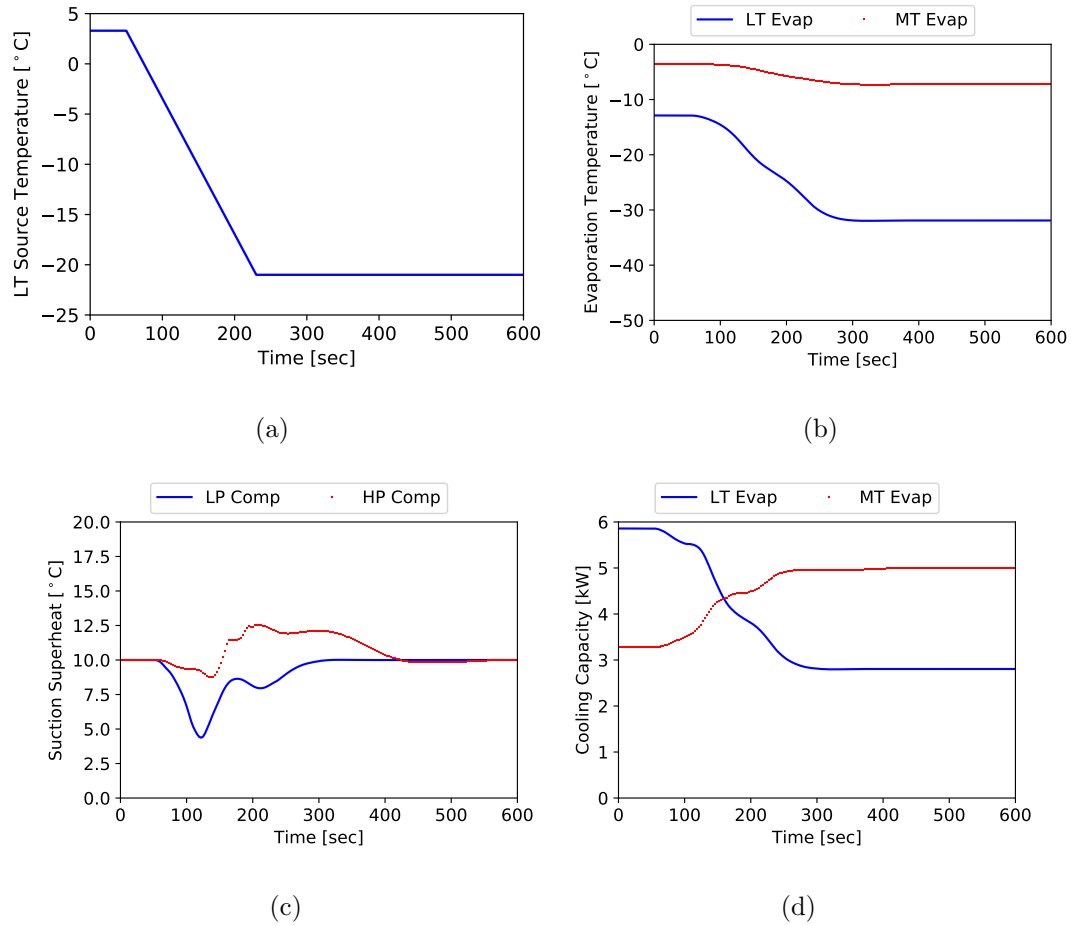


Fig. 6.14. Pull down controls development scenario simulated values of: (a) Source temperature; (b) Evaporation temperatures; (c) Compressor suction superheat; and, (d) Cooling capacities.

For the excitation scenario, the rate of reaction of the EXV controls will play a pivotal role in the reaction. Because the source temperature will eventually return to its original state, the beginning and end points are not of interest in this scenario. The question to be answered is regarding the coupled dynamics of the evaporators that effectively alternate passing varying amounts of mass flow rate to each other in the context of a varying LT source temperature, and whether or not the valves can react in a way that will retain system stability and compressor suction superheat.

The source temperature, evaporation temperatures, compressor suction superheat values, and cooling capacities for the evaporator excitation scenario are plotted against time in Figures 6.15(a), 6.15(b), 6.15(c), and 6.15(d), respectively. The sudden increase of the LT evaporator source temperature results in a momentary increase in LP compressor suction superheat, prompting opening of the LT evaporator EXV. The opening of the LT evaporator EXV results in both an increase in LT evaporator capacity and a decrease in the amount of mass flow rate being passed to the MT evaporator. This only lasts momentarily because the HP compressor has not yet felt the impact of this change, but also results in an increase in HP compressor suction superheat. Therefore, the MT evaporator EXV opens as well. Initially this reduces the HP compressor superheat, but shortly thereafter the coupled effects of the opening of both EXVs results in significant inertia which pushes the evaporators at both compressor suction ports below the target of 10 K. The HP compressor suction superheat falls to a lower value than the LP compressor suction port because the MT evaporator has a higher capacity, and therefore more thermal inertia. As a result of the decreasing superheat, both EXVs then reduce their opening, resulting in an increase in suction superheat at both compressor ports. Additionally, the MT evaporator capacity drops below the LT evaporator capacity momentarily because the lower HP compressor superheat prompts a more severe reduction in orifice diameter from the MT evaporator EXV than that of the LT evaporator EXV. However, a cyclic instability does not ensue because the valve tuning matches the system reasonably well and the rate of change of LT evaporator source temperature is smaller as it returns to the initial set point than it was during the initial excitation. Therefore the control scheme enables the system to absorb the excitation without experiencing a compressor suction superheat value below 4 °C.

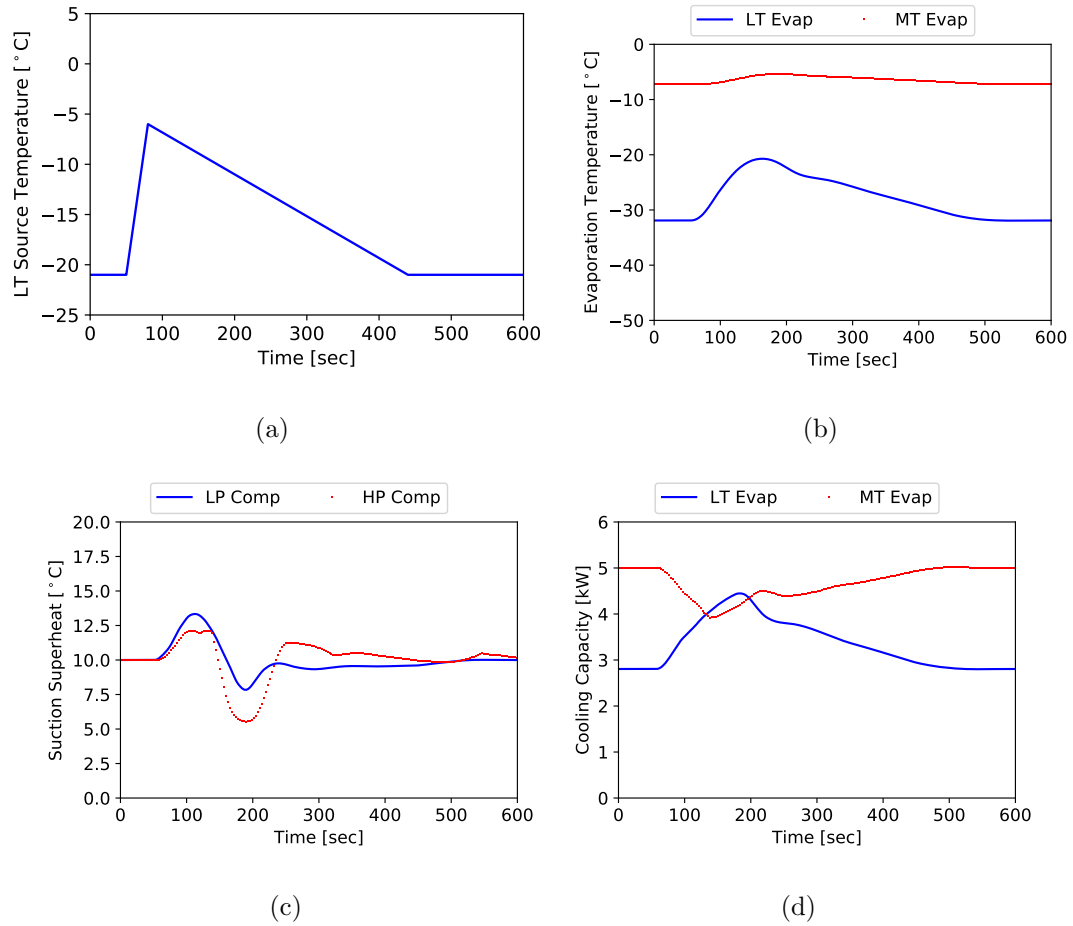


Fig. 6.15. Excitation controls development scenario simulated values of: (a) Excitation scenario source temperature; (b) Excitation scenario evaporation temperatures; (c) Excitation scenario compressor suction superheat; and, (d) Excitation scenario cooling capacities.

#### 6.4 Dynamic Model Validation and Evaluation Conclusions

This chapter presented steady state and transient validation of the dynamic model developed to predict the behavior and performance of the MT economization cycle in the test stand presented in Chapter 2. Following validation, the model was exercised in two transient scenarios to validate its use in developing control schemes. All three compressor stages agreed with data reasonably, but it was concluded that

the first two compressor stages would benefit from additional tuning of Pi group exponents or the application of another compressor mapping technique for increased accuracy. The two-stage compressor with intercooling was characterized effectively, despite the variable IC outlet states. Cycle steady state performance also resulted in reasonable trends with experimental data, but with the tendency of over-throttling the inlets to both evaporators. Physical sources of this error were identified and solutions to remedy them were proposed. The simulation transient behavior followed that of the experimental result, but did so at a consistently faster rate and at a smaller magnitude. Under-prediction of the rate of variation of charge distribution throughout the system is thought to be a significant cause of this trend, as dynamics immediately surrounding valve variations suggested that the model predicted similar behavior to the behavior experienced during testing. Finally, an LT evaporator pull down scenario and an LT evaporator excitation scenario were simulated to assess a PI control scheme applied to each EXV immediately upstream of each evaporator. The control scheme proved to retain safe compressor suction superheat values at all times, and avoided any sustained system instabilities in both scenarios. Future work is to improve the compressor performance characterization accuracy while retaining numerical robustness in dynamic modeling application. Furthermore, the EXV characterization strategy should be improved by more dedicated testing specifically for this purpose. Also, transient simulations should be improved by inclusion of the removed MT evaporator lines as well as increased accuracy of charge migration simulation. A starting point for the latter suggestion is characterization of the flash tank liquid level variation rate. Finally, the model should be exercised for increasingly-complex control schemes employing active variation of all system valves as well as tuning of PI controllers for responses that not only retain compressor suction superheat but also minimize system performance losses.



## 7. CONCLUSIONS, CHALLENGES, AND FUTURE WORK

### 7.1 Conclusions

This thesis aimed to contribute to numerical and experimental research concerning advanced transcritical CO<sub>2</sub> refrigeration technology. The scope of this work ranged from high-fidelity component design to system-level dynamics and control, and consisted of both steady state and transient numerical work along with extensive experimental efforts. In particular, the design, construction, and commissioning of a modular, two-evaporator, multi-stage transcritical CO<sub>2</sub> refrigeration cycle test stand was presented. The test stand was used to compare cycle architectures in an effort to provide a meaningful comparison of the relative benefits of common system modifications with the same compressor and heat exchanger losses. Among these modifications were open economization, compressor intercooling, a variable geometry ejector, and the application of a pump at the gas cooler outlet to provide increased ejector motive nozzle pressure differential. Maximum COP improvements of 6% and 5% were achieved with the economization and ejector cycles, respectively, and both the variable geometry ejector and pump were validated as effective means for ejector control. While the pump increased ejector efficiency up to 41%, its use resulted in a decrease in COP due to low pump and ejector efficiencies.

The successes and challenges associated with the experimental work conducted in this thesis highlighted that advanced cycle architectures can certainly increase cycle efficiency. However, the performance benefits of the modified cycles can be erased by improper sizing or selection of even one system component. Therefore, a well-designed simple refrigeration system that has a robust control scheme will likely outperform a more advanced cycle that was not as well-designed. However, if the designer of the

advanced cycle selects components to operated efficiently and also understands the cycle parameters that impact efficiency, then a design and associated control scheme can be developed that will result in increased efficiency.

An ejector design tool was presented and validated using experimental data, providing guidance on ejector design in contexts ranging from fundamental fluid mechanics and thermodynamics to manufacturing and leak-path prevention. This tool can be applied in multiple working fluids and will output physical ejector dimensions over a broad range of operating conditions and capacities. The model was able to predict ejector dimensions with an MAE of 3% to 4%, and was developed in a way that increased-fidelity sub-component models or component efficiency polynomials could be easily integrated. Following model validation, parametric studies on the impact of component efficiencies and system operating conditions on ejector geometry were conducted. Additionally, differences in the ejector geometry and operation which would result in maximum ejector efficiency versus maximum cycle COP were quantified and discussed.

The experimental testing of an ejector showed that the over and under-sizing of components within an ejector has proven to be a larger hindrance to its performance and applicability than having a nozzle that is 5% more efficient. This observation was in no small part why the ejector design focused on physical dimensions and ratios instead of optimal surface finishes and abstract nozzle geometries. Advanced design is absolutely necessary, but it would appear that all too often advanced design techniques are pursued without understanding of the fundamentals behind their development, resulting in poor performance. The purpose of the ejector model presented was to provide a design tool that was thoroughly explained and was both clear and robust. It is likely that an ejector design with higher-fidelity sub-models and more advanced geometries would result in a higher component efficiency. But the goal was to develop a tool that would usable, effective, and reasonably accurate to support a foundation of ejector design and research that could be used to push the envelope of this technology.

Further numerical efforts consisted of a dynamic model validated against experimental data from the test stand. The dynamic model featured open economization, experimentally-validated compressor maps, and valve characterization that required only the voltage input sent to the EXV stepper motor during experimental testing. The dynamic model agreed with steady state experimental data with a maximum MAE of 18.7% corresponding to the MT evaporator cooling capacity and with most other parameters falling within an MAE of 13%. Transient validation showed that the model followed the same behavior observed experimentally upon actuation of four different valves in the system, but generally predicted system reactions at a faster rate than the experiment. Finally, the dynamic model was able to successfully test control schemes applied during evaporator pull down and evaporator excitation simulations.

Comparing the dynamic modeling predictions to transient experimental data exposed the challenges in dynamic modeling and the nuances of system dynamics. Performing cause-and-effect analyses on inaccuracies in a model of this level of complexity provided context for in-depth discussion and assessment of system dynamics, the connection between components, and the relative timescales of the dynamics present in all thermal systems. Furthermore, relating these dynamics to discrepancies in their numerical predictions exposed which physical phenomena are the most challenging to characterize numerically. The model presented in this work provided an excellent test bed for these discussions, and its numerical deficiencies afforded the discussion of many challenges associated the numerical characterization of advanced thermal system dynamics as well as the identification of next steps to better capture these phenomena.

## 7.2 Challenges and Lessons Learned

Developing and commissioning a test stand as complex as the experiment used in this thesis was wrought with challenges. The traditional strategy of variable isolation to locate the cause of an error was a daunting task due to the sheer number of

variables and sources of error. While the designing and initial commissioning of the test stand brought challenges associated with preliminary modeling, procurement, design, and construction, two particular aspects of fine-tuning the test stand to provide thermodynamically-meaningful results required significantly more effort than any other single facet of the experimental work. The first was gaining confidence in the phase separation that occurred in both flash tanks. While the eventual solutions of adding capacitive liquid level sensors and a sight glass for visual redundancy sound simple enough, practical implementation of these solutions was anything but. The visual sight glasses needed to offer more than 25 cm of visualization to function over a broad range of charge levels, while also being rated down to  $-40\text{ }^{\circ}\text{C}$  as well as over 50 bar. This resulted in a very heavy component that was challenging to mount and connect properly. The capacitive sensors were less cumbersome, but calibration required precise liquid level control and active calibration at the same time, which was a significant challenge in practice. The three flash tank ports from the factory were taken by the one inlet and two outlets. This resulted in the need to cut three additional holes in the flash tank, weld high-pressure female threaded fittings, and then mount the two liquid level measurement devices. Despite tremendous care from an experienced welder, the female threads warped slightly, resulting in a long process of repairs and additional sealant. Lessons learned from the liquid level measurement device installation would be to weld stainless steel tubes to the additional flash tank holes and connect swage fittings, as was done on the initial three ports. This will require more space on the test stand because the studs would stick out further, but would be well worth it. If female fittings are a must, tremendous care should be taken to avoid galling with stainless steel on stainless steel threads, and Loctite sealant specifically for high-temperature applications should be applied. There is no easy way around the capacitive calibration, as control of liquid  $\text{CO}_2$  can require challenging operating conditions.

The second of the most significant experimental challenges was closure of the evaporator energy balance between the refrigerant and secondary loop. Many iterations

of sensor calibration, simplified cycle testing, and fluid property characterization side experiments culminated in the following key points to closing the secondary loop. The first was to run the test stand in simplified architectures such that the variables can be minimized, and increase the complexity only once the energy balance is closed for the simplest of experimental cycle architectures. Of course, this is only effective if the energy balance for the simplified cycle can be closed. The challenges faced even with the simplified cycle were flow rate measurement and the characterization of the EG properties used in the secondary loop. On the refrigerant-side, two of the three Coriolis mass flow meters were located at the outlets of evaporators. While many operating conditions should result in single-phase vapor where the Coriolis flow meters were placed, this was not always the case. The combination of intermittent two-phase flow as well as possible oil led to unreliable measurements. The additional oil was due to liquid refrigerant resting in the evaporators and leaving a disproportionate amount of oil that was then passed through the flow meters upon startup. On the EG-side, the specific gravity of the fluid was measured to try and estimate the EG concentration, but the fluid was not pure EG and attempted specific heat and density characterization proved to be futile. Therefore, it is recommended to replace existing heat transfer fluid with a known concentration of EG if a secondary fluid is inherited for a project. The final lesson learned here was that turbine flow meters placed in the EG line are not accurate across their entire range due to non-linearity of the conversion factor of pulses per minute to flow rates below 10% and above 90% of their rated volumetric flow rates.

From an operation perspective, the first-stage compressor should be replaced with a compressor that is optimized for booster operation and lower evaporation temperature, and the two-stage compressor was found to be slightly undersized. This led to a limitation on compressor current draw and prevented higher gas cooling pressures from being reached and thus, the gas cooling pressure corresponding to a maximum COP was unable to be reached at high ambient conditions.

Challenges and lessons learned from the steady state ejector modeling centered around numerical robustness and propagation of error throughout the model. In particular, the connection of sub-models in numerical series resulted in propagation of error and thus, reduced the accuracy and chance of convergence of models downstream. For example, if the motive nozzle diameter calculation was on the outer limits of the tolerance of the solver, the constant diameter ratio between the motive and suction nozzles would result in error for the suction nozzle. More challenging yet would be the impact the outputs from the nozzles would have on the mixing section solution. The challenge of sub-model error propagation led to a decreased number of converging solutions, and the lesson learned was to defined control volumes such that conservation of energy could be assessed with minimal consideration of previous sub-model outputs. For example, defining the control volume used to assess conservation of energy at the mixing section outlet as the mixing section outlet to the inlets to both nozzles. Defining the control volume in this way would reduce the impact of nozzle sub-model errors on the velocity convergence at the mixing section outlet.

Another aspect of the ejector model that proved to be a challenge was the solver sensitivity to initial guesses and variable bounds. While the bounds could remain constant for the simulations considered in this work, the initial guesses should be varied as a function of the nozzle inlet pressures to maximize the chance of convergence. The only numerical challenge that was based in physical phenomena was the calculation of the two-phase speed of sound. The definition of the two-phase speed of sound is dependent on many assumptions and there is still not a clear best solution. For example, the speed of sound of each respective phase for a given state can be calculated, but how the single-phase speeds of sound impact a homogeneous versus a non-homogeneous mixture is dependent upon slip ratios, equilibrium assumptions, and other challenges associated with two-phase flow phenomena. The two-phase speed of sound expression applied in the model presented herein served its purpose and was also the same applied in the development of the polynomials used for experimental validation. However, the two-phase speed of sound calculation applied in this model

returned an unreasonable trend at lower qualities and reached a numerical asymptote when the solution returned a saturated or sub-cooled liquid state. This proved to limit the ranges of inlet conditions that could be assessed, and the lesson learned would be to apply a correlation that allows a smooth and continuous transition in the speed of sound calculation from two-phase to single-phase liquid.

The most significant challenges associated with the dynamic modeling effort were associated with balancing accuracy with robustness during sub-model development and defining both initial conditions and sub-model characteristics that would result in consistent and efficient model convergence. Challenges associated with the compressor maps were rooted in developing the correlations from a broad enough dataset such that guess values from the dynamic model that were outside of the design envelope would still result in a reasonable mass flow rate from the compressor. This was vital in helping the simulation reach a feasible solution because all remaining sub-models require a feasible mass flow rate to return reasonable results. In short, miscalculation of the compressor mass flow rates will result in significant error in valve expansion as well as evaporator outlet superheat predictions and will significantly decrease the possibility of obtaining a feasible result. However, the compressor map should also fit the dataset well enough such that when the model converges it results in an accurate solution. The lesson learned with compressor mapping was that the compressor mapping technique applied to address the challenge of the two-stage compressor with intercooling needed further tuning to accurately predict compressor performance at lower evaporation temperatures. This situation exemplified the challenge of trade offs in model development, and while additional tuning was conducted in the development of the compressor model applied in this work, more in-depth modifications of the Pi group exponents would have further improved the model accuracy. Characterization of the EXV effective flow area was challenging as well, in that the discharge coefficient calculated from the data was more constant for the sub-critical EXVs than the gas cooler outlet EXV. This very well may have been due to sonic flow being achieved at the throat of the transcritical EXV, but spending the time to accurately characterize

all EXVs through use of a significant amount of experimental data is vital to model accuracy. The lesson learned in EXV characterization was ensuring that the calculations along the path from voltage to effective flow area with water to effective flow area for CO<sub>2</sub> and the ensuing discharge coefficient of the EXV needs to be assessed for each individual valve with at least 15 data points to obtain a reasonably-accurate solution.

Robust initial conditions to the dynamic model were directly related to the compressor maps resulting in a feasible solution. Three aspects of initial conditions need to be considered. The first is the pressure node, the second is the initial specific enthalpy, and the third is the initial wall temperature of tubes and heat exchangers. The first two were more apparent than the third, and not specifying the initial surface temperature of a component only became a hindrance once lines and geometry-based heat exchangers were applied. Not having selected these values made it difficult for the model to predict initial heat transfer gradients throughout the system, which is vital to predicting the initial direction that the next specific enthalpy and pressure values should trend towards. This underlines the importance of understanding the numerical structure behind how the the dynamic model applies differential algebraic equations. Essentially, specifying surface temperatures enables the model to accurately predict not only the state at the current time step, but also which direction the heat will flow to dictate the model guess for the direction of the next time state. The lesson learned was to ensure understanding of how physical specifications allow the model to operate, and how the strengths of the numerical strategies employed by the dynamic model can be taken full advantage of by strategic specification of initial conditions rooted in physical parameters.

### 7.3 Future Work

Experimental future work consists of removing the flash tank upstream of the LT evaporator in order to improve system dynamics and the addition at least one IHX.



The additional IHXs should be placed at the outlet of the gas cooler to facilitate use of the CO<sub>2</sub> pump at higher ambient conditions, as well as at the outlet of the MT flash tank liquid outlet. The latter application will allow movement of the Coriolis mass flow meter currently located at the LT evaporator outlet to the outlet of the new IHX, thus increasing the chance of a reliable single-phase liquid measurement. An ejector optimized for the test stand capacity with smaller mixing section and suction nozzle diameters should also be developed. The flash gas bypass MVs should be replaced with EXVs for electronic control. Finally, PI controllers should be applied to the EXVs to increase stand robustness and automation.

Future work for the ejector design tool is to implement higher-fidelity sub-component models. The ultimate goal would be to transition the model from its current black-box state towards a white-box model that takes complex two-phase flow phenomena into account well enough that experimentally-derived efficiency polynomials are no longer required to produce accurate predictions. In particular, sonic and supersonic two-phase flow correlations should be applied in the context of a non-homogeneous two-phase nozzle model for both motive and suction nozzles. Mixing losses and non-homogeneous flow with friction and heat losses should be assessed through application of modified Rayleigh or Fanno flow predictions in the mixing section. Finally, a model of similar fidelity to those developed for the nozzles should be applied to the diffuser for a more accurate outlet state prediction.

The sub-models applied to the dynamic model are the first focus in this context of the dynamic model future work. Compressor maps with more appropriate correlation exponents or principles should be applied to reduce inaccuracies imparted by this portion on the rest of the model. Furthermore, care should be taken to validate variable speed compressor maps to increase the range of applicability of the model. Added effort should be spent to characterize the EXVs more accurately, possibly even with a dedicated test section, such that the voltage from the experiment can be converted to an effective flow area more accurately. With the removal of the second flash tank recommended in the experimental portion of the next steps, new

experimental data should be taken and used for model validation. From a transient perspective, convective heat transfer and charge distribution dynamics should be investigated thoroughly. In particular, flash tank liquid level dynamics should be compared to experimental dynamics and tuned with separation efficiencies or delays accordingly. From a controls perspective, PI controllers should be applied to each valve on the system to develop control schemes that not only prioritize compressor safety but also minimize performance losses in transient scenarios.

## APPENDICES

## A. APPENDIX A: TABULATED EXPERIMENTAL STEADY STATE DATA

This appendix contains raw data as well as additional post-processed data used in this thesis. For the steady state parametric testing from Section 5, the following tests are reported:

- Tests 1 - 19: Baseline cycle at 14 °C, 19 °C, 24 °C, and 28 °C ambient conditions. Raw data is provided in Tables A.1 through A.10, and post-processed data is provided in Tables A.11 through A.18.
- Tests 20 - 35: MT economization cycle at 14 °C, 19 °C, 24 °C, and 28 °C ambient conditions. Raw data is provided in Tables A.19 through A.23, and post-processed data is provided in Tables A.24 through A.27.
- Tests 36 - 49: Ejector cycle at 14 °C, 19 °C, 24 °C, and 28 °C ambient conditions. Raw data is provided in Tables A.28 through A.32, and post-processed data is provided in Tables A.33 through A.36.
- Tests 50 - 58: Ejector and pump cycle at 14 °C and 19 °C ambient conditions. Raw data is provided in Tables A.37 through A.42, and post-processed data is provided in Tables A.43 through A.47.

The equation of state for CO<sub>2</sub> is provided by Span and Wagner [143] with a reference point for specific enthalpy and specific entropy of 293.15 K and 101.325 kPa.

Table A.1.  
Baseline cycle, temperatures 1 of 2, steady state raw data, tests 1 of 2.

Test	T21.ai	T1_Suc_LP	T2_Dis_LP	T3_Suc_HP	T4_IC.in	T5_IC.out	T6_GC.in	T7_GC.out	T8_MTE.in
[-]	[deg C]	[deg C]	[deg C]	[deg C]	[deg C]	[deg C]	[deg C]	[deg C]	[deg C]
1	14.53	-15.93	70.48	1.14	64.85	20.66	68.25	17.63	-8.53
2	14.25	-16.47	73.79	4.05	60.92	20.38	61.16	18.30	-8.02
3	14.17	-16.44	72.02	1.66	59.53	20.08	57.01	19.09	-8.04
4	13.95	-16.39	73.24	3.87	58.33	19.71	53.06	20.81	-8.08
5	13.85	-16.14	69.06	3.73	59.50	19.23	55.87	19.51	-9.39
6	13.88	-16.40	72.50	3.32	58.56	19.59	54.40	20.06	-8.62
7	19.35	-15.81	71.90	3.39	71.97	25.83	79.82	22.33	-9.32
8	19.36	-15.42	75.74	4.56	65.48	25.55	63.96	25.15	-8.14
9	19.30	-15.81	75.80	3.39	68.64	25.83	70.48	23.57	-8.47
10	19.49	-16.04	74.33	4.45	69.65	25.84	73.86	23.07	-8.20

Table A.2.  
Baseline cycle, temperatures 1 of 2, steady state raw data, tests 2 of 2.

Test	T21.ai	T1_Suc_LP	T2_Dis_LP	T3_Suc_HP	T4_IC.in	T5_IC.out	T6_GC.in	T7_GC.out	T8_MTE.in
[-]	[deg C]	[deg C]	[deg C]	[deg C]	[deg C]	[deg C]	[deg C]	[deg C]	[deg C]
11	19.34	-16.08	74.69	3.92	66.25	25.62	64.52	25.09	-7.19
12	23.65	-15.62	75.12	3.98	70.69	30.08	77.18	27.97	-7.84
13	23.61	-15.71	76.71	5.28	66.22	29.83	65.97	30.71	-6.49
14	23.77	-15.47	79.21	5.05	68.54	30.27	69.78	29.68	-6.30
15	27.88	-14.87	72.65	7.84	73.39	34.17	78.95	32.64	-5.66
16	27.90	-15.49	74.12	6.85	70.82	34.01	75.19	33.38	-5.25
17	28.05	-15.07	74.97	6.46	69.53	34.07	71.89	34.06	-4.65
18	27.96	-14.73	77.31	9.17	68.34	34.23	66.73	33.62	-3.43
19	27.81	-15.01	80.36	9.37	66.52	34.56	62.21	32.34	-2.01

Table A.3.  
Baseline cycle, temperatures 2 of 2, steady state raw data, tests 1 of 2.

Test	T9_MTE_out	T10_Suc_Noz_in	T11_LTE_out	T12_MTw_in	T13_MTw_out	T14_LTw_in	T15_LTw_out	T19_LTE_in
[-]	[deg C]	[deg C]	[deg C]	[deg C]	[deg C]	[deg C]	[deg C]	[deg C]
1	-8.41	-7.87	-19.27	2.92	-7.09	-19.93	-23.90	-28.46
2	-7.71	-7.15	-19.80	3.54	-6.72	-20.44	-24.19	-27.52
3	-7.92	-4.65	-20.04	3.41	-6.73	-20.83	-24.26	-27.94
4	-7.87	-1.15	-19.72	3.36	-6.64	-20.40	-23.94	-27.89
5	-8.98	-1.59	-19.35	1.84	-7.98	-20.00	-23.58	-27.64
6	-8.10	-1.69	-19.90	2.99	-7.07	-20.55	-24.26	-29.16
7	-9.09	-3.82	-19.78	1.29	-7.80	-20.58	-23.92	-28.72
8	-8.07	-3.77	-19.47	1.50	-7.22	-20.29	-23.68	-27.49
9	-8.42	-6.75	-19.76	1.57	-7.38	-20.54	-24.13	-28.37
10	-7.86	-2.96	-20.08	2.48	-6.88	-20.87	-24.30	-28.70

Table A.4.  
Baseline cycle, temperatures 2 of 2, steady state raw data, tests 2 of 2.

Test	T9_MTE_out	T10_Suc_Noz_in	T11_LTE_out	T12_MTw_in	T13_MTw_out	T14_LTw_in	T15_LTw_out	T19_LTE_in
[-]	[deg C]	[deg C]	[deg C]	[deg C]	[deg C]	[deg C]	[deg C]	[deg C]
11	-7.12	-5.42	-20.00	2.93	-6.14	-20.83	-24.22	-28.15
12	-7.91	-6.72	-20.13	1.64	-6.75	-21.02	-24.00	-28.46
13	-6.64	-1.20	-20.14	2.08	-5.63	-20.97	-23.73	-28.05
14	-6.41	-5.10	-20.10	2.66	-5.61	-20.97	-23.94	-28.05
15	-5.16	-4.56	-19.87	3.05	-4.71	-20.81	-23.74	-27.38
16	-5.30	-3.01	-20.27	3.07	-4.40	-20.81	-23.51	-27.03
17	-4.84	-0.59	-19.91	3.13	-3.90	-20.78	-23.33	-27.36
18	-3.15	3.67	-19.74	3.23	-2.99	-20.70	-23.05	-27.37
19	-2.12	6.20	-19.74	3.38	-1.85	-20.63	-22.57	-26.82



Table A.5.  
Baseline cycle, pressures 1 of 2, steady state raw data, tests 1 of 2.

Test	P1_Suc_LP	P2_Dis_LP	P3_Suc_HP	P4_IC_in	P5_IC_out	P6_GC_in	P7_GC_out	P8_Ej_out	P9_MT_FT_out
[-]	[kPa]	[kPa]	[kPa]	[kPa]	[kPa]	[kPa]	[kPa]	[kPa]	[kPa]
1	1455	2781	2699	4627	4606	8463	8343	2800	2729
2	1500	2823	2734	4636	4616	7801	7687	2864	2765
3	1481	2820	2732	4615	4596	7373	7258	3078	2765
4	1483	2815	2724	4557	4541	6952	6848	3384	2757
5	1492	2716	2628	4448	4429	7088	6981	3337	2662
6	1420	2771	2687	4519	4505	7034	6929	3331	2718
7	1449	2711	2619	4697	4648	9205	9092	2709	2662
8	1503	2812	2710	4728	4685	7598	7508	3128	2758
9	1465	2784	2688	4732	4690	8231	8131	2879	2733
10	1434	2799	2707	4768	4730	8675	8572	2809	2750

Table A.6.

Baseline cycle, pressures 1 of 2, steady state raw data, tests 2 of 2.

Test	P1_Suc_LP	P2_Dis_LP	P3_Suc_HP	P4_IC_in	P5_IC_out	P6_GC_in	P7_GC_out	P8_Ej_out	P9_MT_FT_out
[-]	[kPa]	[kPa]	[kPa]	[kPa]	[kPa]	[kPa]	[kPa]	[kPa]	[kPa]
11	1479	2863	2768	4789	4748	7719	7624	2969	2813
12	1460	2814	2726	4930	4895	8817	8718	2847	2766
13	1482	2914	2819	4994	4957	7769	7680	3327	2863
14	1480	2943	2854	5036	5000	8176	8084	2998	2890
15	1513	3001	2912	5222	5184	9048	8927	3055	2947
16	1515	3030	2937	5263	5225	8730	8612	3189	2975
17	1511	3074	2980	5301	5264	8438	8324	3405	3018
18	1512	3168	3070	5381	5338	7987	7869	3813	3110
19	1526	3286	3184	5532	5484	7715	7586	4050	3224

Table A.7.  
Baseline cycle, pressures 2 of 2, steady state raw data, tests 1 of 2.

Test P10_MTE_in P11_MTE_out P12_Suc_Noz_in P13_LTE_in P14_LTE_out P15_LT_FT_in									
[-]	[kPa]	[kPa]	[kPa]	[kPa]	[kPa]	[kPa]	[kPa]	[kPa]	[kPa]
1	2759	2745	2803	1460	1476	2764			
2	2797	2782	2862	1504	1526	2819			
3	2799	2783	3071	1485	1508	3031			
4	2792	2775	3369	1487	1512	3330			
5	2692	2677	3320	1497	1523	3281			
6	2752	2735	3315	1424	1451	3280			
7	2695	2678	2735	1454	1464	2690			
8	2796	2777	3148	1507	1518	3103			
9	2768	2750	2901	1469	1480	2857			
10	2785	2767	2830	1449	1456	2788			

Table A.8.  
Baseline cycle, pressures 2 of 2, steady state raw data, tests 2 of 2.

Test P10_MTE_in P11_MTE_out P12_Suc_Noz_in P13_LTE_in P14_LTE_out P15_LT_FT_in						
[-]	[kPa]	[kPa]	[kPa]	[kPa]	[kPa]	[kPa]
11	2852	2832	2988	1481	1494	2944
12	2802	2778	2857	1462	1485	2810
13	2906	2877	3325	1485	1507	3279
14	2931	2905	3004	1482	1506	2957
15	2988	2961	3059	1512	1549	3009
16	3019	2989	3191	1529	1561	3142
17	3065	3033	3403	1512	1548	3354
18	3164	3128	3802	1511	1547	3757
19	3285	3245	4035	1541	1570	3986

Table A.9.  
Baseline cycle, additional measurements, steady state raw data, tests 1 of 2.

Test	V_dot_w_MT	V_dot_w_LT	W_dot_HPC	W_dot_LPC	W_dot_Fans	EXV_1	EXV_2	EXV_3	EXV_4
[-]	[liter/min]	[liter/min]	[W]	[W]	[W]	[V]	[V]	[V]	[V]
1	10.7	10.1	3862	1039	595	1.75	8.75	10	4.65
2	10.7	9.9	3693	1033	595	2	7.1	10	4.6
3	10.7	10.8	3572	1041	594	2.5	3.35	10	4.4
4	10.6	10.9	3447	1034	591	2.7	2.65	10	4.2
5	10.6	10.7	3491	1006	595	2.05	2.65	10	4.35
6	10.6	10.6	3473	1030	598	2.6	2.65	10	4
7	10.6	10.8	4028	1042	586	1.7	9	10	5
8	10.5	10.6	3610	1064	582	2.3	4.1	10	4.65
9	10.5	9.8	3777	1043	588	2	5.5	10	4.75
10	10.5	9.9	3911	1039	582	1.9	10	10	4.75

Table A.10.  
Baseline cycle, additional measurements, steady state raw data, tests 2 of 2.

Test	V_dot_w_MT	V_dot_w_LT	W_dot_HPC	W_dot_LPC	W_dot_Fans	EXV_1	EXV_2	EXV_3	EXV_4
[-]	[liter/min]	[liter/min]	[W]	[W]	[W]	[V]	[V]	[V]	[V]
11	10.5	10.3	3646	1056	581	2.75	5.75	10	4.75
12	10.5	10.7	4000	1106	575	2.1	10	10	5.1
13	10.5	10.8	3705	1120	576	3.25	3.55	10	4.7
14	10.5	10.8	3821	1155	574	2.5	9	10	4.9
15	10.8	11.1	4077	1068	582	2.7	9	10	5.175
16	10.8	11.1	4003	1071	582	2.9	5.1	10	4.95
17	10.8	11.2	3918	1086	588	2.7	3.9	10	4.85
18	10.8	11.3	3767	1106	587	3.5	3.55	10	4.5
19	10.8	11.4	3676	1128	587	3.85	4.3	10	4.45

Table A.11.  
Baseline cycle, specific enthalpies, steady state data, tests 1 of 2.

Test	h1	h2	h3	h4	h5	h6	h7	h8	h9	h10	h11	h12	h13
[ $-$ ]	[kJ/kg]	[kJ/kg]	[kJ/kg]	[kJ/kg]	[kJ/kg]	[kJ/kg]	[kJ/kg]	[kJ/kg]	[kJ/kg]	[kJ/kg]	[kJ/kg]	[kJ/kg]	[kJ/kg]
1	-55.1	19.1	-57.1	-3.0	-64.2	-39.4	-267.4	-267.4	-267.4	-71.5	-267.4	-267.4	-59.0
2	-56.5	22.2	-54.0	-7.8	-64.9	-43.7	-264.1	-264.1	-264.1	-71.3	-264.1	-264.1	-60.6
3	-56.1	20.4	-57.1	-9.3	-65.0	-45.3	-260.6	-260.6	-260.6	-71.7	-260.6	-260.6	-60.5
4	-56.1	21.7	-54.0	-10.2	-64.5	-46.4	-253.5	-253.5	-253.5	-71.4	-253.5	-253.5	-60.2
5	-56.0	18.1	-52.6	-7.7	-63.1	-43.4	-258.4	-258.4	-258.4	-70.8	-258.4	-258.4	-60.0
6	-55.0	21.3	-54.1	-9.5	-64.0	-45.2	-256.4	-256.4	-256.4	-70.8	-256.4	-256.4	-59.3
7	-54.9	21.1	-52.8	4.9	-56.1	-27.7	-255.8	-255.8	-255.8	-71.0	-255.8	-255.8	-59.4
8	-55.4	24.3	-52.9	-3.1	-57.2	-36.2	-240.6	-240.6	-240.6	-71.8	-240.6	-240.6	-60.1
9	-55.2	24.6	-54.0	0.6	-56.8	-32.7	-249.1	-249.1	-249.1	-71.7	-249.1	-249.1	-59.6
10	-54.9	22.9	-53.0	1.5	-57.5	-32.1	-252.2	-252.2	-252.2	-71.2	-252.2	-252.2	-59.6

Table A.12.  
Baseline cycle, specific enthalpies, steady state data, tests 2 of 2.

Test	h1	h2	h3	h4	h5	h6	h7	h8	h9	h10	h11	h12	h13
[ - ]	[kJ/kg]	[kJ/kg]	[kJ/kg]	[kJ/kg]	[kJ/kg]	[kJ/kg]	[kJ/kg]	[kJ/kg]	[kJ/kg]	[kJ/kg]	[kJ/kg]	[kJ/kg]	[kJ/kg]
11	-55.7	22.8	-54.8	-2.8	-58.2	-36.7	-241.5	-241.5	-241.5	-71.6	-241.5	-241.5	-60.2
12	-54.9	23.6	-53.9	1.3	-53.4	-28.0	-236.5	-236.5	-236.5	-71.5	-236.5	-236.5	-60.2
13	-55.3	24.5	-53.9	-4.8	-54.9	-34.9	-213.4	-213.4	-213.4	-71.9	-213.4	-213.4	-60.6
14	-55.1	26.9	-54.8	-2.3	-54.9	-33.3	-225.2	-225.2	-225.2	-72.2	-225.2	-225.2	-60.5
15	-55.0	19.6	-52.1	1.9	-51.5	-27.5	-218.9	-218.9	-218.9	-71.6	-218.9	-218.9	-61.1
16	-55.7	20.9	-53.9	-1.6	-52.5	-30.4	-211.6	-211.6	-211.6	-72.5	-211.6	-211.6	-61.7
17	-55.2	21.5	-55.1	-3.5	-53.0	-32.7	-201.4	-201.4	-201.4	-72.8	-201.4	-201.4	-61.1
18	-54.8	23.2	-53.1	-5.8	-54.0	-36.2	-179.0	-179.0	-179.0	-72.3	-179.0	-179.0	-60.9
19	-55.4	25.6	-54.8	-9.6	-55.9	-40.7	-157.0	-157.0	-157.0	-73.5	-157.0	-157.0	-61.3



Table A.13.  
Baseline cycle, pressures, steady state data, tests 1 of 2.

Test	p1	p2	p3	p4	p5	p6	p7	p8	p9	p10	p11	p12	p13
[-]	[kPa]	[kPa]	[kPa]	[kPa]	[kPa]	[kPa]	[kPa]	[kPa]	[kPa]	[kPa]	[kPa]	[kPa]	[kPa]
1	1455	2781	2699	4627	4606	8463	8343	2800	2761	2745	2764	1503	1476
2	1500	2823	2734	4636	4616	7801	7687	2864	2801	2782	2819	1550	1526
3	1481	2820	2732	4615	4596	7373	7258	3078	2799	2783	3031	1529	1508
4	1483	2815	2724	4557	4541	6952	6848	3384	2796	2775	3330	1532	1512
5	1492	2716	2628	4448	4429	7088	6981	3337	2695	2677	3281	1544	1523
6	1420	2771	2687	4519	4505	7034	6929	3331	2754	2735	3280	1469	1451
7	1449	2711	2619	4697	4648	9205	9092	2709	2700	2678	2690	1490	1464
8	1503	2812	2710	4728	4685	7598	7508	3128	2792	2777	3103	1552	1518
9	1465	2784	2688	4732	4690	8231	8131	2879	2766	2750	2857	1507	1480
10	1434	2799	2707	4768	4730	8675	8572	2809	2787	2767	2788	1491	1456

Table A.14.  
Baseline cycle, pressures, steady state data, tests 2 of 2.

Test	p1	p2	p3	p4	p5	p6	p7	p8	p9	p10	p11	p12	p13
[ - ]	[kPa]	[kPa]	[kPa]	[kPa]	[kPa]	[kPa]	[kPa]	[kPa]	[kPa]	[kPa]	[kPa]	[kPa]	[kPa]
11	1479	2863	2768	4789	4748	7719	7624	2969	2867	2832	2944	1519	1494
12	1460	2814	2726	4930	4895	8817	8718	2847	2816	2778	2810	1503	1485
13	1482	2914	2819	4994	4957	7769	7680	3327	2923	2877	3279	1523	1507
14	1480	2943	2854	5036	5000	8176	8084	2998	2939	2905	2957	1524	1506
15	1513	3001	2912	5222	5184	9048	8927	3055	2991	2961	3009	1558	1549
16	1515	3030	2937	5263	5225	8730	8612	3189	3025	2989	3142	1575	1561
17	1511	3074	2980	5301	5264	8438	8324	3405	3075	3033	3354	1558	1548
18	1512	3168	3070	5381	5338	7987	7869	3813	3179	3128	3757	1558	1547
19	1526	3286	3184	5532	5484	7715	7586	4050	3303	3245	3986	1587	1570

Table A.15.  
Baseline cycle, primary cycle parameters, steady state data, tests 1 of 2.

Test	m_dot_motive	m_dot_low	COP	Q_dot_LTE	Q_dot_MTE	Q_dot_IC	Q_dot_GC
[-]	[kg/s]	[kg/s]	[-]	[kW]	[kW]	[kW]	[kW]
1	0.045	0.011	1.48	2.2	6.7	2.7	10.2
2	0.045	0.010	1.52	2.1	6.8	2.6	10.0
3	0.046	0.010	1.54	2.1	6.7	2.6	9.9
4	0.047	0.011	1.57	2.1	6.6	2.6	9.8
5	0.045	0.011	1.54	2.1	6.5	2.5	9.7
6	0.047	0.011	1.58	2.2	6.6	2.6	9.9
7	0.043	0.010	1.30	2.0	6.0	2.6	9.7
8	0.045	0.011	1.34	2.0	5.7	2.4	9.2
9	0.043	0.010	1.33	2.0	5.9	2.5	9.4
10	0.044	0.010	1.33	1.9	6.1	2.6	9.6

Table A.16.  
Baseline cycle, primary cycle parameters, steady state data, tests 2 of 2.

Test	m_dot_motive	m_dot_low	COP	Q_dot_LTE	Q_dot_MTE	Q_dot_IC	Q_dot_GC
[-]	[kg/s]	[kg/s]	[-]	[kW]	[kW]	[kW]	[kW]
11	0.046	0.011	1.36	1.9	5.9	2.5	9.3
12	0.043	0.010	1.17	1.8	5.5	2.4	9.0
13	0.047	0.011	1.14	1.7	5.1	2.3	8.3
14	0.046	0.011	1.19	1.8	5.4	2.4	8.8
15	0.047	0.011	1.13	1.8	5.2	2.5	9.0
16	0.047	0.011	1.09	1.7	5.0	2.4	8.6
17	0.048	0.011	1.04	1.6	4.7	2.4	8.1
18	0.052	0.012	0.95	1.5	4.2	2.5	7.4
19	0.055	0.013	0.81	1.2	3.5	2.6	6.4

Table A.17.  
Baseline cycle, additional parameters, steady state data, tests 1 of 2.

Test	$Q_{\dot{\text{loss}}\_C1}$	$Q_{\dot{\text{loss}}\_C2}$	$Q_{\dot{\text{LT}}\_suc}$	$\delta Q_{h\_3}$	$W_{\dot{\text{evap}}\_fans}$
[-]	[kW]	[kW]	[kW]	[kW]	[kW]
1	0.25	0.34	0.04	0.33	0.5
2	0.24	0.63	0.04	0.16	0.5
3	0.26	0.47	0.04	0.27	0.5
4	0.18	0.51	0.05	0.20	0.5
5	0.21	0.57	0.04	0.13	0.5
6	0.19	0.51	0.05	0.24	0.5
7	0.27	0.36	0.05	0.17	0.5
8	0.18	0.42	0.05	0.22	0.5
9	0.22	0.36	0.05	0.23	0.5
10	0.28	0.42	0.05	0.13	0.5

Table A.18.  
Baseline cycle, additional parameters, steady state data, tests 2 of 2.

Test	Q-dot_loss_C1	Q-dot_loss_C2	Q-dot_LT_suc	delta_Q_h-3	W-dot_evap_fans
[-]	[kW]	[kW]	[kW]	[kW]	[kW]
11	0.22	0.30	0.05	0.24	0.5
12	0.32	0.52	0.05	0.19	0.5
13	0.25	0.49	0.06	0.21	0.5
14	0.27	0.41	0.06	0.27	0.5
15	0.21	0.42	0.07	0.13	0.5
16	0.22	0.49	0.07	0.16	0.5
17	0.22	0.46	0.07	0.22	0.5
18	0.13	0.40	0.08	0.20	0.5
19	0.09	0.34	0.08	0.24	0.5

Table A.19.

MT economization cycle, temperatures 1 of 2, steady state raw data.

Test	T21_ai	T1_Suc_LP	T2_Dis_LP	T3_Suc_HP	T4_IC_in	T5_IC_out	T6_GC_in	T7_GC_out	T8_MTE_in	T9_MTE_out
[-]	[deg C]	[deg C]	[deg C]	[deg C]	[deg C]	[deg C]	[deg C]	[deg C]	[deg C]	[deg C]
20	14.25	-16.47	73.79	4.05	60.92	20.38	61.16	18.30	-8.02	-7.71
21	14.63	-16.68	83.25	1.46	63.39	20.92	60.01	19.60	-8.88	-8.75
22	14.74	-15.86	88.13	1.24	63.63	21.21	68.16	18.21	-8.58	-8.44
23	14.48	-16.57	84.85	1.41	62.03	20.89	62.34	18.66	-8.63	-8.49
24	19.30	-15.39	80.94	6.64	62.54	25.48	57.86	27.85	-6.82	-6.61
25	19.32	-15.70	78.87	5.14	64.42	25.83	62.77	25.41	-6.89	-6.72
26	19.50	-15.68	81.76	5.48	63.83	25.83	63.46	25.27	-7.01	-6.82
27	19.45	-15.56	81.78	4.18	65.48	25.86	68.61	23.83	-7.47	-7.31
28	19.63	-15.23	81.28	3.60	68.17	26.21	76.44	22.67	-7.50	-7.35
29	19.47	-15.45	82.73	3.98	66.71	26.14	71.29	23.35	-7.22	-7.08
30	24.01	-16.74	87.37	3.97	68.30	30.90	72.71	29.19	-5.94	-5.81
31	23.95	-16.75	85.66	6.17	66.03	30.50	67.93	30.23	-5.74	-5.59
32	23.92	-15.85	88.90	7.19	66.23	30.64	65.24	31.16	-5.28	-5.13
33	28.40	-14.90	85.85	8.12	63.98	35.47	59.52	32.92	-1.26	-1.08
34	28.66	-15.81	81.86	4.36	67.13	35.38	67.71	34.84	-3.19	-3.06
35	28.59	-15.19	79.71	8.21	70.46	35.38	74.71	34.32	-4.50	-4.39

Table A.20.  
MT economization cycle, temperatures 2 of 2, steady state raw data.

Test	T10_Suc_Noz_in	T11_LTE_out	T12_MTw_in	T13_MTw_out	T14_LTw_in	T15_LTw_out	T19_LTE_in
[-]	[deg C]	[deg C]	[deg C]	[deg C]	[deg C]	[deg C]	[deg C]
20	-7.15	-19.80	3.54	-6.72	-20.44	-24.19	-27.52
21	-8.44	-20.90	1.52	-7.34	-21.78	-25.80	-31.21
22	-8.23	-19.86	2.55	-6.77	-20.73	-24.89	-30.27
23	-8.23	-20.58	2.22	-6.86	-21.22	-25.29	-29.81
24	-6.30	-19.87	3.01	-4.59	-20.74	-25.41	-30.09
25	-6.59	-20.05	3.18	-5.37	-20.94	-25.47	-30.11
26	-6.64	-20.24	3.15	-5.61	-21.17	-25.94	-30.91
27	-7.09	-19.97	2.99	-5.97	-20.75	-25.52	-31.20
28	-6.84	-19.71	3.06	-5.89	-20.45	-25.14	-30.36
29	-6.85	-19.81	3.12	-5.76	-20.62	-25.28	-29.78
30	-5.32	-21.72	3.31	-4.51	-21.13	-25.31	-28.92
31	-5.13	-21.52	3.36	-4.15	-20.91	-25.21	-28.77
32	-4.52	-20.21	3.43	-3.67	-20.91	-25.17	-29.67
33	-0.38	-19.95	3.25	-0.31	-20.80	-24.93	-28.63
34	-2.58	-20.89	3.07	-1.95	-20.87	-25.36	-27.57
35	-4.16	-20.33	2.97	-3.34	-20.99	-25.59	-28.01



Table A.21.  
MT economization cycle, pressures 1 of 2, steady state raw data.

Test	P1_Suc_LP	P2_Dis_LP	P3_Suc_HP	P4_IC_in	P5_IC_out	P6_GC_in	P7_GC_out	P8_Ej_out	P9_MT_FT_out
[-]	[kPa]	[kPa]	[kPa]	[kPa]	[kPa]	[kPa]	[kPa]	[kPa]	[kPa]
20	1500	2823	2734	4636	4616	7801	7687	2864	2765
21	1333	2773	2693	4551	4528	7398	7293	2739	2679
22	1376	2798	2716	4683	4659	8508	8385	2755	2704
23	1398	2793	2712	4626	4604	7811	7697	2753	2700
24	1376	2940	2824	4868	4791	7245	7148	2894	2812
25	1380	2927	2814	4887	4815	7710	7608	2872	2802
26	1343	2916	2800	4896	4827	7819	7718	2866	2786
27	1326	2880	2768	4899	4834	8376	8264	2826	2753
28	1363	2881	2772	4950	4887	9307	9175	2837	2767
29	1396	2904	2795	4960	4906	8747	8628	2859	2789
30	1430	3013	2933	5209	5176	8734	8632	2974	2918
31	1436	3033	2954	5198	5164	8243	8146	2994	2936
32	1403	3064	2990	5195	5160	7918	7826	3035	2972
33	1441	3419	3336	5828	5771	7792	7672	3424	3317
34	1490	3248	3162	5621	5568	8340	8236	3225	3146
35	1474	3132	3050	5476	5428	8868	8764	3090	3031

Table A.22.  
MT economization cycle, pressures 2 of 2, steady state raw data.

Test P10_MTE_in P11_MTE_out P12_Suc_Noz_in P13_LTE_in P14_LTE_out P15_LT_FT_in									
[-]	[kPa]	[kPa]	[kPa]	[kPa]	[kPa]	[kPa]	[kPa]	[kPa]	[kPa]
20	2797	2782	2862	1504	1526	2819			
21	2729	2730	2753	1327	1350	2735			
22	2752	2752	2768	1369	1397	2749			
23	2747	2748	2766	1392	1419	2747			
24	2899	2900	2922	1373	1386	2902			
25	2889	2888	2899	1377	1390	2882			
26	2877	2876	2893	1340	1353	2876			
27	2842	2841	2853	1325	1338	2837			
28	2843	2842	2864	1363	1375	2848			
29	2864	2863	2883	1391	1406	2866			
30	2968	2966	2979	1434	1465	2963			
31	2987	2986	2998	1436	1465	2980			
32	3017	3016	3036	1399	1436	3019			
33	3371	3369	3431	1433	1456	3411			
34	3202	3200	3237	1482	1505	3220			
35	3087	3085	3103	1467	1490	3089			

Table A.23.  
MT economization cycle, additional measurements, steady state raw data.

Test	V_dot_w_MT	V_dot_w_LT	W_dot_HPC	W_dot_LPC	W_dot_Fans	EXV_1	EXV_2	EXV_3	EXV_4	MTFT
[-]	[liter/min]	[liter/min]	[W]	[W]	[W]	[V]	[V]	[V]	[V]	[cm] [%]
20	10.7	9.9	3693	1033	595	2	7.1	10	4.6	0.05 0.25
21	10.7	11.9	3531	1067	588	2	4	10	2.5	7.54 34.34
22	10.7	11.7	3896	1058	587	2.25	5	10	2.55	5.96 27.13
23	10.7	11.8	3692	1049	589	1.9	4.5	10	2.575	6.28 28.61
24	10.4	9.9	3509	1093	583	3.3	4.1	10	2.6	4.55 20.76
25	10.4	9.9	3657	1091	584	2.3	7.85	10	2.55	2.91 13.31
26	10.6	10.0	3707	1076	581	2.25	5.25	10	2.55	2.93 13.38
27	10.6	10.0	3870	1068	582	2.2	6.8	10	2.55	2.24 10.22
28	10.6	9.9	4114	1069	589	1.8	4.8	10	2.56	1.33 6.10
29	10.6	10.0	3976	1068	583	1.9	5.15	10	2.575	1.54 7.07
30	10.5	10.5	4000	1193	582	2.25	7	10	2.8625	11.12 50.66
31	10.4	10.4	3859	1204	574	3	7.8	10	2.8	11.85 53.99
32	10.4	10.4	3727	1225	571	2.8	4.25	10	2.845	12.87 58.64
33	10.4	10.3	3716	1149	572	4	2.45	10	3.01	13.78 62.76
34	10.4	10.2	3920	1121	563	3	3.6	10	2.9	13.56 61.78
35	10.3	10.2	4074	1096	565	3	5.1	10	3	13.11 59.78

Table A.24.  
MT economization cycle, specific enthalpies, steady state data.

Test	h1	h2	h3	h4	h5	h6	h7	h8	h9	h10	h11	h12	h13	h14
[-]	[kJ/kg]	[kJ/kg]	[kJ/kg]	[kJ/kg]	[kJ/kg]	[kJ/kg]	[kJ/kg]	[kJ/kg]	[kJ/kg]	[kJ/kg]	[kJ/kg]	[kJ/kg]	[kJ/kg]	[kJ/kg]
20	-56.5	22.2	-54.0	-7.8	-64.9	-43.7	-264.1	-264.1	-323.9	-71.3	-323.9	-323.9	-60.6	-72.5
21	-53.8	32.3	-56.6	-4.0	-62.1	-40.4	-259.1	-259.1	-327.5	-71.7	-327.5	-327.5	-58.5	-72.0
22	-53.7	37.1	-57.3	-5.0	-64.2	-40.2	-265.9	-265.9	-327.1	-71.7	-327.1	-327.1	-58.2	-72.1
23	-54.8	33.8	-57.0	-6.3	-63.7	-41.7	-263.0	-263.0	-327.1	-71.7	-327.1	-327.1	-59.4	-72.1
24	-53.2	28.7	-52.2	-8.1	-59.3	-42.1	-224.2	-224.2	-323.0	-72.4	-323.0	-323.0	-58.0	-72.7
25	-53.6	26.7	-54.0	-6.0	-59.1	-39.6	-240.2	-240.2	-323.7	-72.3	-323.7	-323.7	-58.3	-72.6
26	-53.0	29.7	-53.3	-6.8	-59.4	-39.8	-241.3	-241.3	-323.8	-72.2	-323.8	-323.8	-57.8	-72.5
27	-52.5	30.0	-54.4	-4.8	-59.4	-37.7	-248.8	-248.8	-325.0	-72.1	-325.0	-325.0	-57.3	-72.4
28	-52.8	29.5	-55.2	-2.0	-59.8	-34.7	-255.0	-255.0	-324.7	-72.2	-324.7	-324.7	-57.7	-72.4
29	-53.6	30.8	-55.1	-3.8	-60.3	-37.4	-251.5	-251.5	-324.0	-72.3	-324.0	-324.0	-58.3	-72.5
30	-55.5	34.8	-57.6	-4.2	-56.9	-34.7	-231.4	-231.4	-320.8	-72.8	-320.8	-320.8	-61.5	-73.0
31	-55.6	32.9	-55.1	-7.0	-57.4	-37.3	-223.1	-223.1	-320.2	-72.9	-320.2	-320.2	-61.3	-73.1
32	-54.1	36.1	-54.3	-6.7	-57.1	-38.0	-213.1	-213.1	-319.0	-72.9	-319.0	-319.0	-59.3	-73.3
33	-53.8	30.4	-59.3	-16.0	-59.5	-46.6	-155.2	-155.2	-308.4	-74.8	-308.4	-308.4	-59.4	-75.5
34	-55.6	27.4	-61.5	-9.7	-56.0	-38.9	-188.9	-188.9	-313.8	-74.0	-313.8	-313.8	-61.4	-74.3
35	-54.7	26.0	-54.0	-4.0	-53.5	-32.8	-208.3	-208.3	-317.5	-73.4	-317.5	-317.5	-60.5	-73.6

Table A.25.

MT economization cycle, specific enthalpies and pressures, steady state data.

Test	h15	p1	p2	p3	p4	p5	p6	p7	p8	p9	p10	p11	p12	p13	p14	p15
[-]	[kJ/kg]	[kPa]	[kPa]	[kPa]	[kPa]	[kPa]	[kPa]	[kPa]	[kPa]	[kPa]	[kPa]	[kPa]	[kPa]	[kPa]	[kPa]	[kPa]
20	-323.9	1500	2823	2734	4636	4616	7801	7687	2864	2801	2782	2819	1550	1526	2864	2864
21	-327.5	1333	2773	2693	4551	4528	7398	7293	2739	2734	2730	2735	1371	1350	2739	2739
22	-327.1	1376	2798	2716	4683	4659	8508	8385	2755	2757	2752	2749	1415	1397	2755	2755
23	-327.1	1398	2793	2712	4626	4604	7811	7697	2753	2753	2748	2747	1437	1419	2753	2753
24	-323.0	1376	2940	2824	4868	4791	7245	7148	2894	2897	2900	2902	1424	1386	2894	2894
25	-323.7	1380	2927	2814	4887	4815	7710	7608	2872	2891	2888	2882	1422	1390	2872	2872
26	-323.8	1343	2916	2800	4896	4827	7819	7718	2866	2881	2876	2876	1385	1353	2866	2866
27	-325.0	1326	2880	2768	4899	4834	8376	8264	2826	2844	2841	2837	1371	1338	2826	2826
28	-324.7	1363	2881	2772	4950	4887	9307	9175	2837	2842	2842	2848	1410	1375	2837	2837
29	-324.0	1396	2904	2795	4960	4906	8747	8628	2859	2865	2863	2866	1438	1406	2859	2859
30	-320.8	1430	3013	2933	5209	5176	8734	8632	2974	2968	2966	2963	1480	1465	2974	2974
31	-320.2	1436	3033	2954	5198	5164	8243	8146	2994	2984	2986	2980	1488	1465	2994	2994
32	-319.0	1403	3064	2990	5195	5160	7918	7826	3035	3022	3016	3019	1444	1436	3035	3035
33	-308.4	1441	3419	3336	5828	5771	7792	7672	3424	3370	3369	3411	1495	1456	3424	3424
34	-313.8	1490	3248	3162	5621	5568	8340	8236	3225	3200	3200	3220	1548	1505	3225	3225
35	-317.5	1474	3132	3050	5476	5428	8868	8764	3090	3088	3085	3089	1526	1490	3090	3090

Table A.26.  
MT economization cycle, primary cycle parameters, steady state data.

Test	m_dot_motive	m_dot_low	m_dot_MTE	m_dot_vap	COP	Q_dot_LTE	Q_dot_MTE	Q_dot_IC	Q_dot_GC
[-]	[kg/s]	[kg/s]	[kg/s]	[kg/s]	[-]	[kW]	[kW]	[kW]	[kW]
20	0.046	0.008	0.027	0.011	1.52	2.1	6.8	2.6	10.1
21	0.045	0.010	0.023	0.012	1.50	2.6	5.9	2.6	9.8
22	0.045	0.010	0.024	0.011	1.47	2.7	6.2	2.7	10.2
23	0.045	0.010	0.024	0.011	1.49	2.7	6.0	2.6	9.9
24	0.048	0.010	0.020	0.019	1.32	2.6	4.9	2.5	8.8
25	0.047	0.009	0.022	0.016	1.38	2.5	5.5	2.5	9.4
26	0.049	0.010	0.023	0.016	1.44	2.7	5.8	2.6	9.9
27	0.048	0.010	0.023	0.014	1.42	2.6	5.9	2.6	10.1
28	0.046	0.010	0.024	0.013	1.36	2.6	5.9	2.7	10.1
29	0.046	0.010	0.023	0.013	1.38	2.6	5.9	2.6	9.9
30	0.047	0.009	0.021	0.017	1.20	2.4	5.1	2.5	9.2
31	0.048	0.010	0.020	0.019	1.20	2.5	4.9	2.4	9.0
32	0.050	0.009	0.019	0.021	1.18	2.5	4.6	2.5	8.7
33	0.057	0.009	0.010	0.037	0.79	2.4	2.3	2.5	6.2
34	0.049	0.010	0.014	0.026	0.95	2.5	3.3	2.3	7.4
35	0.048	0.010	0.017	0.022	1.07	2.6	4.1	2.4	8.5

MT economization cycle, additional parameters, steady state data.  
Table A.27.

Test Q_dot_loss_C1 Q_dot_loss_C2 Q_dot_LT_suc delta_Q_h_3 W_dot_evap_fans						
[ - ]	[kW]	[kW]	[kW]	[kW]	[kW]	[kW]
20	0.42	0.62	0.03	-0.07	0.5	0.5
21	0.22	0.19	0.05	0.34	0.5	0.5
22	0.15	0.45	0.05	0.43	0.5	0.5
23	0.17	0.44	0.05	0.39	0.5	0.5
24	0.30	0.54	0.05	-0.01	0.5	0.5
25	0.34	0.48	0.04	0.06	0.5	0.5
26	0.25	0.46	0.05	0.08	0.5	0.5
27	0.25	0.47	0.05	0.16	0.5	0.5
28	0.27	0.52	0.05	0.20	0.5	0.5
29	0.25	0.53	0.05	0.20	0.5	0.5
30	0.35	0.46	0.06	0.29	0.5	0.5
31	0.35	0.56	0.05	0.15	0.5	0.5
32	0.37	0.41	0.05	0.10	0.5	0.5
33	0.35	0.53	0.05	0.09	0.5	0.5
34	0.29	0.52	0.06	0.39	0.5	0.5
35	0.28	0.65	0.06	0.06	0.5	0.5

Table A.28.  
Ejector cycle, temperatures 1 of 2, steady state raw data.

Test	T21_ai	T1_Suc_LP	T2_Dis_LP	T3_Suc_HP	T4_IC_in	T5_IC_out	T6_GC_in	T7_GC_out	T8_MTE_in	T9_MTE_out
[-]	[deg C]	[deg C]	[deg C]	[deg C]	[deg C]	[deg C]	[deg C]	[deg C]	[deg C]	[deg C]
36	14.38	-15.74	86.51	5.83	59.59	20.79	51.63	24.25	-8.99	-8.24
37	14.48	-15.11	91.21	5.94	59.93	20.63	53.79	22.63	-10.30	-5.61
38	14.27	-15.85	92.87	5.01	58.86	20.26	56.35	20.68	-9.96	-7.39
39	19.46	-15.63	79.49	6.32	65.41	25.90	66.40	24.50	-9.34	-5.59
40	19.56	-15.64	88.12	7.31	64.90	26.06	62.92	25.39	-9.77	-1.21
41	19.28	-16.40	92.36	7.24	63.68	25.61	60.29	26.31	-8.77	-8.52
42	23.81	-15.44	91.55	7.58	65.36	30.74	61.59	31.28	-7.10	2.87
43	23.86	-15.21	88.56	9.44	67.79	30.93	66.31	30.87	-7.58	-1.34
44	23.85	-15.16	91.15	8.49	69.69	30.87	72.20	29.33	-9.60	-5.87
45	23.77	-14.79	91.99	7.51	69.13	30.89	70.07	29.89	-8.00	-5.34
46	23.82	-14.60	91.12	8.09	70.81	30.73	75.56	28.61	-8.70	-8.56
47	28.79	-15.60	87.28	10.28	70.98	36.08	73.69	34.78	-6.00	0.60
48	28.45	-14.88	89.50	10.91	69.17	35.92	68.79	35.02	-5.70	-2.20
49	28.37	-15.19	92.10	10.59	66.83	36.24	62.83	34.50	-4.86	1.03



Table A.29.  
Ejector cycle, temperatures 2 of 2, steady state raw data.

Test	T10_Suc_Noz_in	T11_LTE_out	T12_MTw_in	T13_MTw_out	T14_LTw_in	T15_LTw_out	T19_LTE_in
[-]	[deg C]	[deg C]	[deg C]	[deg C]	[deg C]	[deg C]	[deg C]
36	-8.25	-19.88	1.59	-7.14	-20.75	-24.90	-31.06
37	-4.83	-19.32	1.72	-7.08	-20.29	-24.19	-30.72
38	-7.00	-20.28	2.30	-7.21	-21.22	-24.95	-31.74
39	-4.50	-19.86	2.57	-6.76	-20.51	-24.80	-30.35
40	-0.35	-20.62	1.95	-6.59	-21.54	-25.66	-30.38
41	-8.75	-20.82	2.86	-6.47	-21.58	-25.37	-30.68
42	4.28	-20.44	3.39	-3.71	-21.03	-24.66	-29.65
43	0.65	-19.96	3.32	-4.69	-20.86	-24.33	-28.52
44	-4.56	-20.08	2.19	-5.43	-20.89	-24.73	-29.55
45	-3.93	-19.84	2.66	-5.49	-20.86	-24.59	-30.04
46	-9.08	-19.53	2.22	-6.19	-20.57	-24.00	-29.51
47	2.53	-21.19	2.99	-4.39	-21.10	-24.95	-28.15
48	1.03	-20.42	2.96	-3.85	-20.98	-24.86	-27.87
49	3.35	-20.55	3.10	-2.52	-20.74	-24.50	-27.81

Table A.30.  
Ejector cycle, pressures 1 of 2, steady state raw data.

Test	P1_Suc_LP	P2_Dis_LP	P3_Suc_HP	P4_IC_in	P5_IC_out	P6_GC_in	P7_GC_out	P8_Ej_out	P9_MT_FT_out
[ - ]	[kPa]	[kPa]	[kPa]	[kPa]	[kPa]	[kPa]	[kPa]	[kPa]	[kPa]
36	1340	2813	2742	4576	4534	6692	6600	2840	2685
37	1348	2753	2681	4507	4471	6822	6725	2797	2626
38	1308	2673	2576	4453	4422	7051	6955	2719	2550
39	1358	2872	2764	4849	4804	8040	7937	2850	2747
40	1359	2938	2852	4911	4875	7745	7650	2915	2807
41	1335	2898	2811	4836	4808	7415	7324	2877	2764
42	1406	3108	3050	5247	5217	7620	7534	3176	3009
43	1458	3066	3006	5195	5167	8002	7905	3058	2965
44	1409	2986	2928	5126	5102	8515	8420	2975	2881
45	1385	2990	2935	5117	5093	8275	8182	3046	2890
46	1414	2927	2869	5068	5042	8793	8696	2971	2823
47	1471	3244	3170	5623	5577	8898	8793	3246	3134
48	1487	3327	3251	5706	5656	8503	8394	3331	3218
49	1491	3483	3406	5901	5848	8123	8011	3495	3371

Table A.31.  
Ejector cycle, pressures 2 of 2 and mass flow rate, steady state raw data.

Test P10\_MTE\_in P11\_MTE\_out P12\_Suc\_Noz\_in P13\_LTE\_in P14\_LTE\_out P15\_LT\_FT\_in m\_dot\_Motive

[-]	[kPa]	[kPa]	[kPa]	[kPa]	[kPa]	[kPa]	[g/s]
-----	-------	-------	-------	-------	-------	-------	-------

36	2731	2730	2693	1336	1353	2828	48.014
37	2626	2624	2580	1344	1361	2781	46.664
38	2655	2654	2606	1303	1322	2707	45.637
39	2701	2698	2658	1366	1376	2845	48.358
40	2671	2668	2632	1355	1370	2912	49.357
41	2743	2740	2695	1354	1359	2869	48.804
42	2879	2877	2855	1401	1440	3168	53.037
43	2839	2836	2805	1453	1496	3054	51.236
44	2680	2676	2637	1404	1449	2972	49.137
45	2804	2800	2769	1378	1423	3047	49.482
46	2750	2745	2707	1408	1454	2969	47.827
47	2959	2955	2936	1464	1488	3258	54.052
48	2987	2984	2965	1479	1505	3341	56.324
49	3058	3055	3042	1483	1508	3505	60.413

Table A.32.  
Ejector cycle, additional measurements, steady state raw data.

Test	V_dot_w_MT	V_dot_w_LT	W_dot_HPC	W_dot_LPC	W_dot_Fans	EXV_1	EXV_2	EXV_3	EXV_4	MTFT
[-]	[liter/min]	[liter/min]	[W]	[W]	[W]	[V]	[V]	[V]	[V]	[cm] [%]
36	10.8	10.1	3330	1114	598	0	3.2	10	3.185	8.98 40.95
37	10.8	10.0	3383	1090	588	0	2.9	10	3.425	9.05 41.29
38	10.7	10.0	3499	1098	595	0	2.7	10	3.35	8.30 37.80
39	10.5	10.1	3770	1140	578	0	2.2	10	3.45	5.62 25.61
40	10.4	10.1	3668	1136	584	0	1.9	10	2.95	4.98 22.71
41	10.5	10.2	3569	1104	578	0	2.9	10	3.375	7.20 32.80
42	10.4	10.5	3629	1286	574	0	1.5	10	3.225	16.27 74.09
43	10.4	10.5	3739	1266	578	0	2.8	10	3.6	15.61 71.13
44	10.3	10.7	3906	1255	575	0	2.4	10	3.55	15.01 68.39
45	10.3	10.6	3849	1261	570	0	2.75	10	3.1	14.24 64.94
46	10.2	10.7	3984	1246	568	0	2.5	10	3.5	14.53 66.26
47	10.3	10.0	4081	1117	568	0	1.85	10	3.05	12.38 56.38
48	10.3	10.0	3946	1130	563	0	1.8	10	3.15	13.65 62.20
49	10.3	9.9	3815	1163	564	0	1.7	10	3.1	13.79 62.87

Table A.33.  
Ejector cycle, specific enthalpies, steady state data.

Test	h1	h2	h3	h4	h5	h6	h7	h8	h9	h10	h11	h12	h13	h14
[-]	[kJ/kg]	[kJ/kg]	[kJ/kg]	[kJ/kg]	[kJ/kg]	[kJ/kg]	[kJ/kg]	[kJ/kg]	[kJ/kg]	[kJ/kg]	[kJ/kg]	[kJ/kg]	[kJ/kg]	[kJ/kg]
36	-53.0	35.3	-51.9	-8.8	-62.5	-45.2	-238.0	-185.3	-324.6	-70.9	-324.6	-324.6	-57.5	-72.4
37	-52.5	40.6	-50.7	-7.7	-61.5	-43.3	-246.1	-184.5	-325.9	-64.8	-325.9	-325.9	-57.0	-72.2
38	-52.6	42.8	-50.1	-8.5	-61.2	-42.0	-254.4	-189.1	-328.1	-67.9	-328.1	-328.1	-57.3	-71.9
39	-53.2	27.7	-51.6	-4.4	-58.8	-37.5	-245.2	-186.8	-324.3	-66.3	-324.3	-324.3	-57.9	-72.5
40	-53.2	36.1	-51.8	-5.6	-59.9	-39.8	-240.5	-178.7	-322.4	-59.7	-322.4	-322.4	-58.6	-72.8
41	-53.5	40.8	-51.2	-6.4	-59.4	-40.1	-234.4	-183.4	-323.5	-71.6	-323.5	-323.5	-58.6	-72.6
42	-53.8	38.5	-54.9	-8.3	-58.0	-40.5	-202.1	-162.8	-315.1	-58.1	-315.1	-315.1	-59.6	-74.1
43	-54.4	35.7	-51.6	-4.7	-56.7	-37.1	-216.5	-169.9	-318.4	-63.1	-318.4	-318.4	-60.2	-73.5
44	-53.5	38.9	-51.6	-1.7	-55.7	-33.1	-229.5	-174.0	-320.7	-66.2	-320.7	-320.7	-59.4	-73.0
45	-52.7	39.8	-53.0	-2.3	-55.5	-33.9	-225.1	-175.7	-318.7	-68.2	-318.7	-318.7	-58.7	-73.4
46	-53.0	39.3	-51.1	0.2	-54.9	-30.5	-234.0	-177.7	-320.8	-71.7	-320.8	-320.8	-58.9	-73.0
47	-55.1	33.1	-53.3	-4.7	-54.9	-34.9	-206.0	-164.1	-313.2	-62.8	-313.2	-313.2	-61.3	-74.5
48	-54.6	34.9	-53.9	-7.9	-56.5	-39.0	-194.3	-159.4	-310.9	-67.5	-310.9	-310.9	-60.8	-74.9
49	-54.9	36.5	-57.1	-12.9	-59.4	-45.0	-173.6	-147.4	-306.5	-64.2	-306.5	-306.5	-61.0	-76.0

Table A.34.  
Ejector cycle, specific enthalpies and pressures, steady state data.

Test	h15	h16	p1	p2	p3	p4	p5	p6	p7	p8	p9	p10	p11	p12	p13	p14	p15	p16
[ - ]	[kJ/kg]	[kJ/kg]	[kPa]	[kPa]	[kPa]	[kPa]	[kPa]	[kPa]	[kPa]	[kPa]	[kPa]	[kPa]	[kPa]	[kPa]	[kPa]	[kPa]	[kPa]	[kPa]
36	-324.6	-70.1	1340	2813	2742	4576	4534	6692	6600	2840	2725	2730	2828	1378	1353	2840	2840	2693
37	-325.9	-62.8	1348	2753	2681	4507	4471	6822	6725	2797	2626	2624	2781	1394	1361	2797	2797	2580
38	-328.1	-66.3	1308	2673	2576	4453	4422	7051	6955	2719	2652	2654	2707	1346	1322	2719	2719	2606
39	-324.3	-63.9	1358	2872	2764	4849	4804	8040	7937	2850	2699	2698	2845	1411	1376	2850	2850	2658
40	-322.4	-57.9	1359	2938	2852	4911	4875	7745	7650	2915	2666	2668	2912	1410	1370	2915	2915	2632
41	-323.5	-70.9	1335	2898	2811	4836	4808	7415	7324	2877	2743	2740	2869	1395	1359	2877	2877	2695
42	-315.1	-55.8	1406	3108	3050	5247	5217	7620	7534	3176	2874	2877	3168	1445	1440	3176	3176	2855
43	-318.4	-59.8	1458	3066	3006	5195	5167	8002	7905	3058	2835	2836	3054	1500	1496	3058	3058	2805
44	-320.7	-63.6	1409	2986	2928	5126	5102	8515	8420	2975	2679	2676	2972	1449	1449	2975	2975	2637
45	-318.7	-65.4	1385	2990	2935	5117	5093	8275	8182	3046	2802	2800	3047	1426	1423	3046	3046	2769
46	-320.8	-71.6	1414	2927	2869	5068	5042	8793	8696	2971	2748	2745	2969	1451	1454	2971	2971	2707
47	-313.2	-59.7	1471	3244	3170	5623	5577	8898	8793	3246	2963	2955	3258	1519	1488	3246	3246	2936
48	-310.9	-62.4	1487	3327	3251	5706	5656	8503	8394	3331	2987	2984	3341	1533	1505	3331	3331	2965
49	-306.5	-60.6	1491	3483	3406	5901	5848	8123	8011	3495	3057	3055	3505	1536	1508	3495	3495	3042

Table A.35.  
Ejector cycle, primary cycle parameters, steady state data.

Test	m_dot_motive	m_dot_low	m_dot_MTE	m_dot_vap	eta_ej	w	x_d	dp_ej	COP	Q_dot_LTE	Q_dot_MTE
[-]	[kg/s]	[kg/s]	[kg/s]	[kg/s]	[-]	[-]	[-]	[kPa]	[-]	[kW]	[kW]
36	0.048	0.009	0.023	0.039	0.10	0.482	0.552	110	1.48	2.3	5.9
37	0.047	0.008	0.023	0.039	0.18	0.484	0.557	172	1.45	2.2	5.9
38	0.046	0.008	0.024	0.038	0.10	0.536	0.543	65	1.48	2.1	6.4
39	0.048	0.009	0.024	0.039	0.14	0.492	0.546	152	1.42	2.4	6.1
40	0.049	0.009	0.021	0.041	0.18	0.429	0.576	247	1.34	2.3	5.6
41	0.049	0.008	0.024	0.041	0.12	0.495	0.559	137	1.43	2.1	6.1
42	0.053	0.008	0.018	0.045	0.12	0.337	0.632	299	1.12	2.1	4.6
43	0.051	0.008	0.020	0.043	0.11	0.396	0.606	221	1.19	2.0	5.2
44	0.049	0.009	0.019	0.040	0.16	0.390	0.593	299	1.15	2.3	4.9
45	0.049	0.008	0.021	0.041	0.13	0.422	0.583	246	1.20	2.2	5.2
46	0.048	0.008	0.022	0.040	0.14	0.451	0.577	226	1.18	2.0	5.4
47	0.054	0.009	0.019	0.046	0.10	0.350	0.624	291	1.10	2.1	4.7
48	0.056	0.009	0.018	0.048	0.10	0.319	0.642	347	1.06	2.2	4.4
49	0.060	0.008	0.015	0.052	0.09	0.247	0.690	440	0.94	2.1	3.6

Table A.36.

Ejector cycle, additional parameters, steady state data.

Test	$\dot{Q}_{IC}$	$\dot{Q}_{GC}$	$\dot{Q}_{loss\_C1}$	$\dot{Q}_{loss\_C2}$	$\dot{Q}_{LT\_suc}$	$\dot{Q}_{ej\_suc}$	$\Delta Q_{h\_3}$	$\dot{W}_{evap\_fans}$
[-]	[kW]	[kW]	[kW]	[kW]	[kW]	[kW]	[kW]	[kW]
36	2.6	9.3	0.35	0.43	0.04	0.02	-0.05	0.5
37	2.5	9.5	0.34	0.53	0.04	0.04	-0.10	0.5
38	2.4	9.7	0.37	0.73	0.04	0.04	-0.12	0.5
39	2.6	10.1	0.41	0.46	0.04	0.06	-0.11	0.5
40	2.7	9.9	0.35	0.40	0.05	0.04	-0.08	0.5
41	2.6	9.5	0.34	0.44	0.04	0.02	-0.13	0.5
42	2.6	8.6	0.53	0.23	0.05	0.04	-0.09	0.5
43	2.7	9.2	0.56	0.33	0.05	0.07	-0.26	0.5
44	2.7	9.7	0.45	0.35	0.05	0.05	-0.08	0.5
45	2.6	9.5	0.48	0.28	0.05	0.06	-0.05	0.5
46	2.6	9.7	0.53	0.37	0.05	0.00	-0.18	0.5
47	2.7	9.2	0.37	0.38	0.05	0.06	-0.23	0.5
48	2.7	8.7	0.36	0.37	0.05	0.09	-0.24	0.5
49	2.8	7.8	0.39	0.28	0.05	0.05	-0.19	0.5



Table A.37.  
Ejector and pump cycle, temperatures 1 of 2, steady state raw data.

Test	T21_ai	T1_Suc_LP	T2_Dis_LP	T3_Suc_HP	T4_IC_in	T5_IC_out	T6_GC_in	T7_GC_out	T8_MTE_in	T9_MTE_out
[-]	[deg C]	[deg C]	[deg C]	[deg C]	[deg C]	[deg C]	[deg C]	[deg C]	[deg C]	[deg C]
50	14.59	-15.59	88.57	6.34	59.89	20.90	53.79	22.40	-9.01	-6.42
51	14.55	-16.02	90.45	6.52	59.18	21.18	52.17	23.34	-9.11	-0.28
52	14.49	-15.58	89.48	5.77	59.32	21.15	51.05	24.38	-9.47	1.27
53	14.59	-16.19	87.34	6.85	58.79	21.39	50.18	24.90	-9.54	0.37
54	14.64	-15.69	86.29	6.90	58.68	21.51	49.45	25.37	-9.55	0.87
55	19.43	-15.71	83.52	6.58	65.27	26.10	64.72	24.95	-9.10	-1.43
56	19.37	-14.95	85.38	7.77	64.21	26.21	61.75	25.85	-8.91	-1.58
57	19.42	-14.50	86.95	7.58	63.48	26.32	59.71	26.60	-8.75	-1.66
58	19.64	-14.40	88.05	7.98	62.92	26.52	58.27	27.20	-8.64	0.42

Table A.38.  
Ejector and pump cycle, temperatures 2 of 2, steady state raw data.

Test	T10_Suc_Noz_in	T11_LTE_out	T12_MTw_in	T13_MTw_out	T14_LTw_in	T15_LTw_out	T19_LTE_in
[-]	[deg C]	[deg C]	[deg C]	[deg C]	[deg C]	[deg C]	[deg C]
50	-6.17	-19.61	2.79	-6.46	-20.45	-24.21	-29.95
51	0.29	-19.97	1.99	-6.82	-20.70	-25.22	-29.73
52	1.73	-19.56	1.65	-6.85	-20.39	-24.99	-30.66
53	1.08	-20.02	1.75	-6.76	-20.63	-24.86	-29.87
54	1.42	-19.29	1.59	-6.67	-19.97	-24.40	-29.78
55	-0.91	-20.31	2.21	-6.85	-21.26	-25.41	-31.25
56	-0.89	-19.45	2.19	-6.68	-20.30	-24.49	-29.91
57	-0.79	-18.88	2.29	-6.58	-19.76	-24.06	-30.41
58	0.98	-18.90	2.40	-6.60	-19.85	-24.08	-30.07

Table A.39.  
Ejector and pump cycle, pressures 1 of 2, steady state raw data.

Test	P1_Suc_LP	P2_Dis_LP	P3_Suc_HP	P4_IC_in	P5_IC_out	P6_GC_in	P7_GC_out	P8_Ej_out	P9_MT_FT_out
[-]	[kPa]	[kPa]	[kPa]	[kPa]	[kPa]	[kPa]	[kPa]	[kPa]	[kPa]
50	1388	2810	2728	4582	4550	6916	6818	2856	2693
51	1400	2873	2788	4668	4631	6866	6772	2925	2754
52	1357	2883	2802	4668	4633	6750	6659	2940	2768
53	1394	2948	2867	4748	4712	6771	6675	2958	2838
54	1396	2970	2890	4774	4736	6727	6631	2982	2863
55	1320	2933	2843	4922	4879	7947	7847	2915	2810
56	1386	2995	2899	4986	4942	7744	7642	2976	2869
57	1364	3034	2939	5029	4983	7592	7493	3017	2911
58	1381	3079	2984	5079	5033	7511	7410	3061	2952

Table A.40.  
Ejector and pump cycle, pressures 2 of 2 and mass flow rate, steady state raw data.

Test P10_MTE_in P11_MTE_out P12_Suc_Noz_in P13_LTE_in P14_LTE_out P15_LT_FT_in m_dot_Motive							
[-]	[kPa]	[kPa]	[kPa]	[kPa]	[kPa]	[kPa]	[g/s]
50	2730	2729	2685	1384	1403	2841	47.829
51	2723	2722	2693	1394	1413	2915	49.349
52	2694	2694	2666	1351	1371	2931	49.579
53	2686	2685	2657	1389	1408	2946	51.070
54	2683	2682	2655	1391	1410	2970	51.654
55	2725	2722	2691	1315	1330	2915	49.210
56	2737	2734	2705	1381	1396	2974	50.594
57	2746	2743	2713	1360	1375	3014	51.800
58	2754	2751	2723	1376	1391	3060	52.790

Table A.41.  
Ejector and pump cycle, additional measurements, steady state raw data.

Test	V_dot_w_MT	V_dot_w_LT	W_dot_HPC	W_dot_LPC	W_dot_Fans	EXV_1	EXV_2	EXV_3	EXV_4	MTFT
[-]	[liter/min]	[liter/min]	[W]	[W]	[W]	[V]	[V]	[V]	[V]	[cm] [%]
50	10.8	9.9	3414	1108	593	0	2.2	10	3.4	8.42 38.37
51	10.8	9.9	3389	1145	593	0	1.8	10	2.75	6.11 27.85
52	10.8	9.9	3339	1152	593	0	1.75	10	2.75	7.29 33.27
53	10.7	10.1	3344	1145	590	0	1.65	10	2.75	6.81 31.09
54	10.7	10.1	3320	1144	588	0	1.6	10	2.8	7.16 32.68
55	10.5	10.2	3738	1173	577	0	2.025	10	2.9	4.15 18.96
56	10.5	10.1	3667	1162	578	0	1.9	10	3	4.31 19.64
57	10.5	10.1	3614	1170	578	0	1.85	10	3	4.88 22.26
58	10.5	10.2	3585	1170	580	0	1.775	10	3	5.12 23.37

Table A.42.  
Ejector and pump cycle, pump measurements, steady state raw data.

Test	T16_Pump_in	T17_Pump_out	P16_Pump_out	W_dot_Pump
[-]	[deg C]	[deg C]	[kPa]	[W]
50	22.41	24.26	7845	470
51	23.33	26.51	8426	555
52	24.35	28.90	8915	637
53	24.95	30.40	9357	688
54	25.41	31.92	9675	747
55	24.80	26.49	8419	446
56	25.82	28.80	9022	538
57	26.56	30.74	9506	607
58	27.10	32.59	9964	676

Table A.43.  
Ejector and pump cycle, specific enthalpies, steady state data.

Test	h1	h2	h3	h4	h5	h6	h7	h8	h9	h10	h11	h12	h13	h14
[-]	[kJ/kg]	[kJ/kg]	[kJ/kg]	[kJ/kg]	[kJ/kg]	[kJ/kg]	[kJ/kg]	[kJ/kg]	[kJ/kg]	[kJ/kg]	[kJ/kg]	[kJ/kg]	[kJ/kg]	[kJ/kg]
50	-53.6	37.5	-51.0	-8.5	-62.6	-44.6	-247.5	-245.6	-184.4	-324.1	-68.2	-324.1	-324.1	-58.1
51	-54.3	39.0	-51.7	-10.2	-63.7	-46.8	-243.5	-240.3	-183.5	-322.1	-59.4	-322.1	-322.1	-58.6
52	-53.1	37.9	-52.9	-10.1	-63.8	-47.0	-237.9	-234.1	-181.7	-321.7	-56.9	-321.7	-321.7	-57.5
53	-54.3	35.3	-52.7	-11.5	-65.0	-48.9	-235.5	-230.9	-177.5	-321.2	-57.9	-321.2	-321.2	-58.6
54	-53.9	34.0	-53.0	-11.9	-65.3	-49.6	-232.4	-227.1	-176.6	-320.5	-57.2	-320.5	-320.5	-57.9
55	-52.6	31.4	-52.6	-5.2	-59.9	-39.2	-243.2	-240.3	-182.3	-322.4	-61.0	-322.4	-322.4	-57.5
56	-52.9	32.9	-52.0	-7.2	-60.9	-41.9	-238.6	-235.0	-179.5	-320.7	-61.4	-320.7	-320.7	-57.8
57	-52.1	34.3	-52.9	-8.5	-61.5	-43.5	-234.5	-230.4	-178.5	-319.5	-61.7	-319.5	-319.5	-56.8
58	-52.3	35.1	-53.2	-9.7	-62.1	-45.0	-231.0	-226.2	-177.0	-318.3	-59.1	-318.3	-318.3	-57.1

Table A.44.  
Ejector and pump cycle, specific enthalpies and pressures, steady state data.

Test	h15	p1	p2	p3	p4	p5	p6	p7	p8	p9	p10	p11	p12	p13	p14	p15
[-]	[kJ/kg]	[kPa]	[kPa]	[kPa]	[kPa]	[kPa]	[kPa]	[kPa]	[kPa]	[kPa]	[kPa]	[kPa]	[kPa]	[kPa]	[kPa]	[kPa]
50	-66.9	1388	2810	2728	4582	4550	6916	6818	7845	2856	2724	2729	2841	1430	1403	2856
51	-58.1	1400	2873	2788	4668	4631	6866	6772	8426	2925	2716	2722	2915	1441	1413	2925
52	-55.8	1357	2883	2802	4668	4633	6750	6659	8915	2940	2689	2694	2931	1397	1371	2940
53	-56.4	1394	2948	2867	4748	4712	6771	6675	9357	2958	2683	2685	2946	1434	1408	2958
54	-56.0	1396	2970	2890	4774	4736	6727	6631	9675	2982	2683	2682	2970	1438	1410	2982
55	-59.7	1320	2933	2843	4922	4879	7947	7847	8419	2915	2717	2722	2915	1369	1330	2915
56	-59.9	1386	2995	2899	4986	4942	7744	7642	9022	2976	2732	2734	2974	1432	1396	2976
57	-60.0	1364	3034	2939	5029	4983	7592	7493	9506	3017	2744	2743	3014	1408	1375	3017
58	-57.8	1381	3079	2984	5079	5033	7511	7410	9964	3061	2753	2751	3060	1424	1391	3061



Table A.45.  
Ejector and pump cycle, parameters 1 of 3, steady state data.

Test	h16	h17	p16	p17	m_dot motive	m_dot_low	m_dot_MTE	m_dot_vap	eta_ej	w	x_d	dp_ej
[-]	[kJ/kg]	[kJ/kg]	[kPa]	[kPa]	[kg/s]	[kg/s]	[kg/s]	[kg/s]	[-]	[-]	[-]	[kPa]
50	-72.5	-324.1	2856	2685	0.048	0.008	0.024	0.040	0.12	0.507	0.555	127
51	-72.8	-322.1	2925	2693	0.049	0.009	0.022	0.040	0.14	0.456	0.556	202
52	-72.9	-321.7	2940	2666	0.050	0.010	0.022	0.040	0.15	0.434	0.563	246
53	-73.0	-321.2	2958	2657	0.051	0.009	0.022	0.042	0.15	0.424	0.579	273
54	-73.1	-320.5	2982	2655	0.052	0.009	0.021	0.042	0.15	0.406	0.582	299
55	-72.8	-322.4	2915	2691	0.049	0.009	0.023	0.040	0.14	0.462	0.561	193
56	-73.1	-320.7	2976	2705	0.051	0.009	0.022	0.042	0.15	0.444	0.570	242
57	-73.3	-319.5	3017	2713	0.052	0.009	0.023	0.043	0.15	0.435	0.573	274
58	-73.5	-318.3	3061	2723	0.053	0.009	0.023	0.044	0.15	0.432	0.577	310

Table A.46.  
Ejector and pump cycle, parameters 2 of 3, steady state data.

Test	COP	$\dot{Q}_{LTE}$	$\dot{Q}_{MTE}$	$\dot{Q}_{IC}$	$\dot{Q}_{GC}$	$\dot{Q}_{loss\_C1}$	$\dot{Q}_{loss\_C2}$	$\dot{Q}_{loss\_pump}$
[-]	[-]	[kW]	[kW]	[kW]	[kW]	[kW]	[kW]	[kW]
50	1.36	2.1	6.2	2.6	9.7	0.40	0.53	0.38
51	1.36	2.5	5.9	2.6	9.7	0.27	0.50	0.40
52	1.32	2.5	5.7	2.7	9.5	0.28	0.38	0.45
53	1.29	2.4	5.7	2.7	9.5	0.34	0.42	0.45
54	1.27	2.5	5.5	2.8	9.4	0.32	0.39	0.47
55	1.29	2.3	5.9	2.7	10.0	0.43	0.39	0.31
56	1.27	2.4	5.8	2.7	10.0	0.39	0.44	0.35
57	1.27	2.4	5.8	2.7	9.9	0.37	0.38	0.40
58	1.28	2.4	5.9	2.8	9.8	0.37	0.39	0.42

Ejector and pump cycle, parameters 3 of 3, steady state data.

Table A.47.

Test	$Q_{\text{dot\_LT\_suc}}$	$Q_{\text{dot\_ej\_suc}}$	$\Delta Q_{\text{h\_3}}$	$W_{\text{dot\_evap\_fans}}$	$n_{\text{pump}}$
[-]	[kW]	[kW]	[kW]	[kW]	[rpm]
50	0.03	0.03	0.40	0.5	140
51	0.04	0.03	0.58	0.5	150
52	0.04	0.02	0.69	0.5	160
53	0.04	0.03	0.54	0.5	170
54	0.04	0.03	0.61	0.5	180
55	0.04	0.03	0.54	0.5	145
56	0.04	0.03	0.52	0.5	155
57	0.04	0.04	0.64	0.5	165
58	0.04	0.03	0.64	0.5	175

## **B. APPENDIX B: TABULATED EXPERIMENTAL TRANSIENT DATA**

This appendix contains data as well as additional post-processing for the data used in the transient modeling validation portion of this thesis. Furthermore, the raw data used for compressor map development is included. For the transient validation from Section 6, the following tests are reported:

- Test case 1: MT bypass metering valve flow area increase. Data is provided in Tables B.1 through B.6.
- Test case 2: MT evaporator inlet EXV flow area decrease. Data is provided in Tables B.7 through B.12.
- Test case 3: LT evaporator inlet EXV flow area decrease. Data is provided in Tables B.13 through B.18.
- Test case 4: GC outlet EXV flow area increase. Data is provided in Tables B.19 through B.24.

Raw data from the compressor map development introduced in Section 4 and validated in Section 6 is provided in the following tables:

- Single-stage Dorin compressor data is provided in Tables B.25 and B.26.
- Two-stage Carlyle compressor data is provided in Tables B.27, B.28, and B.29.

Table B.1.  
Specific enthalpies from experimental data from transient validation case study 1, time segment 1 of 2.

Time [s]	h1 [kJ/kg]	h2 [kJ/kg]	h3 [kJ/kg]	h4 [kJ/kg]	h5 [kJ/kg]	h6 [kJ/kg]	h7 [kJ/kg]	h8 [kJ/kg]	h9 [kJ/kg]	h10 [kJ/kg]	h11 [kJ/kg]	h12 [kJ/kg]	h13 [kJ/kg]	h14 [kJ/kg]
0	454.5	509.0	470.6	529.3	467.4	502.4	267.6	267.6	155.3	464.6	470.6	464.6	155.3	155.3
5	454.4	509.0	470.7	529.4	467.4	502.5	267.5	267.5	155.3	464.6	470.7	464.6	155.3	155.3
10	454.4	509.0	470.7	529.3	467.4	502.5	267.4	267.4	155.2	464.6	470.7	464.6	155.2	155.2
15	454.3	509.0	470.7	529.3	467.4	502.5	267.2	267.2	155.3	464.6	470.7	464.6	155.3	155.3
20	454.4	509.0	470.7	529.4	467.4	502.4	267.1	267.1	155.3	464.6	470.7	464.6	155.3	155.3
25	454.4	509.1	470.7	529.3	467.5	502.6	267.1	267.1	155.2	464.6	470.7	464.6	155.2	155.2
30	454.3	509.1	470.7	529.4	467.5	502.6	267.2	267.2	155.2	464.6	470.7	464.6	155.2	155.2
35	454.4	509.1	470.7	529.4	467.5	502.6	267.2	267.2	155.2	464.7	470.7	464.7	155.2	155.2
40	454.6	509.2	470.6	529.4	467.6	502.6	267.2	267.2	155.1	464.7	470.6	464.7	155.1	155.1
45	454.7	509.3	470.4	529.5	467.7	502.7	267.3	267.3	155.1	464.7	470.4	464.7	155.1	155.1
50	454.7	509.4	470.3	529.5	467.8	502.8	267.4	267.4	154.9	464.8	470.3	464.8	154.9	154.9
55	454.6	509.5	470.3	529.6	467.9	502.9	267.5	267.5	154.8	464.8	470.3	464.8	154.8	154.8
60	454.6	509.5	470.4	529.6	467.9	502.9	267.7	267.7	154.7	464.9	470.4	464.9	154.7	154.7
65	454.8	509.5	470.4	529.6	467.9	503.0	267.7	267.7	154.6	464.9	470.4	464.9	154.6	154.6
70	454.8	509.6	470.4	529.7	468.0	502.9	267.7	267.7	154.5	465.0	470.4	465.0	154.5	154.5

Table B.2.  
Specific enthalpies from experimental data from transient validation case study 1, time segment 2 of 2.

Time	h1	h2	h3	h4	h5	h6	h7	h8	h9	h10	h11	h12	h13	h14
[s]	[kJ/kg]	[kJ/kg]	[kJ/kg]	[kJ/kg]	[kJ/kg]	[kJ/kg]	[kJ/kg]	[kJ/kg]	[kJ/kg]	[kJ/kg]	[kJ/kg]	[kJ/kg]	[kJ/kg]	[kJ/kg]
75	454.9	509.7	470.4	529.8	468.0	503.1	267.7	267.7	154.3	465.0	470.4	465.0	154.3	154.3
80	455.0	509.7	470.4	529.8	468.1	503.2	267.7	267.7	154.3	465.1	470.4	465.1	154.3	154.3
85	455.0	509.8	470.5	529.8	468.1	503.4	267.7	267.7	154.2	465.1	470.5	465.1	154.2	154.2
90	455.1	509.8	470.5	529.9	468.1	503.3	267.6	267.6	154.1	465.2	470.5	465.2	154.1	154.1
95	455.2	509.9	470.5	529.9	468.2	503.3	267.6	267.6	154.0	465.2	470.5	465.2	154.0	154.0
100	455.3	510.0	470.5	530.0	468.2	503.5	267.5	267.5	153.9	465.3	470.5	465.3	153.9	153.9
105	455.3	510.1	470.5	530.1	468.3	503.5	267.5	267.5	153.9	465.3	470.5	465.3	153.9	153.9
110	455.4	510.2	470.5	530.1	468.3	503.7	267.5	267.5	153.6	465.4	470.5	465.4	153.6	153.6
115	455.5	510.2	470.4	530.1	468.3	503.7	267.5	267.5	153.5	465.4	470.4	465.4	153.5	153.5

Table B.3.  
Specific enthalpies and pressures from experimental data from transient validation case study 1, time segment 1 of 2.

Time	h15	h16	p1	p2	p3	p4	p5	p6	p7	p8	p9	p10	p11	p12	p13	p14	p15	p16
[s]	[kJ/kg]	[kJ/kg]	[kPa]	[kPa]	[kPa]	[kPa]	[kPa]	[kPa]	[kPa]	[kPa]	[kPa]	[kPa]	[kPa]	[kPa]	[kPa]	[kPa]	[kPa]	[kPa]
0	449.5	454.5	1281	2038	2012	3694	3659	7528	7442	1993	2000	2001	2012	2001	2000	1276	1297	1281
5	449.5	454.4	1285	2034	2011	3690	3656	7517	7444	1992	2000	2001	2011	2001	2000	1277	1297	1285
10	449.4	454.4	1286	2037	2011	3698	3658	7519	7454	1991	2000	2002	2011	2002	2000	1280	1299	1286
15	449.4	454.3	1289	2042	2012	3700	3659	7528	7460	1992	2001	2001	2012	2001	2001	1280	1301	1289
20	449.4	454.4	1286	2039	2012	3692	3656	7532	7465	1992	2000	2001	2012	2001	2000	1278	1298	1286
25	449.4	454.4	1285	2039	2012	3699	3657	7522	7456	1991	1999	2000	2012	2000	1999	1280	1300	1285
30	449.4	454.3	1287	2037	2012	3700	3656	7516	7451	1990	2000	2001	2012	2001	2000	1280	1302	1287
35	449.5	454.4	1282	2035	2011	3700	3658	7531	7466	1989	1999	1999	2011	1999	1999	1272	1294	1282
40	449.7	454.6	1272	2038	2009	3698	3652	7531	7464	1987	1996	1997	2009	1997	1996	1263	1284	1272
45	449.8	454.7	1268	2033	2006	3695	3650	7523	7457	1987	1995	1997	2006	1997	1995	1260	1281	1268
50	449.7	454.7	1269	2028	2005	3698	3650	7506	7443	1982	1992	1994	2005	1994	1992	1261	1283	1269
55	449.7	454.6	1273	2026	2003	3687	3641	7500	7435	1979	1989	1990	2003	1990	1989	1265	1287	1273
60	449.7	454.6	1273	2020	1998	3685	3638	7502	7427	1976	1986	1987	1998	1987	1986	1265	1286	1273
65	449.8	454.8	1267	2019	1995	3687	3638	7499	7426	1972	1982	1983	1995	1983	1982	1259	1279	1267
70	449.8	454.8	1265	2017	1992	3684	3631	7510	7431	1970	1979	1980	1992	1980	1979	1256	1277	1265

Table B.4.  
Specific enthalpies and pressures from experimental data from transient validation case study 1, time segment 2 of 2.

Time	h15	h16	p1	p2	p3	p4	p5	p6	p7	p8	p9	p10	p11	p12	p13	p14	p15	p16
[s]	[kJ/kg]	[kJ/kg]	[kPa]	[kPa]	[kPa]	[kPa]	[kPa]	[kPa]	[kPa]	[kPa]	[kPa]	[kPa]	[kPa]	[kPa]	[kPa]	[kPa]	[kPa]	[kPa]
75	449.9	454.9	1259	2011	1989	3677	3627	7492	7419	1965	1976	1977	1989	1977	1976	1251	1272	1259
80	449.9	455.0	1257	2010	1986	3675	3621	7486	7400	1964	1972	1975	1986	1975	1972	1247	1270	1257
85	450.0	455.0	1255	2005	1982	3674	3616	7467	7395	1963	1970	1972	1982	1972	1970	1246	1268	1255
90	450.1	455.1	1251	2008	1980	3669	3610	7461	7394	1958	1968	1970	1980	1970	1968	1240	1262	1251
95	450.2	455.2	1245	2001	1978	3661	3602	7477	7395	1957	1965	1967	1978	1967	1965	1235	1256	1245
100	450.2	455.3	1241	1998	1974	3653	3600	7463	7388	1953	1961	1963	1974	1963	1961	1232	1253	1241
105	450.3	455.3	1240	1996	1972	3648	3597	7461	7377	1952	1960	1963	1972	1963	1960	1232	1253	1240
110	450.3	455.4	1238	1989	1969	3651	3598	7452	7373	1946	1958	1959	1969	1959	1958	1229	1250	1238
115	450.4	455.5	1230	1993	1966	3649	3596	7444	7363	1943	1953	1955	1966	1955	1953	1224	1245	1230



Table B.5.  
Parameters from experimental data from transient validation case study 1, time segment 1 of 2.

Time	Q_dot_LTE	Q_dot_MTE	T_sh_LPC	T_sh_MTE	T_sh_MPC	T_LTE	T_MTE	LL_FT	W_dot_C1	W_dot_C2
[s]	[kW]	[kW]	[C]	[C]	[C]	[C]	[C]	[%]	[kW]	[kW]
0	3.5	1.8	17.1	23.7	29.2	-33.3	-19.6	41	0.842	3.471
5	3.6	1.7	17.0	23.7	29.3	-33.3	-19.6	41	0.843	3.463
10	3.6	1.7	17.0	23.7	29.3	-33.2	-19.7	42	0.838	3.425
15	3.6	1.8	16.9	23.7	29.3	-33.2	-19.6	41	0.839	3.477
20	3.6	1.8	17.0	23.7	29.3	-33.2	-19.6	41	0.840	3.433
25	3.6	1.8	17.0	23.7	29.3	-33.2	-19.6	43	0.840	3.435
30	3.6	1.7	16.9	23.7	29.3	-33.2	-19.7	44	0.840	3.487
35	3.6	1.8	17.1	23.7	29.3	-33.4	-19.7	43	0.843	3.490
40	3.6	1.7	17.3	23.8	29.2	-33.6	-19.7	43	0.842	3.416
45	3.7	1.7	17.4	23.8	29.1	-33.7	-19.7	42	0.842	3.458
50	3.6	1.7	17.4	23.8	28.9	-33.6	-19.8	43	0.843	3.473
55	3.8	1.6	17.3	23.9	29.0	-33.5	-19.9	44	0.838	3.417
60	3.7	1.5	17.3	24.0	29.1	-33.6	-19.9	45	0.837	3.405
65	3.8	1.5	17.5	24.0	29.1	-33.7	-20.0	43	0.840	3.391
70	3.7	1.5	17.6	24.1	29.1	-33.8	-20.0	43	0.838	3.414

Table B.6.  
Parameters from experimental data from transient validation case study 1, time segment 2 of 2.

Time [s]	$\dot{Q}_{LTE}$ [kW]	$\dot{Q}_{MTE}$ [kW]	$T_{sh\_LPC}$ [C]	$T_{sh\_MTE}$ [C]	$T_{sh\_MPC}$ [C]	$T_{LTE}$ [C]	$T_{MTE}$ [C]	LL_FT [%]	$\dot{W}_{dot\_C1}$ [kW]	$\dot{W}_{dot\_C2}$ [kW]
75	3.8	1.5	17.7	24.2	29.1	-33.9	-20.1	43	0.837	3.426
80	3.7	1.5	17.7	24.2	29.2	-34.0	-20.1	42	0.838	3.445
85	3.7	1.5	17.8	24.3	29.2	-34.0	-20.1	43	0.837	3.437
90	3.7	1.5	17.9	24.3	29.2	-34.1	-20.2	45	0.835	3.406
95	3.8	1.5	18.0	24.3	29.2	-34.2	-20.2	44	0.837	3.409
100	3.8	1.5	18.2	24.4	29.2	-34.3	-20.3	44	0.839	3.398
105	3.8	1.5	18.2	24.4	29.3	-34.3	-20.3	44	0.834	3.383
110	3.8	1.5	18.3	24.5	29.3	-34.4	-20.4	46	0.834	3.401
115	3.8	1.5	18.5	24.6	29.2	-34.5	-20.4	45	0.833	3.477

Table B.7.  
Specific enthalpies from experimental data from transient validation case study 2, time segment 1 of 2.

Time [s]	h1 [kJ/kg]	h2 [kJ/kg]	h3 [kJ/kg]	h4 [kJ/kg]	h5 [kJ/kg]	h6 [kJ/kg]	h7 [kJ/kg]	h8 [kJ/kg]	h9 [kJ/kg]	h10 [kJ/kg]	h11 [kJ/kg]	h12 [kJ/kg]	h13 [kJ/kg]	h14 [kJ/kg]
0	454.4	510.8	472.2	531.7	468.8	504.9	268.1	268.1	152.6	466.0	472.2	466.0	152.6	152.6
5	454.4	510.7	472.2	531.8	468.8	505.0	268.0	268.0	152.5	465.9	472.2	465.9	152.5	152.5
10	454.3	510.7	472.2	531.7	468.8	505.0	268.0	268.0	152.6	465.9	472.2	465.9	152.6	152.6
15	454.4	510.7	472.1	531.7	468.8	504.9	268.0	268.0	152.6	465.9	472.1	465.9	152.6	152.6
20	454.4	510.7	472.1	531.7	468.8	504.9	268.1	268.1	152.6	465.9	472.1	465.9	152.6	152.6
25	454.4	510.8	472.1	531.7	468.9	505.0	268.3	268.3	152.6	465.9	472.1	465.9	152.6	152.6
30	454.4	510.8	472.1	531.7	468.8	505.0	268.4	268.4	152.6	465.9	472.1	465.9	152.6	152.6
35	454.4	510.8	472.0	531.8	468.8	505.0	268.6	268.6	152.5	466.0	472.0	466.0	152.5	152.5
40	454.4	510.9	471.7	531.8	468.9	504.9	268.6	268.6	152.3	466.1	471.7	466.1	152.3	152.3
45	454.5	510.9	471.7	531.8	469.0	505.0	268.6	268.6	152.2	466.2	471.7	466.2	152.2	152.2
50	454.5	510.9	471.7	531.8	469.1	505.0	268.5	268.5	152.0	466.2	471.7	466.2	152.0	152.0
55	454.7	511.0	471.7	531.9	469.2	505.0	268.5	268.5	152.0	466.3	471.7	466.3	152.0	152.0
60	454.8	511.1	471.6	532.0	469.2	505.2	268.6	268.6	151.8	466.4	471.6	466.4	151.8	151.8
65	454.9	511.2	471.6	532.1	469.3	505.3	268.6	268.6	151.7	466.4	471.6	466.4	151.7	151.7
70	455.0	511.3	471.5	532.1	469.4	505.3	268.7	268.7	151.6	466.5	471.5	466.5	151.6	151.6

Table B.8.  
Specific enthalpies from experimental data from transient validation case study 2, time segment 2 of 2.

Time	h1	h2	h3	h4	h5	h6	h7	h8	h9	h10	h11	h12	h13	h14
[s]	[kJ/kg]	[kJ/kg]	[kJ/kg]	[kJ/kg]	[kJ/kg]	[kJ/kg]	[kJ/kg]	[kJ/kg]	[kJ/kg]	[kJ/kg]	[kJ/kg]	[kJ/kg]	[kJ/kg]	[kJ/kg]
75	455.1	511.3	471.5	532.1	469.5	505.5	268.7	268.7	151.4	466.6	471.5	466.6	151.4	151.4
80	455.2	511.4	471.5	532.1	469.7	505.5	268.8	268.8	151.4	466.6	471.5	466.6	151.4	151.4
85	455.4	511.5	471.5	532.2	469.7	505.8	268.7	268.7	151.2	466.7	471.5	466.7	151.2	151.2
90	455.5	511.6	471.4	532.3	469.7	506.1	268.8	268.8	151.1	466.7	471.4	466.7	151.1	151.1
95	455.6	511.7	471.4	532.4	469.7	506.0	268.9	268.9	150.8	466.8	471.4	466.8	150.8	150.8
100	455.7	511.8	471.3	532.4	469.7	505.8	268.9	268.9	150.7	466.8	471.3	466.8	150.7	150.7
105	455.9	511.9	471.2	532.6	469.8	505.7	268.8	268.8	150.5	466.9	471.2	466.9	150.5	150.5
110	456.0	512.1	471.3	532.6	469.9	505.7	268.6	268.6	150.4	467.0	471.3	467.0	150.4	150.4
115	456.1	512.2	471.3	532.7	470.0	506.0	268.6	268.6	150.2	467.0	471.3	467.0	150.2	150.2
120	456.3	512.3	471.2	532.8	470.1	506.0	268.6	268.6	150.1	467.1	471.2	467.1	150.1	150.1
125	456.5	512.4	471.2	532.9	470.2	506.0	268.7	268.7	149.9	467.2	471.2	467.2	149.9	149.9
130	456.6	512.4	471.1	532.9	470.3	506.0	268.9	268.9	149.8	467.2	471.1	467.2	149.8	149.8
135	456.8	512.6	471.0	533.0	470.3	506.1	269.1	269.1	149.6	467.3	471.0	467.3	149.6	149.6
140	457.0	512.7	471.0	533.0	470.3	506.4	269.2	269.2	149.5	467.4	471.0	467.4	149.5	149.5

Table B.9.  
Specific enthalpies and pressures from experimental data from transient validation case study 2, time segment 1 of 2.

Time	h15	h16	p1	p2	p3	p4	p5	p6	p7	p8	p9	p10	p11	p12	p13	p14	p15	p16
[s]	[kJ/kg]	[kJ/kg]	[kPa]	[kPa]	[kPa]	[kPa]	[kPa]	[kPa]	[kPa]	[kPa]	[kPa]	[kPa]	[kPa]	[kPa]	[kPa]	[kPa]	[kPa]	[kPa]
0	449.3	454.4	1279	1959	1938	3558	3527	7377	7299	1917	1925	1927	1938	1927	1925	1273	1293	1279
5	449.3	454.4	1281	1965	1938	3556	3527	7384	7300	1915	1926	1928	1938	1928	1926	1275	1295	1281
10	449.3	454.3	1281	1966	1938	3560	3531	7381	7301	1916	1926	1928	1938	1928	1926	1275	1297	1281
15	449.2	454.4	1280	1966	1939	3564	3532	7383	7296	1917	1926	1929	1939	1929	1926	1275	1297	1280
20	449.3	454.4	1278	1969	1939	3565	3533	7378	7289	1918	1926	1929	1939	1929	1926	1272	1294	1278
25	449.3	454.4	1277	1967	1940	3565	3531	7370	7283	1917	1927	1928	1940	1928	1927	1271	1293	1277
30	449.3	454.4	1277	1967	1939	3564	3530	7369	7289	1916	1926	1928	1939	1928	1926	1271	1293	1277
35	449.3	454.4	1280	1963	1936	3556	3529	7367	7286	1913	1923	1925	1936	1925	1923	1272	1292	1280
40	449.3	454.4	1277	1957	1933	3555	3522	7379	7289	1909	1917	1919	1933	1919	1917	1270	1291	1277
45	449.4	454.5	1274	1951	1929	3558	3515	7377	7289	1906	1914	1916	1929	1916	1914	1267	1287	1274
50	449.5	454.5	1268	1949	1925	3559	3511	7377	7287	1900	1911	1913	1925	1913	1911	1262	1282	1268
55	449.6	454.7	1262	1941	1922	3550	3504	7389	7287	1899	1907	1908	1922	1908	1907	1256	1277	1262
60	449.7	454.8	1256	1940	1918	3547	3499	7375	7287	1896	1904	1904	1918	1904	1904	1247	1270	1256
65	449.9	454.9	1250	1937	1914	3536	3493	7363	7283	1893	1901	1901	1914	1901	1901	1242	1263	1250
70	449.9	455.0	1243	1930	1912	3532	3489	7363	7278	1889	1897	1898	1912	1898	1897	1237	1259	1243

Table B.10.  
Specific enthalpies and pressures from experimental data from transient validation case study 2, time segment 2 of 2.

Time	h15	h16	p1	p2	p3	p4	p5	p6	p7	p8	p9	p10	p11	p12	p13	p14	p15	p16
[s]	[kJ/kg]	[kJ/kg]	[kPa]	[kPa]	[kPa]	[kPa]	[kPa]	[kPa]	[kPa]	[kPa]	[kPa]	[kPa]	[kPa]	[kPa]	[kPa]	[kPa]	[kPa]	[kPa]
75	450.1	455.1	1240	1933	1908	3538	3484	7346	7262	1885	1894	1893	1908	1893	1894	1230	1253	1240
80	450.2	455.2	1233	1926	1904	3534	3476	7353	7255	1883	1890	1891	1904	1891	1890	1224	1247	1233
85	450.3	455.4	1225	1925	1899	3527	3472	7323	7254	1879	1885	1887	1899	1887	1885	1219	1241	1225
90	450.4	455.5	1220	1922	1895	3527	3469	7285	7246	1875	1881	1882	1895	1882	1881	1212	1233	1220
95	450.6	455.6	1212	1915	1892	3516	3467	7294	7245	1867	1877	1878	1892	1878	1877	1203	1225	1212
100	450.7	455.7	1206	1912	1889	3512	3460	7322	7252	1864	1872	1875	1889	1875	1872	1195	1217	1206
105	450.8	455.9	1199	1903	1885	3497	3455	7340	7253	1860	1868	1871	1885	1871	1868	1190	1212	1199
110	450.9	456.0	1192	1898	1880	3497	3451	7332	7237	1857	1864	1867	1880	1867	1864	1183	1205	1192
115	451.1	456.1	1185	1895	1876	3482	3440	7311	7223	1850	1860	1863	1876	1863	1860	1177	1198	1185
120	451.2	456.3	1178	1892	1873	3478	3435	7304	7220	1849	1857	1860	1873	1860	1857	1169	1190	1178
125	451.4	456.5	1170	1887	1868	3463	3428	7308	7213	1843	1853	1854	1868	1854	1853	1160	1182	1170
130	451.5	456.6	1164	1885	1864	3462	3422	7308	7206	1842	1848	1850	1864	1850	1848	1153	1177	1164
135	451.6	456.8	1156	1881	1860	3455	3416	7295	7200	1836	1845	1846	1860	1846	1845	1146	1167	1156
140	451.8	457.0	1146	1874	1853	3456	3411	7266	7199	1833	1839	1841	1853	1841	1839	1138	1159	1146

Table B.11.  
Parameters from experimental data from transient validation case study 2, time segment 1 of 2.

Time	Q_dot_LTE	Q_dot_MTE	T_sh_LPC	T_sh_MTE	T_sh_MPC	T_LTE	T_MTE	LL_FT	W_dot_C1	W_dot_C2
[s]	[kW]	[kW]	[C]	[C]	[C]	[C]	[C]	[%]	[kW]	[kW]
0	3.7	1.4	17.0	25.2	31.0	-33.4	-20.9	44	0.810	3.403
5	3.6	1.5	17.0	25.2	31.0	-33.3	-20.9	45	0.811	3.364
10	3.7	1.4	17.0	25.2	31.0	-33.3	-20.9	45	0.811	3.425
15	3.6	1.5	17.0	25.1	31.0	-33.3	-20.9	43	0.809	3.343
20	3.6	1.4	17.1	25.1	31.0	-33.4	-20.9	44	0.810	3.366
25	3.6	1.4	17.1	25.2	30.9	-33.4	-20.9	44	0.810	3.397
30	3.6	1.5	17.1	25.2	30.9	-33.4	-20.9	43	0.812	3.328
35	3.7	1.4	17.0	25.2	30.8	-33.4	-20.9	44	0.811	3.417
40	3.8	1.2	17.1	25.3	30.6	-33.4	-21.0	43	0.807	3.343
45	3.8	1.1	17.1	25.4	30.6	-33.5	-21.1	44	0.807	3.360
50	3.9	1.1	17.3	25.5	30.6	-33.6	-21.2	46	0.809	3.381
55	3.8	1.2	17.4	25.6	30.6	-33.8	-21.2	46	0.811	3.405
60	3.8	1.2	17.5	25.6	30.5	-34.0	-21.2	48	0.809	3.360
65	3.8	1.2	17.7	25.7	30.5	-34.1	-21.3	46	0.809	3.367
70	3.9	1.1	17.9	25.8	30.5	-34.2	-21.4	47	0.807	3.375

Table B.12.  
Parameters from experimental data from transient validation case study 2, time segment 2 of 2.

Time	Q_dot_LTE	Q_dot_MTE	T_sh_LPC	T_sh_MTE	T_sh_MPC	T_LTE	T_MTE	LL_FT	W_dot_C1	W_dot_C2
[s]	[kW]	[kW]	[C]	[C]	[C]	[C]	[C]	[%]	[kW]	[kW]
75	3.8	1.1	18.0	25.8	30.5	-34.4	-21.4	47	0.809	3.364
80	3.8	1.1	18.1	25.9	30.5	-34.5	-21.5	47	0.807	3.337
85	3.8	1.1	18.4	26.0	30.5	-34.6	-21.5	48	0.808	3.365
90	3.7	1.2	18.5	26.1	30.4	-34.8	-21.6	47	0.807	3.342
95	3.8	1.2	18.7	26.1	30.4	-35.0	-21.7	48	0.808	3.314
100	3.7	1.2	18.9	26.2	30.3	-35.2	-21.8	47	0.810	3.317
105	3.8	1.2	19.1	26.3	30.3	-35.3	-21.9	47	0.811	3.347
110	3.8	1.1	19.2	26.3	30.4	-35.5	-21.9	49	0.813	3.339
115	3.8	1.1	19.4	26.4	30.4	-35.6	-22.0	49	0.811	3.323
120	3.8	1.1	19.6	26.5	30.3	-35.8	-22.0	50	0.809	3.307
125	3.7	1.2	19.9	26.6	30.3	-36.0	-22.1	49	0.809	3.307
130	3.7	1.2	20.1	26.6	30.2	-36.2	-22.2	50	0.813	3.310
135	3.7	1.2	20.3	26.7	30.2	-36.4	-22.3	51	0.812	3.352
140	3.7	1.2	20.6	26.8	30.2	-36.6	-22.3	51	0.809	3.347



Table B.13.  
Specific enthalpies from experimental data from transient validation case study 3, time segment 1 of 2.

Time	h1	h2	h3	h4	h5	h6	h7	h8	h9	h10	h11	h12	h13	h14
[s]	[kJ/kg]	[kJ/kg]	[kJ/kg]	[kJ/kg]	[kJ/kg]	[kJ/kg]	[kJ/kg]	[kJ/kg]	[kJ/kg]	[kJ/kg]	[kJ/kg]	[kJ/kg]	[kJ/kg]	[kJ/kg]
0	458.3	526.8	467.8	526.6	462.5	495.8	262.8	262.8	165.4	459.1	467.8	459.1	165.4	165.4
5	458.9	527.0	467.4	526.6	462.5	495.9	262.8	262.8	165.5	459.1	467.4	459.1	165.5	165.5
10	459.4	527.3	466.8	526.5	462.5	496.0	262.7	262.7	165.5	459.1	466.8	459.1	165.5	165.5
15	459.9	527.5	466.3	526.6	462.4	495.9	262.7	262.7	165.4	459.1	466.3	459.1	165.4	165.4
20	460.3	527.8	466.0	526.5	462.5	495.7	262.7	262.7	165.5	459.1	466.0	459.1	165.5	165.5
25	460.6	528.0	465.7	526.6	462.4	496.0	262.7	262.7	165.4	459.1	465.7	459.1	165.4	165.4
30	460.8	528.2	465.4	526.5	462.5	495.8	262.7	262.7	165.3	459.1	465.4	459.1	165.3	165.3
35	461.2	528.5	465.1	526.5	462.7	496.0	262.7	262.7	165.2	459.2	465.1	459.2	165.2	165.2
40	461.7	528.7	464.8	526.7	462.7	496.2	262.7	262.7	165.1	459.3	464.8	459.3	165.1	165.1
45	462.3	528.9	464.3	526.7	462.8	496.0	262.7	262.7	164.8	459.4	464.3	459.4	164.8	164.8
50	463.0	529.1	463.9	526.9	462.8	496.1	262.7	262.7	164.7	459.4	463.9	459.4	164.7	164.7
55	463.5	529.4	463.4	526.8	463.0	496.3	262.6	262.6	164.5	459.5	463.4	459.5	164.5	164.5
60	464.0	529.5	463.1	526.8	463.2	496.5	262.6	262.6	164.3	459.6	463.1	459.6	164.3	164.3
65	464.5	529.8	462.7	526.9	463.2	496.7	262.6	262.6	164.2	459.6	462.7	459.6	164.2	164.2
70	464.7	529.9	462.5	527.0	463.3	496.6	262.7	262.7	163.9	459.7	462.5	459.7	163.9	163.9

Table B.14.  
Specific enthalpies from experimental data from transient validation case study 3, time segment 2 of 2.

Time [s]	h1 [kJ/kg]	h2 [kJ/kg]	h3 [kJ/kg]	h4 [kJ/kg]	h5 [kJ/kg]	h6 [kJ/kg]	h7 [kJ/kg]	h8 [kJ/kg]	h9 [kJ/kg]	h10 [kJ/kg]	h11 [kJ/kg]	h12 [kJ/kg]	h13 [kJ/kg]	h14 [kJ/kg]
75	464.9	530.0	462.4	527.1	463.4	497.0	262.7	262.7	163.8	459.8	462.4	459.8	163.8	163.8
80	465.1	530.2	462.4	527.1	463.5	497.0	262.8	262.8	163.6	459.9	462.4	459.9	163.6	163.6
85	465.4	530.3	462.3	527.1	463.7	497.2	262.9	262.9	163.5	460.0	462.3	460.0	163.5	163.5
90	465.5	530.5	462.3	527.2	463.8	497.4	263.0	263.0	163.3	460.1	462.3	460.1	163.3	163.3
95	465.6	530.6	462.3	527.2	463.7	497.3	263.1	263.1	163.2	460.1	462.3	460.1	163.2	163.2

Table B.15.

Specific enthalpies and pressures from experimental data from transient validation case study 3, time segment 1 of 2.

Time	h15	h16	p1	p2	p3	p4	p5	p6	p7	p8	p9	p10	p11	p12	p13	p14	p15	p16
[s]	[kJ/kg]	[kJ/kg]	[kPa]	[kPa]	[kPa]	[kPa]	[kPa]	[kPa]	[kPa]	[kPa]	[kPa]	[kPa]	[kPa]	[kPa]	[kPa]	[kPa]	[kPa]	[kPa]
0	452.9	458.3	1138	2343	2318	4152	4128	8305	8185	2293	2308	2310	2318	2310	2308	1126	1150	1138
5	453.5	458.9	1106	2337	2318	4151	4126	8302	8196	2294	2308	2309	2318	2309	2308	1091	1115	1106
10	454.1	459.4	1079	2341	2318	4172	4117	8299	8209	2296	2308	2310	2318	2310	2308	1063	1086	1079
15	454.4	459.9	1056	2343	2319	4160	4125	8302	8205	2293	2308	2309	2319	2309	2308	1042	1065	1056
20	454.8	460.3	1038	2335	2317	4160	4124	8325	8195	2295	2306	2308	2317	2308	2306	1026	1047	1038
25	455.0	460.6	1023	2337	2315	4145	4128	8296	8186	2292	2305	2306	2315	2306	2305	1012	1034	1023
30	455.3	460.8	1011	2336	2314	4156	4121	8306	8199	2289	2303	2304	2314	2304	2303	996.9	1021	1011
35	455.6	461.2	995.7	2328	2311	4165	4111	8301	8202	2285	2299	2300	2311	2300	2299	981.6	1003	995.7
40	456.1	461.7	967.2	2319	2304	4144	4114	8278	8184	2281	2294	2294	2304	2294	2294	950.8	974.8	967.2
45	456.7	462.3	932.9	2317	2297	4141	4102	8293	8170	2273	2286	2288	2297	2288	2286	914.7	938.9	932.9
50	457.3	463.0	899.1	2310	2293	4116	4098	8289	8173	2270	2283	2283	2293	2283	2283	882	905.2	899.1
55	457.8	463.5	868.7	2300	2288	4124	4088	8278	8166	2263	2277	2279	2288	2279	2277	853.4	876.7	868.7
60	458.3	464.0	844.6	2297	2283	4129	4075	8260	8162	2257	2273	2274	2283	2274	2273	827.8	849.9	844.6
65	458.7	464.5	823.6	2292	2278	4108	4078	8243	8145	2254	2268	2269	2278	2269	2268	808.6	830.6	823.6
70	458.9	464.7	812.6	2286	2272	4105	4070	8254	8128	2247	2262	2264	2272	2264	2262	796.4	818.1	812.6

Table B.16.  
Specific enthalpies and pressures from experimental data from transient validation case study 3, time segment 2 of 2.

Time	h15	h16	p1	p2	p3	p4	p5	p6	p7	p8	p9	p10	p11	p12	p13	p14	p15	p16
[s]	[kJ/kg]	[kJ/kg]	[kPa]	[kPa]	[kPa]	[kPa]	[kPa]	[kPa]	[kPa]	[kPa]	[kPa]	[kPa]	[kPa]	[kPa]	[kPa]	[kPa]	[kPa]	[kPa]
75	459.0	464.9	807.1	2280	2268	4084	4068	8223	8119	2242	2257	2259	2268	2259	2257	790	812.9	807.1
80	459.2	465.1	799.6	2278	2263	4092	4056	8210	8109	2236	2253	2253	2263	2253	2253	782.8	805.3	799.6
85	459.3	465.4	791.1	2268	2258	4090	4043	8194	8092	2233	2246	2249	2258	2249	2246	775.3	798	791.1
90	459.4	465.5	786	2264	2254	4072	4038	8170	8073	2227	2242	2244	2254	2244	2242	771.4	794.2	786
95	459.5	465.6	787.6	2263	2249	4067	4034	8180	8059	2224	2238	2240	2249	2240	2238	773.7	793.9	787.6

Table B.17.  
Parameters from experimental data from transient validation case study 3, time segment 1 of 2.

Time	Q_dot_LTE	Q_dot_MTE	T_sh_LPC	T_sh_MTE	T_sh_MPC	T_LTE	T_MTE	LL_FT	W_dot_C1	W_dot_C2
[s]	[kW]	[kW]	[C]	[C]	[C]	[C]	[C]	[%]	[kW]	[kW]
0	3.0	3.5	22.0	35.5	25.8	-36.8	-15.0	18	0.904	0.884
5	2.8	3.7	22.9	35.8	25.4	-37.7	-15.0	18	0.909	3.660
10	2.7	3.8	23.7	35.6	24.9	-38.5	-14.9	18	0.909	3.670
15	2.6	3.9	24.4	36.1	24.5	-39.0	-15.0	18	0.907	3.679
20	2.4	4.1	25.0	37.1	24.2	-39.4	-14.9	18	0.905	3.718
25	2.4	4.1	25.5	37.9	23.9	-39.8	-15.0	18	0.903	3.698
30	2.3	4.1	25.9	37.0	23.7	-40.2	-15.0	18	0.906	3.690
35	2.3	4.2	26.4	36.6	23.4	-40.6	-15.1	18	0.907	3.732
40	2.3	4.1	27.3	39.1	23.1	-41.5	-15.1	18	0.905	3.721
45	2.5	4.0	28.4	39.4	22.7	-42.5	-15.3	18	0.909	3.689
50	2.4	4.1	29.5	40.1	22.4	-43.5	-15.3	19	0.911	3.621
55	2.3	4.2	30.6	39.3	22.0	-44.3	-15.4	19	0.911	3.636
60	2.3	4.2	31.4	39.5	21.7	-45.1	-15.5	19	0.913	3.695
65	2.2	4.3	32.3	40.3	21.4	-45.7	-15.6	19	0.910	3.662
70	2.2	4.3	32.7	40.0	21.2	-46.1	-15.7	19	0.907	3.641

Table B.18.  
Parameters from experimental data from transient validation case study 3, time segment 2 of 2.

Time	$Q_{\text{dot\_LTE}}$	$Q_{\text{dot\_MTE}}$	$T_{\text{sh\_LPC}}$	$T_{\text{sh\_MTE}}$	$T_{\text{sh\_MPC}}$	$T_{\text{LTE}}$	$T_{\text{MTE}}$	$LL_{\text{FT}}$	$W_{\text{dot\_C1}}$	$W_{\text{dot\_C2}}$
[s]	[kW]	[kW]	[C]	[C]	[C]	[C]	[C]	[%]	[kW]	[kW]
75	2.2	4.3	33.0	40.4	21.1	-46.3	-15.7	19	0.903	3.714
80	2.1	4.3	33.4	40.2	21.1	-46.6	-15.8	19	0.901	3.656
85	2.1	4.3	33.8	41.3	21.0	-46.8	-15.9	19	0.894	3.659
90	2.2	4.1	34.0	40.6	21.0	-46.9	-15.9	19	0.892	3.626
95	2.3	4.1	34.1	40.7	21.0	-46.9	-16.0	19	0.884	3.615

Table B.19.  
Specific enthalpies from experimental data from transient validation case study 4, time segment 1 of 2.

Time [s]	h1 [kJ/kg]	h2 [kJ/kg]	h3 [kJ/kg]	h4 [kJ/kg]	h5 [kJ/kg]	h6 [kJ/kg]	h7 [kJ/kg]	h8 [kJ/kg]	h9 [kJ/kg]	h10 [kJ/kg]	h11 [kJ/kg]	h12 [kJ/kg]	h13 [kJ/kg]	h14 [kJ/kg]
0	458.6	526.6	472.9	531.6	465.6	503.4	258.3	258.3	159.5	462.2	472.9	462.2	159.5	159.5
5	458.8	526.4	470.9	531.2	465.4	504.9	258.9	258.9	160.9	461.6	470.9	461.6	160.9	160.9
10	458.3	526.4	470.8	530.6	465	505.1	259.3	259.3	162.1	461	470.8	461	162.1	162.1
15	457.1	526.1	471.3	530.1	464.6	504.6	260.1	260.1	163.1	460.5	471.3	460.5	163.1	163.1
20	455.9	525.8	472.2	529.5	464.3	503.5	261.2	261.2	163.9	460.1	472.2	460.1	163.9	163.9
25	455	525.4	472.6	529.1	463.9	502.7	262.3	262.3	164.8	459.7	472.6	459.7	164.8	164.8
30	454.2	525	473	528.6	463.5	501.7	263.9	263.9	165.4	459.3	473	459.3	165.4	165.4
35	453.6	524.5	473.2	528.2	463.3	500.8	265.8	265.8	166	458.9	473.2	458.9	166	166
40	453.1	524.1	473.3	527.8	463	499.8	268.5	268.5	166.7	458.6	473.3	458.6	166.7	166.7
45	452.7	523.6	473.3	527.5	462.6	498.9	271.4	271.4	167.2	458.4	473.3	458.4	167.2	167.2
50	452.2	523.3	473.3	527.2	462.3	498	274.1	274.1	167.8	458.1	473.3	458.1	167.8	167.8
55	451.7	522.8	473.3	527	462.1	497.1	276.1	276.1	168.2	457.9	473.3	457.9	168.2	168.2
60	450.9	522.5	473.3	526.7	461.8	496.3	276.8	276.8	168.6	457.7	473.3	457.7	168.6	168.6
65	446.4	522.2	473.2	526.4	461.4	495.6	276.9	276.9	169	457.4	473.2	457.4	169	169
70	438.9	521.9	473.1	526.3	461.2	495.2	276.5	276.5	169.5	457.2	473.1	457.2	169.5	169.5

Table B.20.  
Specific enthalpies from experimental data from transient validation case study 4, time segment 2 of 2.

Time	h1	h2	h3	h4	h5	h6	h7	h8	h9	h10	h11	h12	h13	h14
[s]	[kJ/kg]	[kJ/kg]	[kJ/kg]	[kJ/kg]	[kJ/kg]	[kJ/kg]	[kJ/kg]	[kJ/kg]	[kJ/kg]	[kJ/kg]	[kJ/kg]	[kJ/kg]	[kJ/kg]	[kJ/kg]
75	140.7	521.3	473.2	526	461.1	494.7	276	276	170	457	473.2	457	170	170
80	141.2	520.8	473.1	525.6	460.9	494.2	275.3	275.3	170.5	456.7	473.1	456.7	170.5	170.5
85	141.8	520.2	473	525.4	460.7	493.5	274.4	274.4	171	456.4	473	456.4	171	171
90	142	519.7	472.8	525.2	460.4	493	273.5	273.5	171.5	456.2	472.8	456.2	171.5	171.5
95	141.7	519.3	472.2	524.9	460.1	492.8	272.8	272.8	172	455.9	472.2	455.9	172	172
100	141.1	519.1	471.5	524.6	459.7	492	272	272	172.5	455.6	471.5	455.6	172.5	172.5
105	437.1	519.2	470.9	524.5	459.4	491.3	271.3	271.3	172.9	455.4	470.9	455.4	172.9	172.9
110	437.4	519.2	470.3	524.2	459.3	490.9	270.7	270.7	173.2	455.2	470.3	455.2	173.2	173.2
115	438.8	519.2	469.6	523.9	459.3	490.9	270.1	270.1	173.5	455	469.6	455	173.5	173.5



Table B.21.  
Specific enthalpies and pressures from experimental data from transient validation case study 4, time segment 1 of 2.

Time	h15	h16	p1	p2	p3	p4	p5	p6	p7	p8	p9	p10	p11	p12	p13	p14	p15	p16
[s]	[kJ/kg]	[kJ/kg]	[kPa]	[kPa]	[kPa]	[kPa]	[kPa]	[kPa]	[kPa]	[kPa]	[kPa]	[kPa]	[kPa]	[kPa]	[kPa]	[kPa]	[kPa]	[kPa]
0	453.5	458.6	1202	2163	2137	3886	3874	8424	8325	2115	2124	2126	2137	2126	2124	1192	1215	1202
5	453.8	458.8	1188	2210	2178	3926	3886	7976	7858	2156	2167	2169	2178	2169	2167	1177	1199	1188
10	453.3	458.3	1219	2238	2215	3968	3917	7673	7579	2192	2203	2206	2215	2206	2203	1215	1234	1219
15	452	457.1	1293	2277	2246	3995	3942	7508	7429	2223	2234	2236	2246	2236	2234	1290	1309	1293
20	450.9	455.9	1359	2303	2274	4020	3968	7412	7322	2246	2261	2264	2274	2264	2261	1355	1372	1359
25	450	455	1407	2334	2298	4055	3998	7359	7269	2272	2285	2288	2298	2288	2285	1404	1422	1407
30	449.3	454.2	1443	2350	2320	4081	4024	7334	7240	2293	2306	2311	2320	2311	2306	1439	1459	1443
35	448.7	453.6	1471	2378	2339	4112	4046	7321	7226	2312	2326	2331	2339	2331	2326	1470	1489	1471
40	448.2	453.1	1496	2393	2357	4133	4071	7325	7226	2332	2347	2350	2357	2350	2347	1493	1512	1496
45	447.6	452.7	1516	2418	2376	4157	4098	7343	7250	2349	2365	2367	2376	2367	2365	1513	1531	1516
50	446.7	452.2	1534	2427	2393	4168	4128	7397	7289	2366	2380	2384	2393	2384	2380	1530	1551	1534
55	445.3	451.7	1548	2447	2406	4191	4150	7467	7349	2378	2393	2398	2406	2398	2393	1545	1564	1548
60	439.9	450.9	1559	2455	2418	4214	4172	7545	7429	2390	2407	2410	2418	2410	2407	1563	1578	1559
65	437.2	446.4	1572	2474	2431	4239	4199	7615	7496	2405	2418	2424	2431	2424	2418	1584	1597	1572
70	437.2	438.9	1592	2482	2446	4247	4223	7660	7559	2418	2433	2438	2446	2438	2433	1603	1616	1592

Table B.22.  
Specific enthalpies and pressures from experimental data from transient validation case study 4, time segment 2 of 2.

Time	h15	h16	p1	p2	p3	p4	p5	p6	p7	p8	p9	p10	p11	p12	p13	p14	p15	p16
[s]	[kJ/kg]	[kJ/kg]	[kPa]	[kPa]	[kPa]	[kPa]	[kPa]	[kPa]	[kPa]	[kPa]	[kPa]	[kPa]	[kPa]	[kPa]	[kPa]	[kPa]	[kPa]	[kPa]
75	437.2	140.7	1609	2505	2461	4282	4245	7712	7608	2434	2449	2452	2461	2452	2449	1621	1635	1609
80	437.2	141.2	1628	2517	2478	4319	4264	7746	7656	2450	2464	2467	2478	2467	2464	1636	1651	1628
85	437.2	141.8	1640	2537	2493	4338	4284	7793	7693	2467	2480	2484	2493	2484	2480	1648	1662	1640
90	437.3	142	1639	2547	2509	4356	4306	7822	7722	2483	2497	2501	2509	2501	2497	1642	1659	1639
95	437.3	141.7	1630	2568	2526	4381	4338	7855	7745	2499	2514	2518	2526	2518	2514	1627	1647	1630
100	437.3	141.1	1614	2583	2541	4411	4366	7921	7792	2515	2528	2532	2541	2532	2528	1608	1628	1614
105	437.3	437.1	1599	2586	2551	4417	4390	7980	7849	2527	2540	2542	2551	2542	2540	1590	1613	1599
110	437.9	437.4	1583	2600	2562	4449	4403	8007	7888	2537	2551	2555	2562	2555	2551	1574	1596	1583
115	439.6	438.8	1567	2618	2574	4479	4410	8001	7927	2547	2561	2565	2574	2565	2561	1559	1581	1567

Table B.23.  
Parameters from experimental data from transient validation case study 4, time segment 1 of 2.

Time	Q_dot_LTE	Q_dot_MTE	T_sh_LPC	T_sh_MTE	T_sh_MPC	T_LTE	T_MTE	LL_FT	W_dot_C1	W_dot_C2
[s]	[kW]	[kW]	[C]	[C]	[C]	[C]	[C]	[%]	[kW]	[kW]
0	4.199	3.051	21.74	21.17	30.9	-35.25	-17.67	37.97	0.8549	3.639
5	5.415	3.299	22.13	20.57	28.98	-35.61	-17.03	35.85	0.866	3.576
10	4.514	3.738	21.39	19.96	28.8	-34.71	-16.48	33.8	0.8729	3.474
15	3.861	3.987	19.58	19.48	29.13	-32.99	-16.01	30.89	0.8725	3.488
20	3.524	4.008	17.99	19.06	29.84	-31.54	-15.66	28.64	0.8717	3.456
25	3.352	3.94	16.86	18.68	30.22	-30.51	-15.27	25.56	0.8676	3.441
30	3.183	3.795	15.98	18.32	30.51	-29.76	-14.97	24.64	0.8636	3.434
35	2.859	3.836	15.29	18.01	30.64	-29.13	-14.69	21.64	0.8613	3.425
40	2.432	3.863	14.7	17.74	30.67	-28.65	-14.39	21.8	0.8622	3.403
45	2.188	3.78	14.2	17.49	30.66	-28.26	-14.15	20.22	0.8618	3.449
50	1.776	3.848	13.7	17.23	30.6	-27.92	-13.9	19.07	0.861	3.461
55	1.598	3.949	13.2	17.03	30.59	-27.63	-13.72	18.21	0.8654	3.471
60	1.64	3.88	12.34	16.86	30.5	-27.28	-13.55	17.91	0.8684	3.456
65	1.632	3.909	8.21	16.66	30.4	-26.87	-13.35	16.11	0.8691	3.461
70	1.804	3.88	1.603	16.45	30.32	-26.5	-13.15	14.35	0.8675	3.505

Table B.24.  
Parameters from experimental data from transient validation case study 4, time segment 2 of 2.

Time [s]	$\dot{Q}_{LTE}$ [kW]	$\dot{Q}_{MTE}$ [kW]	$T_{sh\_LPC}$ [C]	$T_{sh\_MTE}$ [C]	$T_{sh\_MPC}$ [C]	$T_{LTE}$ [C]	$T_{MTE}$ [C]	$LLFT$ [%]	$\dot{W}_{dot\_C1}$ [kW]	$\dot{W}_{dot\_C2}$ [kW]
75	1.971	3.843	-0.1208	16.27	30.29	-26.16	-12.93	12.85	0.8695	3.543
80	2.129	3.837	-0.2166	16.05	30.19	-25.87	-12.7	12.55	0.8699	3.511
85	2.278	3.785	-0.1776	15.8	30.1	-25.65	-12.47	10.75	0.8739	3.546
90	2.493	3.786	-0.0684	15.57	29.84	-25.76	-12.24	9.566	0.8795	3.554
95	2.591	3.762	-0.0329	15.32	29.29	-26.04	-12.02	8.347	0.887	3.572
100	2.444	3.854	-0.0278	15.12	28.69	-26.41	-11.8	9.095	0.8966	3.607
105	2.475	3.908	0.01695	14.95	28.15	-26.74	-11.63	9.206	0.9019	3.618
110	2.579	3.922	0.273	14.76	27.54	-27.06	-11.49	11.02	0.9123	3.622
115	2.692	3.951	1.488	14.61	26.97	-27.35	-11.36	11.57	0.9185	3.662

Table B.25.  
Single-stage compressor validation raw data, 1 of 2

Point	p_s	p_d	T_s	T_d	m.dot	W.dot
[-]	[kPa]	[kPa]	[C]	[C]	[kg/s]	[kW]
1	2162	3098	-2.23	50.36	0.021	0.931
2	2194	2924	-2.01	43.70	0.021	0.866
3	2053	2771	-5.13	42.60	0.020	0.853
4	1921	2600	-6.99	42.20	0.019	0.832
5	1774	2404	-7.58	42.59	0.017	0.805
6	1754	2381	-8.46	42.78	0.017	0.802
7	2194	2924	-2.01	43.70	0.021	0.866
8	1909	2574	-2.54	46.84	0.018	0.815
9	1793	2514	-1.86	48.82	0.017	0.832
10	1683	2474	-4.47	53.39	0.015	0.849
11	1846	2623	-6.63	49.37	0.017	0.853
12	1323	2833	-4.94	77.33	0.011	0.983
13	1325	2836	-4.88	77.30	0.011	0.984
14	1460	2814	-15.62	75.12	0.012	1.106
15	1482	2914	-15.71	76.71	0.012	1.120
16	1480	2943	-15.47	79.21	0.012	1.155
17	1532	3040	-15.42	80.14	0.012	1.149
18	1430	3013	-16.74	87.37	0.011	1.193
19	1436	3033	-16.75	85.66	0.011	1.204
20	1403	3064	-15.85	88.90	0.011	1.225
21	1379	3178	-15.46	92.62	0.010	1.257
22	1435	3264	-15.42	90.43	0.011	1.308
23	1406	3108	-15.44	91.55	0.011	1.286
24	1458	3066	-15.21	88.56	0.011	1.266

Table B.26.  
Single-stage compressor validation raw data, 2 of 2

Point	p_s	p_d	T_s	T_d	m_dot	W_dot
[-]	[kPa]	[kPa]	[C]	[C]	[kg/s]	[kW]
25	1409	2986	-15.16	91.15	0.011	1.255
26	1385	2990	-14.79	91.99	0.010	1.261
27	1414	2927	-14.60	91.12	0.011	1.246
28	1555	2935	-16.97	68.19	0.013	1.045
29	1670	3349	-14.92	73.54	0.014	1.122
30	1659	3317	-15.21	73.17	0.014	1.112
31	1682	3512	-15.00	77.02	0.014	1.155
32	1625	3383	-15.70	75.74	0.014	1.130
33	1618	3269	-15.79	73.14	0.014	1.115
34	1583	3162	-16.36	72.00	0.013	1.092
35	1570	3118	-16.27	71.89	0.013	1.080
36	1441	3419	-14.90	85.85	0.011	1.149
37	1490	3248	-15.81	81.86	0.012	1.121
38	1474	3132	-15.19	79.71	0.012	1.096
39	1471	3244	-15.60	87.28	0.012	1.117
40	1487	3327	-14.88	89.50	0.012	1.130
41	1491	3483	-15.19	92.10	0.012	1.163

Table B.27.  
Two-stage compressor validation raw data, 1 of 3

Point	p_s.1	p_d.1	p_s.2	p_d.2	T_s.1	T_d.1	T_s.2	T_d.2	m_dot	W_dot
[-]	[kPa]	[kPa]	[kPa]	[kPa]	[C]	[C]	[C]	[C]	[kg/s]	[kW]
1	2979	5049	4989	7459	19.41	71.06	29.86	62.62	0.050	3.522
2	2806	4836	4778	7490	19.38	70.30	29.05	64.84	0.047	3.574
3	2661	4645	4595	7658	17.34	73.95	28.74	70.02	0.043	3.593
4	2500	4452	4407	8059	16.37	77.03	28.27	76.86	0.039	3.682
5	2312	4289	4244	9191	16.21	81.98	27.93	89.37	0.035	3.938
6	2291	4247	4200	9091	15.74	83.32	28.00	89.85	0.035	3.893
7	2806	4836	4778	7490	19.38	70.30	29.05	64.84	0.047	3.574
8	2476	4421	4381	7723	14.27	76.13	28.20	74.15	0.039	3.585
9	2425	4369	4334	7976	14.01	76.63	28.08	77.12	0.038	3.669
10	1968	3658	3625	7248	18.60	82.24	26.30	82.28	0.029	3.353
11	2329	4251	4214	9115	17.20	86.12	28.35	90.94	0.035	3.888
12	2357	4239	4202	8301	15.36	82.85	28.08	83.93	0.036	3.689
13	1941	3609	3575	7208	18.92	83.37	26.22	83.07	0.029	3.329
14	2298	4205	4168	9001	17.04	86.13	28.10	90.67	0.034	3.845
15	2351	4233	4198	8292	14.58	82.49	28.04	83.80	0.036	3.686
16	2376	4344	4284	7820	10.53	72.35	27.46	74.73	0.038	3.658
17	2520	4540	4478	8018	11.68	73.54	28.22	74.49	0.041	3.715
18	2733	4931	4867	8544	7.49	69.14	29.07	73.35	0.046	3.921
19	2736	4936	4871	8550	7.51	69.12	29.07	73.34	0.046	3.922
20	2009	3651	3595	7272	22.24	86.41	26.73	84.33	0.029	3.329
21	1744	3324	3282	8089	24.07	94.61	26.18	98.76	0.024	3.407
22	2121	3936	3889	9447	21.31	95.17	27.86	100.70	0.030	3.844
23	2110	3869	3823	8665	21.55	92.71	27.67	95.22	0.030	3.666
24	2088	3783	3737	7720	21.11	89.97	27.30	87.74	0.030	3.436

Table B.28.  
Two-stage compressor validation raw data, 2 of 3

Point	p_s_1	p_d_1	p_s_2	p_d_2	T_s_1	T_d_1	T_s_2	T_d_2	m_dot	W_dot
[-]	[kPa]	[kPa]	[kPa]	[kPa]	[C]	[C]	[C]	[C]	[kg/s]	[kW]
25	2055	3716	3671	7321	20.59	88.14	27.04	84.60	0.029	3.333
26	2067	3745	3696	7344	20.27	87.16	27.05	84.08	0.030	3.348
27	2726	4930	4895	8817	3.98	70.69	30.08	77.18	0.045	4.000
28	2819	4994	4957	7769	5.28	66.22	29.83	65.97	0.048	3.705
29	2854	5036	5000	8176	5.05	68.54	30.27	69.78	0.048	3.821
30	2943	5105	5067	7413	6.48	64.70	30.06	60.97	0.051	3.591
31	2933	5209	5176	8734	3.98	68.30	30.90	72.71	0.050	4.000
32	2954	5198	5164	8243	6.17	66.03	30.50	67.93	0.051	3.859
33	2990	5195	5160	7918	7.19	66.23	30.64	65.24	0.051	3.727
34	3109	5321	5285	7402	7.82	63.39	30.63	58.05	0.058	3.551
35	3204	5444	5407	7443	9.04	63.13	31.05	57.03	0.057	3.562
36	3050	5247	5217	7620	7.58	65.36	30.74	61.59	0.053	3.629
37	3006	5195	5167	8002	9.44	67.79	30.93	66.31	0.051	3.739
38	2928	5126	5102	8515	8.49	69.69	30.87	72.20	0.049	3.906
39	2935	5117	5093	8275	7.51	69.13	30.89	70.07	0.049	3.849
40	2869	5068	5042	8793	8.09	70.81	30.73	75.56	0.048	3.984
41	2704	4672	4652	7678	16.96	77.67	30.25	72.29	0.042	3.571
42	2839	4861	4870	7077	4.38	60.79	25.32	56.07	0.050	3.464
43	3258	5847	5836	8410	7.53	69.12	39.51	69.51	0.057	3.952
44	3230	5809	5807	8502	7.77	69.65	39.59	70.90	0.056	3.984
45	3426	6020	6021	7854	9.78	67.41	39.82	62.26	0.061	3.737
46	3289	5713	5715	7510	7.31	63.82	35.02	57.98	0.059	3.618
47	3178	5597	5605	7811	5.79	64.74	34.94	62.47	0.056	3.746
48	3078	5480	5495	8324	5.90	67.58	34.97	69.15	0.053	3.917



Table B.29.

Two-stage compressor validation raw data, 3 of 3

Point	p_s_1	p_d_1	p_s_2	p_d_2	T_s_1	T_d_1	T_s_2	T_d_2	m_dot	W_dot
[-]	[kPa]	[kPa]	[kPa]	[kPa]	[C]	[C]	[C]	[C]	[kg/s]	[kW]
49	3034	5430	5450	8530	4.88	68.20	34.88	71.69	0.052	3.977
50	3336	5828	5771	7792	8.12	63.98	35.47	59.52	0.060	3.716
51	3162	5621	5568	8340	4.36	67.13	35.38	67.71	0.055	3.920
52	3050	5476	5428	8868	8.21	70.46	35.38	74.71	0.052	4.074
53	3170	5623	5577	8898	10.28	70.98	36.08	73.69	0.054	4.081
54	3251	5706	5656	8503	10.91	69.17	35.92	68.79	0.056	3.946
55	3406	5901	5848	8123	10.59	66.83	36.24	62.83	0.060	3.815
56	2925	5307	5282	9210	5.86	74.07	35.33	80.12	0.048	4.147
57	2971	5342	5305	8677	3.87	71.22	35.06	74.82	0.050	4.004
58	2967	5345	5305	8202	7.71	68.17	34.64	69.63	0.051	3.863

## C. APPENDIX C: POST-PROCESSING CODE

This appendix contains EES code for post-processing the four system architectures that were experimentally evaluated in Section 5. These codes are used to analyze the raw data taken by the test stand to produce efficiency, energy balance, and thermophysical property calculations along with P-h diagrams.

### C.1 Baseline Cycle Analysis

This post-processing code is used to analyze experimental data taken from the baseline cycle. A P-h diagram for the baseline cycle is provided in Figure 5.1.

```

////////////////////////////////////
"C02 System Data Analysis Script
Both Comps, Both Evaps, No Bypass"
////////////////////////////////////

"!Inputs"
R$ = 'R744'
Text_Data$ = 'ss_4g_10_lookup'

"!System Parameters Call"
T_GC3_ai = lookup(Text_Data$,1,'T21_GC3_ai')
T_amb = T_GC3_ai

m_dot_med = m_dot_tot - m_dot_low

```

```

W_dot_C1 = lookup(Text_Data$,1,'W_Dot_LP_comp')*convert('W','kW')
W_dot_C2 = lookup(Text_Data$,1,'W_Dot_HP_comp')*convert('W','kW')

W_dot_fan_rej = lookup(Text_Data$,1,'W_dot_Fans')*convert('W','kW')
W_dot_fan_abs = 0.5 [kW]

"!Cycle Development"

"1 - LP Suction"
T[1] = lookup(Text_Data$,1,'T1_Suction_LP')
P[1] = lookup(Text_Data$,1,'P1_Suction_LP')
h[1] = enthalpy(R$,P=p[1],T=T[1])
s[1] = entropy(R$,P=p[1],T=T[1])

T_1_sat = temperature(R$,P=p[1],x=1)
T_sh_C1 = T[1] - T_1_sat

"2 - LP Discharge"
T[2] = lookup(Text_Data$,1,'T2_Discharge_LP')
P[2] = lookup(Text_Data$,1,'P2_Discharge_LP')
h[2] = enthalpy(R$,P=p[2],T=T[2])
s[2] = entropy(R$,P=p[2],T=T[2])

h_2s = enthalpy(R$,P=p[2],s=s[1])

eta_iso_C1 = m_dot_low*(h_2s - h[1])/W_dot_C1

Pr_C1 = P[2]/P[1]

"3 - HP Suction"

```

```

T[3] = lookup(Text_Data$,1,'T3_Suction_HP')
P[3] = lookup(Text_Data$,1,'P3_Suction_HP')
h[3] = enthalpy(R$,P=p[3],T=T[3])
s[3] = entropy(R$,P=p[3],T=T[3])

T_3_sat = temperature(R$,P=p[3],x=1)
T_sh_C2 = T[3] - T_3_sat

"Assess adiabatic mixing @ C2 suction E-bal"
m_dot_low*h[2] + m_dot_med*h[10] = m_dot_tot*h_3_test
del_h_3 = (h_3_test - h[3])
delta_Q_h_3 = m_dot_tot*del_h_3

"4 - IC In"
T[4] = lookup(Text_Data$,1,'T4_IC_in')
P[4] = lookup(Text_Data$,1,'P4_IC_in')
h[4] = enthalpy(R$,P=p[4],T=T[4])
s[4] = entropy(R$,P=p[4],T=T[4])

h_4s = enthalpy(R$,P=p[4],s=s[3])

"5 - IC Out"
T[5] = lookup(Text_Data$,1,'T5_IC_out')
P[5] = lookup(Text_Data$,1,'P5_IC_out')
h[5] = enthalpy(R$,P=p[5],T=T[5])
s[5] = entropy(R$,P=p[5],h=h[5])

"6 - GC In"
T[6] = lookup(Text_Data$,1,'T6_GC_in')

```

```

P[6] = lookup(Text_Data$,1,'P6_GC_in')
h[6] = enthalpy(R$,P=p[6],T=T[6])
s[6] = entropy(R$,P=p[6],h=h[6])

h_6s = enthalpy(R$,P=p[6],s=s[5])

eta_iso_C2 = m_dot_tot*(h_6s - h[5] + h_4s - h[3])/W_dot_C2

Pr_C2 = P[6]/P[3]

"7 - GC_out"
T[7] = lookup(Text_Data$,1,'T7_GC_out')
P[7] = lookup(Text_Data$,1,'P7_GC_out')
h[7] = enthalpy(R$,P=p[7],T=T[7])
s[7] = entropy(R$,P=p[7],T=T[7])

"8 - MT FT"
T[8] = temperature(R$,P=p[8],h=h[8])
P[8] = lookup(Text_Data$,1,'P8_Ejector_out')
h[8] = h[7]
s[8] = entropy(R$,P=p[8],h=h[8])

"9 - MTE In"
T[9] = T_MT_evap_in_TC
P[9] = P_MT_evap_in_TC
h[9] = h[8]
s[9] = entropy(R$,P=p[9],h=h[9])

T_MT_evap = T[9]

```

```
T_MT_evap_in_TC = lookup(Text_Data$,1,'T8_MT_Evap_in')
P_MT_evap_in_TC = pressure(R$,T=T_MT_evap_in_TC,x=0)
```

```
"10 - MTE Out"
```

```
T[10] = lookup(Text_Data$,1,'T9_MT_Evap_out')
P[10] = lookup(Text_Data$,1,'P11_MT_Evap_out')
h[10] = enthalpy(R$,P=p[10],T=T[10])
s[10] = entropy(R$,P=p[10],T=T[10])
```

```
T_10_sat = temperature(R$,P=p[10],x=1)
T_10_sh = T[10] - T_10_sat
```

```
"11 - Between Flash Tanks"
```

```
T[11] = temperature(R$,P=p[11],h=h[11])
P[11] = lookup(Text_Data$,1,'P15_LT_FT_in')
h[11] = h[7]
s[11] = entropy(R$,P=p[11],h=h[11])
```

```
"12 - LTE In"
```

```
T[12] = T_LT_evap_in_TC
P[12] = P_LT_evap_in_TC
h[12] = h[7]
s[12] = entropy(R$,P=p[12],h=h[12])
```

```
T_LT_evap = T[12]
```

```
T_LT_evap_in_TC = lookup(Text_Data$,1,'T19_LT_Evap_in')
P_LT_evap_in_TC = pressure(R$,T=T_LT_evap_in_TC,x=0)
```

"13 - LTE Out"

$T[13] = \text{lookup}(\text{Text\_Data}, 1, 'T11\_LT\_Evap\_out')$

$P[13] = \text{lookup}(\text{Text\_Data}, 1, 'P14\_LT\_Evap\_out')$

$h[13] = \text{enthalpy}(R, P=p[13], T=T[13])$

$s[13] = \text{entropy}(R, P=p[13], T=T[13])$

$T_{13\_sat} = \text{temperature}(R, P=p[13], x=1)$

$T_{13\_sh} = T[13] - T_{13\_sat}$

"!System Calculations"

$W_{dot\_C1} = Q_{dot\_loss\_C1} + m_{dot\_low} * (h[2] - h[1])$

$W_{dot\_C2} = Q_{dot\_loss\_C2} + m_{dot\_tot} * ((h[4] - h[3]) + (h[6] - h[5]))$

$Q_{dot\_IC} = m_{dot\_tot} * (h[4] - h[5])$

$Q_{dot\_GC} = m_{dot\_tot} * (h[6] - h[7])$

$Q_{dot\_MTE} = m_{dot\_med} * (h[10] - h[9])$

$Q_{dot\_MTE} = Q_{dot\_MT\_w}$

$Q_{dot\_LTE} = m_{dot\_low} * (h[13] - h[12])$

$Q_{dot\_LTE} = Q_{dot\_LT\_w}$

$Q_{dot\_LT\_suc} = m_{dot\_low} * (h[1] - h[13])$

$E_{bal} = W_{dot\_C1} + W_{dot\_C2} + Q_{dot\_MTE} + Q_{dot\_LTE} - Q_{dot\_IC} -$

$Q_{dot\_GC} - Q_{dot\_loss\_C1} - Q_{dot\_loss\_C2} + Q_{dot\_LT\_suc} - \text{delta\_Q\_h\_3}$

```
Percent_E_bal = 100*(E_bal/(W_dot_C1 + W_dot_C2 + Q_dot_MTE +
    Q_dot_LTE))
```

```
COP_est = (Q_dot_MTE + Q_dot_LTE)/(W_dot_C1 + W_dot_C2
    + W_dot_fan_abs + W_dot_fan_rej)
```

```
delta_Q_dot_MT = Q_dot_MTE - Q_dot_MT_w
```

```
Percent_Waterside_error_MT = 100*(delta_Q_dot_MT)/Q_dot_MTE
```

```
delta_Q_dot_LT = Q_dot_LTE - Q_dot_LT_w
```

```
Percent_Waterside_error_LT = 100*(delta_Q_dot_LT)/Q_dot_LTE
```

```
"!Creating separate array for graphing"
```

```
Duplicate i=1,10
```

```
p_g[i] = p[i]
```

```
h_g[i] = h[i]
```

```
End
```

```
p_g[11] = p[3]
```

```
h_g[11] = h[3]
```

```
p_g[12] = p[10]
```

```
h_g[12] = h[10]
```



```
p_g[13] = p[9]
```

```
h_g[13] = h[9]
```

```
p_g[14] = p[11]
```

```
h_g[14] = h[11]
```

```
p_g[15] = p[12]
```

```
h_g[15] = h[12]
```

```
p_g[16] = p[13]
```

```
h_g[16] = h[13]
```

```
p_g[17] = p[1]
```

```
h_g[17] = h[1]
```

```
////////////////////////////////////
```

```
"!Medium Temp Water-Glycol Solution"
```

```
T_MT_wi = lookup(Text_Data$,1,'T12_MT_w_in') "MT evap water inlet"
```

```
T_MT_wo = lookup(Text_Data$,1,'T13_MT_w_out') "MT evap water outlet"
```

```
T_MT_w_avg = (T_MT_wi + T_MT_wo)/2
```

```
V_dot_MT_w = lookup(Text_Data$,1,'V_dot_w_MT')*convert('liters/min',  
'm^3/sec')
```

```
C_EG_MT = 34.4 [%]
```

```
rho_MT_EG = density(EG,T=T_MT_w_avg,C=C_EG_MT)
```

```
cp_MT_EG = cp(EG,T=T_MT_w_avg,C=C_EG_MT)
```

```

m_dot_MT_EG = V_dot_MT_w*rho_MT_EG

Q_dot_MT_EG = m_dot_MT_EG*cp_MT_EG*(T_MT_wi - T_MT_wo)
Q_dot_MT_w = Q_dot_MT_EG

////////////////////////////////////
"!Low Temp Water-Glycol Solution"

T_LT_wi = lookup(Text_Data$,1,'T14_LT_w_in') "LT evap water inlet"
T_LT_wo = lookup(Text_Data$,1,'T15_LT_w_out') "LT evap water outlet"
T_LT_w_avg = (T_LT_wi + T_LT_wo)/2

V_dot_LT_w = lookup(Text_Data$,1,'V_dot_w_LT')*convert('liters/min',
'm^3/sec')
C_EG_LT = 50

rho_LT_EG = density(EG,T=T_LT_w_avg,C=C_EG_LT)
cp_LT_EG = cp(EG,T=T_LT_w_avg,C=C_EG_LT)
m_dot_LT_EG = V_dot_LT_w*rho_LT_EG

Q_dot_LT_w = m_dot_LT_EG*cp_LT_EG*(T_LT_wi - T_LT_wo)

```

## C.2 MT Economization Cycle Analysis

This post-processing code is used to analyze experimental data taken from the MT economization cycle. A P-h diagram for the MT economization cycle is provided in Figure 5.2.

```

////////////////////////////////////
"C02 System Data Analysis Script
Both Comps, Both Evaps, MT Bypass"
////////////////////////////////////

"!Inputs"
R$ = 'R744'
Text_Data$ = 'ss_5a_25_2020_10_1_lookup'

"!System Parameters Call In"
LL_FT = lookup(Text_Data$,1,'MTFT_R')
T_GC3_ai = lookup(Text_Data$,1,'T21_GC3_ai')
T_amb = T_GC3_ai

W_dot_C1 = lookup(Text_Data$,1,'W_Dot_LP_comp')*convert('W','kW')
W_dot_C2 = lookup(Text_Data$,1,'W_Dot_HP_comp')*convert('W','kW')

W_dot_fan_rej = lookup(Text_Data$,1,'W_dot_Fans')*convert('W','kW')
W_dot_fan_abs = 0.5 [kW]

"!Cycle Development"
"1 - LP Suction"
T[1] = lookup(Text_Data$,1,'T1_Suction_LP')
P[1] = lookup(Text_Data$,1,'P1_Suction_LP')
h[1] = enthalpy(R$,P=p[1],T=T[1])
s[1] = entropy(R$,P=p[1],T=T[1])
m[1] = m_dot_low

```

```
T_1_sat = temperature(R$,P=p[1],x=1)
```

```
T_sh_1 = T[1] - T_1_sat
```

```
"2 - LP Discharge"
```

```
T[2] = lookup(Text_Data$,1,'T2_Discharge_LP')
```

```
P[2] = lookup(Text_Data$,1,'P2_Discharge_LP')
```

```
h[2] = enthalpy(R$,P=p[2],T=T[2])
```

```
s[2] = entropy(R$,P=p[2],T=T[2])
```

```
m[2] = m[1]
```

```
h_2s = enthalpy(R$,P=p[2],s=s[1])
```

```
eta_iso_C1 = m_dot_low*(h_2s - h[1])/W_dot_C1
```

```
Pr_C1 = P[2]/P[1]
```

```
"3 - HP Suction"
```

```
T[3] = lookup(Text_Data$,1,'T3_Suction_HP')
```

```
P[3] = lookup(Text_Data$,1,'P3_Suction_HP')
```

```
h[3] = enthalpy(R$,P=p[3],T=T[3])
```

```
s[3] = entropy(R$,P=p[3],T=T[3])
```

```
m[3] = m_dot_tot
```

```
T_3_sat = temperature(R$,P=p[3],x=1)
```

```
T_sh_3 = T[3] - T_3_sat
```

```
"Assess adiabatic mixing @ C2 suction E-bal"
```

```
m_dot_MT_evap*h[10] + m_dot_MT_vap*h[14] = (m_dot_MT_vap +
m_dot_MT_evap)*h_mix
```

```
m_dot_low*h[2] + (m_dot_MT_vap + m_dot_MT_evap)*h_mix =
m_dot_tot*h_3_test
```

```
del_h_3 = (h_3_test - h[3])
delta_Q_h_3 = m_dot_tot*del_h_3
```

```
"4 - IC In"
```

```
T[4] = lookup(Text_Data$,1,'T4_IC_in')
P[4] = lookup(Text_Data$,1,'P4_IC_in')
h[4] = enthalpy(R$,P=p[4],T=T[4])
s[4] = entropy(R$,P=p[4],T=T[4])
m[4] = m[3]
```

```
h_4s = enthalpy(R$,P=p[4],s=s[3])
```

```
"5 - IC Out"
```

```
T[5] = lookup(Text_Data$,1,'T5_IC_out')
P[5] = lookup(Text_Data$,1,'P5_IC_out')
h[5] = enthalpy(R$,P=p[5],T=T[5])
s[5] = entropy(R$,P=p[5],h=h[5])
m[5] = m[4]
```

```
"6 - GC In"
```

```
T[6] = lookup(Text_Data$,1,'T6_GC_in')
P[6] = lookup(Text_Data$,1,'P6_GC_in')
```

```

h[6] = enthalpy(R$,P=p[6],T=T[6])
s[6] = entropy(R$,P=p[6],h=h[6])
m[6] = m[5]

```

```

h_6s = enthalpy(R$,P=p[6],s=s[5])

```

```

eta_iso_C2 = m_dot_tot*(h_6s - h[5] + h_4s - h[3])/W_dot_C2

```

```

Pr_C2 = P[6]/P[3]

```

```

"7 - GC_out"

```

```

T[7] = lookup(Text_Data$,1,'T7_GC_out')
P[7] = lookup(Text_Data$,1,'P7_GC_out')
h[7] = enthalpy(R$,P=p[7],T=T[7])
s[7] = entropy(R$,P=p[7],T=T[7])
m[7] = m[6]

```

```

"8 - MT FT"

```

```

T[8] = temperature(R$,P=p[8],h=h[8])
P[8] = lookup(Text_Data$,1,'P8_Ejector_out')
h[8] = h[7]
s[8] = entropy(R$,P=p[8],h=h[8])
m[8] = m[7]

```

```

x_8 = quality(R$,P=p[8],h=h[8])

```

```

"9 - MTE In"

```

```

T[9] = T_MT_evap_in_TC
P[9] = P_MT_evap_in_TC

```

```

h[9] = h[15] "MTFT liq outlet"
s[9] = entropy(R$,P=p[9],h=h[9])
m[9] = m_dot_MT_evap

T_MT = temperature(R$,P=p[9],x=1)

T_MT_evap_in_TC = lookup(Text_Data$,1,'T8_MT_Evap_in')
P_MT_evap_in_TC = pressure(R$,T=T_MT_evap_in_TC,x=0)

"10 - MTE Out"
T[10] = lookup(Text_Data$,1,'T9_MT_Evap_out')
P[10] = lookup(Text_Data$,1,'P11_MT_Evap_out')
h[10] = enthalpy(R$,P=p[10],T=T[10])
s[10] = entropy(R$,P=p[10],T=T[10])
m[10] = m[9]

T_sh_MTE = T[10] - T_MT

"11 - LT FT"
T[11] = temperature(R$,P=p[11],h=h[11])
P[11] = lookup(Text_Data$,1,'P15_LT_FT_in')
h[11] = h[9]
s[11] = entropy(R$,P=p[11],h=h[11])
m[11] = m_dot_low

"12 - LTE In - Isenthalpic expansion from MTE in"
T[12] = T_LT_evap_in_TC
P[12] = P_LT_evap_in_TC
h[12] = h[9]

```

```

s[12] = entropy(R$,P=p[12],h=h[12])
m[12] = m[11]

T_LT_evap_in_TC = lookup(Text_Data$,1,'T19_LT_Evap_in')
P_LT_evap_in_TC = pressure(R$,T=T_LT_evap_in_TC,x=0)

"13 - LTE Out"
T[13] = lookup(Text_Data$,1,'T11_LT_Evap_out')
P[13] = lookup(Text_Data$,1,'P14_LT_Evap_out')
h[13] = enthalpy(R$,P=p[13],T=T[13])
s[13] = entropy(R$,P=p[13],T=T[13])
m[13] = m[12]

T_LT = temperature(R$,P=p[12],x=1)

T_sh_LTE = T[13] - T_LT

"14 - MT_FT_vap"
"Assuming x = 1"
T[14] = temperature(R$,P=p[14],x=1)
P[14] = lookup(Text_Data$,1,'P8_Ejector_out')
h[14] = enthalpy(R$,P=p[14],x=1)
s[14] = entropy(R$,P=p[14],x=1)
m[14] = m_dot_MT_vap

"15 - MT_FT_liq"
"Assuming X = 0"
T[15] = temperature(R$,P=p[15],x=0)
p[15] = p[14]

```



```

h[15] = enthalpy(R$,P=p[15],x=0)
s[15] = entropy(R$,P=p[15],x=0)
m[15] = m_dot_MT_liq

```

```

"!System Calculations"

```

```

m_dot_tot = m_dot_MT_vap + m_dot_MT_liq
m_dot_MT_vap = m_dot_tot*x_8
m_dot_MT_liq = m_dot_low + m_dot_MT_evap

```

```

W_dot_C1 = Q_dot_loss_C1 + m_dot_low*(h[2] - h[1])
W_dot_C2 = Q_dot_loss_C2 + m_dot_tot*((h[4] - h[3]) + (h[6] - h[5]))

```

```

Q_dot_IC = m_dot_tot*(h[4] - h[5])
Q_dot_GC = m_dot_tot*(h[6] - h[7])

```

```

Q_dot_MTE = m_dot_MT_evap*(h[10] - h[9])
Q_dot_MTE = Q_dot_MT_w

```

```

Q_dot_LTE = m_dot_low*(h[13] - h[12])
Q_dot_LTE = Q_dot_LT_w

```

```

Q_dot_LT_suc = m_dot_low*(h[1] - h[13])

```

```

E_bal = W_dot_C1 + W_dot_C2 + Q_dot_MTE + Q_dot_LTE -
Q_dot_IC - Q_dot_GC - Q_dot_loss_C1 - Q_dot_loss_C2 +
Q_dot_LT_suc - delta_Q_h_3

```

```
Percent_E_bal = 100*(E_bal/(W_dot_C1 + W_dot_C2 +
Q_dot_MTE + Q_dot_LTE))
```

```
COP_est = (Q_dot_MTE + Q_dot_LTE)/(W_dot_C1 + W_dot_C2 +
W_dot_fan_abs + W_dot_fan_rej)
```

```
delta_Q_dot_MT = Q_dot_MTE - Q_dot_MT_w
```

```
Percent_Waterside_error_MT = 100*(delta_Q_dot_MT)/Q_dot_MTE
```

```
delta_Q_dot_LT = Q_dot_LTE - Q_dot_LT_w
```

```
Percent_Waterside_error_LT = abs(100*(delta_Q_dot_LT)/Q_dot_LTE)
```

```
"!Creating separate array for graphing"
```

```
Duplicate i=1,8
```

```
p_g[i] = p[i]
```

```
h_g[i] = h[i]
```

```
End
```

```
p_g[9] = p[14]
```

```
h_g[9] = h[14]
```

```
p_g[10] = p[10]
```

```
h_g[10] = h[14]
```

`p_g[11] = p[14]`

`h_g[11] = h[14]`

`p_g[12] = p[8]`

`h_g[12] = h[8]`

`p_g[13] = p[15]`

`h_g[13] = h[15]`

`p_g[14] = p[9]`

`h_g[14] = h[9]`

`p_g[15] = p[10]`

`h_g[15] = h[10]`

`p_g[16] = p[3]`

`h_g[16] = h[3]`

`p_g[17] = p[10]`

`h_g[17] = h[10]`

`p_g[18] = p[9]`

`h_g[18] = h[9]`

`p_g[19] = p[11]`

`h_g[19] = h[11]`

`p_g[20] = p[12]`

`h_g[20] = h[12]`

```
p_g[21] = p[13]
```

```
h_g[21] = h[13]
```

```
p_g[22] = p[1]
```

```
h_g[22] = h[1]
```

```
////////////////////////////////////
```

```
"!Medium Temp Water-Glycol Solution"
```

```
T_MT_wi = lookup(Text_Data$,1,'T12_MT_w_in') "MT evap water inlet"
```

```
T_MT_wo = lookup(Text_Data$,1,'T13_MT_w_out') "MT evap water outlet"
```

```
T_MT_w_avg = (T_MT_wi + T_MT_wo)/2
```

```
V_dot_MT_w = lookup(Text_Data$,1,'V_dot_w_MT')*convert('liters/min',  
'm^3/sec')
```

```
C_MT_EG = 34.4
```

```
rho_MT_EG = density(EG,T=T_MT_w_avg,C=C_MT_EG)
```

```
cp_MT_EG = cp(EG,T=T_MT_w_avg,C=C_MT_EG)
```

```
m_dot_MT_EG = V_dot_MT_w*rho_MT_EG
```

```
Q_dot_MT_EG = m_dot_MT_EG*cp_MT_EG*(T_MT_wi - T_MT_wo)
```

```
Q_dot_MT_w = Q_dot_MT_EG
```

```
////////////////////////////////////
```

```
"!Low Temp Water-Glycol Solution"
```



```
Text_Data$ = 'ss_8e_20_2020_10_5_lookup'
```

```
"!System Parameters Call"
```

```
LL_FT = lookup(Text_Data$,1,'MTFT_R')
```

```
T_GC3_ai = lookup(Text_Data$,1,'T21_GC3_ai')
```

```
T_amb = T_GC3_ai
```

```
m_dot_motive = lookup(Text_Data$,1,'m_dot_motive')*convert('g/s',  
'kg/s')
```

```
W_dot_C1 = lookup(Text_Data$,1,'W_Dot_LP_comp')*convert('W','kW')
```

```
W_dot_C2 = lookup(Text_Data$,1,'W_Dot_HP_comp')*convert('W','kW')
```

```
W_dot_fan_rej = lookup(Text_Data$,1,'W_dot_Fans')*convert('W','kW')
```

```
W_dot_fan_abs = 0.5 [kW]
```

```
"!Cycle Development"
```

```
"1 - LP Suction"
```

```
T[1] = lookup(Text_Data$,1,'T1_Suction_LP')
```

```
P[1] = lookup(Text_Data$,1,'P1_Suction_LP')
```

```
h[1] = enthalpy(R$,P=p[1],T=T[1])
```

```
s[1] = entropy(R$,P=p[1],T=T[1])
```

```
m[1] = m_dot_low
```

```
T_suc_C1_sat = temperature(R$,P=p[1],x=1)
```

```
T_sh_C1 = T[1] - T_suc_C1_sat
```

```
"2 - LP Discharge"
```

```

T[2] = lookup(Text_Data$,1,'T2_Discharge_LP')
P[2] = lookup(Text_Data$,1,'P2_Discharge_LP')
h[2] = enthalpy(R$,P=p[2],T=T[2])
s[2] = entropy(R$,P=p[2],T=T[2])
m[2] = m[1]

```

```

h_2s = enthalpy(R$,P=p[2],s=s[1])

```

```

eta_iso_C1 = m_dot_low*(h_2s - h[1])/W_dot_C1

```

```

Pr_C1 = P[2]/P[1]

```

```

"3 - HP Suction"

```

```

T[3] = lookup(Text_Data$,1,'T3_Suction_HP')
P[3] = lookup(Text_Data$,1,'P3_Suction_HP')
h[3] = enthalpy(R$,P=p[3],T=T[3])
s[3] = entropy(R$,P=p[3],T=T[3])
m[3] = m_dot_motive

```

```

T_suc_C2_sat = temperature(R$,P=p[3],x=1)

```

```

T_sh_C2 = T[3] - T_suc_C2_sat

```

```

"Assess adiabatic mixing @ C2 suction E-bal"

```

```

m_dot_MT_vap*h[14] + m_dot_low*h[2] = m_dot_motive*h_3_test
del_h_3 = (h_3_test - h[3])
delta_Q_h_3 = m_dot_motive*del_h_3

```

```

"4 - IC In"

```

```

T[4] = lookup(Text_Data$,1,'T4_IC_in')
P[4] = lookup(Text_Data$,1,'P4_IC_in')
h[4] = enthalpy(R$,P=p[4],T=T[4])
s[4] = entropy(R$,P=p[4],T=T[4])
m[4] = m[3]

```

```

h_4s = enthalpy(R$,P=p[4],s=s[3])

```

```

"5 - IC Out"

```

```

T[5] = lookup(Text_Data$,1,'T5_IC_out')
P[5] = lookup(Text_Data$,1,'P5_IC_out')
h[5] = enthalpy(R$,P=p[5],T=T[5])
s[5] = entropy(R$,P=p[5],h=h[5])
m[5] = m[4]

```

```

"6 - GC In"

```

```

T[6] = lookup(Text_Data$,1,'T6_GC_in')
P[6] = lookup(Text_Data$,1,'P6_GC_in')
h[6] = enthalpy(R$,P=p[6],T=T[6])
s[6] = entropy(R$,P=p[6],h=h[6])
m[6] = m[5]

```

```

h_6s = enthalpy(R$,P=p[6],s=s[5])

```

```

eta_iso_C2 = m_dot_motive*(h_6s - h[5] + h_4s - h[3])/W_dot_C2

```

```

Pr_C2 = P[6]/P[3]

```

```

"7 - GC_out, Ejector Motive"

```



```

T[7] = lookup(Text_Data$,1,'T7_GC_out')
P[7] = lookup(Text_Data$,1,'P7_GC_out')
h[7] = enthalpy(R$,P=p[7],T=T[7])
s[7] = entropy(R$,P=p[7],T=T[7])
m[7] = m[6]

"8 - MT FT, Ejector Out"
T[8] = temperature(R$,P=p[8],h=h[8])
P[8] = lookup(Text_Data$,1,'P8_Ejector_out')
h[8] = enthalpy(R$,P=p[8],x=x_8)
s[8] = entropy(R$,P=p[8],h=h[8])
m[8] = m_dot_motive + m_dot_suction

x_8 = m_dot_MT_vap/((m_dot_MT_vap + m_dot_low)*(1 + w))

"9 - MTE In"
T[9] = T_MT_evap_in_TC
P[9] = P_MT_evap_in_TC
h[9] = h[15] "MTFT liq outlet"
s[9] = entropy(R$,P=p[9],h=h[9])
m[9] = m_dot_suction

T_MT_evap_in_TC = lookup(Text_Data$,1,'T8_MT_Evap_in')
P_MT_evap_in_TC = pressure(R$,T=T_MT_evap_in_TC,x=0)

"10 - MTE Out"
T[10] = lookup(Text_Data$,1,'T9_MT_Evap_out')
P[10] = lookup(Text_Data$,1,'P11_MT_Evap_out')
h[10] = enthalpy(R$,P=p[10],T=T[10])

```

```

s[10] = entropy(R$,P=p[10],T=T[10])
m[10] = m[9]

T_MT = temperature(R$,P=p[9],x=1)

T_sh_MTE = T[10] - T_MT

"11 - LT FT"
T[11] = temperature(R$,P=p[11],h=h[11])
P[11] = lookup(Text_Data$,1,'P15_LT_FT_in')
h[11] = h[9]
s[11] = entropy(R$,P=p[11],h=h[11])
m[11] = m_dot_low

"12 - LTE In - Isenthalpic expansion from MTE in"
T[12] = T_LT_evap_in_TC
P[12] = P_LT_evap_in_TC
h[12] = h[9]
s[12] = entropy(R$,P=p[12],h=h[12])
m[12] = m[11]

T_LT_evap_in_TC = lookup(Text_Data$,1,'T19_LT_Evap_in')
P_LT_evap_in_TC = pressure(R$,T=T_LT_evap_in_TC,x=0)

"13 - LTE Out"
T[13] = lookup(Text_Data$,1,'T11_LT_Evap_out')
P[13] = lookup(Text_Data$,1,'P14_LT_Evap_out')
h[13] = enthalpy(R$,P=p[13],T=T[13])
s[13] = entropy(R$,P=p[13],T=T[13])

```

```
m[13] = m[12]
```

```
T_LT = temperature(R$,P=p[12],x=1)
```

```
T_sh_LTE = T[13] - T_LT
```

```
"14 - MT_FT_vap"
```

```
"Assuming x = 1"
```

```
T[14] = temperature(R$,P=p[14],x=1)
```

```
P[14] = lookup(Text_Data$,1,'P8_Ejector_out')
```

```
h[14] = enthalpy(R$,P=p[14],x=1)
```

```
s[14] = entropy(R$,P=p[14],x=1)
```

```
m[14] = m[3]
```

```
"15 - MT_FT_liq"
```

```
"Assuming X = 0"
```

```
T[15] = temperature(R$,P=p[15],x=0)
```

```
p[15] = p[14]
```

```
h[15] = enthalpy(R$,P=p[15],x=0)
```

```
s[15] = entropy(R$,P=p[15],x=0)
```

```
m[15] = m_dot_suction + m_dot_low
```

```
"16 - Suction Nozzle"
```

```
T[16] = lookup(Text_Data$,1,'T10_Suction_Nozzle_in')
```

```
p[16] = lookup(Text_Data$,1,'P12_Suction_Nozzle_in')
```

```
h[16] = enthalpy(R$,P=p[16],T=T[16])
```

```
s[16] = entropy(R$,P=p[16],h=h[16])
```

```
m[16] = m_dot_suction
```

```

T_suc_noz_sat = temperature(R$,P=p[16],x=1)
T_sh_suc_noz = T[16] - T_suc_noz_sat

"!System Calculations"
w = m_dot_suction/m_dot_motive
x_8_bal = m_dot_MT_vap/m_dot_MT

m_dot_MT_liq = m_dot_low + m_dot_suction
m_dot_MT = m_dot_MT_liq + m_dot_MT_vap
m_dot_motive = m_dot_MT_vap + m_dot_low

W_dot_C1 = Q_dot_loss_C1 + m_dot_low*(h[2] - h[1])
W_dot_C2 = Q_dot_loss_C2 + m_dot_motive*(h[4] - h[3] + h[6] - h[5])

Q_dot_IC = m_dot_motive*(h[4] - h[5])
Q_dot_GC = m_dot_motive*(h[6] - h[7])

Q_dot_MTE = m_dot_suction*(h[10] - h[9])
Q_dot_MTE = Q_dot_MT_w

Q_dot_LTE = m_dot_low*(h[13] - h[12])
Q_dot_LTE = Q_dot_LT_w

Q_dot_LT_suc = m_dot_low*(h[1] - h[13])
Q_dot_ej_suc = m_dot_suction*(h[16] - h[10])

E_bal = W_dot_C1 + W_dot_C2 + Q_dot_MTE + Q_dot_LTE - Q_dot_IC -
Q_dot_GC - Q_dot_loss_C1 - Q_dot_loss_C2 + Q_dot_LT_suc -

```

$$\Delta Q_{h_3} + \dot{Q}_{ej\_suc}$$

$$\text{Percent\_E\_bal} = 100 * (\text{E\_bal} / (\dot{W}_{dot\_C1} + \dot{W}_{dot\_C2} + \dot{Q}_{dot\_MTE} + \dot{Q}_{dot\_LTE}))$$

$$\text{COP\_est} = (\dot{Q}_{dot\_MTE} + \dot{Q}_{dot\_LTE}) / (\dot{W}_{dot\_C1} + \dot{W}_{dot\_C2} + \dot{W}_{dot\_fan\_abs} + \dot{W}_{dot\_fan\_rej})$$

$$\Delta \dot{Q}_{dot\_MT} = \dot{Q}_{dot\_MTE} - \dot{Q}_{dot\_MT\_w}$$

$$\text{Percent\_Waterside\_error\_MT} = 100 * (\Delta \dot{Q}_{dot\_MT}) / \dot{Q}_{dot\_MTE}$$

$$\Delta \dot{Q}_{dot\_LT} = \dot{Q}_{dot\_LTE} - \dot{Q}_{dot\_LT\_w}$$

$$\text{Percent\_Waterside\_error\_LT} = 100 * (\Delta \dot{Q}_{dot\_LT}) / \dot{Q}_{dot\_LTE}$$

"Ejector Performance Quantification"

$$\Delta p_{\text{Ejector}} = p[8] - p[10]$$

$$h_{\text{pdo\_ssi}} = \text{enthalpy}(R, P=p[8], s=s[16]) \text{ "Suction nozzle inlet"}$$

$$h_{\text{si}} = h[16]$$

$$h_{\text{pdo\_smi}} = \text{enthalpy}(R, P=p[8], s=s[7]) \text{ "Motive nozzle inlet"}$$

$$h_{\text{mi}} = h[7]$$

$$\eta_{\text{eject}} = w * ((h_{\text{pdo\_ssi}} - h_{\text{si}}) / (h_{\text{mi}} - h_{\text{pdo\_smi}}))$$

```
"!Creating separate array for graphing"
```

```
Duplicate i=1,8
```

```
p_g[i] = p[i]
```

```
h_g[i] = h[i]
```

```
End
```

```
p_g[9] = p[14]
```

```
h_g[9] = h[14]
```

```
p_g[10] = p[3]
```

```
h_g[10] = h[14]
```

```
p_g[11] = p[3]
```

```
h_g[11] = h[3]
```

```
p_g[12] = p[3]
```

```
h_g[12] = h[14]
```

```
p_g[13] = p[14]
```

```
h_g[13] = h[14]
```

```
p_g[14] = p[8]
```

```
h_g[14] = h[8]
```

```
p_g[15] = p[10]
```

```
h_g[15] = h[10]
```

p\_g[16] = p[16]

h\_g[16] = h[16]

p\_g[17] = p[9]

h\_g[17] = h[9]

p\_g[18] = p[15]

h\_g[18] = h[15]

p\_g[19] = p[8]

h\_g[19] = h[8]

p\_g[20] = p[15]

h\_g[20] = h[15]

p\_g[21] = p[12]

h\_g[21] = h[12]

p\_g[22] = p[13]

h\_g[22] = h[13]

p\_g[23] = p[1]

h\_g[23] = h[1]

////////////////////////////////////

"!Medium Temp Water-Glycol Solution"

T\_MT\_wi = lookup(Text\_Data\$,1,'T12\_MT\_w\_in') "MT evap water inlet"

```
T_MT_wo = lookup(Text_Data$,1,'T13_MT_w_out') "MT evap water outlet"
T_MT_w_avg = (T_MT_wi + T_MT_wo)/2
```

```
V_dot_MT_w = lookup(Text_Data$,1,'V_dot_w_MT')*convert('liters/min',
'm^3/sec')
```

```
C_EG_MT = 34.4 [%]
```

```
rho_MT_EG = density(EG,T=T_MT_w_avg,C=C_EG_MT)
```

```
cp_MT_EG = cp(EG,T=T_MT_w_avg,C=C_EG_MT)
```

```
m_dot_MT_EG = V_dot_MT_w*rho_MT_EG
```

```
Q_dot_MT_EG = m_dot_MT_EG*cp_MT_EG*(T_MT_wi - T_MT_wo)
```

```
Q_dot_MT_w = Q_dot_MT_EG
```

```
////////////////////////////////////
```

```
"!Low Temp Water-Glycol Solution"
```

```
T_LT_wi = lookup(Text_Data$,1,'T14_LT_w_in') "LT evap water inlet"
```

```
T_LT_wo = lookup(Text_Data$,1,'T15_LT_w_out') "LT evap water outlet"
```

```
T_LT_w_avg = (T_LT_wi + T_LT_wo)/2
```

```
V_dot_LT_w = lookup(Text_Data$,1,'V_dot_w_LT')*convert('liters/min',
'm^3/sec')
```

```
C_EG_LT = 50
```

```
rho_LT_EG = density(EG,T=T_LT_w_avg,C=C_EG_LT)
```

```
cp_LT_EG = cp(EG,T=T_LT_w_avg,C=C_EG_LT)
```

```
m_dot_LT_EG = V_dot_LT_w*rho_LT_EG
```



$$Q_{\text{dot\_LT\_w}} = m_{\text{dot\_LT\_EG}} * c_{p\_LT\_EG} * (T_{\text{LT\_wi}} - T_{\text{LT\_wo}})$$

## C.4 Ejector and Pump Cycle Analysis

This post-processing code is used to analyze experimental data taken from the ejector and pump cycle. A P-h diagram for the ejector and pump cycle is provided in Figure 5.4.

```

////////////////////////////////////
"CO2 System Data Analysis Script
Both Comps, Both Evaps, Ejector, Pump"
////////////////////////////////////

"!Inputs"
R$ = 'R744'
Text_Data$ = 'ss_10e180_10_lookup'

"!System Parameters Call"
LL_FT = lookup(Text_Data$,1,'MTFT_R')
T_GC3_ai = lookup(Text_Data$,1,'T21_GC3_ai')
T_amb = T_GC3_ai

m_dot_motive = lookup(Text_Data$,1,'m_dot_motive')*convert('g/s',
'kg/s')

W_dot_C1 = lookup(Text_Data$,1,'W_Dot_LP_comp')*convert('W','kW')

```

```

W_dot_C2 = lookup(Text_Data$,1,'W_Dot_HP_comp')*convert('W','kW')
W_dot_Pump = lookup(Text_Data$,1,'W_dot_Pump')*convert('W','kW')

W_dot_fan_rej = lookup(Text_Data$,1,'W_dot_Fans')*convert('W','kW')
W_dot_fan_abs = 0.5 [kW]

"!Cycle Development"
"1 - LP Suction"
T[1] = lookup(Text_Data$,1,'T1_Suction_LP')
P[1] = lookup(Text_Data$,1,'P1_Suction_LP')
h[1] = enthalpy(R$,P=p[1],T=T[1])
s[1] = entropy(R$,P=p[1],T=T[1])
m[1] = m_dot_low

T_suc_C1_sat = temperature(R$,P=p[1],x=1)

T_sh_C1 = T[1] - T_suc_C1_sat

"2 - LP Discharge"
T[2] = lookup(Text_Data$,1,'T2_Discharge_LP')
P[2] = lookup(Text_Data$,1,'P2_Discharge_LP')
h[2] = enthalpy(R$,P=p[2],T=T[2])
s[2] = entropy(R$,P=p[2],T=T[2])
m[2] = m[1]

h_2s = enthalpy(R$,P=p[2],s=s[1])

eta_iso_C1 = m_dot_low*(h_2s - h[1])/W_dot_C1

```

```
Pr_C1 = P[2]/P[1]
```

```
"3 - HP Suction"
```

```
T[3] = lookup(Text_Data$,1,'T3_Suction_HP')
```

```
P[3] = lookup(Text_Data$,1,'P3_Suction_HP')
```

```
h[3] = enthalpy(R$,P=p[3],T=T[3])
```

```
s[3] = entropy(R$,P=p[3],T=T[3])
```

```
m[3] = m_dot_motive
```

```
T_suc_C2_sat = temperature(R$,P=p[3],x=1)
```

```
T_sh_C2 = T[3] - T_suc_C2_sat
```

```
"Assess adiabatic mixing @ C2 suction E-bal"
```

```
m_dot_MT_vap*h[14] + m_dot_low*h[2] = m_dot_motive*h_3_test
```

```
del_h_3 = (h_3_test - h[3])
```

```
delta_Q_h_3 = m_dot_motive*del_h_3
```

```
"4 - IC In"
```

```
T[4] = lookup(Text_Data$,1,'T4_IC_in')
```

```
P[4] = lookup(Text_Data$,1,'P4_IC_in')
```

```
h[4] = enthalpy(R$,P=p[4],T=T[4])
```

```
s[4] = entropy(R$,P=p[4],T=T[4])
```

```
m[4] = m[3]
```

```
h_4s = enthalpy(R$,P=p[4],s=s[3])
```

```
"5 - IC Out"
```

```
T[5] = lookup(Text_Data$,1,'T5_IC_out')
```

```
P[5] = lookup(Text_Data$,1,'P5_IC_out')
```

```

h[5] = enthalpy(R$,P=p[5],T=T[5])
s[5] = entropy(R$,P=p[5],h=h[5])
m[5] = m[4]

```

"6 - GC In"

```

T[6] = lookup(Text_Data$,1,'T6_GC_in')
P[6] = lookup(Text_Data$,1,'P6_GC_in')
h[6] = enthalpy(R$,P=p[6],T=T[6])
s[6] = entropy(R$,P=p[6],h=h[6])
m[6] = m[5]

```

```

h_6s = enthalpy(R$,P=p[6],s=s[5])

```

```

eta_iso_C2 = m_dot_motive*(h_6s - h[5] + h_4s - h[3])/W_dot_C2

```

```

Pr_C2 = P[6]/P[3]

```

"7 - GC\_out, Ejector Motive"

```

T[7] = lookup(Text_Data$,1,'T7_GC_out')
P[7] = lookup(Text_Data$,1,'P7_GC_out')
h[7] = enthalpy(R$,P=p[7],T=T[7])
s[7] = entropy(R$,P=p[7],T=T[7])
m[7] = m[6]

```

"8 - Pump Outlet, Ejector Motive"

```

T[8] = lookup(Text_Data$,1,'T17_Pump_out')
P[8] = lookup(Text_Data$,1,'P16_Pump_out')
h[8] = enthalpy(R$,P=p[8],T=T[8])
s[8] = entropy(R$,P=p[8],h=h[8])

```

```

h_8s = enthalpy(R$,P=p[8],s=s[7])

"9 - MT FT, Ejector Out"
T[9] = temperature(R$,P=p[9],h=h[9])
P[9] = lookup(Text_Data$,1,'P8_Ejector_out')
h[9] = enthalpy(R$,P=p[9],x=x_9)
s[9] = entropy(R$,P=p[9],h=h[9])
m[9] = m_dot_motive + m_dot_suction

x_9 = m_dot_MT_vap/((m_dot_MT_vap + m_dot_low)*(1 + w))

"10 - MTE In"
T[10] = T_MT_evap_in_TC
P[10] = P_MT_evap_in_TC
h[10] = h[16] "MTFT liq outlet"
s[10] = entropy(R$,P=p[10],h=h[10])
m[10] = m_dot_suction

T_MT_evap_in_TC = lookup(Text_Data$,1,'T8_MT_Evap_in')
P_MT_evap_in_TC = pressure(R$,T=T_MT_evap_in_TC,x=0)

T_MT = T_MT_evap_in_TC

"11 - MTE Out"
T[11] = lookup(Text_Data$,1,'T9_MT_Evap_out')
P[11] = lookup(Text_Data$,1,'P11_MT_Evap_out')
h[11] = enthalpy(R$,P=p[11],T=T[11])
s[11] = entropy(R$,P=p[11],T=T[11])

```

```
m[11] = m[10]
```

```
T_11_sat = temperature(R$,P=p[11],x=1)
```

```
T_sh_MTE = T[11] - T_11_sat
```

```
"12 - LT FT"
```

```
T[12] = temperature(R$,P=p[12],h=h[12])
```

```
P[12] = lookup(Text_Data$,1,'P15_LT_FT_in')
```

```
h[12] = h[10]
```

```
s[12] = entropy(R$,P=p[12],h=h[12])
```

```
m[12] = m_dot_low
```

```
"13 - LTE In - Isenthalpic expansion from MTE in"
```

```
T[13] = T_LT_evap_in_TC
```

```
P[13] = P_LT_evap_in_TC
```

```
h[13] = h[10]
```

```
s[13] = entropy(R$,P=p[13],h=h[13])
```

```
m[13] = m[12]
```

```
T_LT_evap_in_TC = lookup(Text_Data$,1,'T19_LT_Evap_in')
```

```
P_LT_evap_in_TC = pressure(R$,T=T_LT_evap_in_TC,x=0)
```

```
T_LT = T_LT_evap_in_TC
```

```
"14 - LTE Out"
```

```
T[14] = lookup(Text_Data$,1,'T11_LT_Evap_out')
```

```
P[14] = lookup(Text_Data$,1,'P14_LT_Evap_out')
```

```
h[14] = enthalpy(R$,P=p[14],T=T[14])
```

```

s[14] = entropy(R$,P=p[14],T=T[14])
m[14] = m[13]

T_14_sat = temperature(R$,P=p[14],x=1)

T_sh_LTE = T[14] - T_14_sat

"15 - MT_FT_vap"
"Assuming x = 1"
T[15] = temperature(R$,P=p[15],x=1)
P[15] = lookup(Text_Data$,1,'P8_Ejector_out')
h[15] = enthalpy(R$,P=p[15],x=1)
s[15] = entropy(R$,P=p[15],x=1)
m[15] = m_dot_MT_vap

"16 - MT_FT_liq"
"Assuming X = 0"
T[16] = temperature(R$,P=p[16],x=0)
p[16] = p[15]
h[16] = enthalpy(R$,P=p[16],x=0)
s[16] = entropy(R$,P=p[16],x=0)
m[16] = m_dot_suction + m_dot_low

"17 - Suction Nozzle"
T[17] = lookup(Text_Data$,1,'T10_Suction_Nozzle_in')
p[17] = lookup(Text_Data$,1,'P12_Suction_Nozzle_in')
h[17] = enthalpy(R$,P=p[17],T=T[17])
s[17] = entropy(R$,P=p[17],h=h[17])
m[17] = m_dot_suction

```

```
T_suc_noz_sat = temperature(R$,P=p[17],x=1)
```

```
T_sh_suc_noz = T[17] - T_suc_noz_sat
```

```
"!System Calculations"
```

```
w = m_dot_suction/m_dot_motive
```

```
x_9_bal = m_dot_MT_vap/m_dot_MT
```

```
m_dot_MT_liq = m_dot_low + m_dot_suction
```

```
m_dot_MT = m_dot_MT_liq + m_dot_MT_vap
```

```
m_dot_motive = m_dot_MT_vap + m_dot_low
```

```
W_dot_C1 = Q_dot_loss_C1 + m_dot_low*(h[2] - h[1])
```

```
W_dot_C2 = Q_dot_loss_C2 + m_dot_motive*(h[4] - h[3] + h[6] - h[5])
```

```
W_dot_pump = Q_dot_loss_pump + m_dot_motive*(h[8] - h[7])
```

```
Q_dot_IC = m_dot_motive*(h[4] - h[5])
```

```
Q_dot_GC = m_dot_motive*(h[6] - h[7])
```

```
Q_dot_MTE = m_dot_suction*(h[11] - h[10])
```

```
Q_dot_MTE = Q_dot_MT_w
```

```
Q_dot_LTE = m_dot_low*(h[14] - h[13])
```

```
Q_dot_LTE = Q_dot_LT_w
```

```
Q_dot_LT_suc = m_dot_low*(h[1] - h[14])
```

```
Q_dot_ej_suc = m_dot_suction*(h[17] - h[11])
```



$$E_{bal} = W_{dot\_C1} + W_{dot\_C2} + Q_{dot\_MTE} + Q_{dot\_LTE} + W_{dot\_pump} - \\ Q_{dot\_IC} - Q_{dot\_GC} - Q_{dot\_loss\_C1} - Q_{dot\_loss\_C2} - Q_{dot\_loss\_pump} + \\ Q_{dot\_LT\_suc} - \Delta Q_{h\_3} + Q_{dot\_ej\_suc}$$

$$Percent\_E_{bal} = 100 * (E_{bal} / (W_{dot\_C1} + W_{dot\_C2} + W_{dot\_pump} + Q_{dot\_MTE} \\ + Q_{dot\_LTE}))$$

$$COP_{est} = (Q_{dot\_MTE} + Q_{dot\_LTE}) / (W_{dot\_C1} + W_{dot\_C2} + W_{dot\_pump} \\ + W_{dot\_fan\_abs} + W_{dot\_fan\_rej})$$

$$\Delta Q_{dot\_MT} = Q_{dot\_MTE} - Q_{dot\_MT\_w}$$

$$Percent\_Waterside\_error\_MT = 100 * (\Delta Q_{dot\_MT}) / Q_{dot\_MTE}$$

$$\Delta Q_{dot\_LT} = Q_{dot\_LTE} - Q_{dot\_LT\_w}$$

$$Percent\_Waterside\_error\_LT = 100 * (\Delta Q_{dot\_LT}) / Q_{dot\_LTE}$$

"Ejector Performance Quantification"

$$\Delta p_{Ejector} = p[9] - p[11]$$

$$h_{pdo\_ssi} = \text{enthalpy}(R, P=p[9], s=s[17]) \text{ "suction nozzle inlet"}$$

$$h_{si} = h[17]$$

$$h_{pdo\_smi} = \text{enthalpy}(R, P=p[9], s=s[8]) \text{ "motive nozzle inlet"}$$

$$h_{mi} = h[8]$$

```
eta_eject = w*((h_pdo_ssi - h_si)/(h_mi - h_pdo_smi))
```

```
"PD Machinery Quantification"
```

```
eta_pump = (m_dot_motive*(h_8s - h[7]))/W_dot_pump
```

```
p_r_pump = p[8]/p[7]
```

```
delta_p_pump = p[8] - p[7]
```

```
"!Creating separate array for graphing"
```

```
Duplicate i=1,9
```

```
p_g[i] = p[i]
```

```
h_g[i] = h[i]
```

```
End
```

```
p_g[10] = p[15]
```

```
h_g[10] = h[15]
```

```
p_g[11] = p[3]
```

```
h_g[11] = h[15]
```

```
p_g[12] = p[3]
```

```
h_g[12] = h[3]
```

```
p_g[13] = p[3]
```

$h\_g[13] = h[15]$

$p\_g[14] = p[15]$

$h\_g[14] = h[15]$

$p\_g[15] = p[9]$

$h\_g[15] = h[9]$

$p\_g[16] = p[11]$

$h\_g[16] = h[11]$

$p\_g[17] = p[17]$

$h\_g[17] = h[17]$

$p\_g[18] = p[10]$

$h\_g[18] = h[10]$

$p\_g[19] = p[16]$

$h\_g[19] = h[16]$

$p\_g[20] = p[9]$

$h\_g[20] = h[9]$

$p\_g[21] = p[16]$

$h\_g[21] = h[16]$

$p\_g[22] = p[13]$

$h\_g[22] = h[13]$

```
p_g[23] = p[14]
```

```
h_g[23] = h[14]
```

```
p_g[24] = p[1]
```

```
h_g[24] = h[1]
```

```
////////////////////////////////////
```

```
"!Medium Temp Water-Glycol Solution"
```

```
T_MT_wi = lookup(Text_Data$,1,'T12_MT_w_in') "MT evap water inlet"
```

```
T_MT_wo = lookup(Text_Data$,1,'T13_MT_w_out') "MT evap water outlet"
```

```
T_MT_w_avg = (T_MT_wi + T_MT_wo)/2
```

```
V_dot_MT_w = lookup(Text_Data$,1,'V_dot_w_MT')*convert('liters/min',  
'm^3/sec')
```

```
C_EG_MT = 34.4 [%]
```

```
rho_MT_EG = density(EG,T=T_MT_w_avg,C=C_EG_MT)
```

```
cp_MT_EG = cp(EG,T=T_MT_w_avg,C=C_EG_MT)
```

```
m_dot_MT_EG = V_dot_MT_w*rho_MT_EG
```

```
Q_dot_MT_EG = m_dot_MT_EG*cp_MT_EG*(T_MT_wi - T_MT_wo)
```

```
Q_dot_MT_w = Q_dot_MT_EG
```

```
////////////////////////////////////
```

```
"!Low Temp Water-Glycol Solution"
```

```
T_LT_wi = lookup(Text_Data$,1,'T14_LT_w_in') "LT evap water inlet"
T_LT_wo = lookup(Text_Data$,1,'T15_LT_w_out') "LT evap water outlet"
T_LT_w_avg = (T_LT_wi + T_LT_wo)/2

V_dot_LT_w = lookup(Text_Data$,1,'V_dot_w_LT')*convert('liters/min',
'm^3/sec')

C_EG_LT = 50

rho_LT_EG = density(EG,T=T_LT_w_avg,C=C_EG_LT)
cp_LT_EG = cp(EG,T=T_LT_w_avg,C=C_EG_LT)
m_dot_LT_EG = V_dot_LT_w*rho_LT_EG

Q_dot_LT_w = m_dot_LT_EG*cp_LT_EG*(T_LT_wi - T_LT_wo)
```

## REFERENCES

## REFERENCES

- [1] BP, “BP Statistical Review of World Energy,” pp. 1–56, 2018.
- [2] USEIA, “U.S. Energy Information Agency Monthly Energy Review - April 2018,” 2018. [Online]. Available: <http://large.stanford.edu/courses/2018/ph241/green1/docs/doe-eia-0035-2018-4.pdf>
- [3] RIVM, “Contribution of HFCs to the Greenhouse Effect,” *The Netherlands National Institute for Public Health and the Environment, Ministry of Health, Welfare and Sport*, 2018.
- [4] C. Harvey, “CO<sub>2</sub> Emissions Reached an All-Time High in 2018,” *Scientific American*, 2018. [Online]. Available: <https://www.scientificamerican.com/article/co2-emissions-reached-an-all-time-high-in-2018/>
- [5] UN, “The Kyoto Protocol to the United Nations Framework Convention on Climate Change,” 1998.
- [6] S. A. Tassou, Y. Ge, A. Hadawey, and D. Marriott, “Energy consumption and conservation in food retailing,” *Applied Thermal Engineering*, vol. 31, no. 2-3, pp. 147–156, 2011.
- [7] E. Union, *Fluorinated greenhouse gases 2018*, 2018, no. 21.
- [8] E. A. Heath, “Amendment to the Montreal protocol on substances that deplete the ozone layer (Kigali amendment),” *International Legal Materials*, vol. 56, no. 1, pp. 193–205, 2017.
- [9] N. Abas, A. R. Kalair, N. Khan, A. Haider, Z. Saleem, and M. S. Saleem, “Natural and synthetic refrigerants, global warming: A review,” *Renewable and Sustainable Energy Reviews*, vol. 90, pp. 557–569, 2018.
- [10] Y. Heredia-Aricapa, J. M. Belman-Flores, A. Mota-Babiloni, J. Serrano-Arellano, and J. J. Garcia-Pabón, “Overview of low GWP mixtures for the replacement of HFC refrigerants: R134a, R404A and R410A,” *International Journal of Refrigeration*, vol. 111, pp. 113–123, 2020.
- [11] M. H. Kim, J. Pettersen, and C. W. Bullard, “Fundamental process and system design issues in CO<sub>2</sub> vapor compression systems,” *Progress in Energy and Combustion Science*, vol. 30, no. 2, pp. 119–174, 2004.
- [12] T. Ma, W.-x. Chu, X.-y. Xu, Y.-t. Chen, and Q.-w. Wang, “An experimental study on heat transfer between supercritical carbon dioxide and water near the pseudo-critical temperature in a double pipe heat exchanger,” *International Journal of Heat and Mass Transfer*, vol. 93, pp. 379–387, 2016.

- [13] A. M. Bahman, D. Ziviani, and E. A. Groll, "A generalized moving-boundary algorithm to predict the heat transfer rate of transcritical CO<sub>2</sub> gas coolers," *International Journal of Refrigeration*, 2020.
- [14] I. H. Bell, J. Wronski, S. Quoilin, and V. Lemort, "Pure and pseudo-pure fluid thermophysical property evaluation and the open-source thermophysical property library CoolProp," *Industrial & Engineering Chemistry Research*, vol. 53, no. 6, pp. 2498–2508, 2014.
- [15] J. S. Brown, S. F. Yana-Motta, and P. A. Domanski, "Comparative analysis of an automotive air conditioning systems operating with CO<sub>2</sub> and R134a," *International Journal of Refrigeration*, vol. 25, no. 1, pp. 19–32, 2002. [Online]. Available: <http://www.sciencedirect.com/science/article/pii/S0140700701000111>
- [16] J. Sarkar, "Transcritical CO<sub>2</sub> Refrigeration Systems: Comparison With Conventional Solutions and Applications," *International Journal of Air-Conditioning and Refrigeration*, vol. 20, no. 04, p. 1250017, 2012.
- [17] B. Yu, J. Yang, D. Wang, J. Shi, and J. Chen, "An updated review of recent advances on modified technologies in transcritical CO<sub>2</sub> refrigeration cycle," *Energy*, p. 116147, 2019.
- [18] J. S. Baek, E. A. Groll, and P. B. Lawless, "Theoretical performance of transcritical carbon dioxide cycle with two-stage compression and intercooling," *Proceedings of the Institution of Mechanical Engineers, Part E: Journal of Process Mechanical Engineering*, vol. 219, no. 2, pp. 187–195, 2005.
- [19] L. Cecchinato, M. Chiarello, M. Corradi, E. Fornasieri, S. Minetto, P. Stringari, and C. Zilio, "Thermodynamic analysis of different two-stage transcritical carbon dioxide cycles," *International Journal of Refrigeration*, vol. 32, no. 5, pp. 1058–1067, 2009. [Online]. Available: <http://dx.doi.org/10.1016/j.ijrefrig.2008.10.001>
- [20] N. Agrawal, S. Bhattacharyya, and J. Sarkar, "Optimization of two-stage transcritical carbon dioxide heat pump cycles," *International Journal of Thermal Sciences*, vol. 46, no. 2, pp. 180–187, feb 2007. [Online]. Available: <https://www.sciencedirect.com/science/article/pii/S1290072906000718>
- [21] S. Elbel and P. Hrnjak, "Flash gas bypass for improving the performance of transcritical R744 systems that use microchannel evaporators," *International Journal of Refrigeration*, vol. 27, pp. 724–735, 2004.
- [22] R. Cabello, D. Sánchez, J. Patiño, R. Llopis, and E. Torrella, "Experimental analysis of energy performance of modified single-stage CO<sub>2</sub> transcritical vapour compression cycles based on vapour injection in the suction line," *Applied Thermal Engineering*, vol. 47, pp. 86–94, 2012. [Online]. Available: <http://dx.doi.org/10.1016/j.applthermaleng.2012.02.031>
- [23] R. Llopis, L. Nebot-andrés, R. Cabello, D. Sánchez, and J. Catalán-gil, "Experimental evaluation of a CO<sub>2</sub> transcritical refrigeration plant with dedicated mechanical subcooling," *International Journal of Refrigeration*, vol. 69, pp. 361–368, 2016. [Online]. Available: <http://dx.doi.org/10.1016/j.ijrefrig.2016.06.009>



- [24] K. Yazawa, S. Dharkar, O. Kurtulus, and E. A. Groll, "Optimum design for thermoelectric in a sub-cooled trans-critical CO<sub>2</sub> heat pump for data center cooling," in *2015 31st Thermal Measurement, Modeling & Management Symposium (SEMI-THERM)*. IEEE, 2015, pp. 19–24.
- [25] I. H. Bell, E. A. Groll, and J. E. Braun, "Performance of vapor compression systems with compressor oil flooding and regeneration," *International Journal of Refrigeration*, vol. 34, no. 1, pp. 225–233, 2011.
- [26] A. Chesi, G. Ferrara, L. Ferrari, and F. Tarani, "Setup and characterisation of a multi-purpose test rig for R744 refrigerating cycles and equipment," *International Journal of Refrigeration*, vol. 35, no. 7, pp. 1848–1859, 2012. [Online]. Available: <http://dx.doi.org/10.1016/j.ijrefrig.2012.06.005>
- [27] E. A. Groll, J.-h. Kim, and E. A. Groll, "Review Article : Review of Recent Advances toward Transcritical CO<sub>2</sub> Cycle Technology Review of Recent Advances toward Transcritical CO<sub>2</sub> Cycle Technology," *HVAC&R Research*, vol. 13, no. 3, pp. 499–520, 2007.
- [28] R. Llopis, L. Nebot-andrés, D. Sánchez, J. Catalán-gil, and R. Cabello, "Subcooling methods for CO<sub>2</sub> refrigeration cycles : A review," *International Journal of Refrigeration*, vol. 93, pp. 85–107, 2018. [Online]. Available: <https://doi.org/10.1016/j.ijrefrig.2018.06.010>
- [29] A. Bahman, R. Barta, D. Ziviani, and E. Groll, "CO<sub>2</sub> Heat Pump: Fundamentals and Application," X.-R. Zhang, Ed. Wiley, 2019, ch. Expansion.
- [30] D. M. Robinson and E. A. Groll, "Efficiencies of transcritical CO<sub>2</sub> cycles with and without an expansion turbine," *International Journal of Refrigeration*, vol. 21, no. 7, pp. 577–589, nov 1998. [Online]. Available: <https://www.sciencedirect.com/science/article/pii/S0140700798000243>
- [31] J. Baek, E. Groll, and P. Lawless, "Piston-cylinder work producing expansion device in a transcritical carbon dioxide cycle. Part I: experimental investigation," *International Journal of Refrigeration*, vol. 28, no. 2, pp. 141–151, 2005.
- [32] N. Czapla, H. Inamdar, R. Barta, and E. A. Groll, "Theoretical Analysis of the Impact of an Energy Recovery Expansion Device in a CO<sub>2</sub> Refrigeration System," *Proc. of the 23rd International Compressor Engineering Conference at Purdue*, p. Paper 1550, 2016.
- [33] B. Yang, X. Peng, Z. He, B. Guo, and Z. Xing, "Experimental investigation on the internal working process of a CO<sub>2</sub> rotary vane expander," *Applied Thermal Engineering*, vol. 29, no. 11, pp. 2289–2296, 2009. [Online]. Available: <http://www.sciencedirect.com/science/article/pii/S1359431108004602>
- [34] R. Barta, J. Hugenroth, and E. Groll, "Modeling of S-RAM energy recovery compressor integration in a transcritical carbon dioxide cycle for application in multi-temperature refrigerated container systems," in *13th IIR Gustav Lorentzen Conference*, vol. 2018-June, 2018.
- [35] L. Hays and J. Brasz, "A Transcritical CO<sub>2</sub> Turbine-Compressor," *Proc. of the 17th International Compressor Engineering Conference at Purdue*, p. Paper 137, 2004.

- [36] D. Westphalen and J. Dieckmann, "Scroll expander for carbon dioxide air conditioning cycles," *Proc. of the 17th International Compressor Engineering Conference at Purdue*, vol. Paper 690, 2004.
- [37] A. A. Murthy, A. Subiantoro, S. Norris, and M. Fukuta, "A review on expanders and their performance in vapour compression refrigeration systems," *International Journal of Refrigeration*, vol. 106, pp. 427–446, 2019.
- [38] N. Gay, "Refrigerating System," *US Patent 1,836,318*, 1931.
- [39] A. Newton, "Capacity Control for Multiple-Phase Refrigeration Systems," *US Patent 3,670,519*, 1972.
- [40] C. A. Kemper, G. F. Harper, and G. A. Brown, "Multiple-phase ejector refrigeration system," *US Patent 3,277,660*, 1966.
- [41] C. Lucas and J. Koehler, "Experimental investigation of the COP improvement of a refrigeration cycle by use of an ejector," *International Journal of Refrigeration*, vol. 35, no. 6, pp. 1595–1603, 2012.
- [42] S. Elbel and P. Hrnjak, "Experimental validation of a prototype ejector designed to reduce throttling losses encountered in transcritical R744 system operation," *International Journal of Refrigeration*, vol. 31, no. 3, pp. 411–422, may 2008.
- [43] J. Köhler, C. Richter, W. Tegethoff, and C. Tischendorf, "Experimental and theoretical study of a CO<sub>2</sub> ejector refrigeration cycle," in *Vortrag, VDA Winter Meeting, Saalfelden*, 2007.
- [44] F. Liu, Y. Li, and E. A. Groll, "Performance enhancement of CO<sub>2</sub> air conditioner with a controllable ejector," *International Journal of Refrigeration*, vol. 35, no. 6, pp. 1604–1616, sep 2012.
- [45] A. Hafner, S. Poppi, P. Neksa, S. Minetto, and T. M. Eikevik, "Development of commercial refrigeration systems with heat recovery for supermarket building," in *Proc. of the 10th IIR Gustav Lorentzen Conference on Natural Refrigerants*, 2012, pp. 25–27.
- [46] A. Hafner, S. Försterling, and K. Banasiak, "Multi-ejector concept for R-744 supermarket refrigeration," *International Journal of Refrigeration*, vol. 43, pp. 1–13, 2014.
- [47] M. Haida, K. Banasiak, J. Smolka, A. Hafner, and T. M. Eikevik, "Experimental analysis of the R744 vapour compression rack equipped with the multi-ejector expansion work recovery module," *International Journal of Refrigeration*, vol. 64, pp. 93–107, 2016.
- [48] Danfoss, "Danfoss Multi Ejector Solution," *Danfoss.com*, 2019. [Online]. Available: <https://www.danfoss.com/en-us/products/valves/dcs/electric-expansion-valves/multi-ejector-solution/>
- [49] Carel, "EmJ - Carel Electronic Modulating Ejector," *Carel.com*, 2019.
- [50] S. Elbel and N. Lawrence, "Review of recent developments in advanced ejector technology," *International Journal of Refrigeration*, vol. 62, pp. 1–18, 2016.

- [51] G. Besagni, R. Mereu, and F. Inzoli, "Ejector refrigeration: a comprehensive review," *Renewable and Sustainable Energy Reviews*, vol. 53, pp. 373–407, 2016.
- [52] D. Li and E. A. Groll, "Transcritical CO<sub>2</sub> refrigeration cycle with ejector-expansion device," *International Journal of Refrigeration*, vol. 28, no. 5, pp. 766–773, 2005.
- [53] F. Liu and E. A. Groll, "Study of ejector efficiencies in refrigeration cycles," *International Journal of Refrigeration*, vol. 52, pp. 360–370, 2013.
- [54] C. Lucas, J. Koehler, A. Schroeder, and C. Tischendorf, "Experimentally validated CO<sub>2</sub> ejector operation characteristic used in a numerical investigation of ejector cycle," *International Journal of Refrigeration*, vol. 36, no. 3, pp. 881–891, 2013.
- [55] F. Liu, "Review on ejector efficiencies in various ejector systems," *Proc. of the International Refrigeration and Air Conditioning Conference*, p. Paper 1533, 2014.
- [56] M. Palacz, M. Haida, J. Smolka, A. J. Nowak, K. Banasiak, and A. Hafner, "HEM and HRM accuracy comparison for the simulation of CO<sub>2</sub> expansion in two-phase ejectors for supermarket refrigeration systems," *Applied Thermal Engineering*, vol. 115, 2017.
- [57] M. Palacz, J. Smolka, W. Kus, A. Fic, Z. Bulinski, A. J. Nowak, K. Banasiak, and A. Hafner, "CFD-based shape optimisation of a CO<sub>2</sub> two-phase ejector mixing section," *Applied Thermal Engineering*, vol. 95, pp. 62–69, 2016.
- [58] Y. He, J. Deng, Y. Li, and L. Ma, "A numerical contrast on the adjustable and fixed transcritical CO<sub>2</sub> ejector using exergy flux distribution analysis," *Energy Conversion and Management*, vol. 196, pp. 729–738, 2019.
- [59] M. Haida, J. Smolka, A. Hafner, M. Mastrowski, K. B. Palacz Michał and Madsen, A. J. Nowak, and K. Banasiak, "Numerical investigation of heat transfer in a CO<sub>2</sub> two-phase ejector," *Energy*, vol. 163, pp. 682–698, 2018.
- [60] M. Mastrowski, J. Smolka, A. Hafner, M. Haida, and M. Palacz, "Experimental study of the heat transfer problem in expansion devices in CO<sub>2</sub> refrigeration systems," *Energy*, vol. 173, pp. 586–597, 2019. [Online]. Available: <https://doi.org/10.1016/j.energy.2019.02.097>
- [61] M. Haida, R. Fingas, W. Sz wajnoch, J. Bodys, M. Malacz, J. Smolka, and A. Nowak, "The R744 vapour compression test rig designed for visualisation of two-phase flow inside ejectors," *Proc. of 25th IIR International Congress of Refrigeration*, p. Paper 1347, 2019.
- [62] C. Arpagaus, F. Bless, J. Schiffmann, and S. S. Bertsch, "Multi-temperature heat pumps: A literature review," *International Journal of Refrigeration*, vol. 69, no. 2012, pp. 437–465, 2016.
- [63] P. Gullo, A. Hafner, and K. Banasiak, "Transcritical R744 refrigeration systems for supermarket applications: Current status and future perspectives," *International Journal of Refrigeration*, vol. 93, no. 2018, pp. 269–310, 2018.

- [64] P. Gullo, K. Tsamos, A. Hafner, Y. Ge, and S. A. Tassou, "State-of-the-art technologies for transcritical R744 refrigeration systems—a theoretical assessment of energy advantages for European food retail industry," *Energy Procedia*, vol. 123, pp. 46–53, 2017.
- [65] M. Karampour and S. Sawalha, "State-of-the-art integrated CO<sub>2</sub> refrigeration system for supermarkets: A comparative analysis," *International Journal of Refrigeration*, vol. 86, 2018.
- [66] Y. T. Ge and S. A. Tassou, "Thermodynamic analysis of transcritical CO<sub>2</sub> booster refrigeration systems in supermarket," *Energy Conversion and Management*, vol. 52, no. 4, pp. 1868–1875, 2011.
- [67] V. Sharma, B. A. Fricke, and P. Bansal, "Evaluation of a transcritical CO<sub>2</sub> supermarket refrigeration system for the USA market," Oak Ridge National Lab.(ORNL), Oak Ridge, TN (United States);, Tech. Rep., 2015.
- [68] B. Fricke, S. Zha, V. Sharma, and J. Newel, "Laboratory Evaluation of a Commercial CO<sub>2</sub> Booster Refrigeration System," *Proc. of the 16th International Refrigeration and Air Conditioning Conference at Purdue*, p. Paper 2286, 2016.
- [69] S. Sawalha, "Theoretical evaluation of trans-critical CO<sub>2</sub> systems in supermarket refrigeration. Part II: System modifications and comparisons of different solutions," *International Journal of Refrigeration*, vol. 31, no. 3, pp. 525–534, 2008.
- [70] —, "Theoretical evaluation of trans-critical CO<sub>2</sub> systems in supermarket refrigeration. Part I: Modeling, simulation and optimization of two system solutions," *International Journal of Refrigeration*, vol. 31, no. 3, pp. 516–524, 2008.
- [71] V. Sharma, B. Fricke, and P. Bansal, "Comparative analysis of various CO<sub>2</sub> configurations in supermarket refrigeration systems," *International Journal of Refrigeration*, vol. 46, pp. 86–99, 2014.
- [72] P. Gullo, B. Elmegaard, and G. Cortella, "Advanced exergy analysis of a R744 booster refrigeration system with parallel compression," *Energy*, vol. 107, pp. 562–571, 2016.
- [73] P. Gullo and A. Hafner, "Thermodynamic Performance Assessment of a CO<sub>2</sub> Supermarket Refrigeration System with Auxiliary Compression Economization by using Advanced Exergy Analysis," *Int. J. Thermodynamics*, vol. 20, no. 4, pp. 220–227, 2017.
- [74] J. Schönenberger, A. Hafner, K. Banasiak, and S. Girotto, "Experience with ejectors implemented in a R744 booster system operating in a supermarket," in *11th IIR Gustav Lorentzen Conference on Natural Refrigerants, Hangzhou, China*, 2014.
- [75] A. Hafner, J. Schönenberger, K. Banasiak, and S. Girotto, "R744 ejector supported parallel vapour compression system," in *Proceedings of the 3rd IIR International Conference on Sustainability and Cold Chain, London, UK*, 2014, pp. 23–25.

- [76] P. Gullo, G. Cortella, and A. Polzot, "Energy and environmental comparison of commercial R744 refrigeration systems operating in warm climates," in *Proceedings of the 4th IIR Conference on Sustainability and the Cold Chain*, 2016, pp. 7–9.
- [77] P. Gullo, K. M. Tsamos, A. Hafner, K. Banasiak, T. G. Yunting, and S. A. Tassou, "Crossing CO<sub>2</sub> equator with the aid of multi-ejector concept: A comprehensive energy and environmental comparative study," *Energy*, vol. 164, pp. 236–263, 2018.
- [78] N. Abdin, A. Hafner, S. Girotto, F. Menten, Y. Pruss, and R. Savigliano, "CO<sub>2</sub> commercial refrigeration system in Jordan," *Proc. of 25th IIR International Congress of Refrigeration*, p. Paper 1044, 2019.
- [79] S. Minetto, R. Brignoli, C. Zilio, and S. Marinetti, "Experimental analysis of a new method for overfeeding multiple evaporators in refrigeration systems," *International Journal of Refrigeration*, vol. 38, pp. 1–9, 2014.
- [80] C. Amaris, K. M. Tsamos, and S. A. Tassou, "Analysis of an R744 typical booster configuration, an R744 parallel-compressor booster configuration and an R717/R744 cascade refrigeration system for retail food applications. Part 1: Thermodynamic analysis," *Energy Procedia*, vol. 161, pp. 259–267, 2019.
- [81] B. Ballot-Miguet, G. Dejardins, B. Quaro, A. Defruit, and D. Rousset, "Increasing the performances of a CO<sub>2</sub> refrigeration system using cool thermal energy storage for subcooling: a supermarket application," *Proc. of 25th IIR International Congress of Refrigeration*, p. Paper 726, 2019.
- [82] A. Beghi, M. Rampazzo, and S. Zorzi, "Reinforcement learning control of transcritical carbon dioxide supermarket refrigeration systems," *IFAC-PapersOnLine*, vol. 50, no. 1, pp. 13 754–13 759, 2017.
- [83] G. Cortella, P. D'Agaro, and M. A. Coppola, "Simulations and field tests of a CO<sub>2</sub> refrigerating plant for commercial refrigeration," in *Proceedings of the 13th IIR Gustav Lorentzen Conference on Natural Refrigerants*, 2018.
- [84] P. D'Agaro, M. A. Coppola, and G. Cortella, "Field tests, model validation and performance of a CO<sub>2</sub> commercial refrigeration plant integrated with HVAC system," *International Journal of Refrigeration*, vol. 100, pp. 380–391, 2019.
- [85] V. Casson, L. Cecchinato, M. Corradi, E. Fornasieri, S. Girotto, S. Minetto, L. Zamboni, and C. Zilio, "Optimisation of the throttling system in a CO<sub>2</sub> refrigerating machine," *International Journal of Refrigeration*, vol. 26, no. 8, pp. 926–935, 2003.
- [86] S. Girotto, S. Minetto, and P. Neksa, "Commercial refrigeration system using CO<sub>2</sub> as the refrigerant," *International Journal of Refrigeration*, vol. 27, no. 7, pp. 717–723, 2004.
- [87] Á. Á. Pardiñas, A. Hafner, and K. Banasiak, "Novel integrated CO<sub>2</sub> vapour compression racks for supermarkets. Thermodynamic analysis of possible system configurations and influence of operational conditions," *Applied Thermal Engineering*, vol. 131, pp. 1008–1025, 2018.

- [88] R. Cabello, D. Sánchez, R. Llopis, and E. Torrella, "Experimental evaluation of the energy efficiency of a CO<sub>2</sub> refrigerating plant working in transcritical conditions," *Applied Thermal Engineering*, vol. 28, no. 13, pp. 1596–1604, 2008.
- [89] L. Cecchinato, M. Corradi, and S. Minetto, "A critical approach to the determination of optimal heat rejection pressure in transcritical systems," *Applied Thermal Engineering*, vol. 30, no. 13, pp. 1812–1823, 2010.
- [90] M. Graziano, V. Energy, I. M. Pritoni, and W. C. E. Center, "Cloudfridge: a cloud-based control system for commercial refrigeration systems," *ACEEE Summer Study on Energy Efficiency in Buildings, Tech. Rep*, 2014.
- [91] G. Lorentzen, "Revival of carbon dioxide as a refrigerant," *International Journal of Refrigeration*, vol. 17, no. 5, pp. 292–301, jan 1994. [Online]. Available: <https://www.sciencedirect.com/science/article/pii/0140700794900590>
- [92] S. A. Tassou, J. S. Lewis, Y. T. Ge, A. Hadawey, and I. Chaer, "A review of emerging technologies for food refrigeration applications," *Applied Thermal Engineering*, vol. 30, no. 4, pp. 263–276, 2010. [Online]. Available: <http://dx.doi.org/10.1016/j.applthermaleng.2009.09.001>
- [93] G. Panozzo, G. Minotto, and A. Barizza, "Transport et distribution de produits alimentaires: situation actuelle et tendances futures," *International Journal of Refrigeration*, vol. 22, no. 8, pp. 625–639, 1999.
- [94] IIR, "Guide to Refrigerated Transport," 1995.
- [95] A. Stack and D. P. Finn, "Modeling and validation of a multi-evaporator vapor compression cycle subject to non-uniform loading in transport refrigeration applications," *Proc. of the 9th International Refrigeration and Air Conditioning Conference at Purdue*, p. Paper 617, 2002.
- [96] G. A. Ibrahim, "Effect of sudden changes in evaporator external parameters on a refrigeration system with an evaporator controlled by a thermostatic expansion valve," *International Journal of Refrigeration*, vol. 24, no. 6, pp. 566–576, 2001.
- [97] R. Shah, A. Alleyne, and C. W. Bullard, "Dynamic Modeling and Control of Multi-Evaporator Air-Conditioning Systems," *ASHRAE Transactions*, vol. 110, p. 109, 2004.
- [98] N. Lawrence, S. Elbel, and P. S. Hrnjak, "Design and validation of a transcritical CO<sub>2</sub> mobile refrigerated container system for military applications," in *13th IIR Gustav Lorentzen Conference on Natural Refrigerants*. International Institute of Refrigeration, 2018, pp. 882–890.
- [99] R. B. Barta, J. J. Hugenroth, and E. A. Groll, "Modeling and control strategy of a transcritical carbon dioxide cycle for application in multi-temperature refrigerated container systems," in *13th IIR Gustav Lorentzen Conference*, 2018.
- [100] S. S. Bertsch and E. A. Groll, "Two-stage air-source heat pump for residential heating and cooling applications in northern U.S. climates," *International Journal of Refrigeration*, vol. 31, no. 7, pp. 1282–1292, nov 2008. [Online]. Available: <https://www.sciencedirect.com/science/article/pii/S0140700708000273>

- [101] T. He, C. Xia, Y. Zhao, L. Li, and P. Shu, "An Experimental Study on Energy Recovery by a Pelton-Type Expander in a Domestic Refrigeration System," *HVAC&R Research*, vol. 15, no. 4, pp. 785–799, 2009. [Online]. Available: <https://www.tandfonline.com/doi/abs/10.1080/10789669.2009.10390864>
- [102] X. Wang, Y. Hwang, and R. Radermacher, "Two-stage heat pump system with vapor-injected scroll compressor using R410A as a refrigerant," *International Journal of Refrigeration*, vol. 32, no. 6, pp. 1442–1451, 2009. [Online]. Available: <http://www.sciencedirect.com/science/article/pii/S0140700709000814>
- [103] X. Xu, Y. Hwang, and R. Radermacher, "Transient and steady-state experimental investigation of flash tank vapor injection heat pump cycle control strategy," *International Journal of Refrigeration*, vol. 34, no. 8, pp. 1922–1933, dec 2011. [Online]. Available: <https://www.sciencedirect.com/science/article/pii/S0140700711001927>
- [104] M. Wang, Y. Zhao, F. Cao, G. Bu, and Z. Wang, "Simulation study on a novel vane-type expander with internal two-stage expansion process for R-410A refrigeration system," *International Journal of Refrigeration*, vol. 35, no. 4, pp. 757–771, jun 2012. [Online]. Available: <https://www.sciencedirect.com/science/article/pii/S0140700711002945>
- [105] Z. Zhang and L. Tian, "Exergy Analysis of a Subcritical Refrigeration Cycle with an Improved Impulse Turbo Expander," *Entropy*, vol. 16, no. 8, pp. 4392–4407, 2014.
- [106] R. B. Barta, D. Ziviani, and E. A. Groll, "Experimental analyses of different control strategies of an R-410A split-system heat pump by employing a turbomachinery expansion recovery device," *International Journal of Refrigeration*, vol. 112, pp. 189–200, 2020. [Online]. Available: <https://doi.org/10.1016/j.ijrefrig.2019.12.027>
- [107] D. Ladd, "Systems and methods for multi stage refrigeration," *U.S. Patent Number US 10,465,983 B2*, 2019.
- [108] —, "Systems and methods for multi stage refrigeration," *U.S. Patent Number US 10,514,201 B2*, 2019.
- [109] —, "Systems and methods for multi stage refrigeration," *U.S. Patent Number US 10,514,202 B2*, 2019.
- [110] —, "Systems and Methods for Multi-Stage Refrigeration," *U.S. Patent Number US 2018 / 0231304 A1*, 2018.
- [111] F. Liu, E. A. Groll, and D. Li, "Investigation on performance of variable geometry ejectors for CO<sub>2</sub> refrigeration cycles," *Energy*, vol. 45, no. 1, pp. 829–839, 2012. [Online]. Available: <http://www.sciencedirect.com/science/article/pii/S0360544212005385>
- [112] ARI, "ARI 540-99, Positive Displacement Refrigerant Compressors and Compressor Units," pp. Arlington, VA: Air-Conditioning and Refrigeration, 1999.
- [113] A. 44, *Refrigeration Handbook (IP)*, Atlanta, 2014.

- [114] F. Liu and E. Groll, "Recovery of Throttling Losses by a Two-Phase Ejector in a Vapor Compression Cycle," *ARTI Project 10110-01 Final Report*, 2008.
- [115] B. N. Taylor and C. E. Kuyatt, "NIST Technical Note 1297 1994 Edition, Guidelines for Evaluating and Expressing the Uncertainty of NIST Measurement Results," *National Institute of Standards and Technology*, pp. 1–20, 1994.
- [116] K. Banasiak, A. Hafner, and T. Andresen, "Experimental and numerical investigation of the influence of the two-phase ejector geometry on the performance of the R744 heat pump," *International Journal of Refrigeration*, vol. 35, no. 6, pp. 1617–1625, 2012.
- [117] A. Attou and J.-M. Seynhaeve, "Steady-state critical two-phase flashing flow with possible multiple choking phenomenon: Part 1: physical modelling and numerical procedure," *Journal of Loss Prevention in the Process Industries*, vol. 12, no. 5, pp. 335–345, 1999.
- [118] C. E. Brennen, "Fundamentals of Multiphase Flows," 2005.
- [119] K. E. Ringstad, Y. Allouche, P. Gullo, Å. Ervik, K. Banasiak, and A. Hafner, "A detailed review on CO<sub>2</sub> two-phase ejector flow modeling," *Thermal Science and Engineering Progress*, p. 100647, 2020.
- [120] B. Hubacher and E. A. Groll, "Measurement of Performance of Carbon Dioxide Compressors," *ARTI Project 611-10070 Final Report*, vol. Herrick La, no. 2002-24, pp. 140–141, 2002.
- [121] H. Elmqvist, "A structured model language for large continuous systems," *Ph.D. Thesis, Department of Automatic Control, Lund Institute of Technology*, 1978.
- [122] A. Desideri, "Dynamic Modeling of Organic Rankine Cycle Power Systems," PhD Thesis, University of Liege, 2016.
- [123] H. Tummescheit, "Design and implementation of object-oriented model libraries using modelica," Ph.D. dissertation, Lund University, 2002.
- [124] J. Bonilla, L. J. Yebra, and S. Dormido, "Chattering in dynamic mathematical two-phase flow models," *Applied Mathematical Modelling*, vol. 36, no. 5, pp. 2067–2081, 2012.
- [125] V. Mehrmann and L. Wunderlich, "Hybrid systems of differential-algebraic equations - Analysis and numerical solution," *Journal of Process Control*, vol. 19, no. 8, pp. 1218–1228, 2009. [Online]. Available: <http://dx.doi.org/10.1016/j.jprocont.2009.05.002>
- [126] "Dassault Systems - DYMOLA Systems Engineering," 2019. [Online]. Available: <https://www.3ds.com/products-services/catia/products/dymola>
- [127] TLK-thermo, "TIL Suite simulates Thermal Systems," 2018. [Online]. Available: <https://www.tlk-thermo.com>
- [128] S. E. Mattson, H. Elmqvist, and J. F. Broenink, "Modelica: An international effort to design the next generation modelling language," *Journal A, Benelux Quarterly Journal on Automatic Control*, vol. 38, no. 3, pp. 16–19, 1998.



- [129] E. W. Lemmon, M. L. Huber, and M. O. McLinden, “NIST reference fluid thermodynamic and transport properties–REFPROP,” *NIST standard reference database*, vol. 23, p. v7, 2002.
- [130] R. Petzold, “A Description of DASSL: A Differential/Algebraic System Solver,” 1982.
- [131] H. Baehr and K. Stephan, *Waerme-und Stoffuebertragung, 2 Auflage*. Springer, 1996.
- [132] A. Cavallini, D. D. Col, L. Doretti, M. Matkovic, L. Rossetto, C. Zilio, and G. Censi, “Condensation in horizontal smooth tubes: a new heat transfer model for heat exchanger design,” *Heat Transfer Engineering*, vol. 27, no. 8, pp. 31–38, 2006.
- [133] C. Kondou and P. Hrnjak, “Heat rejection from R744 flow under uniform temperature cooling in a horizontal smooth tube around the critical point,” *International Journal of Refrigeration*, vol. 34, no. 3, pp. 719–731, 2011.
- [134] P. K. Konakov, “A new correlation for the friction coefficient in smooth tubes,” *Berichte der Akademie der Wissenschaften der UDSSR*, vol. 51, 1946.
- [135] Y. J. Chang and C. C. Wang, “A generalized heat transfer correlation for louver fin geometry,” *International Journal of Heat and Mass Transfer*, vol. 40, no. 3, pp. 533–544, 1997.
- [136] M. H. Kim and C. W. Bullard, “Air-side thermal hydraulic performance of multi-louvered fin aluminum heat exchangers,” *International Journal of Refrigeration*, vol. 25, no. 3, pp. 390–400, 2002.
- [137] G. A. Longo, G. Righetti, and C. Zilio, “A new computational procedure for refrigerant condensation inside herringbone-type Braze Plate Heat Exchangers,” *International Journal of Heat and Mass Transfer*, vol. 82, pp. 530–536, 2015.
- [138] M. Holger, “VDI Heat Atlas,” *VDI Heat Atlas*, 2010.
- [139] J. M. Mendoza-miranda, A. Mota-babiloni, and J. J. Ramírez-minguela, “Comparative evaluation of R1234yf, R1234ze (E) and R450A as alternatives to R134a in a variable speed reciprocating compressor,” *Energy*, vol. 114, pp. 753–766, 2016.
- [140] H. Li and J. E. Braun, “A method for modeling adjustable throat-area expansion valves using manufacturers’ rating data,” *HVAC&R Research*, vol. 14, no. 4, pp. 581–595, 2008.
- [141] K. E. Gungor and R. H. S. Winterton, “Simplified general correlation for saturated flow boiling and comparisons of correlations with data,” *Chemical Engineering Research & Design*, vol. 65, no. 2, pp. 148–156, 1987.
- [142] J. Zhu and S. Elbel, “Experimental investigation of a novel expansion device control mechanism: Vortex control of initially subcooled flashing R134a flow expanded through convergent-divergent nozzles,” *International Journal of Refrigeration*, vol. 85, pp. 167–183, 2018. [Online]. Available: <https://doi.org/10.1016/j.ijrefrig.2017.09.023>

- [143] R. Span and W. Wagner, “A new equation of state for carbon dioxide covering the fluid region from the triple-point temperature to 1100 K at pressures up to 800 MPa,” *Journal of physical and chemical reference data*, vol. 25, no. 6, pp. 1509–1596, 1996.